Nelson, Kayleigh (2020) *Materials fundamental study of the properties and deformation of titanium alloys at room temperature.* PhD thesis.

https://theses.gla.ac.uk/75180/

Copyright and moral rights for this work are retained by the author

A copy can be downloaded for personal non-commercial research or study, without prior permission or charge

This work cannot be reproduced or quoted extensively from without first obtaining permission in writing from the author

The content must not be changed in any way or sold commercially in any format or medium without the formal permission of the author

When referring to this work, full bibliographic details including the author, title, awarding institution and date of the thesis must be given

Enlighten: Theses
https://theses.gla.ac.uk/
research-enlighten@glasgow.ac.uk



University of Glasgow

Materials Fundamental Study of the Properties and Deformation of Titanium Alloys at Room Temperature.

Kayleigh Nelson

Submitted in fulfilment of the requirements for the
Degree of Doctor of Philosophy

School of Engineering
College of Science and Engineering
University of Glasgow

April 2019

Declaration of Originality

All work in this thesis has been carried out by the author unless otherwise explicitly stated.

The author confirms that the following thesis has been composed by herself without undue assistance. All references have been clearly stated in accordance with departmental requirements, in both the text and the bibliography. All data and findings herein belong to the author and have not been falsified or embellished.

This work has not been previously, or concurrently, submitted for other courses or within any other exam processes.

Signed,

Kayleigh Nelson

Abstract

The titanium alloy, Ti-6Al-4V is investigated to increase the current understanding of deformation in this significant alloy at a variety of length-scales. The strain rate sensitivity of titanium alloys is generally considered negligible, however, parallels observed in the rate dependant behaviour have led to a renewed interest in the room temperature deformation. The results of a strain rate jump (SRJ) have been examined using combined high energy x-ray diffraction and microscopy techniques. This deformation is compared to that of constant strain rates where the SRJ is observed to cause texture strengthening and good alignment post jump with the higher constant strain rate for billet Ti-6Al-4V. Microstructural changes have been tracked during deformation via in situ high energy x-ray diffraction in the form of lattice strain evolution.

Rolled plate Ti-6Al-4V products (UDR and CR) have been compared with the cross rolled material exhibiting the highest strength in the direction of loading. Crystallographic texture has been examined using EBSD analysis. Lattice strain evolution is captured, again using synchrotron high energy XRD. Good macroscopic alignment is observed in the stress-strain response between SRJ and constant strain rate conditions where the timing of the jump does not appear to influence this phenomenon. The strain rate sensitivity cannot be adequately captured macroscopically by a single parameter as lattice strain evolution is dependant on crystallography. An effective moduli dependant on material texture is suggested for Ti-6Al-4V product forms.Computational, CPFE modelling has been performed on various instantiated microstructures to enable the prediction of lattice strain evolution for each of the product forms analysed. The impact of macrozones and texture elements is observed to influence this evolution.

The β phase in Ti-6Al-4V is often neglected in analysis due to its low volume fraction, the in situ examination of both Ti-6Al-4V and Ti-6.5Al, an alloy designed to replicate the α phase, question the validity of this simplification where the omission of the β phase is observed to dampen the strain hardening response compared to Ti-6Al-4V. α-phase Ti-Al alloys of varying aluminium contents have also been examined showing differing hardening responses, strain rate sensitivity and increasing strength with increased aluminium content.

Acknowledgements

The author would like to acknowledge those who have made the work presented here possible. The research has been sponsored by the EPSRC, in the form of a DTA studentship, by Rolls-Royce, for insightful discussions, continued support and additional funding and by Timet, for supplying the material to make these experiments possible.

Additional thanks to those at Cornell University for welcoming me as a Visiting Scientist, notably Professors Matt Miller and Paul Dawson for their supervision and Dr Darren Pagan for being instrumental in the success of all experiments at CHESS.

Many people have been integral to the completion of this work in a multitude of ways, each of which I am extremely thankful for. To my extended list of primary supervisors, Dr Euan Wielewski, Prof Liz Tanner, Dr Andrew McBride and everyone else in the Materials & Manufacturing Research Group, cheers guys!

Finally, the continued support of my family and friends has been inspirational and undoubtedly made an impact on my success, for which I am extremely grateful. Liam, cheers for putting up with me during the whole process and hearing far more about it than anyone should ever have to!

Nomenclature

Abbreviations used within the text have been compiled here alphabetically.

AGI	Average Grain Intercept
APS	Advanced Photon Source
BC	Boundary Condition
BCC	Body-Centred Cubic
BSE	Back-Scattered Electron
CALPHAD	Computer Coupling of Phase Diagrams and Thermochemistry
CCD	Charge-Coupled Device
CHESS	Cornell High-Energy Synchrotron Source
CPFE	Crystal Plasticity Finite Element
CP	Crystal Plasticity
CR	Cross-Rolled
CRSS	Critically Resolved Shear Stress
DIC	Digital Image Correlation
DOF	Depth of Field
EBSD	Electron Back-Scatter Diffraction
EBSP	Electron Back-Scatter Pattern
EDM	Electrical discharge machining
EDX	Energy Dispersive X-ray spectroscopy
FCC	Face-Centred Cubic
FEA	Finite Element Analysis
GAM	Grain Average Misorientation

GND	Geometrically Necessary Dislocation
GRM	Grain Relative Misorientation
GUI	Graphical User Interface
HAZ	Heat Affected Zone
HCP	Hexagonal Close-Packed
HDF	Hierarchical Data Format
HEDM	High Energy Diffraction Microscopy
IPF	Inverse Pole Figure
ISAAC	Imaging Spectroscopy and Analysis Centre
MSST	Maximum Shear Stress Theory
ODF	Orientation Distribution Function
PF	Pole Figure
RCL	Relative Characteristic Length
RHS	Right Hand Side
RD	Rolling Direction
RVE	Representative Volume Element
SEM	Scanning Electron Microscope
SLM	Selective Laser Melting
SRS	Strain Rate Sensitivity
TIFF	Tagged Image File Format
TD	Transverse Direction
UDR	Uni-Directionally Rolled
UTS	Ultimate Tensile Strength
XRD	X-Ray Diffraction

Contents

Declaration of Originality i

Abstract ii

Acknowledgements iii

Nomenclature iv

Introduction x

I Titanium: Material properties, continuum modelling and experimental procedures 1

1 Material Description and Production of Titanium Alloys 2

1.1 Extraction and Alloy Production . . . 2
1.2 Methods of Processing Titanium Alloys . . . 3
1.3 Alloying . . . 5
1.3.1 Constituent Materials and Phases of Titanium alloys . . . 6
1.4 Ti-6Al-4V Products . . . 8
1.4.1 Billet Material . . . 9
1.4.2 Unidirectionally Rolled Material . . . 9
1.4.3 Cross-Rolled Material . . . 10
1.4.4 Ti-Al alloys of varying aluminium content . . . 11
1.5 Heat Treatment Regimes . . . 11
1.6 Microstructure . . . 12
1.7 Macrozones . . . 14
1.8 Crystallography . . . 15
1.8.1 Representing Orientations . . . 17
1.8.2 Representing Crystallographic Texture . . . 19

2 Continuum Description of Polycrystalline Plasticity 23

2.1 Introduction . . . 23
2.2 Dislocation and Slip . . . 24
2.3 Mathematical Modelling of Plasticity . . . 29

2.4 Crystal Plasticity . . . 31
2.5 Kinematics . . . 32
2.5.1 FEpX Model . . . 33
2.6 Yield Function . . . 35

3 Experimental Methodology and Data Analysis 37
3.1 Tensile Testing . . . 37
3.1.1 Specimen Design . . . 38
3.2 High Energy X-Ray Diffraction . . . 40
3.2.1 Diffraction Principles . . . 40
3.2.2 Synchrotron High Energy X-ray Diffraction . . . 41
3.2.3 Powder Diffraction . . . 43
3.2.4 Equipment . . . 45
3.2.5 DIC and Load Frame Data . . . 48
3.2.6 Synchrotron Data Collection . . . 50
3.3 Powder Diffraction Analysis . . . 52
3.3.1 Azimuthal Bin Width . . . 56
3.4 Lattice Strain Evolution . . . 58
3.5 Electron Back-scatter Diffraction . . . 59
3.5.1 SEM Operation . . . 59
3.5.2 EBSD Preparation . . . 63
3.5.3 EBSD Post Processing . . . 64

II Experimental Results and Computational Simulations 66

4 Strain rate sensitivity of Ti-6Al-4V using high energy synchrotron XRD 67
4.1 Macroscopic Response . . . 67
4.1.1 EBSD Analysis . . . 68
4.1.2 Lattice Strains . . . 74
4.1.3 Strain Rate Evolution . . . 77
4.2 Discussion . . . 78
4.3 Conclusions . . . 79

5 High energy XRD of commercial Ti-6Al-4V rolled plates 81
5.1 Overview . . . 81
5.2 Effect of the SRJ at different engineering strains . . . 84
5.2.1 Lattice Strains . . . 84
5.2.2 EBSD . . . 89
5.3 Comparison between UDR and CR material . . . 92
5.3.1 Macroscopic Response . . . 92
5.3.2 EBSD . . . 94
5.3.3 Lattice Strains - α Phase . . . 96

5.4 Comparison between CR material in the rolling direction and at 45 degrees. 101
5.4.1 Macroscopic Response 102
5.4.2 Lattice Strains 103
5.5 Strain Rate Sensitivity 108
5.5.1 Lattice Strain Rate Sensitivity 110
5.6 UDR Initial Behaviour 110

6 Crystal Plasticity Finite Element Method 112
6.1 Building Representative Models 112
6.1.1 Pre-processing - Mesh Instantiation & Visualisation 113
6.1.2 Initial Parameter Studies 113
6.1.3 Boundary Conditions 116
6.1.4 Mesh Convergence 119
6.1.5 Elastic Constants 121
6.1.6 Slip System Strengths 122
6.1.7 Randomised Microstructures 124
6.2 Modelling Ti-6Al-4V 126
6.2.1 Product Forms 127
6.2.2 Modelling Macrozones 130
6.3 Computational Results 132
6.4 3,000 Grain Instantiations 133
6.4.1 Macroscopic Response 133
6.4.2 Lattice Strain Response 135
6.4.3 Constant Strain Rate comparison 137
6.5 1,500 Grains (symmetric) 141
6.5.1 Macroscopic Response 141
6.5.2 3D Results 142
6.5.3 Lattice Strain Response 144
6.6 Discussion & Conclusions 149

III Further Experimental Studies of Specific Industrial Interest 150

7 Aluminium Content in Titanium alloys 151
7.1 Macroscopic Response 152
7.2 Lattice Strain Measurements 153
7.3 Discussion 161

8 Single and dual-phase titanium alloys 162
8.1 Macroscopic Response 162
8.2 Lattice Strain Response 163
8.3 Microstructure 166
8.4 Discussion 169

8.5 Conclusions 171

9 Summary & Conclusions **173**
9.1 Conclusions 173
9.2 Limitations 175
9.3 Potential Future Work 175

A Specimen Design Drawings **177**

B Uniaxial tensile testing - failure behaviour **180**
B.1 Setup 180
B.2 Results 181

Introduction

Titanium alloys have great industrial significance in the aerospace sector. They are used in many high value engineering applications, including in critical jet engine components due to their high specific strength and good resistance to corrosion. Significant gains in jet engine performance could be realised if engineers had modelling/simulation tools capable of better predicting the deformation and failure behaviour of this important class of materials. To this end, this thesis provides an integrated experimental and computational study of the fundamental properties and deformation of titanium alloys at room temperature.

The research presented here is directly applicable to the aerospace industry, in particular the design and life-extension of jet engine components. Furthering the understanding and analysis of the onset and propagation of deformation and failure in titanium alloys has the potential to significantly improve the performance of jet engines. However, understanding deformation and failure in titanium alloys is non-trivial, as microstructure, crystallographic texture and the resultant mechanical properties are simultaneously anisotropic and heterogeneous. The use of Ti-based alloys is ubiquitous in jet engines, where Figure 1 highlights the main alloys and their applications [6]. Increasing titanium usage is also observed in airframes [91].

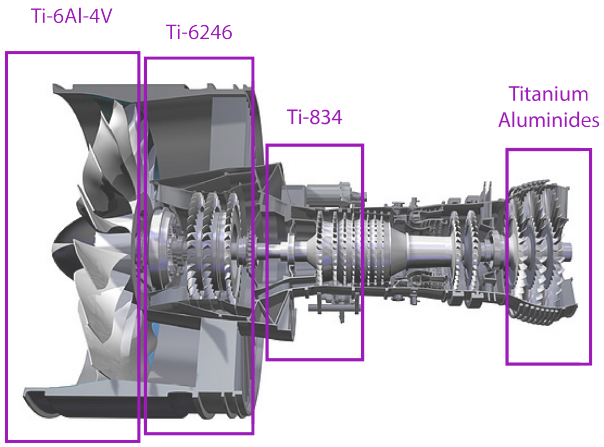


Figure 1: Representation of jet engine internals, highlighting the areas where different titanium alloys have been utilised, adapted from [63, 83]. Note this illustration is indicative of the use of titanium alloys and does not directly relate to the specific engine pictured.

Materials in service do not typically abide by the controlled monotonic or cyclic loading used heavily in research. Consequently, it is important to not only understand the behaviour under these conditions but at the in service loading that is difficult to quantify, this is where strain rate effects are significant. The response of a material at a particular time and strain rate can be fairly well predicted. However, in changing between these states, it is difficult to predict whether further detrimental effects are being imposed on the component. This research aims to address this problem through the examination of jumps in strain rate.

The research focus here is the room temperature deformation of titanium alloys with the aim of developing and enhancing modelling tools capable of predicting deformation and failure. Yield in titanium alloys will be explored using in situ micro-mechanical testing and advanced microscopy techniques. Data generated from these experiments will be used to inform advanced crystal scale finite element simulations that capture deformation and potentially predict eventual failure at the microscopic scale. Differences between the simulations and experiments will be investigated to enable further refinement of predictive capabilities. Modelling increases the available data where experiments are not only expensive but constrained. A variety of commercial Ti-6Al-4V product forms are studied in this work with particular emphasis on the strain rate sensitivity and the effect of strain rate jumps at the microscopic, crystal and macroscopic scales.

The time dependant mechanical behaviour of titanium alloys is responsible for a wide range of non-intuitive failure modes. Whilst cold dwell fatigue is probably the most documented, notched high cycle fatigue (HCF) behaviour is equally important with respect to component design and alloy optimisation. The strain field in a notch and the resulting stress 'offload' have clear similarities to dwell in that there is a large property debit for poorly developed microstructures. However, the experimental and modelling difficulties of such regimes are only just beginning to allow insight to the mechanistic stack up associated with the large HCF strength differentials exhibited by different product forms of the same alloy. It is interesting to note that interstitials such as O, N and C have a strong influence on rate sensitivity from -50°C to 200°C in a strain rate range typically used in tensile testing. As such any inference around the behaviour in component load regimes where longer load cycles or strain control exists should be made with caution.

This thesis has been segmented into three parts. Part I focuses on the materials and experimental methodologies. It contains a continuum description of deformation, defining terms used throughout this thesis. Part II contains the bulk of the experimental work including high energy x-ray diffraction experiments where crystal-scale computational modelling has been used to relate to experiments and improve the reliability of results. The third and final part details further high energy x-ray diffraction experiments which are of industrial interest. A summary of the thesis and suggested future work concludes the presentation.

Part I

Titanium: Material properties, continuum modelling and experimental procedures

Part I serves as an introduction to the materials used, the deformation of polycrystalline materials and a detailed overview of the experiments performed.

Chapter 1

Material Description and Production of Titanium Alloys

Named after the mythical titans, titanium was discovered independently by W. Gregor in the UK in 1791 and by M.H. Klaproth in Germany in 1793. As the ninth most abundant element in the earth's crust (4^{th} metallic element), titanium is a strong, hard yet light metal. Titanium has a comparatively high strength, with titanium-based alloys being as strong as low-carbon steels whilst around 45% less dense. These alloys are also twice as strong as aluminium alloys but only 60% more dense [64]. The corrosion resistance of titanium and its alloys is high due to titanium's affinity for interaction with oxygen. This allows for the almost instantaneous creation of a thin surface oxide layer which acts as a barrier to corrosion. Due to this unique combination of properties, titanium alloys are highly desirable in aerospace applications. Bio-compatibility is also high for titanium, allowing for its extensive use in medical impants. Novel advances in titanium alloys for biomedical applications [152] and the 3D printing of titanium-based alloys [32] are being realised.

The energy requirements and expenses incurred in the complex extraction and processing regimes of titanium are significant, preventing the widespread adoption of titanium and its alloys despite the aforementioned benefits [59]. The inherent hardness and issues due to the chemistry/oxidation behaviour cause excessive tool wear during the machining of titanium based alloys, further increasing the manufacturing costs in comparison to more common engineering materials [168].

1.1 Extraction and Alloy Production

The titanium extraction process is costly and difficult with the pure element finally being extracted in 1910, over 100 years after its inital discovery. The extraction of titanium begins with the chlorination of rutile ore, mainly $Ti0_2$, in a mixture of chlorine and coke to produce titanium tetrachloride ($TiCl_4$). The $TiCl_4$ is then reduced by the Kroll process, often using magnesium, in an inert atmosphere, ususally argon, producing a

titanium sponge and a magnesium chloride by-product [111]. This titanium sponge is generally mixed with alloying elements, where multi-stage melting is employed to produce ingots which are then processed via re-melting and finishing. A schematic of the overall process is shown in Figure 1.1. Recycling of magnesium, chlorine and scrap titanium alloys can be incorporated into this expensive process. For example, the oxidisation of $TiCl_4$ produces titanium dioxide (which is widely used in various products such as paints and plastics) and chlorine. This chlorine may be re-introduced into the early chlorination process.

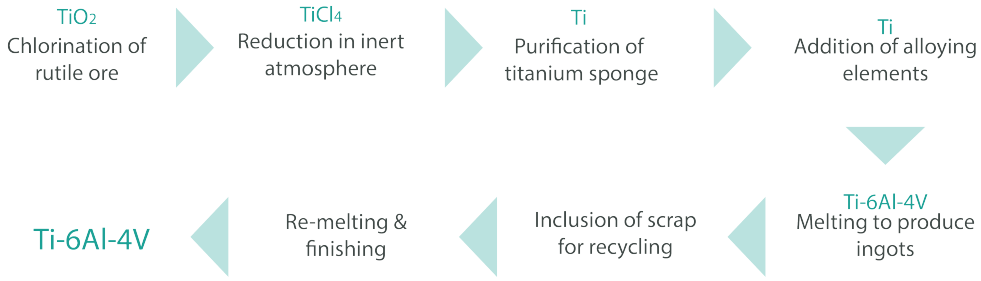


Figure 1.1: Process of titanium alloy creation from rutile ore, using Ti-6Al-4V as an example and omitting common recycling procedures for clarity.

An inert atmosphere is important in titanium alloy production due to the reactivity of titanium. Titanium normally produces an oxide layer, however, during processing, molten titanium is unable to form a stable oxide layer and may spontaneously ignite on contact with air. Further dangers include water leaks into furnaces which may cause explosions and the dangers involved in the handling of titanium powders [163]. Titanium sponge is also sensitive to air, therefore an inert atmosphere is again employed in the sponge production process to ensure the highest quality end product.

1.2 Methods of Processing Titanium Alloys

The aerospace industry requires premium quality titanium alloys, any inclusions or defects contained in titanium alloys for these critical applications will have significant detrimental effects; at best these defective materials will be recycled as scrap. The incorporation of a plasma or electron beam cold hearth melting (EB-CHM) process is used to ensure products are of very high quality and contain as few defects as possible [230]. The two major processes currently used in titanium alloy production are EB-CHM and vacuum arc re-melting (VAR).

Electron Beam - Cold Hearth Melting

Electron beam cold hearth melting, EB-CHM as outlined in Figure 1.2, is used in the production of titanium alloys where the cold hearth process melts, refines and recrystallises the material. Input raw materials are melted by the electron beam and, in melt form, the material flows under vacuum conditions. High-density contaminants, which would otherwise form inclusions, are removed via gravity separation in the cold hearth,

where they sink into the 'skull'. The conditions of the EB-CHM process mean low density inclusions are subject to very high temperatures in the melt over a long period of time causing them to dissipate, effectively removing them from the end product [166]. This method is increasingly effective due to continuing advances in the control of the heat flux within the molten metal. The refined molten metal is finally channelled into the water-cooled copper crucible and forms ingots. In comparison to the traditional triple VAR process, EB-CHM produces very clean metal alloys with few remaining impurities due to the vacuum aiding the vaporisation of volatile impurities. As described below, VAR alone is generally unable to remove all of these impurities. Low-cost raw material forms, including recycled titanium scrap, can be re-used in the cold hearth melting of titanium alloys effectively. A further advantage of this melting is the ability to decouple the heat input from the melt rate, where this is intrinsically linked in VAR.

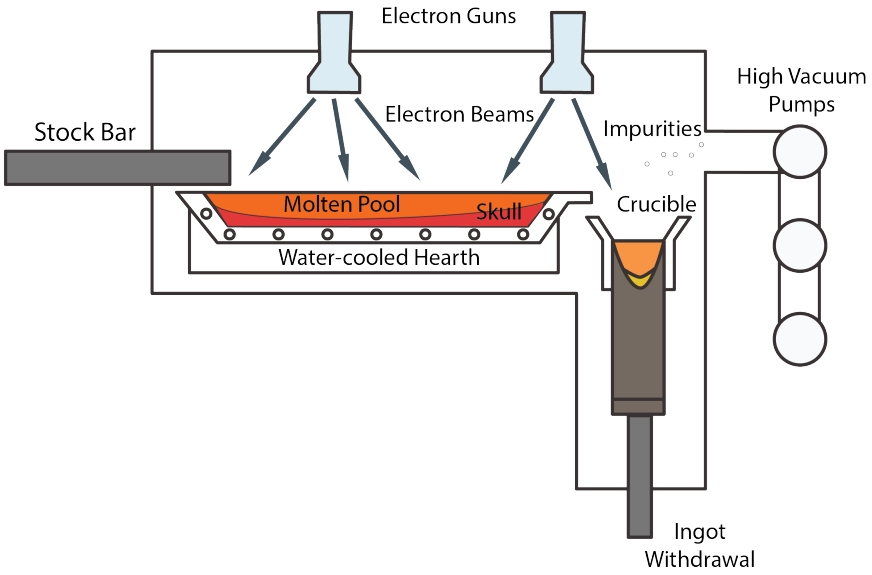


Figure 1.2: Schematic showing the overall electron beam cold hearth melting process, re-drawn from [181].

The EB-CHM process is used widely in the production of commercially pure titanium (cp-Ti). Accurate control of material composition is required, limiting the use of EB-CHM for titanium alloys. In this case, subsequent vacuum arc remelting is incorporated to ensure homogenisation of material [165]. Additionally, in Ti-6Al-4V, a significant proportion of the aluminium is evaporated during the EB-CHM process, therefore accurate prediction and compensation for this loss is required [182]. Alternatively, plasma cold hearth melting is used where a high level of chemistry control is required.

Vacuum Arc Remelting

Vacuum Arc Remelting (VAR) is often incorporated in processing, post EB-CHM, to ensure a homogeneous chemical composition throughout the ingot, see Figure 1.3. VAR is used frequently in high value applications, as in the double or triple re-melted VAR process, which has been used in the creation of a variety of titanium

products due to its simplicity and versatility. The VAR process is performed in a vast copper cylindrical crucible, where, in the vacuum furnace, the ingot is treated as an electrode and the material is melted within the vacuum chamber. A large DC current is fed through the electrode causing it to melt. This current creates an arc between the electrode and the melted ingot at the base, allowing for a continuous melt, hence the term vacuum arc remelting. As drops from the melting electrode fall into the melt pool of the solidifying ingot at the base of the chamber, the exposed surface area of each drop causes gases (and therefore impurities) to be evaporated from the product [54]. This leads to a uniform alloy product with homogeneous chemical and physical properties. The VAR process requires a constant melt rate. However this is often difficult to achieve, resulting in perturbations during solidification, potentially leading to adverse material properties [217].

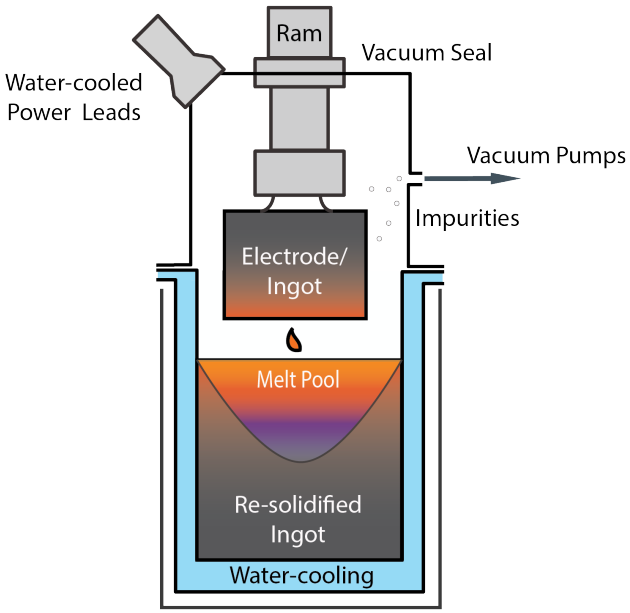


Figure 1.3: Schematic showing the vacuum arc re-melting process, adapted from [36].

1.3 Alloying

Most of the titanium extracted globally is used in alloy production, including the comercially pure Ti alloy series. Titanium loses strength with increasing temperature. Alloying aims to improve its working range and machinability. The future of titanium lies in new innovations in titanium alloy development, where alloying allows materials to be desgined with a specific combination of material properties [24]. Novel alloying advancements are being realised, such as a very hard cubic Ti-Au alloy, which is approximately 4 times harder than pure titanium [191].

In the aerospace industry, titanium alloys are traditionally used for airframes and in aero-engines due to their structural properties, where high specific strength and good corrosion resistance are required [132]. cp-Ti is used in air-frames due to its strength and high formability. Alloys such as Ti-6Al-4V and Ti-6Al-2Sn-

4Zr-2Mo are used within jet engines due to the requirement for high strength and heat resistant materials. The applicability of titanium alloys to the consumer automotive industry is limited primarily due to cost, as although raw material is abundant, extraction and specialised production are prohibitively expensive [177].

1.3.1 Constituent Materials and Phases of Titanium alloys

Titanium, as an allotropic metal, may exist as either a close-packed hexagonal (HCP) structure, common in elemental metals, or as a body centred cubic (BCC) structure above the beta transus temperature, approximately 883°C for pure titanium. The BCC beta phase remains stable up to the melting point of titanium (1677°C).

The classification of titanium alloys is defined by the crystallite phase. Key classifications include; α, β and $\alpha + \beta$ phases. The α phase is composed of a single phase HCP crystalline structure while the β phase consists of a BCC structure. Figure 1.4 shows a representation of these individual crystallite phases.

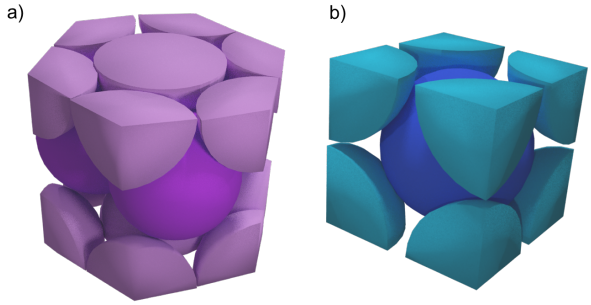


Figure 1.4: 3D representation of unit cells for a) hexagonal close-packed (HCP) α and b) body-centred cubic (BCC) β phases of titanium alloys, showing their atomic arrangements.

Alpha (α) Phase

The microstructure of α alloys contains only the HCP α phase, where no β is retained after cooling from above the beta transus temperature, regardless of the cooling rate. These α alloys contain either neutral alloying elements (i.e. tin) or α stabilisers such as aluminium or oxygen. The level of oxygen content leads to increased strength and an increased fatigue life compared to pure titanium. α alloys are generally employed in areas requiring high processability [91]. These alloys are not generally heat treatable but their high levels of creep resistance and corrosion resistance (the highest of the titanium alloy classes) make them particularly desirable for elevated temperature applications [213].

Beta (β) Phase

β alloys conisst primarily of the β phase and are generally formed via cooling from above the beta transus temperature where the inclusion of sufficient beta stabilisers allows them to retain a BCC beta phase after cooling, generally via quenching. This category includes stable and metastable β as well as β-rich α+β which

is more ductile than standard α+β alloys. β phase stabilisers include molybdenum, silicon and vanadium. β alloys are versatile, offering the highest specific strength at room temperature, as well as high toughness and fracture resistance. However, their usage is limited due to increased costs and difficulties in processing these alloys [37]. Processing above the beta transus leads to a fine recrystallised β grain structure whereas processing below this leads to fine β within a controlled α phase morphology [212].

Generally, α-phase titanium alloys are stronger, especially in high temperature applications, but with a reduced ductility, whilst the β-phase titanium alloys are significantly more ductile. This increased ductility is due to the larger number of available slip planes in the BCC structure of the β-phase alloys.

Dual Alpha + Beta ($\alpha + \beta$) Phase

α + β alloys contain a mixture of both α and β phases at room temperature. These dual-phase α + β alloys tend to be rich in β-stabilising elements allowing them to contain multiple phases at various temperature ranges. This group includes Ti-6Al-4V, one of the most common commercial titanium alloys in the aerospace industry due to its favourable combination of comparatively high strength, light weight and excellent corrosion resistance [162]. Near α and near β classifications also exist, near β alloys have a higher level of β stabilising elements than the conventional α + β alloys, but not enough to fully retain 100% of the β phase on cooling. Near α contain only a small volume fraction of β grains, these are generally dispersed between the larger α grains. Near-α alloys have higher strength than the fully α phase alloys due to the inclusion of this small fraction of the ductile β phase.

Alloying elements act as either α or β stabilisers. These increase or decrease the phase transition temperature. The alloying elements considered here are aluminium, an α stabiliser and vanadium, a β stabiliser [140]. The high strength, good ductility and corrosion resistance of common titanium alloys are due to the mixture of both α and β phases.

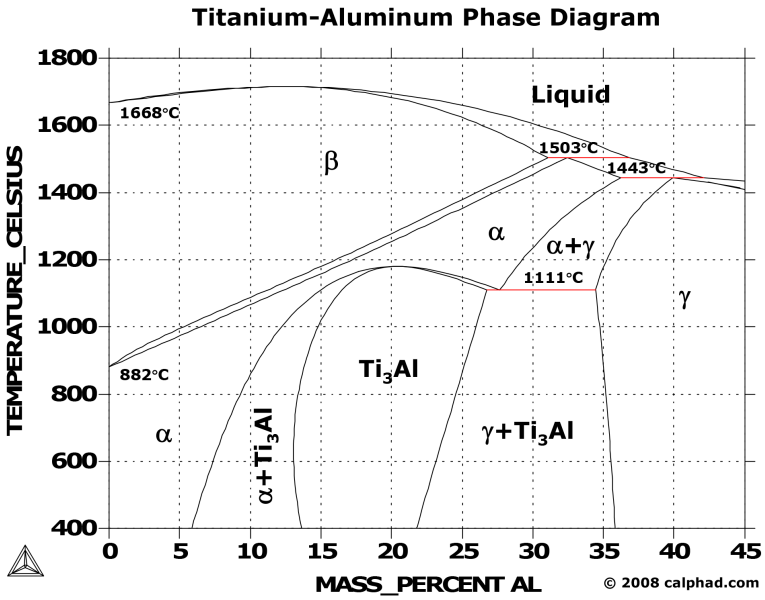


Figure 1.5: Phase diagram of Ti-Al created using the CALPHAD method, expressed in weight %, extracted from Kattner et al [100].

Aluminium stabilises and strengthens the α phase, raising the beta transus temperature [132]. The beta transus temperature is 882°C for commercially pure titanium, however in the Ti-6Al-4V alloy, this is increased to 995°C due to the additional aluminium content. The inclusion of aluminium also reduces the density. The phase diagram for Ti-Al alloys is shown in Figure 1.5, created using the CALPHAD method, which extrapolates properties of multicomponent systems via the creation of a database from temperature, pressure and composition data [100]. The inclusion of vanadium, a β stabiliser, provides an increased volume of the more ductile β phase, which is generally found to be around 5-10% in Ti-6Al-4V.

1.4 Ti-6Al-4V Products

Ti-6Al-4V has a wide processing window and can currently be used up to operating temperatures of ∼350°C [68] with continuing efforts to improve the operating temperature range of these alloys under constant development. Ti-6Al-4V contains 6% by weight aluminium and 4% by weight vanadium. Trace elements such as hydrogen and carbon are often present, where oxygen and iron are deliberate additions. The maximum allowable amount of these trace elements to ensure product conformity is defined in Table 1.1. Various product forms of Ti-6Al-4V are the focus of this work, these commercial products have undergone different processing regimes as discussed in the proceeding sections. All products described and investigated here have been provided by Timet Corp, Witton, UK. These include billet, unidirectionally rolled and cross rolled product forms of Ti-6Al-4V.

Table 1.1: Maximum amounts of constituent elements in airspace grade Ti-6Al-4V in wt% (data provided by Timet) [196].

Ti	Al	V	Fe	O	C	N	H
Balance	5.5 - 6.75%	3.5 - 4.5 %	< 0.40%	<0.20%	< 0.08%	< 0.03%	< 0.015%

1.4.1 Billet Material

The billet is a part-finished round product which has undergone a triple VAR process to produce an ingot. This is followed by typical ingot forming procedure in an open die forge for a number of steps. Open die forging is the process of deforming a hot piece of metal between multiple dies that do not completely enclose the material. The overall shape of the metal is altered as the dies hammer the material from multiple directions. Products formed through open forging often need secondary machining and refining to achieve the tolerances required for the finished specifications. The repeated working of the material through the deformation process increases the strength of the grain structure however it can cause particular regions to have increased internal stresses which leads to heterogeneity of the grain structure. The exact process has been omitted as it falls under Timet's intellectual property and is not available for distribution. A 21 mm thick slice from a 200 mm diameter extruded billet has been used here and is defined herein as the billet material. Specimens were cut radially from the as-received billet as outlined in Figure 1.6. Chemical analysis has been performed on a section of this billet by Timet, the results are given in Table 1.2

Table 1.2: Chemical analysis results of the billet Ti-6Al-4V.

Element	Al	Fe	Ni	Si	Ti	V	O	N	C
Amount	5.69 %	0.159 %	0.031 %	0.03 %	Bal.	3.71 %	0.1964 %	0.0048 %	0.021 %

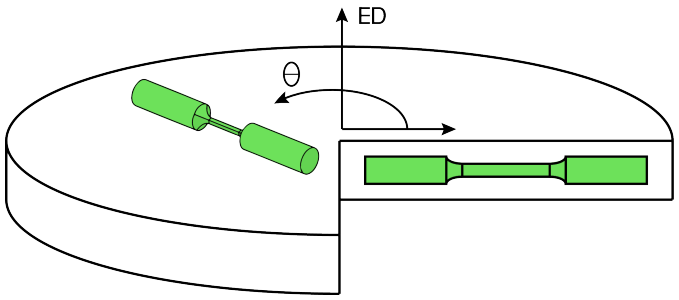


Figure 1.6: Specimens designed for in situ uniaxial tensile tests, were cut radially from the Ti-6Al-4V billet as shown, where ED is the direction of extrusion. Figure not to scale.

1.4.2 Unidirectionally Rolled Material

The unidirectionally rolled (UDR) material was supplied in the form of a 340 mm x 180 mm x 15 mm plate, where specimens were extracted from the as-received plate as outlined in Figure 1.7. The processing route of this production scale material begins with an EB-CHM followed by a single VAR regime to produce an ingot, see Section 1.2 for clarification. The ingot was then open-die forged using a combination of β working and α-β working to create an intermediate slab. Further α-β rolling in a single direction reduced this slab to its

final dimensions, plus a machining allowance. The slab was then creep flattened. Vacuum creep flattening is used to produce a flat plate with negligible macroscopic residual stress prior to subsequent machining [92].

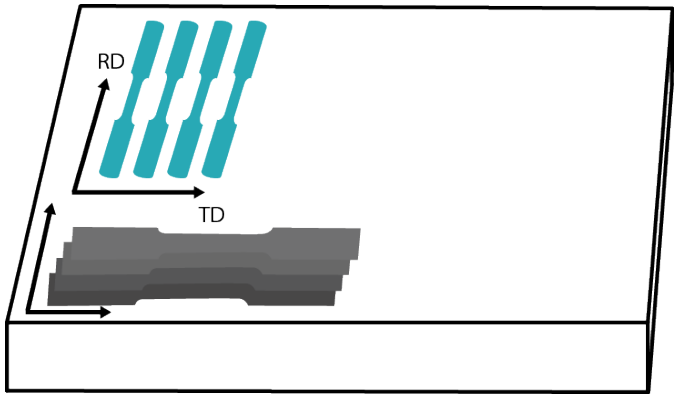


Figure 1.7: Illustration showing orientation of specimens removed from the UDR plate showing the location of specimens and how these have been extracted from the plate material with reference to the rolling direction (RD) and transverse direction (TD) (not to scale).

1.4.3 Cross-Rolled Material

The cross rolled (CR) material follows the same basic processing route as the UDR rolled plate; EB-CHM and VAR followed by open die-forging with β and α-β working to produce an intermediate slab. The final rolling stages from the slab differ as the rolling is performed in two perpendicular directions rather than in a single direction as for the UDR plate, hence the 'cross-rolled' terminology. The cross-rolling was performed in the $\alpha + \beta$ phase field, meaning both phases are retained. The rolling direction for this material is defined as the direction of the final rolling stage.

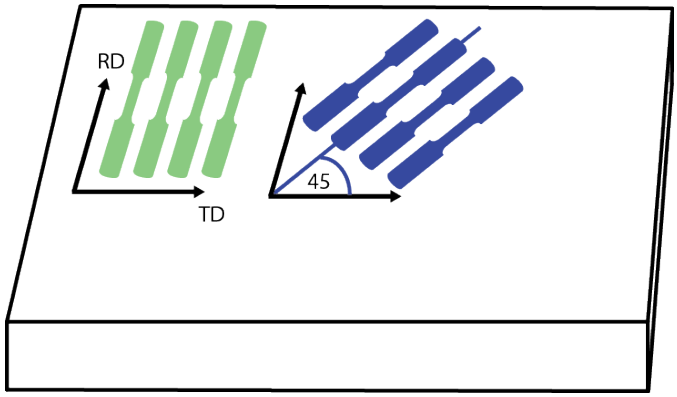


Figure 1.8: Representation of CR plate showing specimens extracted parallel to the final rolling direction (RD) and at 45 degrees to the rolling directions, (not to scale).

The as-received material was supplied in the form of a 340 mm x 180 mm x 20 mm plate. This piece had undergone a further α-β heat treatment which does not alter the overall texture (dominated by rolling process) but causes the surface to be slightly oxidised, making it simple to identify each plate visually. Specimens were

cut from the cross-rolled Ti-6Al-4V plate as shown in Figure 1.8. The supplied plate is a typical example of the CR plate widely used in many industries, including for aerospace applications.

1.4.4 Ti-Al alloys of varying aluminium content

Produced in lab-scale quantities by Timet, Ti-0Al, Ti-3Al and Ti-6.5Al have all undergone identical processing procedures. Initial button materials, originally UDR with varying aluminium contents, have been double melted on a tungsten electrode arc melter. This is essentially a small scale VAR process with inert gas, ensuring a homogeneous distribution of alloying elements and low porosity.

All buttons were annealed at 1100°C for 1h to transform to the β phase. These rectangular buttons were subsequently β-forged. A third forging stage was employed to reduce the buttons to 26 mm x 26 mm, where they are then air-cooled to room temperature. The buttons were heated to 870°C and further cross-rolled followed by sub-transus rolling using shaped rollers. A final rolling procedure was conducted to reduce the material to a final cross section of 10 mm x 10 mm via a four-step process. The material was then straightened under a balance and finally air-cooled. The final rolled bar product, of dimensions 10 mm x 10 mm x 300 mm was sectioned and specimens were extracted so the loading direction aligns with the rolling direction. Ti-6.5Al has been designed to replicate the α-phase in Ti-6Al-4V and each of the Ti-6.5Al, Ti-3Al and Ti-0Al products have been deformed in situ at CHESS, the results of both are compared and discussed in Part III as experiments of industrial interest.

1.5 Heat Treatment Regimes

The heat treatment of titanium is another expensive processing step as it may require a vacuum or inert atmosphere during the treatment duration. Heat treating in air and machining the final parts may be used alternatively where a clean surface is required. The heat treatment of titanium alloys may be performed to relieve machining stresses, to anneal or age the material, or to optimise for particular mechanical properties, i.e. to grow grains to particular sizes or in particular directions. Titanium alloys may be stress relieved via heat treatments, which may be achieved for some alloys with minimal adverse effect on the materials strength or ductility [138]. Further straightening or flattening of titanium alloys is required post heat treatment to ensure dimensional requirements are met. However, these processes are not simple and as a result, creep flattening or hot straightening processes are generally employed post heat treatment at annealing temperatures.

Annealing is a form of heat treatment which increases the ductility and reduces the hardness of the material via atom migration in the crystal lattice. This decreases the number of dislocations, increasing the material workability [53]. The material is heated to above the recrystallisation temperature (approximately 950°C for Ti-6Al-4V), held at this high temperature for a duration, then cooled. The effect of annealing is highly dependent on the combination of the material, temperatures used, heating rates and cooling rates. Annealing

consists of three phases: recovery, recrystallisation and grain growth. In the recovery phase, internal stresses are reduced through the removal of dislocations, but overall grain size and shape are not affected. The recrystallisation stage involves the nucleation of new grains, which are free of strain, replacing the grains previously deformed by internal stresses. Grain growth is the final and often least desirable stage, where the microstructure becomes coarser and the material loses strength [207]. Hot or cold working after the annealing process is employed to alter the material structure. These subsequent heat treatments are often employed to gain specific desired properties.

To improve the fracture toughness of titanium alloys, both recrystallisation annealing and β annealing are employed. β annealing is performed at temperatures just above the relevant beta transus temperature to prevent excessive grain growth. Recrystallisation annealing is often performed to achieve a large volume fraction of α precipitaties, this involves heating to the high temperature range in the α-β phase field followed by a very slow cooling rate. Recrystallisation annealing has mostly replaced β annealing for critical airframe components [57]. Argon is often used to quickly cool the treated titanium alloys to temperatures where no further metallurgical effects are kinetically favoured i.e., around 200°C. Argon is preferable to helium as it is significantly heavier than air, preventing oxygen from interacting with the titanium. It is also cheaper.

Heat treatments may cause shrinkage or growth of materials. This is dependent on a wide variety of factors, meaning that the volumetric change is difficult to precisely account for. This main shape change is due to the difference between theα and β at homogenisation temperatures. Post-heat treatment, creep flattening and addional machining of parts is performed to ensure the material adheres to the desired final tolerances. Creep flattening consists of heating the titanium sheet between two clean, flat sheets of steel in an inert furnace atmosphere [138].

1.6 Microstructure

In addition to processing, the constituent alloying elements affect the overall microstructure and phase morphology. The microstructure is highly significant as it impacts both the tensile strength and fracture toughness of titanium alloys. Heat treatments and processing methods have a profound impact on the final microstructure and are often performed for microstructural control. Figure 1.9 shows a selection of various common Ti-6Al-4V microstructures using optical microscopy after polishing and etching [11].

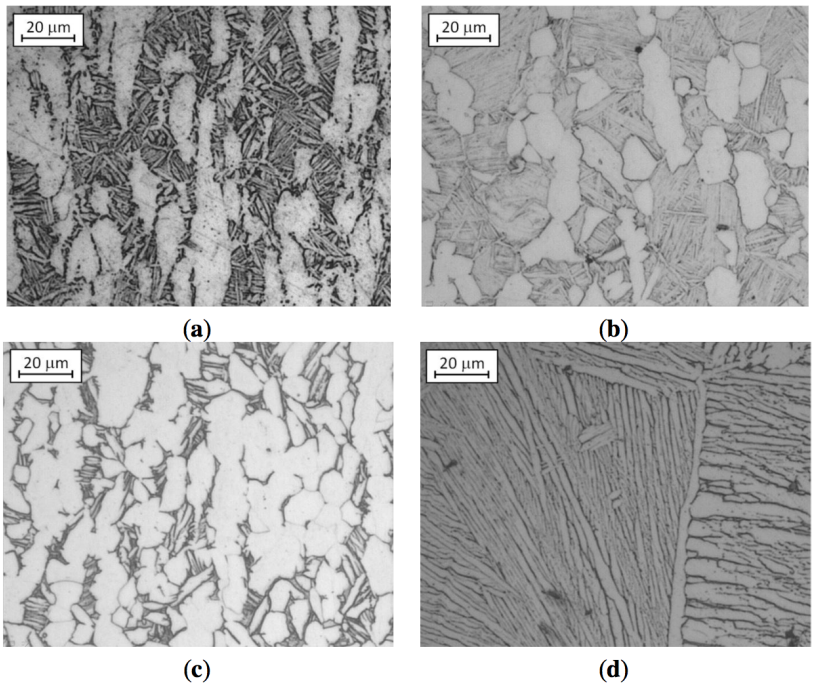


Figure 1.9: Optical microscope images of Ti-6Al-4V microstructures showing examples of (a) mill annealed; (b) bimodal; (c) fully equiaxed and (d) fully lamellar microstructures, as found in [11] (all scale bars = 20 μm).

Typical primary processing for titanium alloy bar products involves forging in both the β and the $\alpha + \beta$ phase fields. As titanium alloys are heated to the $\alpha + \beta$ phase field, both the α and β phases have different morphologies where the α phase (lamellar, equiaxed or a mixture of the two) is generally distributed within the β matrix. β working is performed to obtain fine, homogeneous beta grains whereas subsequent $(\alpha + \beta)$ forging will break down the lamellar structures formed during β forging. An equiaxed, bimodal or trimodal microstructure may be generated from thermo-mechanical processing in the $(\alpha + \beta)$ phase field [84].

Microstructural control is becoming increasingly significant alongside the popularity of additive manufacturing [3]. Selective Laser Melting (SLM), a form of additive manufacturing, produces porous microstructures for which deconstruction to an ultra-fine microstructure is used to improve the material properties [222]. Ultra-fine microstructures with harmonic structures, described by spherical inclusions in the bulk ultra-fine grained microstructures, are often cited as the future of titanium alloys [104].

The final crystallographic texture is generally formed from the processing and heat treatments, where crystallographic texture is defined as the distribution of orientations of the polycrystals in a polycrystalline material. This combined with the direction of loading affects the overall mechanical properties of the material. Bache et al [12] showed the significant impact of texture on the mechanical properties of highly-textured Ti-6Al-4V. The expected microstructures for all products described in this study are equiaxed and contain grain sizes in the range of tens of microns.

1.7 Macrozones

Macrozones are regions consisting of an aggregate of crystallographically aligned α grains. An example of a macrozone is shown in the Inverse Pole Figure (IPF) map of the deformed UDR Ti-6Al-4V shown in Figure 1.10. Macrozones may also be described as regions within a polycrsyalline material that effectively act as a single, large grain [65]. These are alternatively also termed 'microtextured regions' within aspects of the literature.

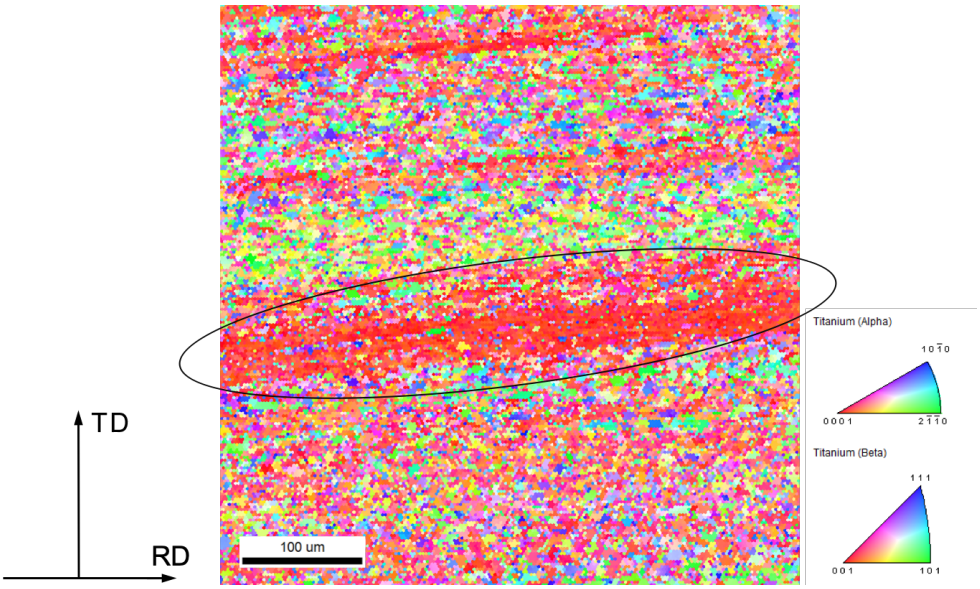


Figure 1.10: IPF map of the UDR plate showing basal-orientated macrozone (circled) in the direction of rolling, surrounded by more randomly oriented, equiaxed grains.

The formation of macrozones is due to the primary α grains remaining crystallographically coherent to the prior β grains upon cooling. The microstructure of these macrozones is a direct result of the prior β grain boundaries and variant selection [78]. Macrozones in Ti-6Al-4V are expected to have a significant effect on deformation behaviour, particularly in fatigue crack initiation. The current hypothesis suggests dislocations pile up at the interfaces between macrozones. This is where the strain accumulates and ultimately leads to the initiation of a crack [28, 228].

Lunt [129] observed bands of similarly orientated grains in Ti-6Al-4V cross-rolled plate and larger, more obvious macrozones in the UDR and forged bar products. These bands were generally separated by regions of randomly orientated grains and had a significant efffect on the macroscopic behaviour. It is therefore important to be aware of the influence of these macrozones in the current study, where the size of these macrozones compared to the specimen gauge section may be similar. Additionally, in macrozones where either basal or prismatic slip is easily achieved, numerous micro-cracks are evident throughout the macrozone. The coalescence of these cracks is likely to lead to premature failure [119]. Echlin et al [60] dealt with the dependence of strain localisation on the microstructure and macrozones in Ti-6Al-4V. The study concluded

that different types of slip are activated with differing crystallographic textures i.e. pyramidal and prismatic slip being more easily activated in rolled materials due to the texture induced by the rolling process.

The effect of macrozones in Ti-6Al-4V under uniaxial tensile loading conditions is examined further by Lunt et al [130] where it is considered that macrozones control the onset of yield at a microstructural level. Macrozones have been shown to effect the localisation of plasticity within the polycrystalline aggregate. It is suggested that the strain localisation occurs early in the deformation process, prior to macroscopic yield [99].

1.8 Crystallography

Johannes Kepler defined the first mathematical description of a crystal and is credited with the discovery of the geometry which enables the 'packing of spheres' - a fundamental concept in modern crystallography. This 'close packing' describes both phases in Ti-6Al-4V [101]. The crystallography, particularly the crystallographic texture, affects the bulk material parameters and must be accounted for. Figure 1.11 shows the unit cell and symmetry properties of the HCP α and BCC β phases.

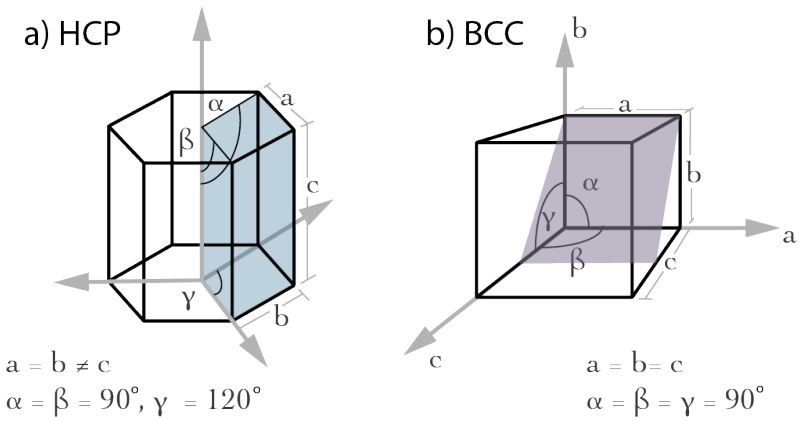


Figure 1.11: Representation of a) α phase HCP unit cell and b) BCC β unit cells, showing crystal symmetries.

As the crystals are periodic, the set of atoms within the crystal are distributed over a set of parallel and equidistant planes, termed lattice planes. The lattice plane spacing is calculated for cubic symmetry, where the cubic cell is bounded by the same length in each direction ($a = b = c$) and all angles are 90° in the BCC unit cell (Figure 1.11b). The interplanar lattice spacing d for a cubic system is given by

$$\frac{1}{d} = \sqrt{\frac{h^2 + k^2 + l^2}{a^2}}, \tag{1.1}$$

where a is the length of the side of the unit cell and h, k and l are the Miller Indices. These describe the crystallographic plane, where each index is related to the point at which the plane intercepts the bounds of the unit cell. For example, a plane defined by the hkl(012) will intercept the BCC unit cell, see Figure 1.11b, at b = 1 (the edge of the unit cell) and c = 1/2. This relationship is more complex for the hexagonal symmetry

in an HCP crystal (as in the α phase of titanium), where the interplanar spacing may be calculated as

$$\frac{1}{d} = \sqrt{\frac{4}{3}\left(\frac{h^2 + hk + k^2}{a^2}\right) + \frac{l^2}{c^2}}, \tag{1.2}$$

where a and c are the lengths indicated in Figure 1.11a. The hexagonal structure is very similar to a tetragonal crystal structure due to its symmetry, where for the hexagonal cell, of the three sides, two of them are equal ($a = b \neq c$) and two of the interaxial angles are 90° while the third is 120°.

The Miller indices (hkl) for cubic structures, or Miller-Bravais $(hkil)$ for hexagonal structures, are used to identify different planes of atoms [142]. For example, in diffraction, as each diffraction peak is associated with a particular plane of atoms, this allows analysis of the materials atomic structure and extrapolation to the overall microstructure. The notation $[hkl]$ denotes the crystallographic direction normal to the plane described by (hkl). Table 1.3 further describes the notation adopted.

Table 1.3: Notation convention for Miller and Miller-Bravais indices, noting the different types of brackets used for each case.

(hkl) / $(hkil)$	Miller / Miller-Bravais indices of a plane, or set of parallel planes
$\{hkl\}$ / $\{hkil\}$	Miller / Miller-Bravais indices representing a family of symmetrically equivalent planes
$[uvw]$ / $[uvtw]$	Miller / Miller-Bravais indices of a direction (set of parallel directions)
$, uvw >$ / $< uvtw >$	Miller / Miller-Bravais indices representing a family of symmetrically equivalent directions

The $[hk.l]$ convention is used here to describe a crystallographic direction of a hexagonal crystal using Miller-Bravais indices where the i value is represented by a single dot as this value is dependant on both h and k as $i = -(h + k)$.

The crystallographic directions examined in this work include both α phase (HCP) and β phase (BCC), as outlined in both Figure 1.12 and Table 1.4.

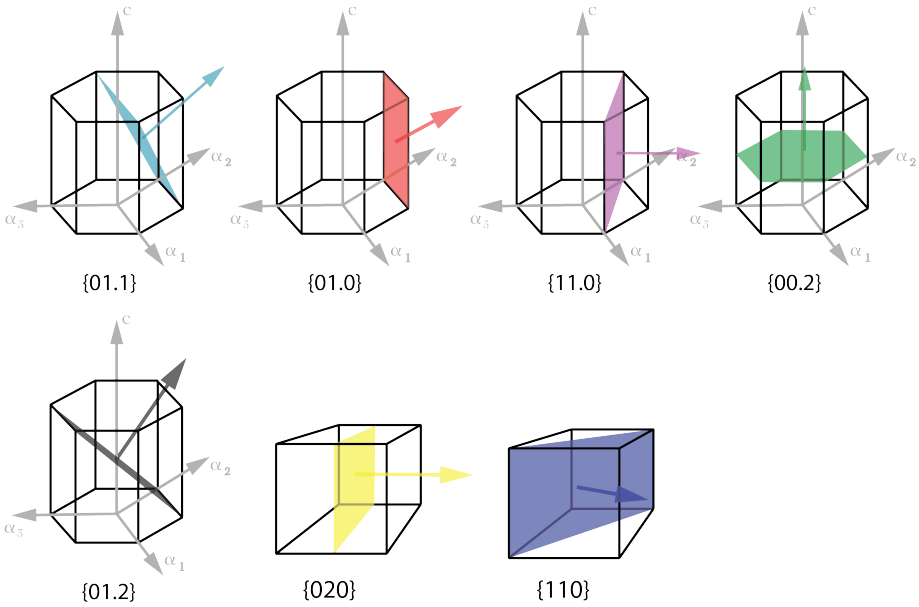


Figure 1.12: Selection of crystallographic directions of both α and β phases.

Table 1.4: Further information on the multiplicity of particular crystallographic planes, extracted from [161] where an asterisk denotes values subject to change in crystals with lower symmetry, which remain of the same crystal class.

Miller-Bravais Family	Phase	multiplicity
{10.0}	α	6
{00.2}	α	2
{10.1}	α	12*
{10.2}	α	12*
{10.3}	α	12
{11.0}	α	12*
{21.0}	α	12
{110}	β	24*
{020}	β	6

1.8.1 Representing Orientations

Appropriate representation of both orientation and rotation is required in dealing with complex crystallography. There are a variety of methods commonly employed including Euler angles, Rodrigues, quaternions and axis-angle respresentations. Euler and Rodrigues representations are adopted here. The orientation of a crystallographic lattice can be described with respect to the laboratory frame by a rotation. This description follows the passive convention, where the rotation is defined such that the laboratory frame is brought into coincidence with the crystal frame [29].

Conversion between various orientation descriptors is required as, for example, Euler angles are output from electron back-scatter diffraction (EBSD) analysis but the analysis software may use quaternions internally

for faster computation times, the format of the data output is significant. Switching between conventions is relatively simple as these are well established conversions.

Euler Angles

Euler angles are a common way of defining a rotation by combining three successive rotations around different axes. Various conventions exist depending on the axes chosen and order of rotations. The Euler-Bunge convention has been used throughout this work. This involves an initial rotation ϕ_1 around the Z-axis, then Φ around the new X-axis and finally ϕ_2 around the new Z-axis as illustrated in Figure 1.13. The orientation matrix $\mathbf{R}$ is then expressed as a combination of the three rotations expressed in matrix form as

$$\mathbf{R} = \mathbf{R}_{\phi_1}\ \mathbf{R}_{\mathbf{\Phi}}\ \mathbf{R}_{\phi_2}. \tag{1.3}$$

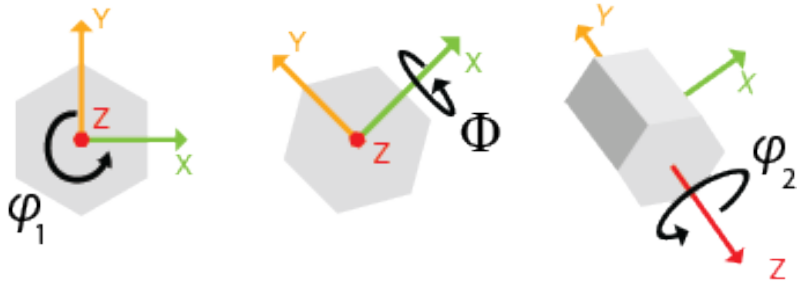


Figure 1.13: Representation of rotation via Euler-Bunge convention. Adapted from [184].

Euler-Rodrigues Representation

The Rodrigues' rotation formula is an efficient way to rotate a vector in space using an axis and angle of rotation. Its vectoral representation is mathematically simple and the subdomains induced by symmetry have planar surfaces [203]. The Euler-Rodrigues vector $\mathbf{r}$ may be described by the Rodrigues parameters, $[r_x, r_y, r_z]$, which are defined by $r_i = \tan(\theta/2)s_i$, where θ is the angle of rotation and i = 1,2,3. These rotations are performed around the unit vector $\underline{s}$ which describes the axis of rotation that $\mathbf{r}$ is rotated around [45]. Derivation of this is visualised in Figure 1.14 where $\mathbf{r}$ is decomposed into components parallel and perpendicular to the rotation axis.

In Rodrigues space, crystallographic fibre textures are visualised as straight lines. A fibre in orientation space can be seen as a line connecting two different orientations, but is more commonly used to compare crystallographic direction with specimen direction, in which case, all crystals with orientations that align parallel to the specimen direction are included in this fibre. Kumar and Dawson [113] have performed pioneering work on the fundamental region in Rodrigues space, this is smallest subsection of the space where all orientations may be visualised.

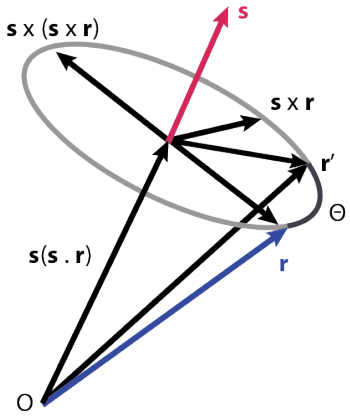


Figure 1.14: Rodrigues rotation formula decomposition, adapted from [176].

1.8.2 Representing Crystallographic Texture

Grains within a polycrystalline material are comprised of many crystals, these crystals are all orientated in different directions, this is known as their crystallographic orientation. In materials science, texture is defined as the overall crystallographic texture, meaning the distribution of crystallographic orientations found in a polycrystalline sample.

There are a variety of ways to describe the texture of a material. Common texture representations involve Euler angles, discrete orientations, angle-axis pairs, Rodrigues, quaternions, spherical harmonics or orientation distribution functions (ODFs). To analyse texture, orientation must be defined, therefore rotations must be defined first as orientations are the physical result of a set of rotations, see Section 1.8.1. Texture analysis is likely to be presented in the form of either Pole figures (standard or inverse) or ODFs, both of which have been used here. The main purpose of texture representation is to enable examination of crystal orientations without regarding spatial characteristics, essentially examining a distribution of discrete orientations [107]. Crystallographic texture can be examined from a subset of the available EBSD data. There are further ways to define crystallographic texture but these are generally also a distillation of EBSD data. Distillations of data can enhance the interpretation of results.

1.8.2.1 Pole Figures

Pole figures are perhaps the most common texture representation due to their current familiarity within materials science community and these are one of the simplest ways of physically interpreting the experimentally obtained data. Pole figures are a 2D representation of the crystallographic texture obtained via stereographic projection. The process of generating pole figures is outlined in Figure 1.15.

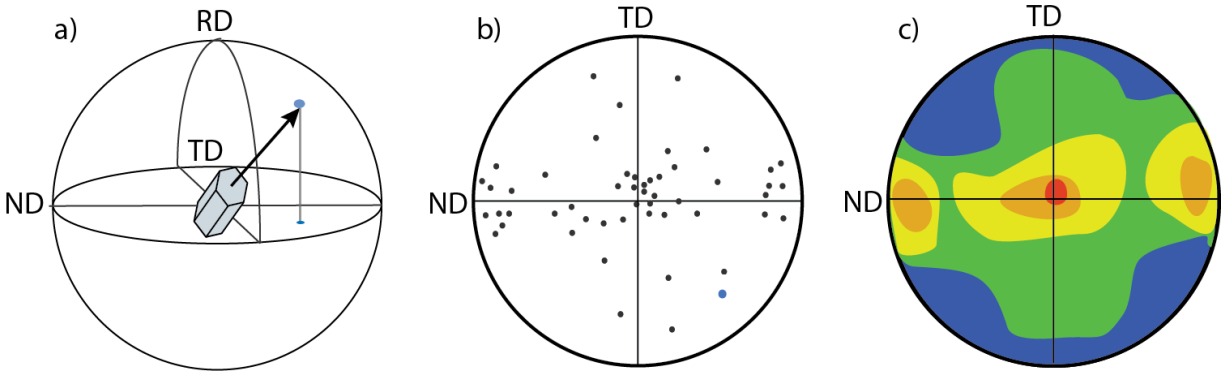


Figure 1.15: Representation of pole figure creation, where a) shows a crystal defined by its normal and where this normal intercepts the sphere, b) shows the combined response of multiple crystals analysed in the form of a flattened sphere, c) shows the finalised pole figure showing intensity levels (where RD is the rolling direction, TD is the transverse direction and ND is normal to the loading direction).

The direction of any 3D vector in a crystal can be described as a point on the unit reference sphere. A plane representing crystallographic orientation is placed at the origin of the unit sphere, as in Figure 1.15a. The point of intersection between this plane normal and the sphere is a measure of the arrangement of this plane within the crystal. The plane normal will intersect the sphere at two diametrically opposite points. The point of intersection on the positive hemisphere uniquely identifies this line and this is defined as a pole. The hemisphere is projected onto a 2D map and a pole figure plot is obtained (Figure 1.15b). This plot shows sample directions aligned with a specific crystallographic pole. Described thus far is a single crystal response represented as a point on the projected plane, a distribution of poles will be displayed as a collection of points on this plane (Figure 1.15b & c), commonly in the form of an intensity map.

A pole figure can be generated by different methods as a variety of means exist to flatten a hemisphere onto a 2D plane. The most common projection method is stereographic projection, this preserves the angles rather than the area of the sphere, meaning the angle between two lines will be consistent in both the hemisphere and the projection. However, this will alter the apparent density of the poles. Alternatively, an equal area projection can be used, this preserves the apparent density but distorts the angles in the projection [189]. This type of projection is often used by cartographers and has been used in pole figures here due to the desire for comparison of pole figure intensity. This projection accounts for angular distortion, this same distortion is present in each instance allowing for comparison.

Some crystal orientations are described as equivalent due to their resultant orientation being the same despite a different set of rotations being used to arrive at this result. It may not be possible to distinguish the actual orientation 'history'. To analyse texture in a sensible manner, orientations must be uniquely identified, i.e. by a single rotation. Usually selecting the rotation with the minimal rotation angle about an axis in a standard stereographic triangle is sufficient. There are two conventions used to define a rotation which appear frequently in the literature (termed active and passive rotations). Although these are very similar, it is imperative that one is aware which method is being used. Active transformations are defined by a transformation

of space, relative to a stationary co-ordinate system, this is essentially 'left' matrix multiplication given by

$$\mathbf{u'} = \mathbf{ABu} \tag{1.4}$$

where **A** and **B** are rotation matrices, and **u'** is the rotated vector **u**. In passive transformations, the space remains fixed and the co-ordinate system rotates. For an observer attached to the rotating co-ordinate system, this would seem to rotate in reverse of the active transformation. The sense and the order of the rotation are reversed, with the matrix rotation for the passive transformation is written as,

$$\mathbf{u'} = \mathbf{A^T B^T u} \, . \tag{1.5}$$

Inverse pole figures show the crystallographic planes aligned with a specific sample direction. This has useful application in examining specimens where the processing history strongly affects specific directions i.e. preferred orientations or textures are apparent. The construction of inverse pole figures is similar to that of traditional pole figures. However, the poles are not projected onto a plane defined by sample geometry but a vector along a sample direction is projected onto the planes determined by local crystallographic orientation [190]. Due to the symmetry of cubic systems, the inverse pole figure can be divided into 24 stereo-graphic triangles as shown in Figure 1.16.

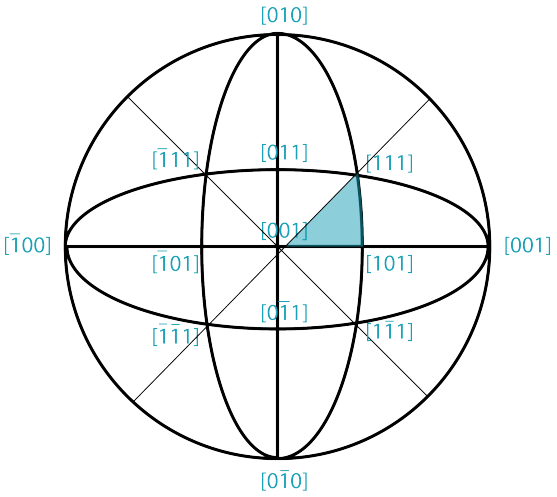


Figure 1.16: 24 stereoscopic triangles showing the fundamental area of symmetry for cubic systems.

It is vital to understand that pole figures (and inverse pole figures) do not explicitly indicate the crystallographic orientations within the polycrystal, only the orientations of selected crystalline planes/directions, this is a fraction of the available data from the EBSD. Sophisticated methods exist for determining the most probable crystal orientation distributions by examining the pole figures of multiple crystallographic planes. However, there are more direct ways to represent texture which better reflect the materials true crystal orientation, the use of which is application dependent. Pole figures and orientation distribution functions are sufficient here.

1.8.2.2 Orientation Distribution Function

The distribution of crystallographic orientations in a bulk sample can be represented by an orientation distribution function (ODF). This describes the frequency of occurrence of particular crystal orientations in an imaginary three-dimensional space defined as orientation space [210]. An ODF may be defined mathematically in any space where a continuous description of rotations is adopted. The information contained in an ODF may be used to determine the anisotropic properties of polycrystalline materials. A pole figure may be described as a subset of the data available in an ODF as the projection of multiple points in an ODF map results in a single point in a PF. Various orientation spaces may be used in the presentation of ODFs; Rodrigues orientation space is used here.

Chapter 2

Continuum Description of Polycrystalline Plasticity

2.1 Introduction

Deformation is observed in crystalline metals at a variety of length-scales, from the movement of interstitial atoms and dislocations in the lattice structure to grain boundary interactions and necking of the bulk material. Deformation is of particular interest to engineers as it ultimately leads to component failure. Understanding the underlying causes and quantifying the amount of deformation a material can safely withstand are integral to materials science and engineering, as unexpected failure has sudden and drastic consequences.

In continuum mechanics, the material is modelled as a continuous mass or body, where the body is required to be deformable. Certain physical phenomena may be modelled assuming that material exists as a continuum. Continuum representations of solid materials are generally successful even though physical materials have microscale discontinuities and even cracks which are not explicitly accounted for. Modelling solids as a continuum has been employed since the 19th century and advances in computation have allowed significant improvement in this field, reducing computation times and enabling increasingly complex models [114].

Elastic behaviour is generally simple to represent whereas the onset and continuation of plasticity is of particular interest and is notably more complex to model. Elastic deformation is a reversible process where a material, under the action of a force, is deformed; this deformation is reversible and the initial positions of the atoms are restored after the material is unloaded. There are multiple ways to model plasticity as it impacts a variety of length scales, leading to the observation of different deformation phenomena. Here, the focus is the microscale where crystallographic slip in individual crystals leads to visible deformation.

2.2 Dislocation and Slip

Dislocation theory is a widely accepted theory of plastic deformation as the observation of dislocations is possible through various techniques including transmission electron microscopy (TEM). Dislocations are imperfections in the crystal lattice. These dislocations affect the material properties, lowering the yield stress (from theoretical values) and allow plastic deformation to occur [194]. The growth of a crystalline material from melt or vapour, leads to the creation of dislocations. Dislocations may also be nucleated during phase transformations or due to irregular grain boundaries [90].

Edge and screw dislocation representations are shown in Figure 2.1. Generally, a mixture of dislocation types exist in crystalline materials [31]. Lattice distortion due to dislocations may be quantified using the Burgers vector.

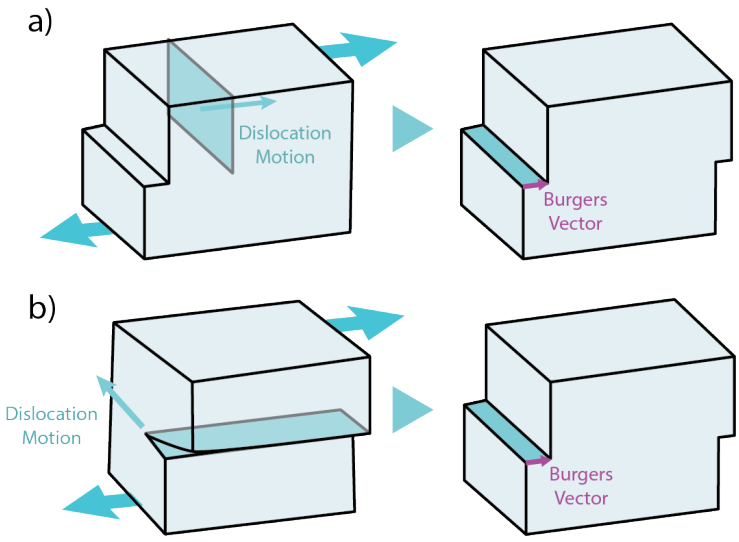


Figure 2.1: Representation of the effect of individual a) edge and b) screw dislocations, where the dislocation line moves in the same direction as the dislocation motion for edge dislocations and perpendicular to the direction of dislocation motion for screw dislocations. Adapted from Callister [31].

Dislocations can 'pile up' at obstacles, such as grain boundaries, leading to high stress concentrations (the Stroh model) which may become sites for cracks to initiate [188]. Sufficient energy is required to pass these sites [160].

Dislocation Types Geometrically necessary dislocations (GNDs) were first proposed by Nye [154] as dislocations whose geometric properties were not annihilated by other crystal dislocations. Figure 2.2 shows how dislocations are necessary to allow for lattice curvature. These intrinsic defects can only be observed at the microscale, where they have significant effects, but are not visible in the overall macroscopic plastic strain [76]. Strain hardening can be described as GNDs preventing the motion of other dislocations.

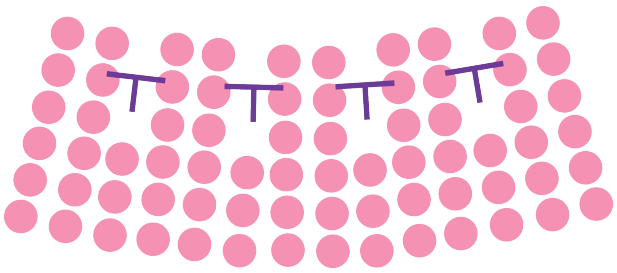


Figure 2.2: Geometrically necessary dislocations, GNDs, shown within the curvature of an atomic lattice.

Statistically stored dislocations (SSDs) are assumed to have evolved from trapping during plastic deformation [9]. SSDs have been discovered to have no overall geometric effect as their distribution allows any effects to be termintated by other SSDs [7].

It is not curently possible to distinguish GNDs from SSDs locally. The total dislocation density is the sum of the GNDs and SSDs. However, interactions of short range order occur between GNDs and SSDs, improving the hardening response [9]. Back stresses are also caused by GND accumulation, these long range stresses effect both the strain hardening and the strengthening of a material [223]. Arsenlis and Parks [8] showed these dislocations as randomly generated and randomly oriented within a material and therefore their effects appear uniform macroscopically. GNDs are sometimes defined by the deviation from this homogeneity. GNDs and their applications in describing metal plasticity were reviewed by Gao and Huang [76] citing the significance of accurately quantifying GND density.

2.2.0.1 Crystallographic Slip

A portion of a crystal is able to slide and be displaced under shear. This is termed crystallographic slip. Slip typically occurs along the most atomically dense planes and involves a slip plane and direction, the combination of which is termed a slip system, see Figure 2.3. Dislocations enable slip as dislocation glide allows deformation to occur at lower stresses than normally possible for a whole plane of atoms. Dislocation glide describes the movement of dislocations along crystallographic planes. Slip occurs first in the most favourably oriented grains. As these grains deform, the load is redistributed to the neighbouring grains ensuring compatibility and equilibrium between the grains. Miller index notation is used to describe slip planes and directions, see Section 1.8. The direction of slip is parallel to the Burgers vector.

Alpha phase HCP titanium alloys exhibit five main slip systems, these include the basal {00.1} <1120>, prismatic {10.0} <1120>, first order pyramidal {10.1} <1120>, and two second order pyramidal systems {10.1} <1123> & {11.2}<1123>. Plastic deformation is mostly accommodated by the basal or prismatic slip along the Burgers vector <a>, whereas slip is more difficult to initiate on the pyramidal slip systems [27]. These potential slip systems for the α phase are shown in in Figure 2.4. In HCP crystals, basal slip is visible as a rotation around the <a> axis and prismatic slip as a rotation around the <c>-axis in EBSD patterns [40].

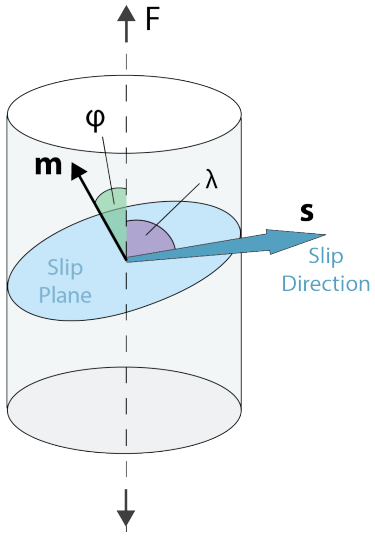


Figure 2.3: Representation of slip system showing slip plane with normal m and s, the direction of slip where F is the applied load, λ is the angle between the applied for and the slip direction. φ is the angle between the slip direction normal and the applied force.

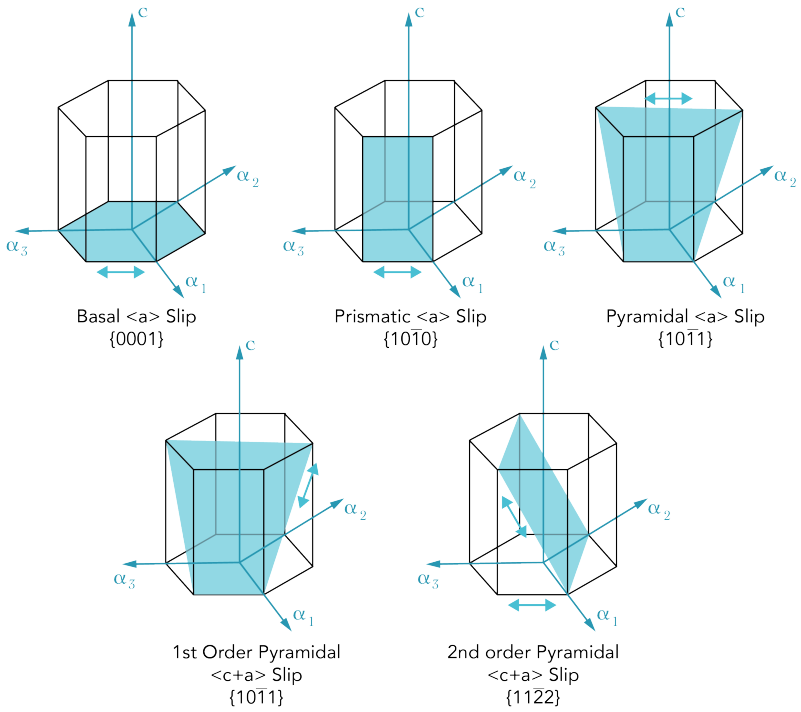


Figure 2.4: Slip systems in titanium α (HCP) phase with arrows denoting slip direction. Adapted from [14].

Slip causes individual grains to be distorted and as the direction of slip varies between grains, some grains are therefore unable to deform until adjacent grains can accommodate this deformation. Polycrystals tend to be stronger than their single crystal counterparts, as a higher stress is required to initiate global deformation. To initiate slip, the shear stress acting in the slip direction, along a slip plane must reach a critical value. This is termed the critically resolved shear stress (CRSS). The CRSS ($\boldsymbol{\tau}^{\alpha}$) is the amount of stress required to overcome this resistance to dislocation motion.

$$\tau^{\alpha} = \mathbf{s}^{\alpha} \, \boldsymbol{\tau} \, \mathbf{m}^{\alpha} \tag{2.1}$$

where the applied shear stress $\boldsymbol{\tau}$ is projected onto the slip system. $\mathbf{s}^{\alpha}$ is the direction of slip and $\mathbf{m}^{\alpha}$ is the slip plane normal. This may be alternatively written as

$$\tau^{\alpha} = \boldsymbol{\tau} : \mathbf{s}^{\alpha} \otimes \mathbf{m}^{\alpha} \tag{2.2}$$

where $\mathbf{s}^{\alpha} \otimes \mathbf{m}^{\alpha}$ is the Schmid tensor.

The slip systems in Ti-6Al-4V are known to require different levels of CRSS to activate slip. CRSS values for titanium can be extracted using high energy XRD [209]. The CRSS required for activation of <a>-type basal slip is generally lower than that of other slip systems for HCP materials, slip occurs readily and is the dominant deformation mode of room temperature titanium based alloys. For HCP titanium alloys, the primary basal or prismatic slip systems are not sufficient to accommodate c-axis deformation, either twinning or secondary <c+a> slip modes are required to fully model plastic deformation. Deformation involving the c-components may be accommodated by either β-phase deformations or via grain boundary sliding [225].

Surface observations in metals indicate that slip consists of intermittent events localised along slip bands [109]. Slip bands are regions of localised slip in crystals, these bands are widened by the accumulation of dislocations but cannot cross grain boundaries. Slip bands are especially significant in high cycle fatigue as they impinge on grain boundaries causing high stress concentrations, leading to failure [72].

2.2.0.2 Twinning

Twinning, in addition to slip, is a deformation mechanism that occurs in polycrystalline materials. Single crystal experiments have shown that twinning occurs both initially the elastic region and when high levels of plastic deformation are reached, depending on the crystal structure [39]. In twinning, the movement of atoms is small. This process is usually observed to occur much faster than slip, leading to twinning being observed in high stress rate conditions. Early attempts to understand twinning are introduced by Mahajan and Williams [133]. Twinning occurs when two separate crystals share lattice points, shear is accommodated due to the local crystal re-orientation. For deformation twinning, a 180° rotation or reflection of the crystallographic lattice about a specific axis or plane must exist. Contact and penetration twins form differently. Contact twins have a defined shared surface whereas penetration twins are composed of two interpenetrating crystals, leading to an irregular composition. A contact twin is shown schematically in Figure 2.5. Disagreements in the literature still persist regarding the nucleation and propagation of twins in crystal structures [39].

Depending on factors such as composition, grain size, strain rate, temperature and deformation direction (tension or compression), titanium alloys may deform both by twinning and slip [16]. Twinning and slip are the main plastic deformation modes in crystalline materials. Slip research has dominated as it it not only more

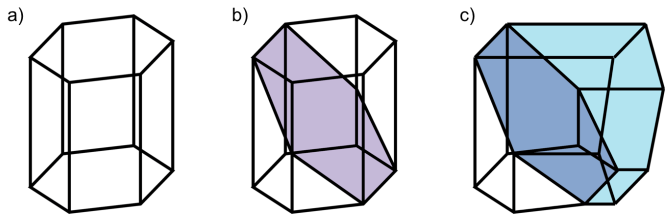


Figure 2.5: Representation of a) a single HCP unit cell, b) HCP cell with available twin plane highlighted and c) a contact twin parallel across the twin plane.

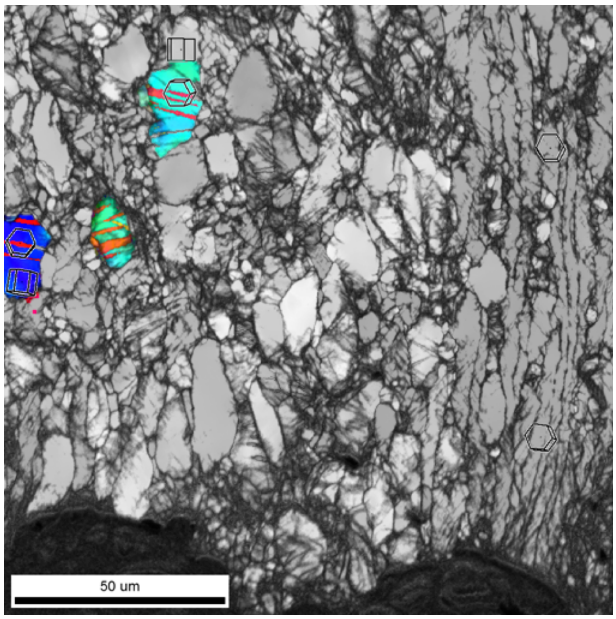


Figure 2.6: Example of twinning in Ti-6Al-4V as shown under EBSD at a depth of around 50 microns from the fracture surface, captured via FEI Quanta 200F SEM, scale bar = 50 microns.

frequently observed, but is also easier to predict and analyse, thus twinning mechanisms and their effects are generally less well understood. Both twinning and slip start from defects, these are disordered regions or boundaries between different crystalline grains [70].

Twinning behaviour has been observed in less symmetric hexagonal crystals, such as titanium. Pure α titanium does twin at temperatures below 500°C, and at low strain rates, additionally, studies show that higher loading rates tends to promote twinning and suppress slip [202]. In cp-Ti, either {10.2} and {11.1} tensile twinning and {11.4} and {11.2} compression twinning modes may activate [115]. Whereas in Ti-6Al-4V, twinning is restricted to the {10.2} and {11.1} crystallographic planes [116]. Aluminium and oxygen are known to supress twinning of titanium alloys [224]. It is postulated that twinning occurs where slip is unable to accommodate deformation [206]. An example of how twinning in Ti-6Al-4V appears in EBSD is shown in Figure 2.6 for cross-rolled Ti-6Al-4V material deformed until failure under quasi-static loading conditions.

Twinning is not expected to be observed here due to the quasi-static strain rates, room temperature loading and comparatively low strains employed. However, limitations of the areas scanned via EBSD mean there may be unobserved twinning within the material. In Ti-6Al-4V, deformation is predominantly in the form of slip,

where the inclusion of aluminium acts to suppress twinning [23]. Ti-6Al-4V does not generally twin except at high strain rates or at elevated temperatures. However, Prakash et al [167] suggests that in compression, twinning is present at room temperature and at low, bordering on quasi-static, strain rates. Follansbee noted that deformation twinning is observed in addition to planar slip at high strain rates [73]. Wielewski et al [215] suggest that during compression, tensile twins form preferentially in macrozones orientated for α-type slip, linking the presence of macrozones with twinning in Ti-6Al-4V .

In the case of binary Ti-Al alloys, a complex relationship exists between the aluminium content and the activated deformation mechanisms. Generally, increasing aluminium content is deemed to inhibit twinning. However this relationship is complex with the formation of Ti_3Al and the role of slip on the activation of twinning [71, 151].

2.3 Mathematical Modelling of Plasticity

The motivations for modelling polycrystalline materials are varied. Atomistic models are used in an attempt to understand and model the motion of individual atoms in the material. These are used to analyse and understand deformation due to quantum effects, interstitial atoms and size effects [105]. These have an intrinsic length scale - the atomic scale. At a molecular level, molecular dynamics (MD) models are employed to study the physical movement of atoms and molecules. These have been used to model the phase transformations that occur in titanium alloys [227]. Dislocation dynamics deals with discrete dislocations and dislocation patterns, which have been utilised to extract microscale plasticity parameters [34]. Crystal plasticity models account for grain interactions and deformation predominantly via slip and twinning. These are often used to extract material properties that are otherwise difficult to quantify. Experimental validation is critical for the verification of simulations [219]. Macroscopic modelling of titanium alloys is performed at the component level, such analysis is often used to predict, for example, the fatigue life [136] or the effectiveness of additively manufactured titanium alloys compared to traditionally formed parts [33]. An example of modelling polycrystalline deformation is given by Ghosh and colleagues [77, 183] where constitutive equations were developed and the analysis was calibrated using experimental data, generating statistically equivalent virtual microstructures.

A simplified model used to represent a large stochastic system is termed a mean field approach, this is where a large number of individual components are used to represent a complex system via their interactions [121]. Approximation is often performed using averaging strategies as fully modelling crystal behaviour from ab-initio or first principle methods results in very small-scale analyses which are not representative of the bulk behaviour. It remains computationally expensive to analyse representative quantities in this way [15].

2.3.0.1 Iso-stress (Sachs) and Iso-strain (Taylor) Models

Iso-stress and iso-strain approaches are well-established models, devised respectively by Sachs in 1928 [178] and Taylor in 1938 [195]. In 1970, Kocks [108] published 15 years of work on single and polycrystal deformation, including extensive experiments and a comparison of both the Taylor and Sachs models. Sachs and Taylor models are analytical methods which are known to violate either compatibility, equilibrium conditions or, sometimes, both [187]. However, they laid the foundations for further, more advanced models.

The iso-stress model defines stress as being homogeneous in each grain, therefore each individual crystal will experience the same stress state. The Sachs model is a lower-bound model, as it neglects intergranular constraints, leading to underestimated effective energy in the system [102]. Equilibrium is satisfied. However, the compatibility between strains is disrupted, leading to grains which eventually violate compatibility. This occurs as each grain undergoes slip in its dominant slip system, causing deformation which is incompatible at the grain boundaries [118]. The model is limited to single crystal slip. However, multiple slip is typical in actual material deformation, and where this is a prominent feature, the Sachs model becomes increasingly inaccurate. The Sachs model has been used to examine the relationship between the local texture and fatigue behaviour by analysing macrozones in Ti-6Al-4V [120].

Taylor [195] defined the simple iso-strain model, where each crystal is exposed to the same strain conditions (plastic deformation is defined as being homogeneous at the macroscale). Therefore, all grains undergo some deformation, this generates an average response and results in an approximation of the upper bounds of strength. The model can be used to obtain a stress-deformation relationship of a polycrystal aggregate from measured single crystal behaviour. This early theory has limitations, including the violation of equilibrium across grain boundaries. The iso-strain model is severely limited in the modelling of HCP polycrystals due to their high anisotropy of slip and low symmetry, as grain anisotropy causes the Taylor model to violate equilibrium. [118] The Iso-strain model is intrinsically better at predicting situations where multiple slip is prevalent. In 1934, Taylor [194] defined two main theories on crystalline behaviour: either a perfect crystal existed and, as portions of the crystal slip and are rotated, they 'lock' the crystal impeding slip, allowing the flawed crystal to withstand greater loads than a perfect crystal. Or, alternatively, the perfect crystal is inherently strong and internal defects increase the crystal's ability to slip. Taylor understood slip to propagate through the crystal in the same manner as a crack, considering a unit dislocation and movement through material.

The Taylor model has been extended with various Taylor-type models being devised, most notably the full constraint (FC) [22] and relaxed constraint [172, 205] Taylor models. The FC model imposes identical plastic deformation through all grains, overestimating the stress and texture intensity. The relaxed constraint model relaxes the imposed constraints of strain homogeneity, improving model accuracy despite allowing for the 'controlled' violation of compatibility.

Self consistent models are an evolution of the previously described approaches. Initially, a 3D ellipsoidal inclusion was defined by Eshelby [67] to study the effects of an inclusion of a material with a different elastic mod-

ulus, and analytical solutions were defined. The self consistent model may be used to analyse polycrstalline materials [112], where a single crystal is modelled within a matrix of homogeneous material. Interactions are determined by regarding the crystal as a matrix inclusion. The stress-strain response at the macroscale is related simply to the local, microscale behaviour of the crystal inclusion.

Although each grain is treated as deforming individually, there is still a high level of homogeneity within the actual grain. Additionally, no real structure evolution is determined using this model due to the relationship between single and polycrystalline flow. In situ neutron diffraction has been used to successfully test an elasto-plastic self-consistent model. This model allows the determination of CRSS and hardening parameters at both the meso- and microscale whilst the specimen undergoes deformation [79, 80]. Viscoplastic polycrystals can be also modelled using a self-consistent approach to estimate their non-linear behaviour [143]. Complexities arise as the models are developed to include fully anisotropic behaviour, where models become increasingly computationally expensive.

Lebensohn's VPSC (visco-plastic self consistent) model [123] operates at continuum level yet is sensitive to microscale factors due to its coupling with finite elements. It is possible to model recrystallisation and crystal anisotropy using this method [122]. VPSC models have been employed to analyse titanium based alloys for the prediction of texture and anisotropy [75] and the simulation of the bending of titanium [106]. The VPSC model is often defined as a compromise between the fast yet limited Taylor models and the more complex and computationally intensive crystal plasticity finite element (CPFE) methods.

2.4 Crystal Plasticity

CPFE (crystal plasticity finite element) modelling is based on the assumption that plastic deformation is the cumulative effect of slip in all individual grains within a material. Finite element analysis (FEA) is often used to predict the mechanical behaviour of structures at component level [233]. Microscopic properties are therefore homogenised to simplify models, enabling faster computation. Micro-mechanical finite element models discretise a polycrystalline aggregate into finite elements, allowing for non-uniform deformation via spatially varying properties. Crystal plasticity based finite element (CPFE) models are extensions of traditional FEA, utilising crystal plasticity constitutive models, which allow incorporation of both texture and material parameters to be input at the grain level and predict the resulting stress-strain response and texture evolution.

CPFE predictions are easily compared with experiments due to the current experimental ability to accurately quantify deformation at the crystal scale to a high level of detail by probing a variety of quantities. The variety of applications for CPFE modelling is extensive and the ability to consider both the micro- and macroscopic scale is invaluable [175]. Interactivity between these mechanisms may be implemented, allowing highly complex yet realistic scenarios to be modelled. CPFE may be utilised as a 'virtual mechanical laboratory' [110] where calculated material parameters are compared with experimentally established ones for verification of the virtual results.

Potential improvements to the CPFE method lie in further understanding twinning and its interaction with slip. Twinning is often neglected in analyses due to its increased complexity and relative rarity. The generation of new crystal orientations must be defined for twinned crystals, which requires increased computational effort. Kalinindi [97] successfully integrated twinning into a CPFE method using a relaxed configuration of the twinned crystals. Staroselsky and Anand [187] allowed slip and twinning to be modelled concurrently. Numerous assumptions have been made regarding twinning due to the difficulties in accounting for twinned deformation and subsequent orientations. CPFEM has been used extensively to model deformation in titanium alloys. Recent work involves examining the effect of temperature on the ductility of cp-Ti, the effect of the β phase on the micro-mechanical response of dual-phase titanium alloys and explicit modelling of Ti-6Al-4V phases to examine additively manufactured products [10, 98, 157].

2.5 Kinematics

Kinematics mathematically describes motion in a body of interest, where the deformation of a model is captured via the relative motion of individual points. The notation used here means scalars are written as lower case whereas vectors are lower case but bold and tensors will be both bold and upper case.

A material point here is described by an infinitesimally small volume element. In order to track specific regions of this body, each point is defined by its initial reference location. The undeformed reference configuration B_0 is transformed to the current deformed configuration, B_t via the motion $\boldsymbol{\varphi}$, where $\mathbf{X}$ and $\mathbf{x}$ describe the same point in the reference and current configurations respectively, that is

$$\mathbf{x} = \boldsymbol{\varphi}\left(\mathbf{X}, t\right). \tag{2.3}$$

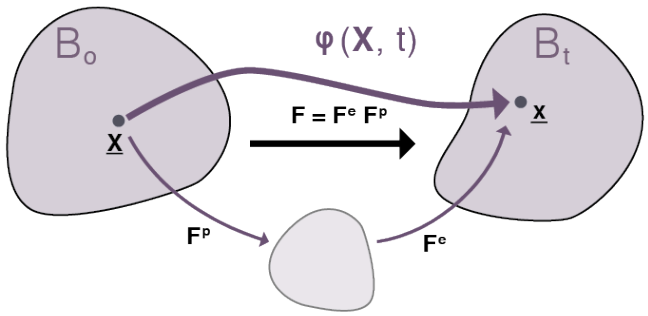


Figure 2.7: Visualisation of deformation kinematics.

The deformation gradient, $\mathbf{F}$ describes the change in length and angle between infinitesimal line segments of the initial and current state of the material. This important descriptor of the applied deformation state is

defined by

$$\mathbf{F} = \text{Grad } \boldsymbol{\varphi} \quad \text{where} \quad F_{ij} = \frac{\partial \boldsymbol{\varphi}_i}{\partial X_j}. \tag{2.4}$$

In this description, deformation can be fully described in terms of stretches and rotations, as such a multiplicative elasto-plastic decomposition is used to decompose $\mathbf{F}$ into an elastic and plastic parts, as

$$\mathbf{F} = \mathbf{F}^e \, \mathbf{F}^p \tag{2.5}$$

where $\mathbf{F}^e$ is the elastic and $\mathbf{F}^p$ is the plastic tensor, representing the elastic and plastic components of deformation respectively. The plastic deformation $\mathbf{F}^p$ is controlled fully by plastic slip in this case as

$$\mathbf{F}^p = \sum_\alpha \gamma^\alpha \;\; \mathbf{s}^\alpha \otimes \mathbf{m}^\alpha \tag{2.6}$$

where $\mathbf{s}^\alpha \otimes \mathbf{m}^\alpha$ defines the Schmid tensor and γ^α describes the plastic shear of the α slip system where

$$\sum_1^n ()^\alpha = \sum_\alpha () \tag{2.7}$$

The rate of change of the deformation gradient, $\dot{\mathbf{F}}$ is

$$\dot{\mathbf{F}} = \frac{\partial}{\partial t}\left[\frac{\partial \boldsymbol{\varphi}}{\partial \mathbf{X}}\right] = \frac{\partial}{\partial \mathbf{X}}\left[\frac{\partial \boldsymbol{\varphi}}{\partial t}\right] = \frac{\partial \mathbf{v}}{\partial \mathbf{X}} = \text{Grad } \mathbf{v}. \tag{2.8}$$

Here, $\mathbf{v}$ is the velocity. The rate of change of the deformation gradient can be written in terms of the spatial velocity gradient and the deformation gradient by

$$\boldsymbol{\ell} =: \frac{\partial \mathbf{v}}{\partial \mathbf{x}} = \frac{\partial \mathbf{v}}{\partial \mathbf{X}} \, \frac{\partial \mathbf{X}}{\partial \mathbf{x}} = \dot{\mathbf{F}} \, \mathbf{F}^{-1} \;\; \text{thus} \;\; \dot{\mathbf{F}} = \boldsymbol{\ell} \, \mathbf{F}. \tag{2.9}$$

2.5.1 FEpX Model

Crystal plasticity based finite element simulations are performed here using the FEpX software [49]. FEpX has been designed to simulate mechanical behaviour at the grain aggregate level. It is established in simulating quasi-static monotonic loading as prescribed in the current experiments. Anisotropy of elasticity in the hexagonal crystal symmetry and anisotropic plasticity based and rate dependant slip are also included. Limitations of FEpX include the omission of twinning and creep behaviour, however, neither of these are required here. The kinematic decomposition details both elastic and plastic behaviour. The plasticity model is viscoplastic, rate dependant and non-linear.

All parts of the decomposition alter the material state from the reference to a new configuration are as described by previous kinematics, Section 2.5. The primary solution field variable in FEpX is velocity $\mathbf{v}$. Slip

is the only mode of plastic deformation considered. The three slip systems include <a>-type basal, prismatic and pyramidal slip, see Figure 2.8.

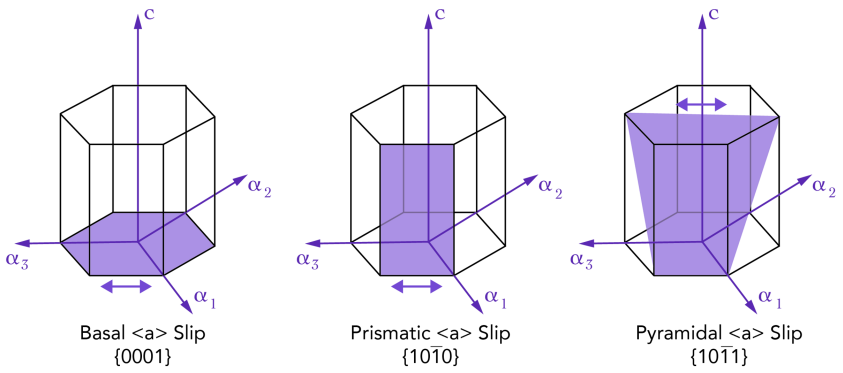


Figure 2.8: Active slip systems available in FEpX for HCP crystals.

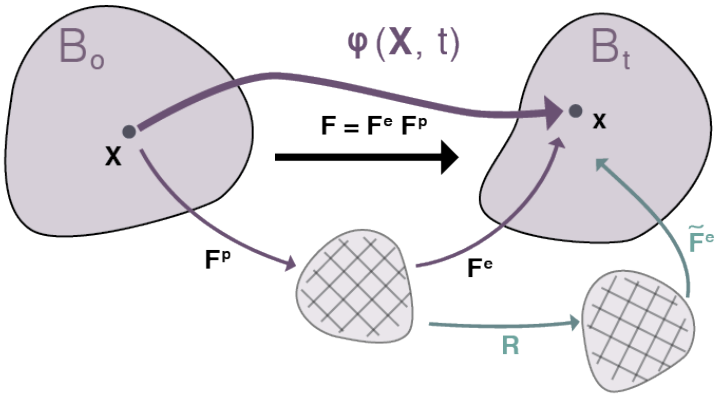


Figure 2.9: Deformation kinematics including decomposition of the plastic part of the deformation gradient $\mathbf{F}^p$ as used in FEpX.

The deformation gradient $\mathbf{F}$ is further decomposed as,

$$\mathbf{F} = \mathbf{F}^e \, \mathbf{F}^p = \left(\tilde{\mathbf{F}}^e \, \mathbf{R}\right) \mathbf{F}^p \tag{2.10}$$

as in Figure 2.9 where $\mathbf{R}$ deals with the rotation. The spatial velocity gradient $\boldsymbol{\ell}$ can be separated into elastic $\boldsymbol{\ell}^e$ and plastic $\boldsymbol{\ell}^p$ components.

$$\boldsymbol{\ell} = \boldsymbol{\ell}^e + \boldsymbol{\ell}^p \tag{2.11}$$

where the plastic component is further decomposed into symmetric and skew symmetric parts, the rate of deformation tensor $\mathbf{d}^p$ and the plastic spin tensor $\mathbf{w}^p$ respectively, as

$$\boldsymbol{\ell}^p = \mathbf{d}^p + \mathbf{w}^p, \tag{2.12}$$

where

$$\mathbf{d}^p = \frac{1}{2}\left[\ell^p + \ell^{p\mathrm{T}}\right] \tag{2.13}$$

$$\mathbf{w}^p = \frac{1}{2}\left[\ell^p - \ell^{p^{\mathrm{T}}}\right]. \tag{2.14}$$

where substituting the spatial velocity gradients gives

$$\mathbf{d}^p = \sum_\alpha \dot{\gamma}\,\frac{1}{2}\left[\mathbf{s}^\alpha \otimes \mathbf{m}^\alpha + \mathbf{m}^\alpha \otimes \mathbf{s}^\alpha\right] = \sum_\alpha \dot{\gamma}\,\mathbf{P}^\alpha, \tag{2.15}$$

where $\mathbf{P}^\alpha$ is the symmetric Schmid tensor.

2.6 Yield Function

Kinetics describes the state of internal stress in a body. Small strain assumptions are made to describe the elastic behaviour, this classical approach means displacement of each material point is linearly dependant. The (Kirchoff) stress $\boldsymbol{\tau}$ is related to the elastic strain via

$$\boldsymbol{\tau} = \mathbf{C}\,\boldsymbol{\epsilon}^e \tag{2.16}$$

where $\mathbf{C}$ is the elastic tensor which captures the crystal symmetry and $\boldsymbol{\epsilon}^e$ is the elastic component of the infinitesimal strain tensor $\boldsymbol{\epsilon}$. Assuming small strains this is

$$\boldsymbol{\epsilon} = \frac{1}{2}\left(\frac{\partial \mathbf{u}}{\partial \mathbf{x}} + \frac{\partial \mathbf{u}}{\partial \mathbf{x}}^T\right), \tag{2.17}$$

where the elastic part $\boldsymbol{\epsilon}^e$ is then

$$\boldsymbol{\epsilon}^e = \boldsymbol{\epsilon} - \boldsymbol{\epsilon}^p. \tag{2.18}$$

A flow rule is used to describe the plastic behaviour. The onset of plasticity occurs when yield conditions are met. As the stress in the direction of slip τ^α reaches the yield stress, the crystal will slip as

$$\tau^\alpha = \boldsymbol{\tau} : \mathbf{s}^\alpha \otimes \mathbf{m}^\alpha. \tag{2.19}$$

For example, the yield function for isotropic hardening is

$$f\left(\tau^\alpha,\ g^\alpha\right) = |\tau^\alpha| - (\sigma_y + g^\alpha) \tag{2.20}$$

Here σ_y is the initial yield stress and g^α is hardening, where the hardening rate $\dot{g}^\alpha$ is defined by a modified Voce hardening law as

$$\dot{g}^\alpha = h_0\left(\frac{g_s^\alpha(\dot{\gamma}) - g^\alpha}{g_s^\alpha(\dot{\gamma}) - g_0^\alpha}\right)\dot{\gamma}. \tag{2.21}$$

Here h_0 and g_0 are the hardening rate coefficient and initial slip system strength respectively and

$$g_s^\alpha\left(\dot{\gamma}\right) = g_0^\alpha\left(\frac{\dot{\gamma}}{\dot{\gamma}_{s0}}\right)^{m'} \tag{2.22}$$

where

$$\dot{\gamma} = \sum_{\alpha} |\dot{\gamma}^{\alpha}| \tag{2.23}$$

g_0^{α} is the initial saturation strength, $\dot{\gamma}_{s0}$ and m' are the saturation strength rate scaling coefficient and exponent respectively.

The yield surface for a single crystal is built from the combination of the slip system yield functions f^{α} as indicated in Figure 2.10. A stress state within the space ($f^{\alpha} < 0 \; \forall \; \alpha$) indicates elastic behaviour whilst on the yield surface indicates plastic behaviour.

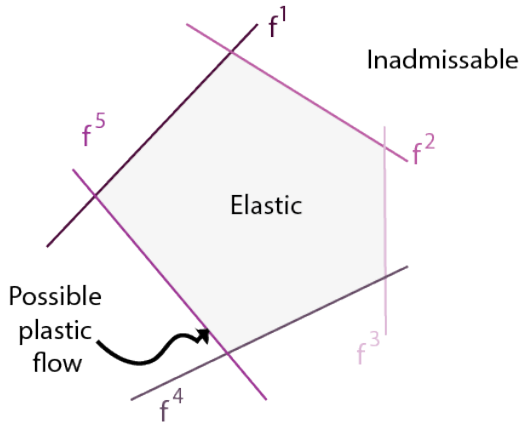


Figure 2.10: Multi-axial plasticity yield surface where the blue dot represents a stress state which remains within the yield surface ($f < 0$) and therefore the behaviour is elastic. The red dot represents a stress state at the bounds of the yield surface and will induce plastic flow.

To complete the formulation, the visco-plastic flow relation for the slip rate is in the form of a power law where

$$\dot{\gamma}^{\alpha} = \dot{\gamma}_0 \left(\frac{\tau^{\alpha}}{|g^{\alpha}|} \right)^{\frac{1}{m}} \operatorname{sgn}\left(\tau^{\alpha}\right). \tag{2.24}$$

Here m is the strain rate sensitivity parameter and $\dot{\gamma}_0$ is the fixed-state strain rate scaling coefficient.

Chapter 3

Experimental Methodology and Data Analysis

In this chapter, all experiments performed in this work are described in detail, including the rationale for the tests performed. Experiments performed include in situ uniaxial tensile tests at a synchrotron source (CHESS, NY, USA) enabling the concurrent measurement of lattice strain evolution and macroscopic stress-strain response during early deformation and yield. Experiments involving a strain rate jump are analysed in depth for Ti-6Al-4V. Post experiment, these specimens are examined using advanced microscopy techniques such as EBSD to characterise the microstructure and crystallographic texture. This combination of techniques provides a comprehensive analysis of titanium alloy behaviour at room temperature for multiple length-scales. Further ex situ tensile tests were also performed to analyse failure.

3.1 Tensile Testing

Uniaxial tensile testing applies deformation along a single axis, and the force generated is measured, usually using a load frame and a load cell. Many testing machines allow control of either displacement, strain or force. This is a well established, reliable and reproducible test method used to obtain the macroscopic response. The combination of high energy synchrotron x-ray diffraction and uniaxial tension testing allows the collection of concurrent lattice strain evolution and macroscopic response during deformation. Hart [87] outlined a useful theory of tensile testing, focusing on the influence of the strain rate sensitivity on the flow stress. Fundamental uniaxial tensile test regimes employed in this work are summarised in Table 3.1. Tests are performed in displacement control until an engineering strain of $\sim$6% is reached. Engineering strain is defined as the amount of deformation in the direction of the applied force divided by the initial length of the specimen. The strain rate jump experiment (SRJ) is of particular interest in calculating the strain rate sensitivity as it allows examination of the material at multiple strain rates with a consistent microstructure.

Table 3.1: Overview of experiments performed.

Experiment	Description	Duration
Lower strain rate	Constant strain rate of 10^{-4} s^{-1}, quasi-static loading under uniaxial tension to ~6% engineering strain.	600s
Higher strain rate	Constant strain rate of 10^{-3} s^{-1}, uniaxial tensile loading to ~6% engineering strain.	60s
Jump in strain rate	Initial strain rate of 10^{-4} s^{-1} until 3% engineering strain, rising instantaneously to 10^{-3} s^{-1} and continuing at this strain rate until ~6% engineering strain.	330s

3.1.1 Specimen Design

A specimen with a 1 mm^2 square cross section and 8 mm gauge length was designed to be used at CHESS, the Cornell High Energy Synchrotron Source. Smaller than conventional mechanical testing specimens are required to allow the incident x-ray beam to penetrate the entire sample whilst undergoing deformation. The sample size is reduced to capture full powder diffraction rings in a suitable time frame. A balance between the applied strain rate and detector resolution is required. The square cross-section samples allow for simple beam alignment and directions can be identified post-experiment when the deformed specimens are later dissected for microscopy. This also ensures consistency in direction between the samples. A diagram showing a sample specimen with an incident beam of synchrotron light and the resulting diffraction rings is shown in Figure 3.1. Further information on the high energy x-ray diffraction setup is described in Section 3.2.3.

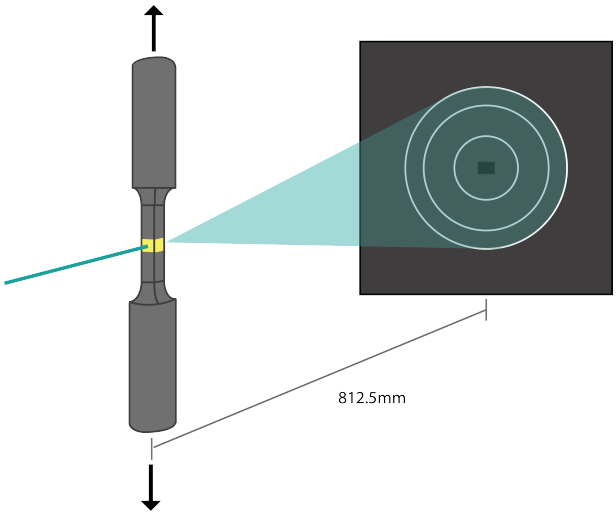


Figure 3.1: Schematic showing an incident beam striking the sample gauge section and an example of the resultant powder diffraction rings formed on an area detector.

Standard 'dog-bone' tensile specimens have been designed for the ex situ uniaxial tensile tests. These have been designed to examine the effect of the strain rate jump on failure. Specimens were tested in a Zwick Roell 250kN load frame. Technical drawings of both specimen designs described are shown in Appendix A.

Specimen manufacture is a key consideration particularly for the smaller CHESS samples. Wire electrical discharge machining (EDM) was employed for all specimens. EDM uses electrical discharges, or sparks, to manufacture desired forms. It is an ideal process for these small specimens due to its ability to machine complex shapes that would otherwise be difficult to produce using conventional manufacturing methods. It can also cut hard materials to very high tolerances with little surface damage or distortion [171]. This is ideal for titanium alloys. Conventional methods are more likely to induce sub-surface damage on titanium alloys due to the excessive cutting tool pressures required. This will also cause heat to build up within the sample, which is minimal in the EDM process. As no direct contact exists between the tool and work-piece in EDM, weaker materials and intricate sections may be machined with low speeds, obtaining samples with very little surface damage or residual stresses.

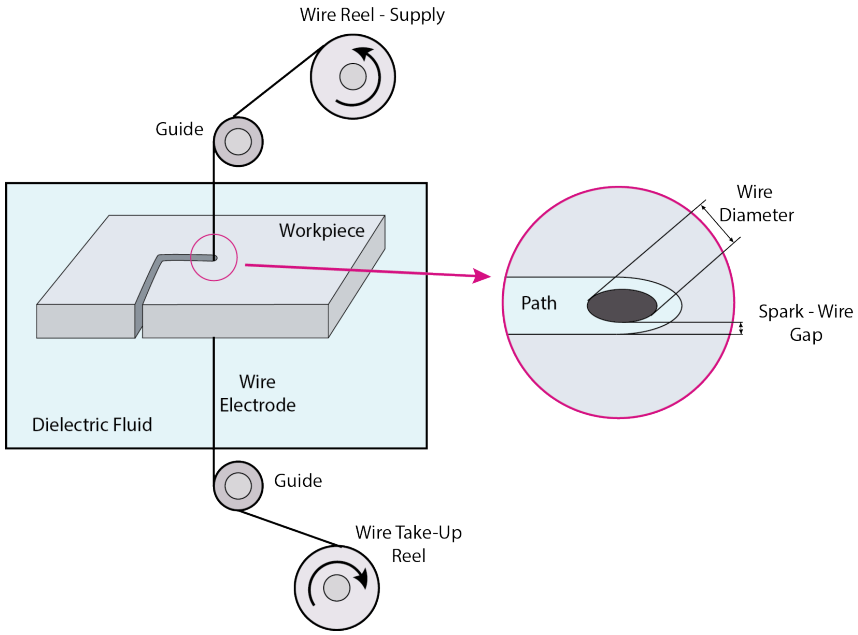


Figure 3.2: Schematic showing the wire-EDM process, adapted from Mahapatra and Patnaik [134].

Wire EDM, as used here, has increased precision over standard EDM, allowing for intricate patterns to be cut. Wire EDM discharges current through a thin wire which is held taut. This acts as a cathode and is guided along the desired cutting path. The entire process is performed whilst submerged in a dielectric fluid which filters and directs the sparks [93]. A schematic showing the wire EDM process is given in Figure 3.2. A skim cut may follow the main wire cut to remove thin slivers of material (in the order of tens of microns) for increased design accuracy. This involves the wire being passed back over the roughed surface with a low power setting and a low pressure flush. The number of skim passes used is dependent on the required final accuracy and surface finish. The wire EDM process is also highly controllable which is ideal for the tight tolerances required, particularly in the area surrounding the transition from the cylindrical grip sections to the square cross section of the CHESS specimen.

3.2 High Energy X-Ray Diffraction

High energy x-ray diffraction (XRD) has been traditionally used for physics-based research to resolve single crystal structures and more recently to further understand the structure and early deformation of bulk poly-crystalline materials and nano-particles [88]. High energy XRD is becoming an increasingly common tool for materials characterisation, particularly in deformation analysis, due to advances such as the 3D detection and visualisation of XRD cones with the use of moving or multiple area detectors [4]. From the shape, intensity change and discontinuities observed in the 3D cones, data including sample coarseness, diffraction depth, grain size and grain distribution can be extracted. The following sections will discuss basic diffraction principles, the overall synchrotron function and the powder diffraction process in detail. The equipment used and key considerations are also outlined.

3.2.1 Diffraction Principles

Diffraction phenomena, dealing with wave interactions, can be utilised in a variety of ways in materials characterisation and analysis. Techniques employed for texture analysis are often based on the diffraction from a crystalline specimen, whether the preferred method involves electrons, neutrons or x-rays depends on the desired wavelength of the incident radiation source.

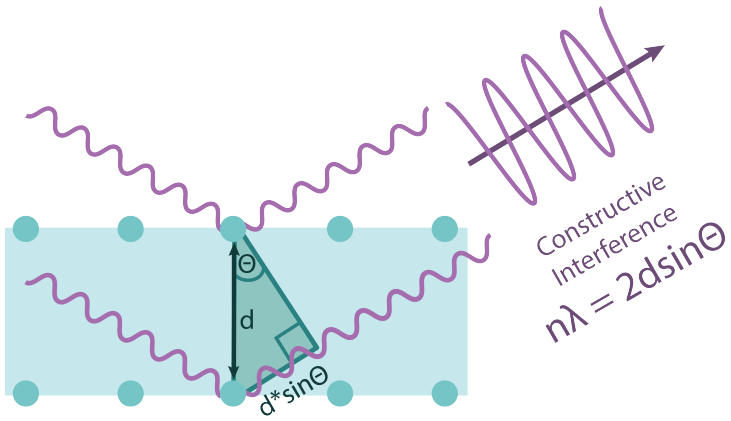


Figure 3.3: Schematic of Bragg condition being met, showing constructive interference as beam strikes surface layers of a crystalline material.

A schematic of Bragg's law showing constructive interference as the incident beam strikes rows of atoms at the surface layers of the material of interest is shown in Figure 3.3. Bragg diffraction occurs when radiation, with a wavelength of size comparable to the materials interatomic spacing being scattered is reflected from the material's crystallographic lattice planes with an interplanar distance d. The scattered wave-forms may or may not remain in phase and interfere constructively. The path difference between both wave-forms is then given by $2d \sin\theta$, where θ is the scattering angle. Constructive interference occurs at $n\lambda = 2d \sin\theta$. Destructive interference is caused when $n\lambda \neq d \sin\theta$ and the wavelengths are out of phase, thus diffraction peaks are only observed where constructive interference occurs.

3.2.2 Synchrotron High Energy X-ray Diffraction

Diffraction experiments can be performed using high energy sources (>50 keV). A synchrotron, neutron or equivalent source is required to generate these high energy x-rays. A synchrotron was used in this research to capture sufficient diffraction patterns during the dynamic deformation processes. This is possible due to the intense synchrotron light which allows a realistic quasi-static loading regime to be performed on a sample large enough to be representative of the bulk material. Synchrotron x-rays are advantageous due to their inherent high brightness and monochromatic beam, which is highly tuneable [197].

A brief description of overall synchrotron function is outlined schematically in Figure 3.4. A synchrotron is named due to the need for changes in magnetic field to be carefully synchronised with the change in energy, otherwise the beam is lost. Essentially, as the particles in the accelerator ring increase in energy, the strength of the magnetic field guiding them must be continuously altered to keep the particles moving along the same path, they must be synchronised.

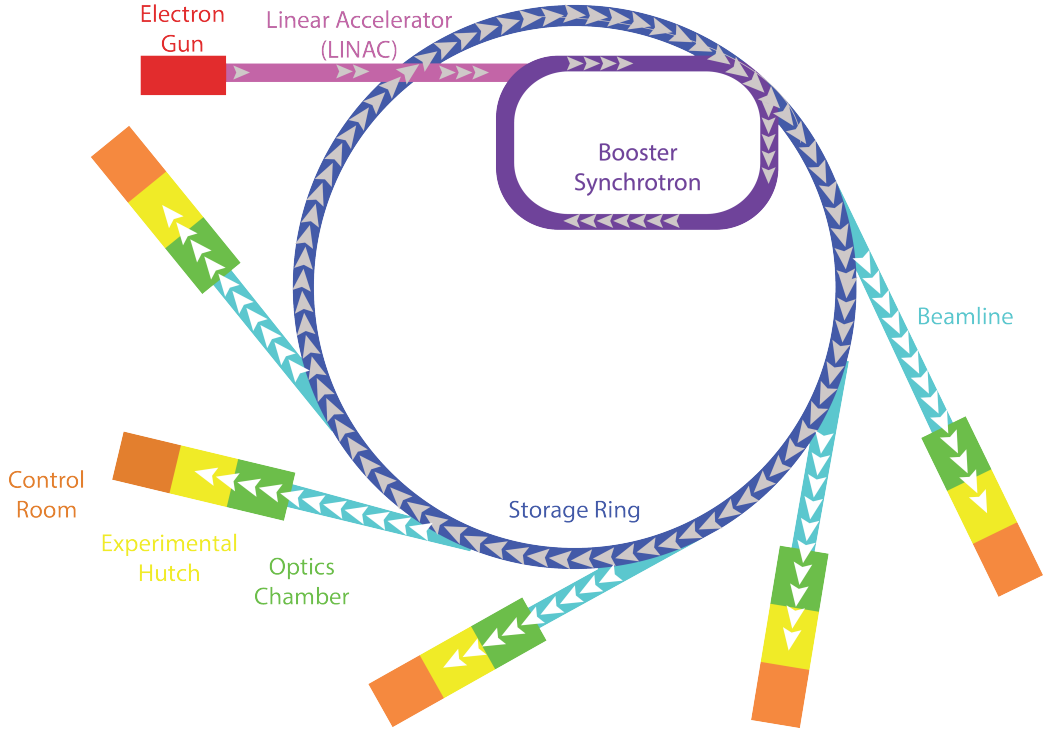


Figure 3.4: Simplification of overall synchrotron function showing the path of electrons around the setup in grey, white arrows depict the synchrotron x-rays directed into different beam lines, where the capabilities in each beam line differ.

Three particle accelerators form the basis of a synchrotron; the linear accelerator (or Linac), booster synchrotron and the large storage ring. Bunches of electrons are emitted from an electron gun and into the linear accelerator where they are accelerated by the electric field. These are then fed into the booster synchrotron where they are accelerated to very high speeds in a vacuum environment. The electrons gain energy until they reach speeds just below the speed of light ($\sim$3 x 10^8 m s^{-1}). The electrons are then injected into the storage ring where insertion devices known as 'wigglers' and 'undulators' force oscillations onto the electrons.

This forced deflection produces high intensity x-rays, termed synchrotron light. The extracted beam of synchrotron light is then channelled into one of the waiting beam-line stations. There are three chambers within each station; the optics, experimental and control chambers.

The optics chamber is where the beam is focused and filtered. Silicon mirrors, slits and crystals are used to filter the frequencies/light and focus the beam to the required dimensions. Attenuation, in the form of steel plates of varying thickness', is used to control the intensity of the beam, ensuring the level reaching the detector is adequate to propagate through the specimen without causing damage to the detector. A crystal monochromator can be used to select a single wavelength of radiation by removing any unwanted wavelengths from the incident x-ray beam. Typical wavelengths range from 0.01 to 10 nanometres for high energy XRD.

The experimental hutch is where the focused beam strikes the sample. The beam penetrates the sample and interacts with the atoms and molecules in the crystallographic lattice. The diffracted cones are captured and this facilitates study at the crystallographic scale. Specialised cameras and detectors capture these interactions. On a diffraction beam line, this interaction produces a diffraction pattern which is often captured by a carefully positioned area detector. This pattern is then analysed to extract sample properties. Finally, the control room houses the scientists and staff. This is where all experimental data is gathered, prepared and potentially analysed.

A variety of materials can be sampled, from small proteins to sections of aircraft engines with this equipemnt. Additionally, a wide variety of experiments can be performed in situ, with the obvious exception of areas where x-ray interference would negatively impact results. Experiments described in the literature involve integrating tensile testing equipment to observe evolving microstructures or stresses in bulk metallic samples [126, 141].

Two types of high energy diffraction microscopy (HEDM) exist; near-field and far-field HEDM. Near-field HEDM techniques are performed with the specimen placed close to the area detector (order of mm). Grain orientation maps with micron scale resolution may be output, allowing observation of the crystallographic orientations, both intragranular and between the grains. While the far-field HEDM technique allows measurement of the centroid average elastic strain tensor and crystallographic orientation in individual grains [20]. The far-field technique often employs some form of the rotating crystal method to enable more crystallographic directions to interfere constructively according to Bragg's Law, leading to increased responses on the detector. It is prohibitively difficult to employ a modified rotating crystal method with continuous diffraction experiments such as those considered in this work. In far-field HEDM, large sample to detector distances are used (in comparison to those in near-field HEDM) where the position of the diffracted response is dominated by both x-ray energy and lattice configuration. A study containing concurrent far and near-field HEDM, cited as being particularly useful for crystal plasticity based FE model validation, has recently been presented [201].

In this work, a far-field diffraction technique is used. This particular technique is termed powder diffraction, where an aggregate of crystals acts in the same manner as a powder of individual crystallites. Far-field experiments lack intragranular resolution but volumetric averaged responses may be sufficient in describ-

ing grain-scale mechanical behaviour by employing analysis techniques such as those described by Bernier et al [20]. A significant advantage of the high energy XRD technique is that it is non-destructive, allowing further microstructural analysis of the deformed material once samples are removed from the synchrotron. This holds for both near and far-field techniques. In this study, EBSD has been performed on deformed samples.

Synchrotron and neutron high energy XRD techniques are compared by Anthony et al [38]. Neutron diffraction effectively is used as a strain gauge, measuring the spacing of the materials atomic layers. It also has application in non-destructively studying the distribution of compressive/tensile stresses within bulk engineering components. High energy neutron diffraction has been used to determine the elastic constants of Ti-6Al-4V [30] and more recently, to observe texture evolution during phase transformation in Ti-6Al-4V [155]. A recent review on neutron diffraction suggests it has much in common with synchrotron XRD [5]. However, synchrotron XRD is the preferred method for time-resolved studies due to the comparatively high intensity of synchrotron light, therefore faster processes can be observed, ideal for the uniaxial tensile tests previously described. Although the strain rates are quasi-static and deemed 'low', the prescribed rates are still at the limits of this technique.

In situ x-ray diffraction analyses are important due to their ability to track microstructural changes during deformation processes and provide detailed real-time information on complex and concurrent phenomena. Synchrotron based XRD is invaluable in validating crystal plasticity based predictive models for phenomena such as work hardening, where parameters cannot be easily quantified by investigating only post-tested specimens.

3.2.3 Powder Diffraction

Single crystal x-ray diffraction is a well established experimental technique commonly used in the determination of a crystal unit cell. It can be used to view variations in the crystal lattice depending on constituent element chemistry. The cell dimensions and atomic positions can be determined with very high precision. The need for this precision is driven by the significance of crystal structure in understanding a variety of physical material properties [18]. Early evaluation of single crystal diffraction is described by Kabsch et al [96]. Single crystals can be difficult to grow, particularly where accurate dimensions and constituent materials are required to ensure the single crystal is representative of a bulk material or where there is a phase changes

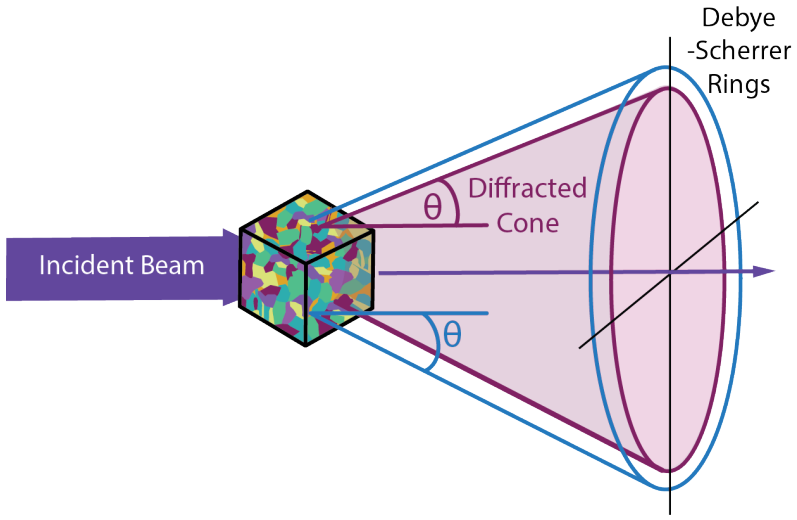


Figure 3.5: Example diffraction cones and Debye-Scherrer rings resulting from powder diffraction experiments, adapted from [17].

An overview of the powder diffraction response is shown in Figure 3.5. Powder diffraction conditions were achieved with the Ti-6Al-4V specimens as the polycrystalline structure acts in a similar manner to a collection of single crystals, or a powder. Where a single crystal response would appear simply as spots on the area detector (known as Laue spots), the polycrystalline structure will appear as an aggregate of reflections from each response that meet the Bragg diffraction condition. This aggregate response forms powder diffraction rings, as diffraction from particular interplanar lattice spacing will produce a cone of diffracted x-rays at a fixed θ (as defined in Figure 3.3). Figure 3.5 shows cones of diffracted x-rays and the resulting Debye-Scherrer rings on the detector due to powder diffraction. An example of the raw, output diffraction rings for Ti-6Al-4V is shown in Figure 3.6.

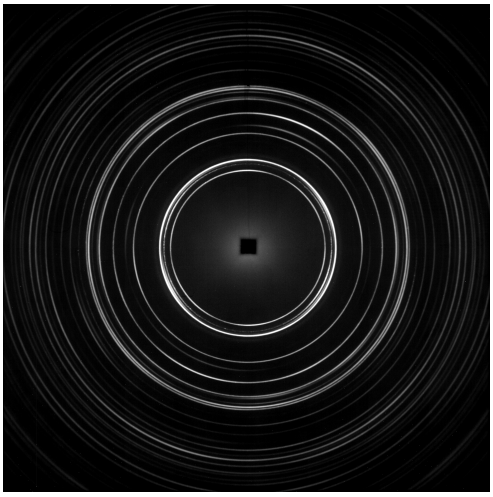


Figure 3.6: Actual Debye-Scherrer rings resulting from XRD experiment of billet Ti-6Al-4V taken from the GE2 detector where the texture may be inferred from the non-uniform diffraction rings with sections of increased intensity.

Powder diffraction is a non-destructive technique. The samples analysed can contain a mixture of materials, but the response is restricted to crystalline structures. Powder diffraction may be performed on either a solid polycrystal or an actual powder, of either organic and inorganic material. The technique is fast and can quickly characterise and analyse unknown materials of long-range order (periodic atomic arrangement). The powder diffraction method is used to obtain the averaged response of bulk material, however, samples are still constrained by size due to the fact the beam must be able to penetrate the entire sample. A polycrystalline sample will contain thousands of crystals, therefore, all possible diffraction peaks should be observed. The resulting diffraction patterns are generated from only a fraction of crystals within the sample as only these are able to contribute to overall diffraction pattern as other responses are annihilated by destructive interference [44].

Images from the detector are captured throughout the duration of the experiment, such as those in Figure 3.6 which shows undeformed billet Ti-6Al-4V. Changes in averaged lattice spacings are evident in the expansion and contraction of the powder diffraction rings tracked thorughout the experiment. Averaged lattice strain responses of particular crystallographic directions were extracted by analysis of the detector image sequence. Errors in strain measurements using x-ray diffraction of the order of 10^{-4} or better can be readily achieved [208]. The fibre averaged lattice strains for each family of crystallographic planes can be calculated [13].

3.2.4 Equipment

The high-energy XRD experiments are performed at the F2 station at CHESS, Ithaca, NY, USA. The setup within the experimental hutch is shown in Figure 3.7. The F2 beam line is predominantly used for high energy x-ray experiments including near-field, far-field diffraction and tomography. Beam intensity is available at 38-80 keV. F2 yields high-energy x-rays with the highest level of flux obtainable at CHESS. An in situ Bose 3330 testing machine (3kN capacity) with capabilities for tensile, compressive, and fatigue loading, including high-cycle fatigue, was used for all experiments performed at CHESS. Multiple load cells dependent on required application are available.

Sample positioning with an accuracy of greater than 1 micron in all three directions allows for accurate positioning of the incoming beam onto individual grains. The load frame is run in displacement control, where stage rotation is controlled using the Spec software. Spec is a Unix-based software package, widely used for instrument control and data acquisition in synchrotron x-ray diffraction [192].

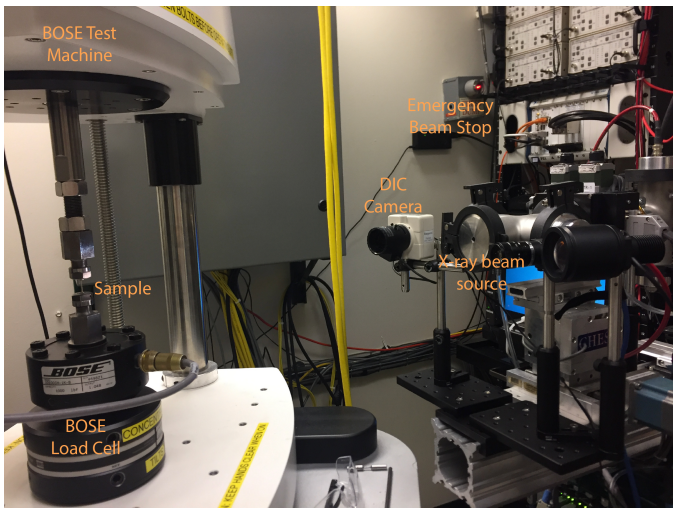


Figure 3.7: Experimental setup in the optics chamber at CHESS, showing x-ray beam location and Bose load frame with sample in place. The camera used for DIC (digital image correlation) is connected to the rotation stage. To the left of this image is the area detector.

3.2.4.1 Detectors

The detector is perhaps the most significant piece of equipment in these experiments. Its placement from the sample dictates which parts of the diffracted cones are recorded. Output from the detectors is in the form of a sequence of images which are subsequently analysed to obtain the averaged lattice strain responses. Two different detectors have been used in this work as multiple sets of experiments were performed at different times and more advanced detectors were available for the second set of experiments.

A single GE2 Detector was used in the December 2016 beam-run whereas two Dexela detectors (FF1 and FF2) were used in December 2017. The CHESS GE2 detector operation limits each experiment to 240 frames of detector output. Raw files from the GE2 detector are in the form of a sequence of images showing the resulting diffraction patterns. The following settings are required to import the sequence into ImageJ: 16-bit unassigned image type with little-endian byte order and an image offset of 8192 bytes. ImageJ is an open source image processing program primarily designed for scientific visualisations [173]. However, for the Dexela results, due to the complexity of file types (HDF5) the image sequence had to be visualised using the HEX-RD GUI [21]. The GE2 analysis is simpler as it contains the entire powder diffraction ring within a single image, so finding the centre and fitting peaks is much more intuitive, as the full rings are readily available to be averaged over.

The Dexela is a more advanced detector, originally designed for medical imaging, with high speed and sensitivity which allowed a sampling rate of 10 Hz to be used. The prescribed setup is at the high end of the detector's capabilities. An example of detector output from both detectors is shown in Figure 3.8. Statistics on both detector setups are outlined in Table 3.2. The Dexela is actually defined by two separate yet identical detectors, which were orientated vertically (one above the other) during the experiments, this means each detector captures different sections of the powder diffraction pattern. The combination of multiple detectors

Table 3.2: Feature comparison for CHESS GE2 and Dexela detectors used in the two sets of experiments, where the Dexela FF1 and FF2 detectors are identical and both have been described under the Dexela heading.

	December 2016	**December 2017**
Model	CHESS GE2	Dexela
Energy Range	20-90 keV	12-120 keV
Size	410 x 410 mm	290.8 x 229.8 mm
Resolution	2048 x 2048	3888 x 3072
Pixel Size (μm)	200 x 200 μm	74.8 x 74.8 μm
Max Frame Rate	8 Hz	26 Hz
Read-Out Time	160 ms	38 ms

allows the entire resulting diffraction pattern to be captured at a very high resolution. The top and bottom arcs of the pattern are expected to show the same response due to symmetry, therefore if only one detector gathers data, the result from the other may be used as a contingency. This was not valid for all directions but was true for the loading direction which is of particular interest. The Dexela FF2 detector does not obtain the same angular resolution as FF1, this allows the transverse direction to be resolved in FF1 only. One of the main drawbacks of the Dexela detectors was the large file size. The smallest file size for a single experiment was approximately 16 GB using this setup, rising to 160 GB for the slower strain rate experiment (10^{-4} s^{-1}). Difficulties relating to data access and analysis are common for prohibitively large files.

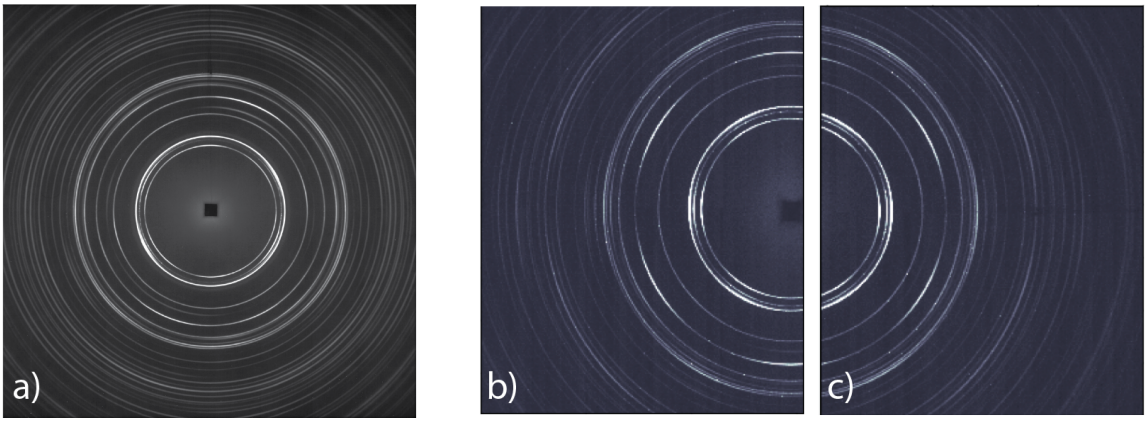


Figure 3.8: Raw detector output from a) the CHESS GE2 detector, and b), c) the outputs from Dexela FF1 and FF2 detectors respectively, where these have been rotated for presentation.

Hierarchical Data Format (HDF) is a set of file formats (HDF5) designed to store and organise large amounts of data and is particularly suited to storing time series data. However it cannot be accessed easily, requiring specific software to view and interact with the data, particularly when dealing with large file sizes. File sizes of the raw detector output for the low strain rate test (the most computationally expensive) rise from around 2 GB (December 2016 using the GE2 detector) to 160 GB with the Dexela (December 2017). This does not include any of the additional files generated from the load frame data, DIC or any initial data analysis.

3.2.5 DIC and Load Frame Data

Digital image correlation (DIC) is an optical non-contact method which measures and tracks coordinates in a collection of images, in this case for the evaluation of deformation. By analysing the sequence of photographs captured, displacements, and therefore the strain accumulation in a particular direction during the test can be calculated [139]. DIC is used to track strain in the gauge section and this can be linked to the lattice strain measurements from the powder diffraction patterns. DIC images were loaded into GOM Correlate software for DIC analysis, which may be used for static and dynamic component testing [43]. The area required to be analysed is defined and the resulting pattern evolution tracked and analysed.

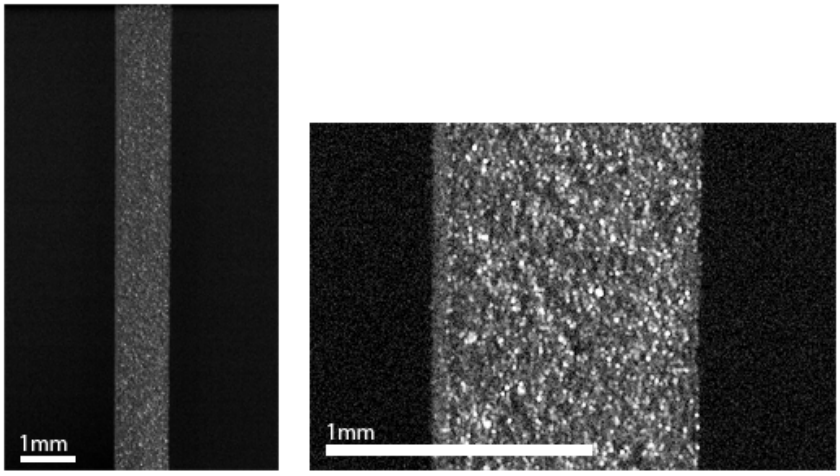


Figure 3.9: Example of DIC images showing natural surface pattern from EDM (scale bars = 1 mm)

Photographs were captured during the entire test duration, with the number of images dependent on the test setup. The images were stored in a sequence as high resolution TIFF files. Most TIFF file formats are uncompressed and designed to be independent of particular hardware or software. TIFF files can be re-sized, increasing the resolution (i.e. number of dots per inch) then transferred between computers and from one application to another multiple times without loss of quality or compatibility issues [147]. However, files are significantly larger than other standard image file formats e.g. JPG or PNG. The December 2016 setup resulted in 2048 by 2048 pixel TIFF files, requiring 2.6 MB per image (240 images total). In contrast, for the December 2017 results, the DIC setup was similar but resulted in 6000 images of 10 Mb each. Equivalent tests required 624 Mb and 60 Gb (60,000 Mb) of storage space when using the 2016 and 2017 setups respectively.

A sample DIC image is shown in Figure 3.9. A speckle pattern is usually sprayed on with paint, however, due to the mechanical properties of the wire EDM process, the material surface is naturally patterned. This is visible in Figure 3.9, therefore there was no need to artificially create a patterned surface.

DIC image capture was successful, but unfortunately the high frequency meant that these files were stored in a memory buffer prior to being written to disk. This resulted in all of the timings becoming inconsistent so the strains extracted from DIC images cannot be reliably compared to lattice strain data as extracted. Addi-

tionally, fewer images were captured during the test than anticipated, and as images were not captured during the software buffering period, this lead to unidentified gaps in the data of unknown duration. Attempts were made to rectify this issue, however low confidence in the final results have led to the modified cross-head displacement being utilised as an alternative strain measurement method.

The load frame records data of the force on the specimen, the cross-head displacement and test duration. The engineering stress σ and strain ϵ were calculated from these simply using $\sigma = F/A$ and $\epsilon = \partial l/l_0$ where F is the force acting on the specimen, ∂l is the change in length and l_0 is the inital gauge length. This method of strain calculation is less accurate than DIC strain calculation method due to the measurement of cross-head position movement not being the same as the actual mechanical strain in the sample. Under certain circumstances, the cross-head movement can be sufficient, although it is not ideal [145]. The incorporation of a strain gauge or extensometer should be considered for future experiments, however these may impede beam interrogation of the sample.

Very small 'blips' were observed in the load frame data (around 3-4 MPa, which is almost negligible compared to the values measured), see Figure 3.10. These small inaccuracies are likely due to interference caused by surroundings, i.e. the equipment used to control high energy x-rays. The periodic nature and magnitude of these imply that they are simply an acquisition artefact. Data smoothing to remove these was performed using a filter (difference equation) in Matlab [156], as the frequency was known and appeared consistent.

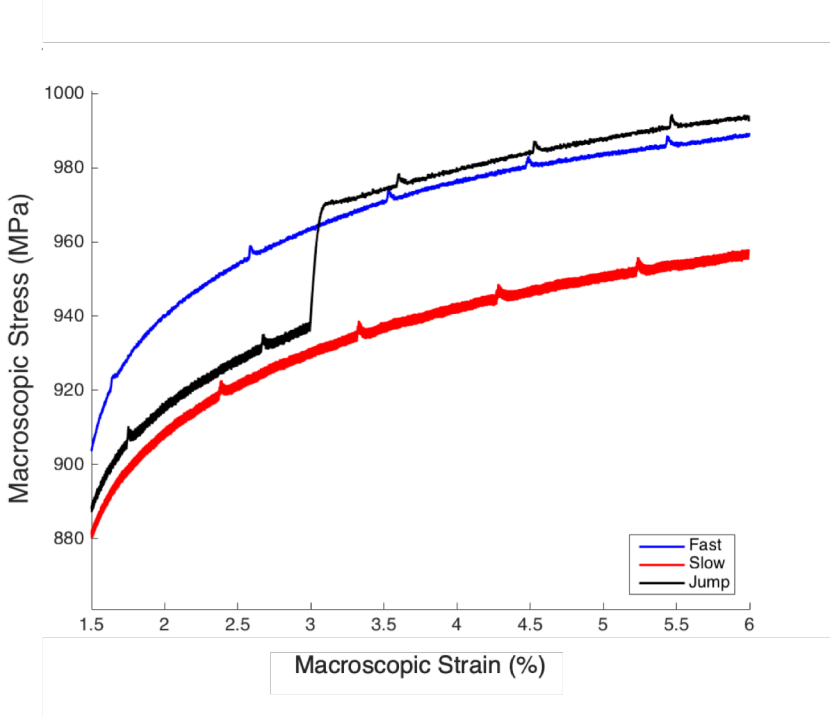


Figure 3.10: Macroscopic stress-strain behaviour is shown for the CR material, showing periodic 'blips' at a displacement of approximately every 0.8mm (machine strain).

As the initial DIC frames were fairly reliable and the behaviour is expected to remain elastic in this region, the modified cross head displacement is calculated. This is verified against the the salvageable DIC data allowing accurate displacement values to be extracted, allowing the elastic compliance in the test rig to be accounted for. Extraction of macroscopic response was consistent for all experiments, the entire process was repeated for every sample tested. DIC analysis has been performed using DICe [200] and compared with the recalculated response, accounting for the elastic compliance of test rig. The stress-strain response is corrected as follows,

$$\epsilon_{act} = \epsilon_{meas} - \sigma(\frac{1}{E_{meas}} - \frac{1}{E_{mat}}) \tag{3.1}$$

where the actual strain in the specimen ϵ_{act} is calculated from the stress σ and the Young's moduli of the combined response E_{meas}. The expected material moduli E_{mat} is obtained from DIC data.

3.2.6 Synchrotron Data Collection

Beam-time is allocated at CHESS with a short time between proposal acceptance and the start date of the actual beam run, meaning experiments have to be planned, with specimens designed and machined in anticipation of acceptance. Time frames and setup requirements mean that preparation is key for a successful beam run. It can also be difficult to predict issues which may arise, some of which are outwith the users control due to the complex nature of high energy x-ray science. This also means the repetition of experiments is rare.

Continuous experiments incorporating high energy x-ray diffraction prove difficult to setup as the timing of all individual components is highly significant. The load frame, rotational stage, DIC equipment, control of x-ray beam, moveable detector shield and actual detector must all operate simultaneously as expected and without delay. Differences in setup are also required for the different experiments. The data acquisition rates and the ability to save results without inducing buffering and delaying acquisition must be carefully considered. Lienert et al [127] performed powder diffraction experiments at the Advanced Photon Source (APS), a similar facility to CHESS, with a method particularly applicable to the current research.

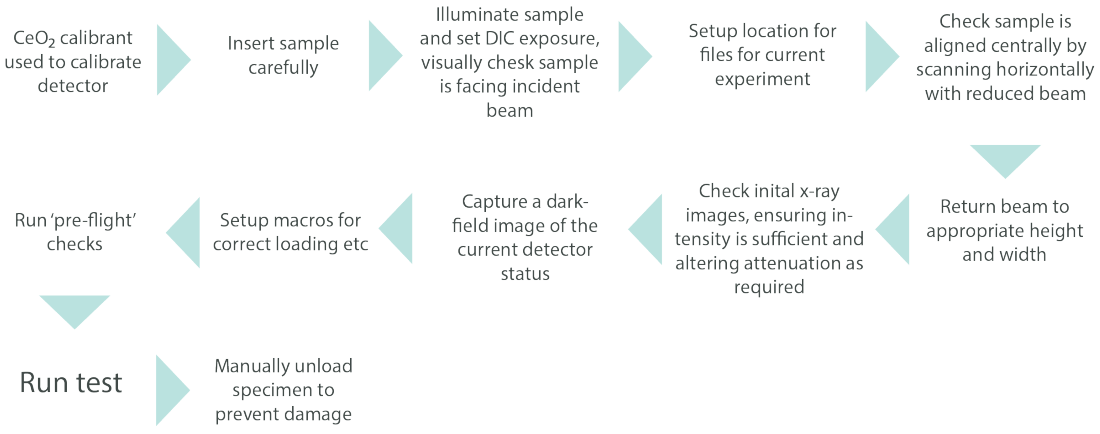


Figure 3.11: Flow chart of preliminary setup process for each in situ experiment.

The experimental setup procedure is outlined in Figure 3.11. As samples are small, care must be taken to ensure specimens are not torqued during tightening of the collets. Detector calibration and a quick analysis of the initial powder diffraction pattern is performed to ensure the correct attenuation is in place to give a sufficiently intense response. 'Pre-flight checks' are conducted to check the operation of individual components before running each experiment, reducing the chances of errors in the experiment. The level of attenuation required predominately depends on the intensity of the powder diffraction response. Therefore, the level of attenuation is controlled depending on the specimen, this is particularly important when changing between material products. Most of the materials studied are forms of Ti-6Al-4V. However, the crystallographic texture and microstructure also play a significant part in what is actually diffracted and the overall intensity. Therefore differences in the materials are evident from the powder diffraction rings. Attenuation is controlled by the placement of steel plates of variable thickness in steps of 0.25 mm. Higher levels of attenuation reduce the beam and therefore the intensity of the diffracted response. Attenuation is controlled aiming for an approximate intensity of 1500 for the brightest peaks, where units are arbitrary. This ensures the detector capabilities are not exceeded, preventing the 'blow out' of pixels.

For sample alignment, the beam size is decreased and a high level of attenuation is positioned to ensure accurate alignment between the centre of the sample and the incident x-ray beam. The beam is scanned across the sample horizontally, encompassing the entire width of the gauge section. A drastic reduction in intensity is observed where the sample interrupts the path of the beam. Therefore allowing the stage to be accurately positioned using Spec to micron precision. Macros are then set up, controlling various parts of the experimental setup, in particular dealing with timing of different interconnected components. These are usually well-established and may be readily modified to suit individual experimental requirements. The combined setup is initially tested on a spare sample to ensure the entire process functions as expected.

Detector calibration is important due to the small length-scales involved in this process. A CeO_2 (cerium oxide) calibrant is used to ensure the detector was correctly aligned and calculations of detector tilt and sample-to-detector distance are made. These extracted parameters are later incorporated into the analysis. A 'dark-field' image is captured, this is the result on the detector with the 'garage door' closed, i.e. the state of the detector with no x-rays. This image was then subtracted from all subsequent frames in the experiment to ensure no 'dead pixels' remain in the analysis. A 'dead pixel' is where the intensity reads artificially low in certain pixels due to the detector being damaged. This leads to spurious results, particularly as averaging is used widely later in the powder diffraction analysis.

Table 3.3: Major experimental parameters from the December 2016 beam-run at CHESS.

Experimental Parameters	**Value**
Beam Energy	61.332 keV
Beam Size	1 x 1.6 mm
Detector	CHESS GE2
Sample-Detector distance	812.5 mm
Calibrant	CeO_2
Sample Gauge Dimensions	1 x 1 x 8 mm

Table 3.3 outlines the experimental parameters of the experiments run at CHESS in December 2016. These parameters were used in the generation of required files for analysis in Apex-rd, which is a collection of Matlab scripts used for the analysis of high energy XRD data. Important attributes such as detector type, beam energy, beam height, beam width and sample-detector distance are used as input. The detector is calibrated with information on the calibrant type and the location of the files containing detector output for calibration, i.e. the calibrant diffraction rings. This step includes the results of the detector held in the initial position and again after a rotation of 180° to ensure the best fit of the data. This also helped to ensure optimal beam alignment.

The experiments on the billet (December 2016) were limited by the time taken to save powder diffraction images from the detector. 240 detector images were captured during each experiment, meaning the acquisition rate is dependent on the test conditions. The slower strain rate (10^{-3} s^{-1}) provided the highest acquisition rate (2.5 images/s) with an overall duration of 600 seconds, whereas the 10^{-4} s^{-1} strain rate corresponds to 0.25 images/s. Therefore, in the jump experiment, as both strain rates are used, a total of 240 detector images are collected; 218 prior to the jump and only 22 post jump.

For consistency, in the second beam-run (December 2017) experiments were repeated using parameters as close to the initial parameters as possible, with differences mainly arising due to the use of an alternative detector setup. The same acquisition rate (a rate of 10 images/s) was used for all of the December 2017 experiments, regardless of test duration. This is significantly higher than used previously, leading to a far higher data resolution. The increased acquisition rate (10 Hz) led to 6,000 detector images being collected for the 10^{-4} s^{-1} (slower) and 600 images for the 10^{-3} s^{-1} (faster) strain rates respectively. Increasing the number of frames after the jump in strain rate in the jump experiments from 22 to almost 300 images with multiple frames captured during the actual jump. Increasing the sampling rate was desired primarily to increase the amount of data acquired around the jump in strain rate, ensuring this was captured sufficiently by multiple data points. The experimental data can still be down-sampled to compare with previously acquired data.

3.3 Powder Diffraction Analysis

Analysis of the in situ XRD experiments requires the tracking of multiple powder diffraction patterns throughout the material deformation. The rings are analysed and the peak shifting, due to expansion/contaction of the rings, shows the displacement of lattice planes, which is related to the evolution of the lattice strain in the material. The process used in the powder diffraction analysis is outlined in Figure 3.12. First, the image sets are loaded into the analysis software. Two different processing software methods have been utilised in this work: Apex-rd and Hex-rd [21]. Apex-rd is a collection of Matlab scripts used to examine XRD data. Hex-rd is written using Python, an open source programming language. The use of different detectors (for reasons outlined in Section 3.2.4), necessitates different output types, which are processed using different software. Both software packages contain similar routines for analysing the data and comparable results may be obtained.

The Apex-RD script is described here. It prompts the user for details of the experiments such as the detector used, the beam height, beam width and the calibrant type. Input parameters such as crystal type and expected *c* and *a* values allow expected ring locations to be predicted, see Section 1.8. The optimal peak width and the size of the radial integration segment are chosen to give the most accurate response, ensuring peaks are correctly identified. Apex-RD has a GUI which is used to select multiple points on the inner detector ring of the calibrant, the results from the combination of this and the input values allow for optimisation of detector tilt and the definition of a more accurate sample-detector distance. These variables are then stored in an 'instrument' file which is initialised prior to the analysis of the actual experimental results.

The detector response is segmented azimuthally and the number of azimuthal bins may be altered. Azimuthal bins are numbered anti-clockwise from 0° as shown in Figure 3.12. 20 azimuthal bins were used (CHESS GE2, full diffraction rings) leading to a sufficient azimuthal bin size. An even number of azimuthal bins ensured the loading direction (90 degrees to the horizontal) is captured adequately, i.e. the loading direction is contained in the centre of the segment to be analysed. The loading direction is defined as the direction of loading on the gauge section, the response reflected at 180° on the diffraction pattern should give the same results. A similar process was used to segment the Dexela data, but an odd number of bins was required to ensure accurate definition of the loading direction, this is due to the Dexela combining two individual detectors. An example using 5 azimuthal bins is shown in Figure 3.12.

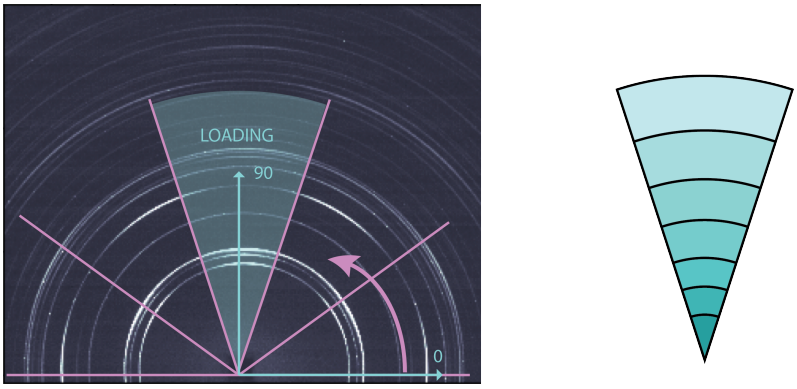


Figure 3.12: The process of analysing powder diffraction results, from azimuthal and radial binning of data to the comparison of the results in subsequent frames, enabling calculation of diffraction ring location and intensity, therefore the extraction of displacement and the calculation of lattice strain measurements. Here, five azimuthal bins have been created, each 36° wide.

Azimuthal bins were then segmented radially, the segments 'flattened' and peaks detected. Setting a peak of 2 pixels/bin (the highest recommended), leads to an increased resolution as an averaging mesh is placed over the image and the intensity is integrated between points, allowing for sub-pixel resolution. This increases the analysis time, but also increases the accuracy of peak detection. Uniformity must be considered as the intensity of peaks in particular directions may differ depending on the width of the segment. For example, in Figure 3.12, where certain reflections do not give uniform intensity around the entire ring. Ideally a line scan would convey the differences in each peak, however, in textured materials, this must be widened to ensure sufficient representation of all required crystallographic directions. This must be balanced with large bin sizes where averaging over segments containing both high and low intensities may reduce the accuracy of the

response. The reorientation of grains will cause a change in the point intensities but the response within the segment may appear similar and therefore appear unchanged in the analysis.

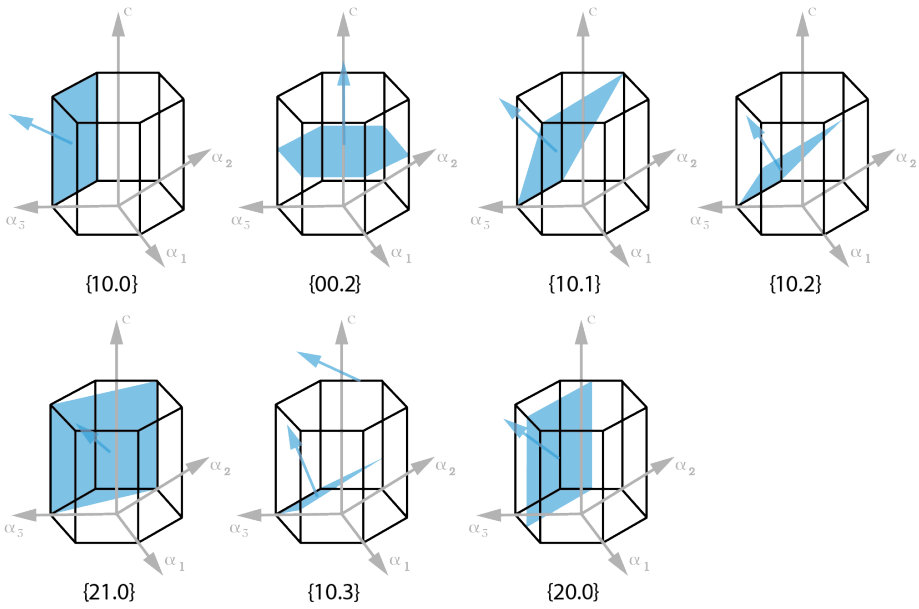


Figure 3.13: Crystallographic responses from the GE2 detector, containing only α phase responses.

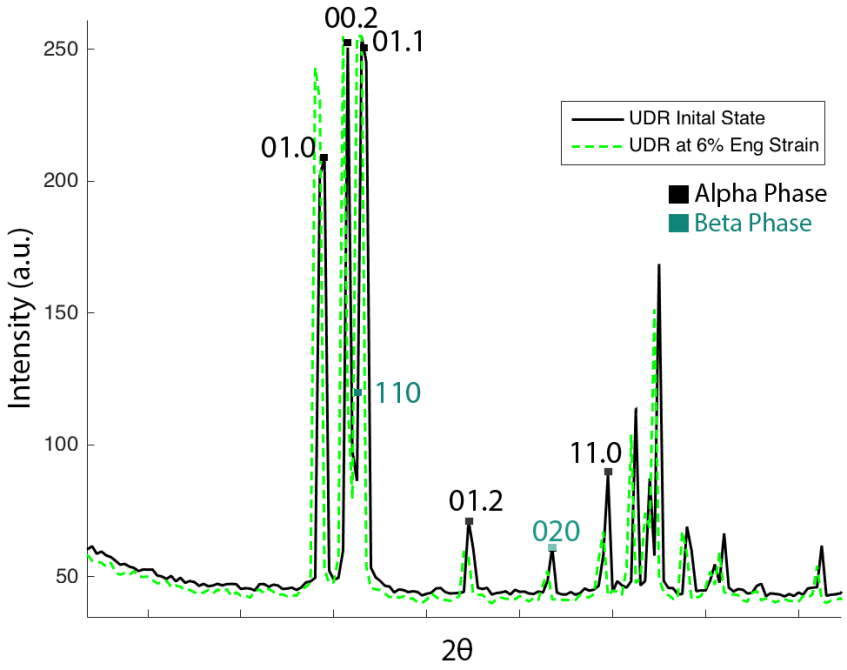


Figure 3.14: Labelled peaks showing the intensity along detector output rings for the undeformed UDR material and UDR at 6% engineering strain showing peak locations and corresponding crystallographic directions. α phase responses are labelled in black whereas the β phase reflections are cyan. Data is taken from the Dexela FF1 detector data in the loading direction, the actual analysis is performed at a higher resolution than the current image.

Miller (cubic) or Miller-Bravais (hexagonal) indices are used to identify different planes of atoms, see Section 1.8 for a detailed description. The reflections analysed in this work are visualised in Figure 3.13, and a section of the peak data is shown in Figure 3.14. A graph showing the peaks and their distance from the centre is shown for the as-received UDR material in Figure 3.15. The distance from a peak to the centre of the detector is calculated. The lattice plane spacing and therefore the resulting lattice strains are extracted for the chosen crystallographic directions. As the peaks shift due to strain within the crystal lattice, the contraction of the powder diffraction rings is observed, this indicates an increase in strain in the material. This contraction is evident in Figure 3.14 where peaks are observed as being closer to the centre of the detector after deformation.

The Dexela detector has a high resolution enabling the detection of peaks of both the α and β phases of Ti-6Al-4V. However, the [110] and [01.1] peaks are very close, with responses overlapping significantly. As a result, the analysis software tends to pick up data from the combined reflections for each of the peaks. The [110] result is neglected in the analysis as it is not possible to decouple the individual results accurately. This can be clearly observed in Figure 3.15 where the overlapping response leads to spurious results. It is possible to decouple these peaks mathematically by means of a modified Lorentzian function [204]. However for simplicity, as the magnitude of [01.1] dominates the response, it will be considered whilst the [110] is neglected. The lattice strain response from these peaks whilst coupled is shown in Figure 3.16, where the parallel responses indicate the same peak is being identified and analysed for both responses.

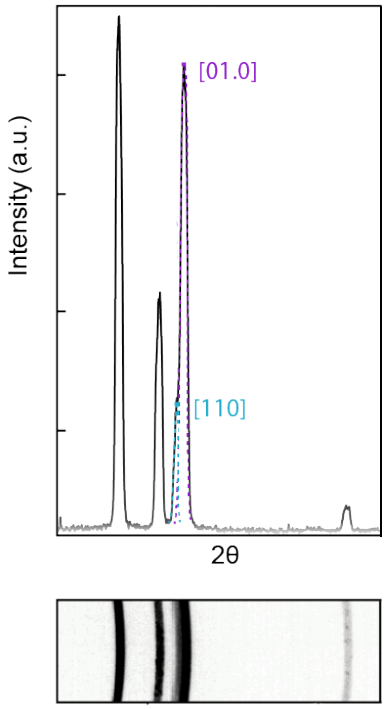


Figure 3.15: Overlap of the {110} and {01.0} diffraction peaks for the initial UDR product, where the individual responses are difficult to decouple.

Incorporated within the analysis code is a check for scrambled frames. This check is designed to identify any inaccurate readings due to scrambled detector images and replaces values with those obtained from the

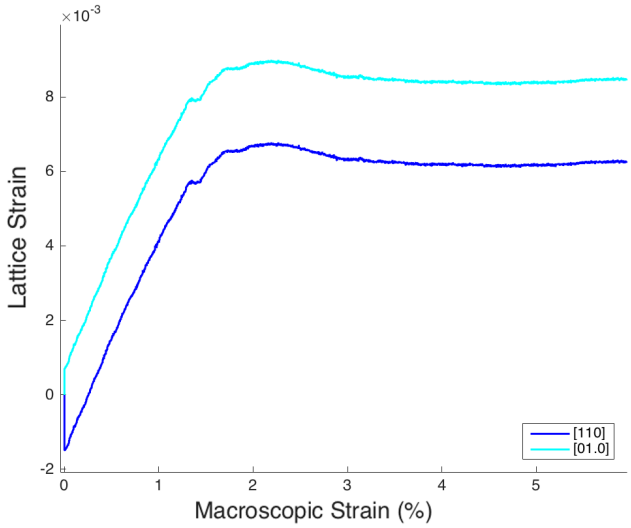


Figure 3.16: Lattice strain response of {110} (dark blue) and {01.0} (pale blue) crystallographic directions, where the symmetry of the response and non-zero initial strain indicate that the same response is being analysed for both crystallographic directions.

previous frame, effectively removing the scrambled frame data from subsequent analysis 'Scrambled' frames, as in Figure 3.17, exist at approximately 1 in every 10,000 frames. These are unavoidable and are dealt with during the initial processing of the results. Once identified, they are removed by replacing the data from them with that of the previous frame. However, this identification acts individually for all peaks considered but occasionally neglects scrambled responses where, on average, the values remain within the acceptable threshold. Therefore, any significant and immediate changes in lattice strain that are identified for a single frame are manually investigated to ensure these are not the result of a scrambled frame. For any remaining scrambled data points, values were manually replaced as per the process within the software.

Results are analysed accounting for multiplicity. Multiplicity is the number of symmetrically equivalent reflections and is dependant on diffraction symmetry and class of reflection [161]. Analyses were run choosing diffraction rings with the high levels of multiplicity and those which remained sufficiently close to the centre. This was due to the intensity of the diffraction rings being significantly reduced for x-rays which have been diffracted further. Also, the rings furthest from detector may suffer from peak broadening.

3.3.1 Azimuthal Bin Width

Choosing an appropriate bin size for all of the data extracted from the second set of experiments (2017) is non trivial. A small bin size is preferred but this may need to be increased to capture evolution in all directions of interest. Where there is insufficient data in the segment, the bin width must be increased. The same bin size has been used for all lattice strain analysis of the Ti-6Al-4V plates in Chapter 5. A larger bin size has been required for the analysis of the Dexela results (2016), where the lower resolution necessitates wider bins. Wider azimuthal bins are subject to error as averaging is performed over each peak, but as the interest is in comparative results, a consistent bin size is preferred over a reduced bin width.

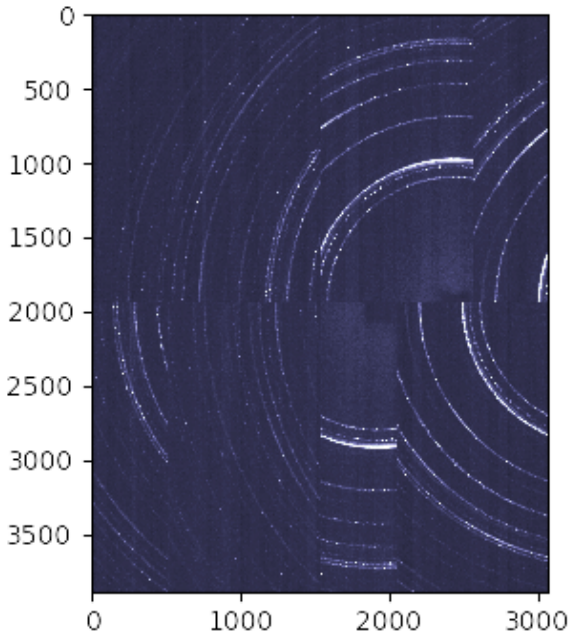


Figure 3.17: Example of detector image where the result has been scrambled; a rare occurrence, estimated at 1 in every 10,000 frames, which must be removed from the analysis.

Data has been analysed using a variety of bin widths to identify the most appropriate choice. All desired crystallographic directions were analysed for the CR material. This material is textured and contains larger grain sizes than UDR. Analysis has therefore been performed on the CR material at 45 degrees for a variety of bin widths, ranging from 12 to 60 degrees. Results appear to converge at 16° and wider. In Figure 3.18 the difference between 12° and 14° is drastic and is deemed too sensitive to be used. This remains the case for additional hkls. It is evident that an effective moduli is dependant on the bin size selected. As the bulk of the analysis is comparative, the 16° results are employed. The effect of the bin size on other Ti-6Al-4V product forms is examined to ensure this does not significantly alter these results, see Figure 3.18. The slower, constant strain rate test was examined as this contains the highest resolution of data points so variations are more likely to be identified. Values vary depending of selected bin width but overall the trends remain the same showing that the larger bin size produces acceptable results, particularly as evolution is compared.

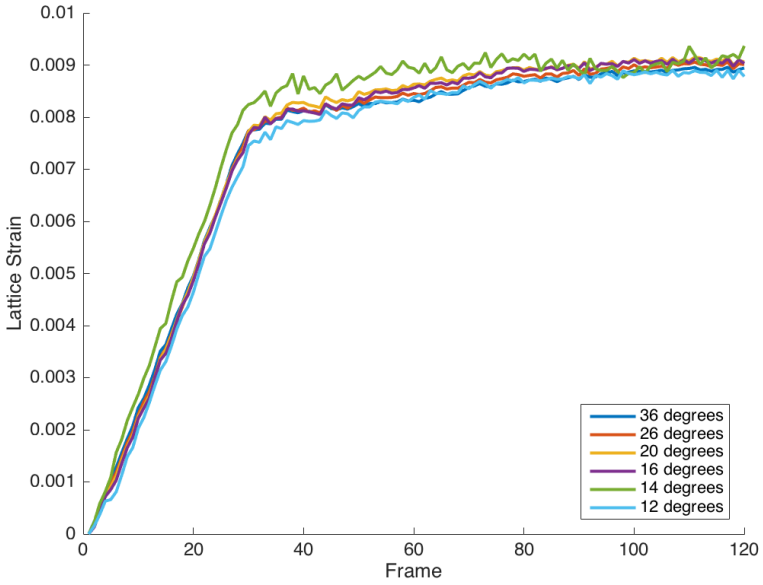


Figure 3.18: Graph comparing the results of lattice strain in the {10.0} direction for bin widths ranging from 12 degrees to 36 degrees, where 120 frames are equally spaced throughout the experiment

3.4 Lattice Strain Evolution

Lattice strain evolution can be extracted from in situ XRD data using established techniques to track changes in lattice plane spacing via the examination of diffraction peak positions. These lattice strains are intrinsically elastic as these describe the stretching of the atomic lattice of the crystalline material. Experiments are currently limited to low strain rates and small deformations due to the allowable acquisition rates. However, the effect of the surrounding plasticity is evident in continuing deformation. Averaged lattice responses in particular crystallographic directions are generally considered when studying lattice strain evolution.

The ability to study materials under unixaial tension with in situ lattice strain measurements is fairly well established at room temperature and low strain rates [41, 221]. Various tests have been conducted on titanium based alloys under different loading conditions (uniaxial [52] and biaxial [66]) where the lattice strain evolution is examined. Stapleton [186] analysed the evolution of lattice strains showing the [200] orientation of the β phase is particularly compliant and that the load partitions to this orientation during plastic deformation in the case of a textured Ti-6Al-4V forged bar. Evolution of the intergranular stresses in a titanium alloy undergoing creep deformation has also been analysised via high energy XRD techniques [180].

3.5 Electron Back-scatter Diffraction

To completely quantify the microstructure, electron back-scatter diffraction, EBSD is an invaluable tool used to gather extensive crystallographic orientation data. EBSD allows nano- to macro-scale characterisation and quantification of materials. It is often used to examine crystallographic orientation, misorientation and deformation within a microstructure. It may also be used to show the location and distribution of grains, phases and their chemistry. The EBSD characterisation technique may be used to study any crystalline material. The technique involves uncovering structure, crystal orientation and phase of materials in an SEM [65]. EBSD is used as a microstructural analysis technique in metal alloy design and production to analyse bulk microstructures which allows control of physical properties.

To ensure a crystalline material sample is suitable for EBSD it must be electrically conductive, not decompose in a vacuum or under the beam of electrons and have a very smooth surface. Specific regimes for preparing samples for EBSD require mounting samples, grinding their surfaces and multiple polishing steps to achieve successively finer finishes, see Section 3.2.4. Sampling non-planar surfaces can be problematic, so the areas chosen to be examined are locations where the local topography and damage level allow for clear patterns to reach the detector.

3.5.1 SEM Operation

In an SEM, a focused beam of electrons is scanned across a sample. Electrons either interact with the sample and bounce back onto a detector, or excite electrons in the sample causing these to be released and picked up by an alternative detector. These groups of electrons are termed back-scattered electrons (BSEs) and secondary electrons respectively. BSEs reflect at different angles depending on the constituent elements in the sample, making analysis of the BSE maps ideal for the analysis of topography and crystallographic texture. Secondary electrons only interact with the top layer of atoms, giving details about the sample surface, allowing a general idea of the specimen material and surface structure. The microscope collects the resulting electrons and their intensities, the detectors store this information where intensity is visually mapped as image brightness. Figure 3.20 shows the FEI Quanta 200F SEM used to perform EBSD in this study, the inside of the SEM is shown in Figure 3.19.

Energy dispersive x-ray spectrometry (EDX) can be incorporated in the SEM allowing simultaneous detection of the elements in the sample during imaging. Energy levels of emitted x-rays are characteristic of particular chemical elements, depending on the energy of the incident electrons and the atomic structure thereby allowing for the identification of the elements present in the sample. Phase identification is often a simple process where a single point is taken, the chemistry and electron back-scatter pattern (EBSP) are acquired simultaneously. A structural database is searched using the acquired chemical information. The EBSP is indexed as normal and in matching these results, the phase can be identified [137].

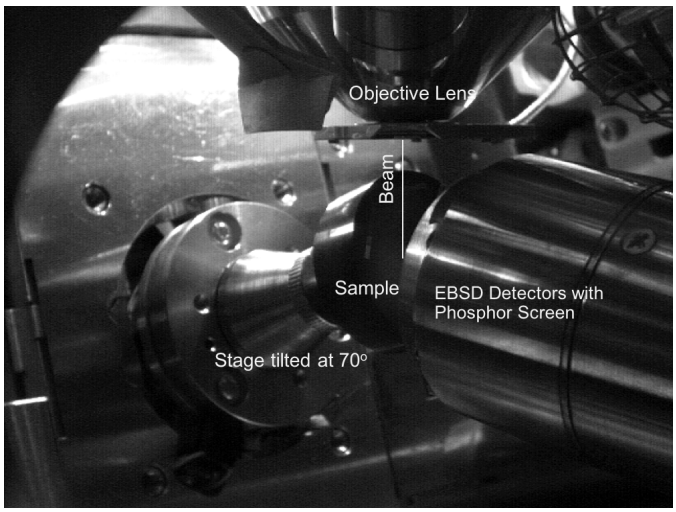


Figure 3.19: Gray-scale photograph taken by internal SEM camera showing a mounted specimen held at 70 degrees to the detector, with the detector at working distance of approximately 10 mm.

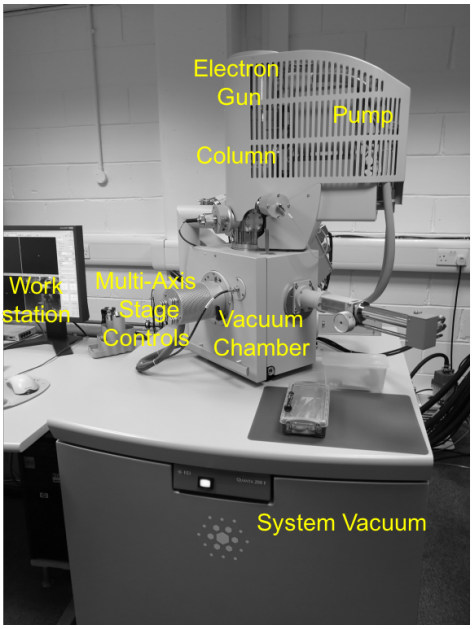


Figure 3.20: FEI Quanta 200F SEM located in ISAAC, Glasgow, used to perform EBSD.

On occasion, a carbon coating is added to improve the EBSD image and allow the SEM acceleration voltage to be increased with the SEM operating on High Vac mode, improving beam penetration through the thin amorphous, conductive carbon layer.

The essential EBSD operation is outlined in Figure 3.21. The electron beam strikes the specimen and the scattering produces back-scatter electrons in all directions. These electrons travel along a plane, generating Kikuchi bands, whose widths are determined by Bragg's Law and the specimen-detector distance. Back-scattered electrons then hit the imaging phosphor and produce light which is detected by the charged-coupled device (CCD) camera and converted to an image which is then processed.

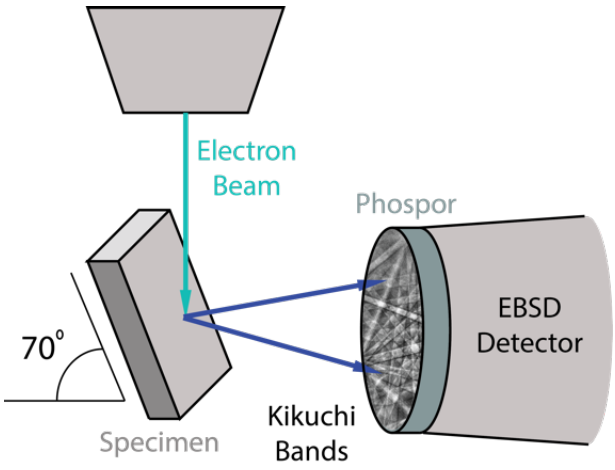


Figure 3.21: Simplified EBSD operation schematic.

Every Kikuchi line is associated with Bragg diffraction from one side of a single set of lattice planes. Two of these Kikuchi lines form bands, defining the electron diffraction from individual crystals. The initial pattern is converted into crystal orientation data via the Hough transformation, which is used to accurately detect Kikuchi bands. The Hough transform identifies the positions of the Kikuchi bands, converts the image captured by the camera into a representation in Hough space, where a straight line from the image space (x, y) is represented by a single point (ρ, θ) in Hough space by;

$$\rho = x \cos\theta + y \sin\theta, \tag{3.2}$$

where ρ is the distance from the origin and θ is the angle from the x-axis. These peaks in Hough space are easily detected and are used to calculate the original band positions accurately. The phase and orientation of which are matched to particular crystallographic orientations. A 'matching' algorithm then compares these detected bands with those calculated from the crystal structure of the phase of interest and the EBSP is resolved, identifying the crystal orientation of the sample under the beam. If the band detection matches with the reflector calculation, the phase has been discriminated and the orientation determined, this is also referred to as indexing. The final phase and orientation is verified and maps are then built using this data, this process is outlined in Figure 3.22. The Hough transform for each pixel is stored and may be reprocessed after data acquisition.

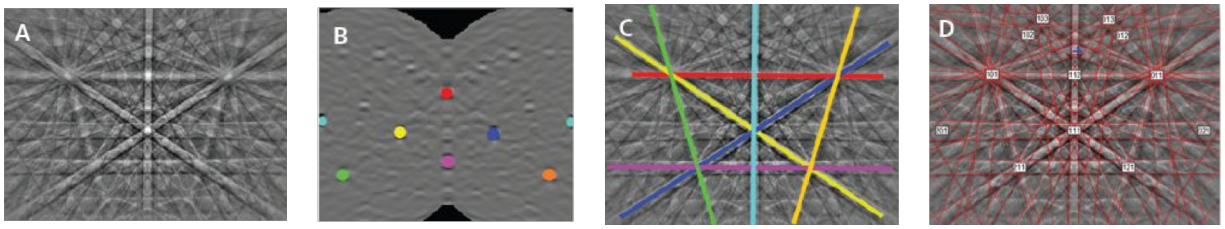


Figure 3.22: Outline of method traditionally used to find peaks using Hough space, adapted from [158] where a) shows the back-scattered pattern, b) the peaks identified in Hough space, c) bands in the original diffraction pattern corresponding to the peaks found in the Hough transform and d) the fully-indexed pattern with red bands indicating Kikuchi bands.

Factors affecting the quality of EBSD patterns include the specimen atomic number(s), grain size, level of preparation damage (i.e. the surface finish) and the inclusion of any surface contamination or amorphous sections. The Hough transform can be configured to optimise detection involving a wide range of these conditions, both operational and sample specific.

The contrast of the final image is important and is linked to the pattern quality. As only a small amount of the electrons arriving at the phosphor screen are back-scattered, the pattern is superimposed on a background. This EBSP background also affects the quality of the final pattern. Therefore, background removal is required to enhance the contrast of the pattern, this can be done by either background subtraction, or background division and is particularly important in dealing with materials of lower atomic numbers as these naturally result in a low pattern contrast. The accelerating voltage plays a significant role in the final contrast, with bands being broader and less sharp at lower accelerating voltages.

Examining the effects of strain via EBSD is essential to the current research. EBSD can be used to analyse strain after testing and compared to the 'non-loaded' material (not truly unstrained due to the residual strains induced in processing and manufacturing - where there some level of residual stress remains despite heat treatments). Random or disordered dislocations degrade the pattern quality. However, plastic strain can manifest as ordered dislocation arrays which can cause semi-continuous lattice rotation within a grain. This is measurable as 'intragranular' misorientation. Essentially, misorientation ican be used as a method of quantifying plastic deformation [26]. Misorientation is described as the difference in crystallographic orientation between two crystallites, this value is highly dependent on what is considered the reference value. For example, misorientation may be defined from a set point, the nearest neighbouring crystal, or from the average within the current grain.

Grouping of grains by the amount of strain is used to analysis the plastic strain in the material. Segmenting the data by accumulated strain allows examination of recrystallisation, therefore crystals can be identified as being deformed or recrystallised [216]. Strain visualisation can be done relative to a selected reference point (cumulative rotation) or to each pixel relative to the surrounding pixels (local rotation). For the local rotation, each orientation is surrounded by eight nearest neighbouring pixels.

Modern EBSD approaches involve using image comparison techniques where a comprehensive database of crystal responses at given orientations is emplyed to speed up this process. Inclusion of strain mapping and 3D microscopy demonstrate how EBSD techniques continue to evolve, termed high resolution EBSD [216]. As this technique has been developed and combined with chemical analysis and serial sectioning methods, it has become possible to access complete three-dimensional chemistry, phase and crystal orientation information. In short, the microstructural state of polycrystals may now be completely quantified [137].

3.5.2 EBSD Preparation

EBSD was performed using an SEM. The SEM employed was an FEI Quanta 200F based at ISAAC (Imaging Spectroscopy and Analysis Centre, University of Glasgow) with EDAX's OIM software used to analyse results [61]. To characterise the microstructures of Ti-6Al-4V and other titanium products, EBSD was conducted at two resolutions; high resolution scans over a small area and lower resolution scans over a larger area.

For examination by EBSD, preparation is required to achieve a flat, highly polished surface. The process used is described in this section. The deformed, post-test specimens are sectioned carefully to examine the centre of the gauge section via EBSD. The deformed and undeformed sections to be analysed were extracted as outlined in Figure 3.23. To avoid unnecessarily damaging the specimens, these were cut at a low speed using a Struers MiniTom with a diluted Corrozip 1:16 cooling solution. Hot mounting of the specimens using the CitoPress with a conductive Polyfast resin was performed directly after sectioning. Hot mounting was performed at 180°C for 3.5 minutes then water cooled for a further 1.5 minutes. A conductive resin was used to eliminate issues arising from charging and drift. A two-step grinding process was performed on a Struers LaboForce-50 automatic polisher to remove any deformation induced by cutting.

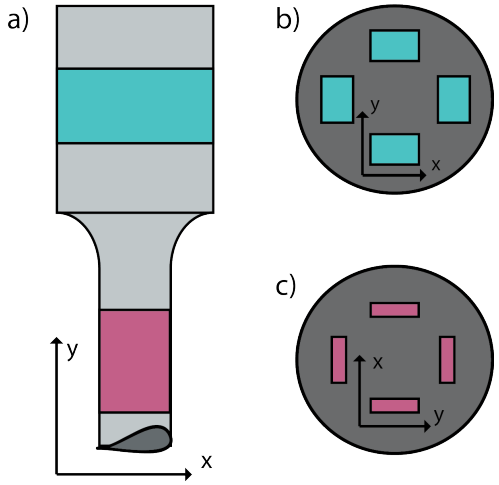


Figure 3.23: a) Cross-section of Ti-6Al-4V specimen, showing areas to be analysed via EBSD, i.e. deformed gauge and undeformed grip sections. b) How the undeformed grip sections are mounted in the Polyfast resin, these have been oriented as such to ensure the centre of the section can be captured whilst the mount is held at 70° in the SEM, c) shows mounting of multiple deformed gauge sections. Multiple specimens have been mounted together to accelerate the grinding and polishing process.

Initial grinding is performed with water lubrication and 220 grit diamond disc (MD-Piano) with a force of 30 N at 300 rpm for 5-10 minutes until a planar surface is achieved. A second step used 9 micron diamond DiaPro Allegro suspension with a 30 N load (for a 30 mm diameter sample) at 150 rpm, again for a further 5-10 minutes. A visual inspection was carried out to ensure a planar surface and no visible specimen damage, the level of material removed was also measured periodically until the centre of the gauge section was reached.

An automatic polish with a colloidal silica suspension (0.04μm) was performed at 150 rpm, again using a load of 20 N. The time taken to achieve the desired level of surface polish ranged from 40 minutes to 1.5 hours. Specimens were placed in a Vibromet vibratory polisher for a further 16 hours with a dilution of the same colloidal silica suspension (OP-S NonDry). The higher the quality of the polish, the faster the SEM can categorise Kikuchi bands, meaning scan times are dependant on the material and polishing regime. Additionally, if the polish is of too low quality, the resulting pattern will not have sufficient contrast. Scratches on the surface interfere with acquisition therefore, these patterns are unable to be distinguished, leading to uncategorised sections.

Data from the high resolution scans are compared in the form of inverse pole figure (IPF) maps where differences from the initial microstructure are evident. Further analysis was performed on these high resolution scans such as examining the misorientation and spread of grain sizes. Quantitative measurements have been extracted from the data in the large area scans, primarily in the form of pole figures. Care has been taken to ensure orientations of individual sections remain consistent. This is particularly important where the grip section is used to analyse the undeformed microstructure, Figure 3.23.

3.5.3 EBSD Post Processing

An IPF map showing crystal orientation is often a desired output from EBSD. This is a visually simple way to display crystallographic orientation, however, it is important to note IPF maps do not give complete information about the crystal orientation. Orientation is obtained at every pixel, and the colour is determined by either an inverse pole figure or Euler angles. There are a variety of maps which can be visualised using the data acquired from EBSD. The orientation map, pattern quality and grain boundaries can all be shown explicitly. Combinations of these maps are common, for example, a phase map overlaid with map showing grain boundaries presents the phase distribution well.

Obtaining high quality IPF maps requires a high scanning resolution in comparison to the grain size of the material. EBSD scans with a step size of 0.5 microns were used to generate IPF maps. IPF maps were cleaned using grain fit (tolerance angle of 5° and minimum grain size of 2 microns) with an additional next neighbour fit with confidence index of greater than 0.1 (occasionally set to greater than 0.01) for the Ti-6Al-4V where the total number of points changed remains below 10%. Points with very low confidence index are omitted, e.g. where areas of mounting resin were scanned alongside the Ti-6Al-4V, this normally only occurs in the large area scans when attempting to analyse the entirety of the gauge section for the extraction of texture measurements.

Texture measurements are calculated from large area scans in the form of equal area pole figures. These have been used simply for comparison to other Ti-6Al-4V product forms and after different loading conditions. Pole figures have been constructed from texture calculations, the {00.1}, {10.0} and {10.1} directions have been chosen to calculate texture and build equal angle pole figures. Grain size analysis has been performed on all product forms where the Average Grain Intercept (AGI) method is used to calculate grain sizes. AGI

is a technique used to quantify the average crystal size of a material by drawing randomly positioned line segments on a micrograph, counting how often each line segment intersects a grain boundary and finding the ratio of intercepts to line length [220]. The line intercept method allows twin boundaries and low-angle grain boundaries to be identified, these can be filtered from the data as required. No grain boundary etching or reflected light orientation contrast is required. The shape of the grains is often analysed by examination of aspect ratios and the orientation of the major axis.

Misorientation, geometrically necessary dislocation (GND) density, grain size, grain spherocity, Schmid factor and additional maps can be calculated from the EBSD data-set. This may be performed within the software and is described in further detail where relevant.

Part II

Experimental Results and Computational Simulations

Chapter 4

Strain rate sensitivity of Ti-6Al-4V using high energy synchrotron XRD

Titanium alloys are strain rate and temperature sensitive [193]. Understanding of the SRJ and its effects enables better prediction of actual in service components which are subject to loading at a variety of differing strain rates in service. Strain rate sensitivity is particularly evident in the compressive behaviour of titanium alloys. Additionally, these alloys are also known to exhibit a tension-compression asymmetry [150]. In this section, three in situ uniaxial tensile tests have been performed at room temperature on billet Ti-6Al-4V, with two constant strain rate tests (10^{-3} s^{-1} and 10^{-4} s^{-1}) and a final test involving a jump between these strain rates at a particular strain value. The macroscopic and lattice strain responses are analysed to examine the radial strain rate sensitivity of billet Ti-6Al-4V using both the constant strain rate tests and SRJ test. All experiments were performed in situ at CHESS under powder diffraction conditions, where the averaged lattice strain responses are extracted as detailed in Section 3.3.

4.1 Macroscopic Response

The macroscopic stress-strain responses of the three tests are shown in Figure 4.1. It is evident that the strain rate jump (SRJ) results follow the same path as the lower strain rate experiment until the jump, where the response rises almost instantly to align with that of the higher strain rate. This continued alignment shows the instantaneous jump in strain rate has a unique impact on the overall response, potentially independent of the strain rate history. The macroscopic stress immediately after the jump is 895.2 MPa, slightly higher than the stress at the equivalent post-jump strain (886.2 MPa), but remains within the bounds of experimental error. The difference in stress between the two constant strain rates is of similar magnitude to that of the stress increase observed during the SRJ experiment. The resulting stress strain curve settles showing very well aligned values with the higher strain rate response.

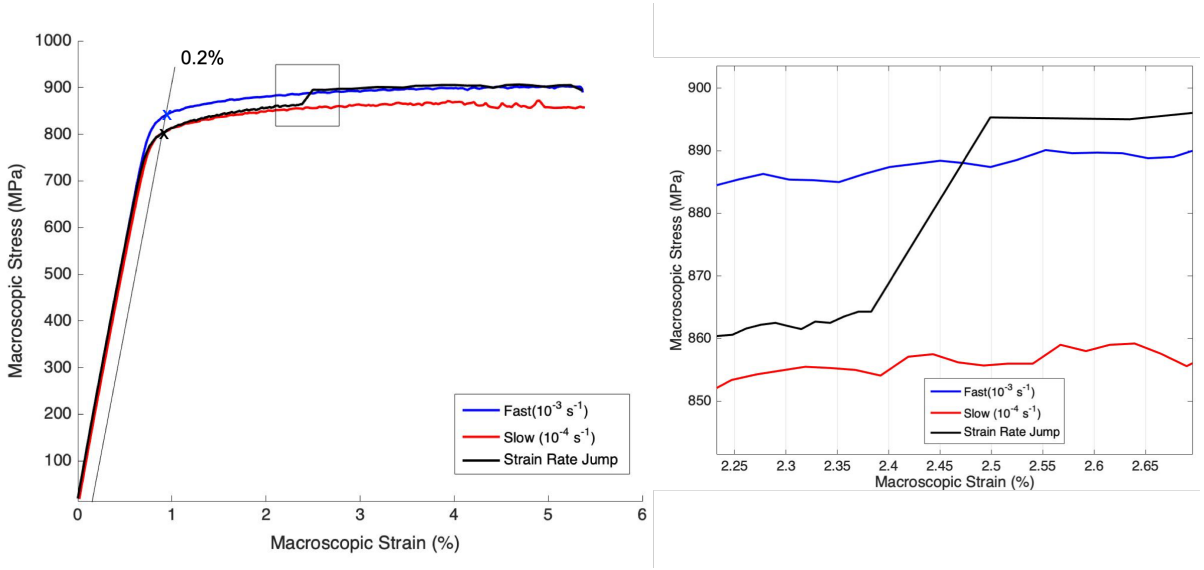


Figure 4.1: Macroscopic stress-strain response of specimens deformed at 10^{-3} s^{-1} (blue), 10^{-4} s^{-1} (red) and a jump between these strain rates (black), where the 0.2% offset stress is shown.

Table 4.1: Comparison of the macroscopic stresses at yield and at 5% engineering strain for each of the experiments performed on billet Ti-6Al-4V. Data has been acquired from the load frame and corrected for the load frame compliance, as detailed in Section 3.2.5.

Test	Yield Stress MPa	Stress at 2.35% MPa	Stress at 2.6% MPa	Stress at 5% Eng strain MPa
Lower (10^{-4} s^{-1})	807.3 MPa	855.3 MPa	859.1 MPa	858.0 MPa
Higher (10^{-3} s^{-1})	846.2 MPa	885.4 MPa	889.5 MPa	899.6 MPa
Jump	810.3 MPa	862.1 MPa	894.9 MPa	901.8 MPa

Table 4.1 summarises the overall stresses at yield and 5% engineering strain, where the yield stress is calculated at 0.2% strain [47]. The stress immediately prior to and after the jump are also compared. The increase in stress between the initial yield point and at 5% strain is 5.3% and 5.7% of the yield stress for the lower and higher constant strain rates respectively. These show a similar hardening response which is independent of strain rate (this is not unexpected for similar, quasi-static strain rates at room temperature). These results are potentially suggestive of the deformation moving between yield surfaces to cause such alignment under the action of a jump in strain rate. Current data shows a more gradual gradient during the jump than the initial elastic moduli. The material behaviour during the jump is difficult to quantify macroscopically due to the small number of points captured, with very few during the jump. Thus it is not possible to currently predict whether the jump is purely elastic or otherwise and therefore comments on the nature of the yield surface and its evolution are limited.

4.1.1 EBSD Analysis

A plane through the centre of the gauge section, coincident with the loading direction (and thus normal to the incident beam) has been extracted from the specimen, another section is removed from the undeformed grip

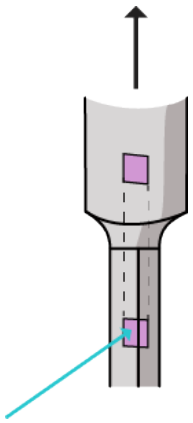


Figure 4.2: Location of areas analysed via EBSD, normal to the incident beam striking the sample gauge section.

sections. These are indicated in Figure 4.2. These areas have been analysed post experiment to observe changes in the distribution of crystallographic orientations. Specimens were prepared according to polishing regimes outlined in Section 3.5, with an additional carbon coating added to improve the EBSD quality, allowing the SEM acceleration voltage to be increased and the SEM to operate in High Vacuum mode.

In observation of the IPF maps, Figures 4.3(a-d), it is evident that the crystallographic directions observed are similar in both the constant strain rate experiments (Figures 4.3b and 4.3c) but dissimilar in the post jump IPF map (Figure 4.3d), due to a significant macrozone in the analysed region. This is actually more microstructurally similar to the crystallographic orientations observed in the undeformed case (Figure 4.3a). The effect of the differing crystallographic directions may impact the level of misorientation observed. However, there appears to be no correlation between areas of particular orientation and level of misorientation.

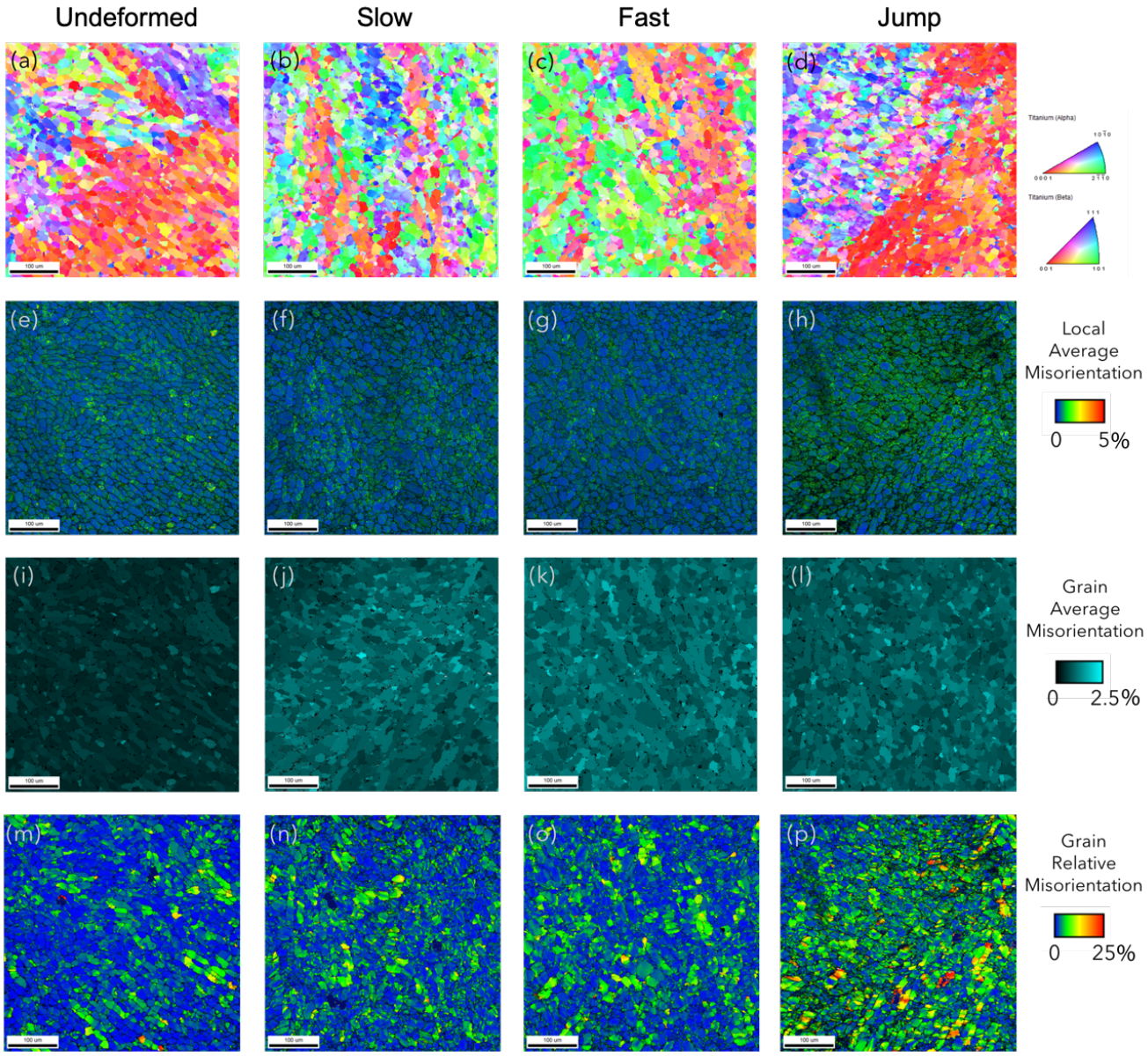


Figure 4.3: IPF maps of (a) the undeformed billet material, (b) the deformed (to ∼5.5% strain) via the slower strain rate, (c) deformed by the higher strain rate and (d) deformed via 'jump' conditions. The local average misorientation for each of these microstructures respectively is shown in (e-h). The grain averaged misorientation (i-l) and grain relative misorientation (m-p) are also included. All scale bars = 100μm.

Various forms of misorientation are shown in Figure 4.3 where 4.3(e-h), show the local average misorientation (LAM), otherwise defined as the misorientation between neighbouring crystals. Figure 4.3(i-l) shows the resulting misorientation of each individual point averaged over each grain - the grain averaged misorientation (GAM), see Lehockey et al [125] for further clarification on the definitions used here. The grain relative misorientation (GRM) plots, Figure 4.3(m-p), show the deviation in each grain using the grain averaged orientation as a reference, this is particularly useful for examining intra-granular misorientation. The LAM and GRM for the jump case are shown in Figures 4.3h and 4.3p respectively, highlighting a significant increase in intra-granular misorientation in comparison to the microstructures deformed via constant strain rates.

Comparing the graphs of the grain averaged misorientation data in Figure 4.4, where the data has been classified into 30 bins, it is evident that there is a difference in GAM in the response of Ti-6Al-4V after the SRJ test. The IPF maps for the GAM do not explicitly show a difference. However, in examination of the data, a greater spread of misorientation is observed for the SRJ case in Figure 4.4. This greater misorientation spread supports the hypothesis that the SRJ has a particular effect on Ti-6Al-4V at the microscale. The assumption that the bulk of orientation change happens at or after the jump has been made as the microstructure is expected to be similar to that of the slow strain rate prior to the jump, where the behaviour does appear similar both macroscopically, see Figure 4.1 and at the crystal scale, as discussed in Section 4.1.2.

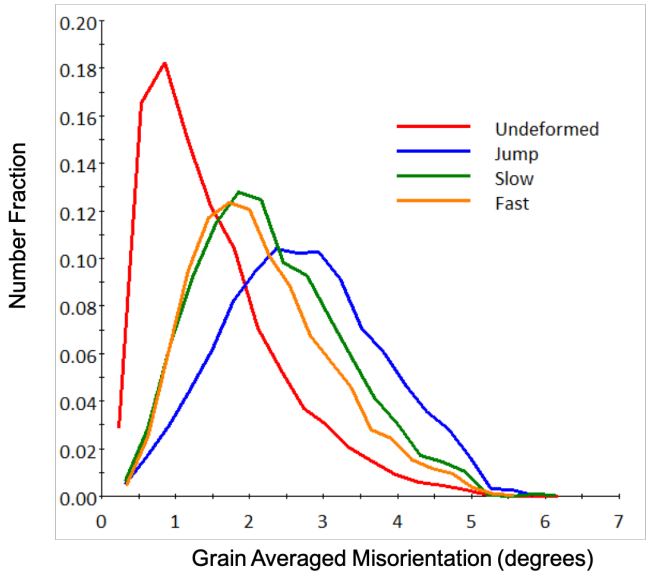


Figure 4.4: Distribution of Grain Averaged Misorientation (GAM), for the undeformed and each of the deformed billet microstructures at ∼5.5% engineering strain, showing increased misorientation for all of the deformed states.

4.1.1.1 Grain Size and Shape

Comparative grain size and shape analysis is performed to ensure these parameters do not significantly influence the bulk response. The grain shape distribution shows little difference between the materials, despite comparing both the deformed and undeformed microstructures, suggesting that, at ∼5.5% engineering strain, the grain shape aspect ratio remains fairly consistent between the deformed and undeformed specimens. The average grain sizes have been calculated from high resolution EBSD scans, see Table 4.2.

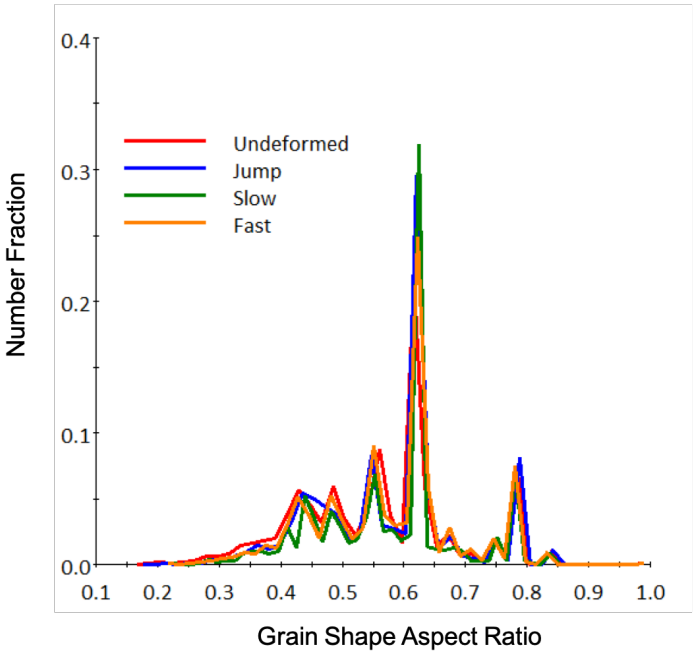


Figure 4.5: Grain shape aspect ratios showing a similar distribution for all states of the billet material, including the undeformed condition. The undeformed condition is extracted from gripped section of the SRJ specimen.

A 12.1% decrease in the average grain size for the jump specimen is significant, particularly at only ∼5.5% engineering strain. Grain size and microstructure are known to influence the flow stress and therefore strain rate sensitivity, which may impact the overall stress-strain response of the materials. However, the actual values and deviation are fairly consistent in magnitude.

Table 4.2: Overall average grain sizes calculated from EBSD high resolution scans and the percentage reduction calculated from the average grain size of the undeformed Ti-6Al-4V billet, loaded normal to the radial direction.

Test	Avg Grain Size	Std Dev	% Reduction
Undeformed	13.82μm	5.63	
Lower (10^{-4} s^{-1})	12.74μm	5.44	7.8%
Higher (10^{-3} s^{-1})	13.32μm	5.89	3.6%
Jump	12.15 μm	5.632	12.1%

4.1.1.2 Crystallographic Texture

EBSD has been performed over a larger area to ensure a sufficient representative bulk average texture was captured, see Section 3.5 for details. It is not well established within the community how large the scanned area should be to capture representative behaviour of the material. Texture evolution shows the tendency for crystals to orient themselves in specific directions. Here, the averaged initial and final textures for each case

are examined in the form of equal area pole figures. Overall crystallographic texture for the material discussed is predominantly induced by the rolling process. The deformed responses are similar showing minimal differences between the three deformed textures. The crystallographic textures involved here are indicitive of those found in a typical billet titanium alloys [46]. However, the strength of the texture is far greater in the jump than for the higher strain rate, indicating that the SRJ has aided this increased texture development, see Figure 4.6. Due to the smaller average grain size observed in the jump case, more grains are included in the analysis. This may account for a portion of the increased intensity, but the values indicated can only account for a percentage of the increased intensity.

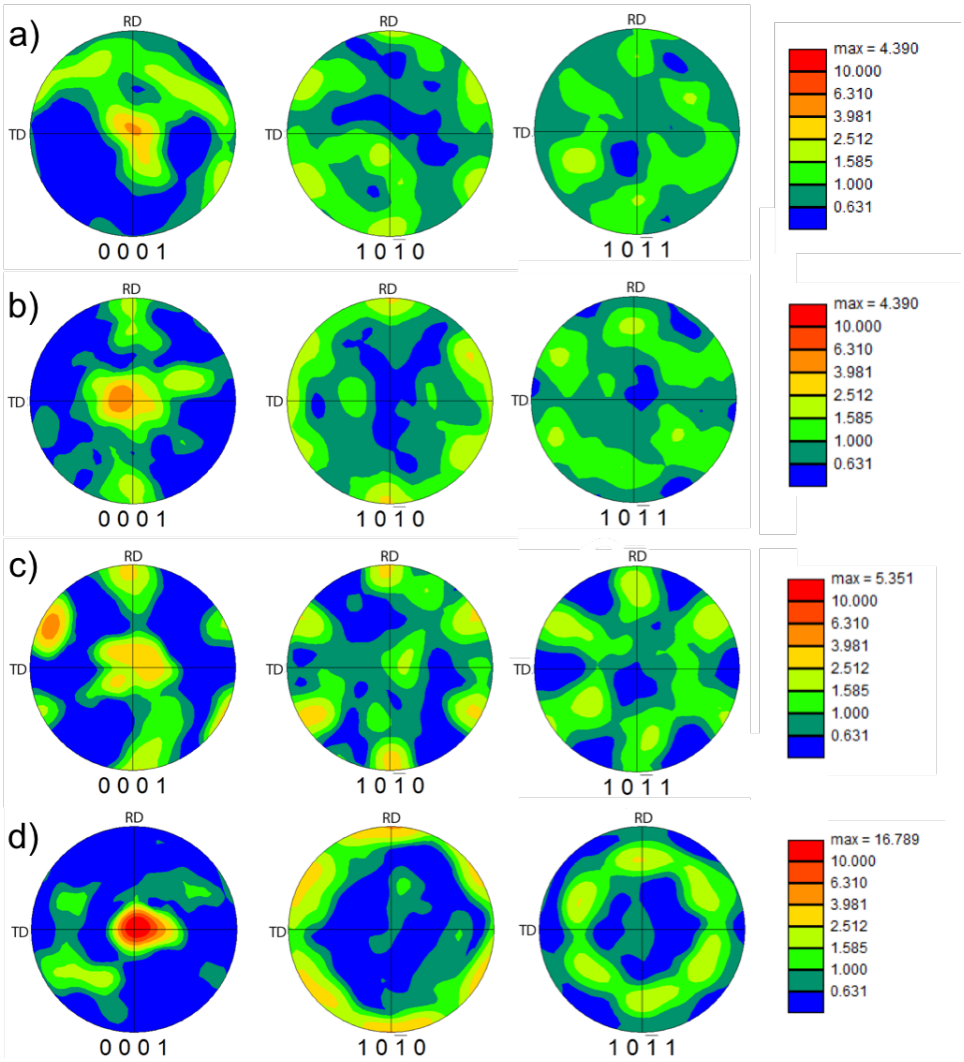


Figure 4.6: Pole figures for three directions a) in the undeformed case, b) for the slower strain rate, c) the higher strain rate and d) the jump between strain rates, where the maximum intensity for each set is shown in the relevant key.

Pole figures, see Figure 4.6, are uniformly scaled to the same values. This highlights the more intense textured response for the specimen deformed via the SRJ. It is worth noting that the areas used to generate PF showing textures are not the same as those used for the IPF maps in Section 4.1.1, therefore the increased texture intensity and greater misorientation are not simply alternative representations of the same data. The apparent

difference is most likely due to the instantaneous nature of the jump affecting the microstructure. This may be effectively considered as a very high strain rate for a small duration and this is likely to have different deformation effects from the quasi-static constant strain rates.

4.1.2 Lattice Strains

Lattice strains are tracked throughout the deformation by analysis of high energy XRD data. Increasing lattice strains are expected in the loading direction during uniaxial tension. The crystallographic directions analysed in this section are visualised in Figure 4.7. Lattice strains are inherently purely elastic, however, in the averaged responses here, where the effect of the surrounding plasticity impeding the continued lattice strain accumulation is visible.

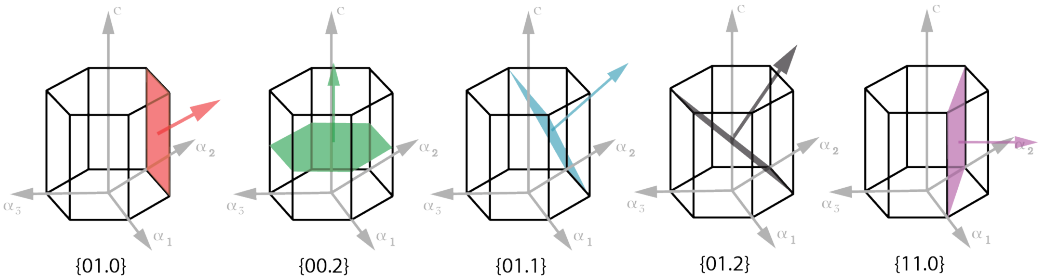


Figure 4.7: Crystallographic directions studied in this chapter, where lattice strain evolution is analysed in these directions.

The azimuthal bin size used is approximately 26 degrees to ensure the loading direction is adequately captured, this is identical for all experiments in this chapter. Lattice strain evolution for the constant strain rate tests is given in Figure 4.8 where a) and b) are the lower and higher strain rates respectively. The post yield behaviour shows a trend of minimal lattice strain accumulation post yield in most crystallographic directions for the higher of the two strain rates. Some reduction is observed with increasing strain for the {11.0} direction.

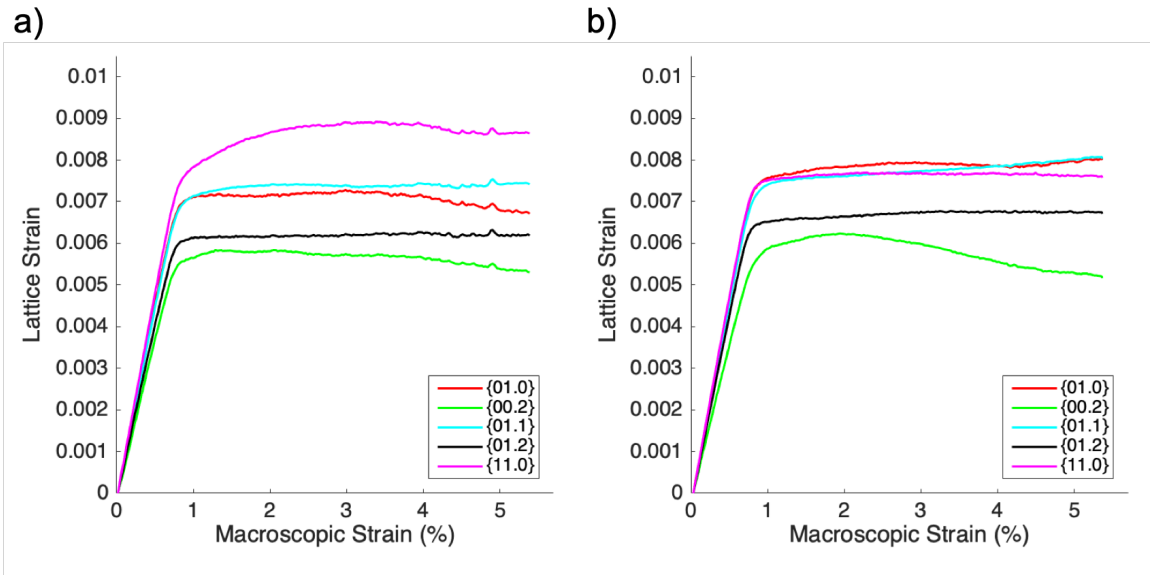


Figure 4.8: Lattice strain plotted against macroscopic strain, showing the evolution of lattice strain for constant strain rate experiments where a) is the lower strain rate ($10^{-4}s^{-1}$)and b) is the higher strain rate, ($10^{-3}s^{-1}$).

Interestingly, the lattice strains accumulated at yield are more spread out for the lower strain rate, see Figure 4.9. The lattice strains at yield are larger for the higher strain rate for all directions except the {11.0} direction which is greater for the slower strain rate.

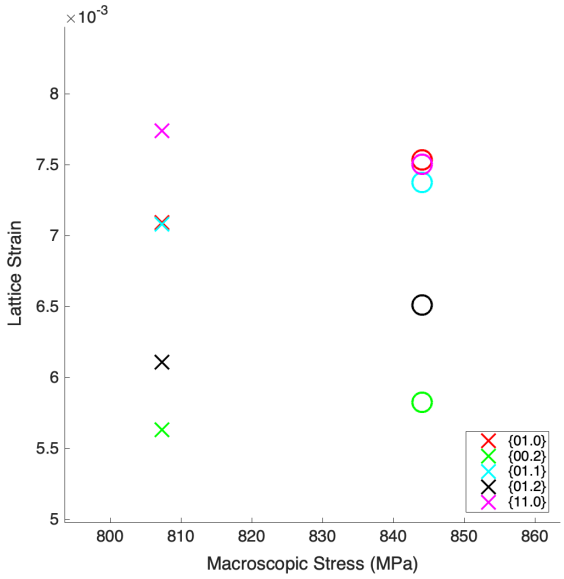


Figure 4.9: Lattice strains plotted at yield for both constant strain rate experiments, where X denotes the lower strain rate and O, the higher strain rate

The lattice strains in both the loading and transverse directions are shown for the strain rate jump in Figure 4.10 where the jump is evident in all the responses for both the loading and transverse directions. The {00.2}

direction is seen to be significantly higher in both the loading and transverse directions, accumulating significantly higher lattice strain than in other directions. It is also a particularly noisy response even in the elastic region. Confidence in the accuracy of this result is however low.

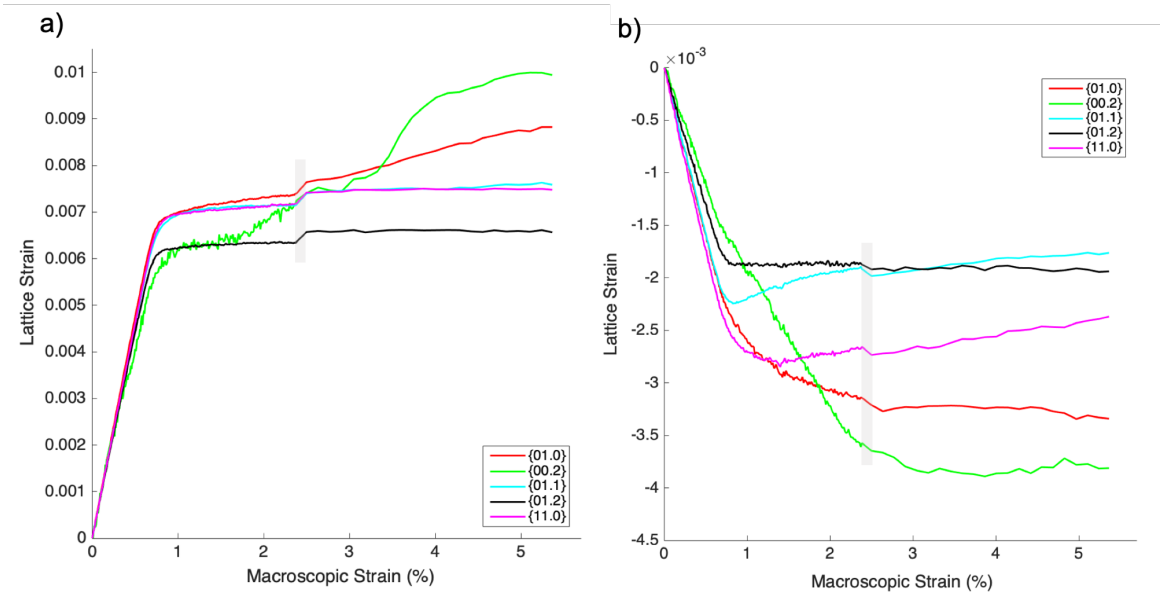


Figure 4.10: Lattice strain evolution of each crystallographic direction for the strain rate jump test, in both a) the loading and b) the compressive lattice strains in the transverse direction, where the effect of the SRJ is highlighted.

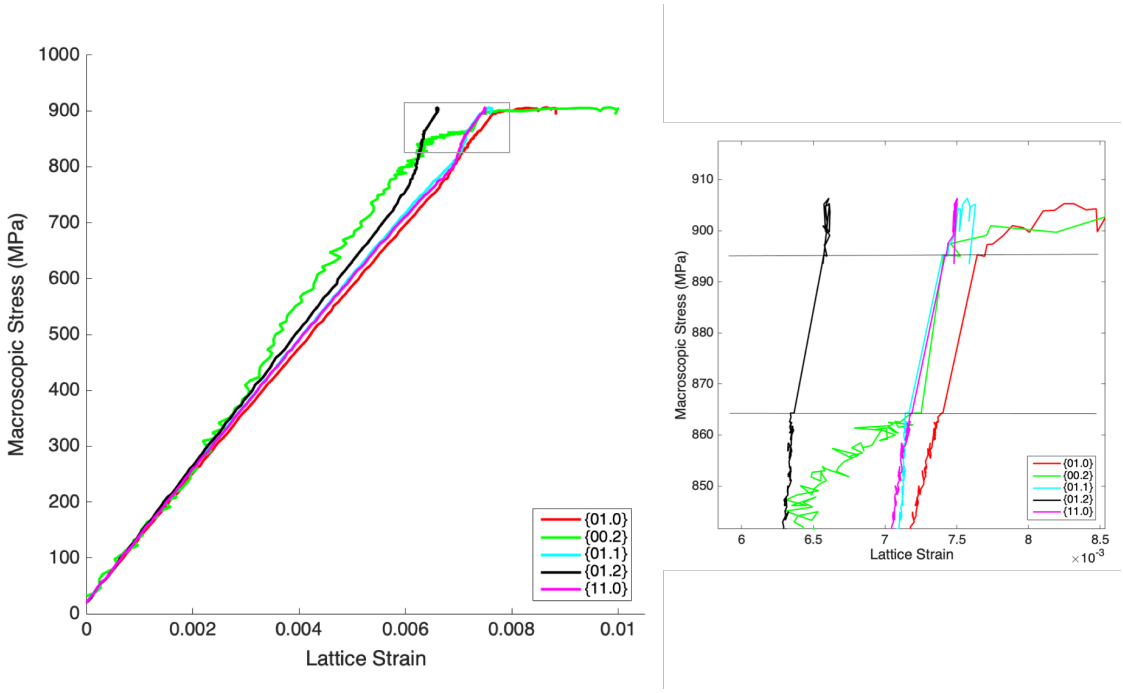


Figure 4.11: Macroscopic stress plotted against lattice strain of each crystallographic direction for the SRJ test.

Lattice strain is presented against macroscopic stress for the SRJ experiment in Figure 4.11. For each crystallographic direction, the gradient during the jump differs between crystallographic orientation, see Table 4.3. This can be viewed as an effective moduli, indicating the strength of each crystallographic direction The initial gradient in each direction has been compared to the gradient during the jump. Ideally an increased number of data points during this jump is required to fully observe the effect of the strain rate jump.

Table 4.3: Gradients of initial lattice strain evolution compared to those during the strain rate jump, both in the direction of loading, units in GPa.

Direction	**{01.0}**	**{00.2}**	**{01.1}**	**{01.2}**	**{11.0}**
SRJ (initial - loading)	112.368	130.500	115.788	121.612	114.796
SRJ (jump - loading)	129.167	196.203	132.479	149.038	133.620
% Difference	14.9%	50.3%	14.4%	22.6%	16.4%

An effective modulus has been calculated between 100 and 700 MPa for each experiment, the results are summarised in Table 4.4. The values for each direction are very consistent between crystallographic directions for the three tests performed. This indicates a directional modulus for the different directions in HCP α Ti-6Al-4V. It is of interest to identify whether these moduli are dependant on the material texture.

Table 4.4: Effective modulus of initial lattice strain evolution in each crystallographic direction, units in GPa.

Direction	**{01.0}**	**{00.2}**	**{01.1}**	**{01.2}**	**{11.0}**
Slow	113.176	137.134	114.031	126.852	105.624
Jump	112.368	130.500	115.788	121.612	114.796
Fast	110.695	147.148	114.224	121.490	110.239

4.1.3 Strain Rate Evolution

Strain Rate Sensitivity (SRS) indicates the general relationship between the flow stress and strain at a constant temperature and strain rate [131]. Experimental loading conditions are generally grouped depending on loading rate, either as low, quasi-static or higher, dynamic loading rates. In quasi-static rates, inertial effects are negligible, thus a quais-static load for one material may not be quasi-static for another. The stress-strain response of a material under quasi-static loading differs from that at dynamic loading rates, likely due to the different deformation mechanisms activated [148].

Generally, a single parameter, the strain rate sensitivity m is used to describe the rate dependent behaviour of metals under quasi-static loading. A meaningful rate sensitivity exponent is derived from experiments in an attempt to capture the behaviour of Ti-6Al-4V at multiple strain rates [75]. Deformation in titanium alloys is generally more anisotropic (both elastically and plastically) at the grain scale than other non-HCP alloys, and it is therefore thought that the strain rate sensitivity is likely to differ with respect to grain orientations

and the corresponding slip systems [82]. The intrinsic anisotropy of strain rate sensitivity in single crystal α titanium has been outlined by Zhang et al [231]. This study has important considerations for the current body of work, particularly in dealing with the validity of determining a single strain rate sensitivity parameter for a material.

The deformation mechanisms in Ti-6Al-4V have been identified for low and high strain rates [42]. Nano-indentation techniques may alternatively be used to investigate SRS [95]. However, for materials with high mechanical anisotropy, the nano-indentation techniques tend to underestimate the magnitude of the materials anisotropy [211]. For quasi-static loading, as performed here, as the strain rate increases, the strength is seen to increase at the expense of the ductility [232]. Strain rate sensitivity identification techniques for in situ tensile experiments are compared, suggesting the techniques compared herein can be reliably and interchangeably used to measure the SRS accurately for a wide variety of materials. A SRJ test is recommended to extract the SRS parameter m [164]. The equation used for both techniques is

$$\left(\frac{\sigma_2}{\sigma_1}\right)^m = \frac{\dot{\epsilon}_2}{\dot{\epsilon}_1} \tag{4.1}$$

where stresses for the constant strain rate method (CSRM) correspond to the values at 3% engineering strain. This has been compared to the averaged post yield behaviour and the differences appear negligible, see Table 4.5. The strain rate jump tests uses the values of stress immediately prior to and after the jump in strain rate. Strain rate sensitivity values for billet Ti-6Al-4V in the radial direction, are calculated at 3% engineering strain using the CSRM and strain rate jump test. A suggested m value for billet Ti-6Al-4V is deemed to be approximately 0.0016.

Table 4.5: Gradients of initial compressive lattice strain evolution in the transverse direction compared to gradients of compressive lattice strain during the strain rate jump.

Method	CSRM	SRJ
at 3%	0.016161	0.015925
Averaged	0.016461	0.015930

4.2 Discussion

Radially sectioning the billet is not the optimal method here as deviations within the material are likely to influence the microstructure as, due to how the billet is formed, from a large cuboid to a cylinder, the compressive stresses imposed in particular areas are substantially higher, impacting the material properties. In future experiments, specimens would be extracted from particular areas along the length of the billet instead to account for such.

Extension of this analysis past 5.5% engineering strain would be ideal, however this is limited as the ability to observe lattice strains is only viable for small strain conditions in the current XRD setup [44]. However, testing the material to failure would allow examination of the effect of a strain rate jump on eventual failure. There is a tendency for the lattice strain values to converge around the same value towards the end of the ex-

periment. This is particularly evident in the 10^{-3} s $^{-1}$ case, Figure 4.8, so testing to failure may be performed ex situ.

Further efforts to understand the effects of the jump are required. It appears to cause a higher level of misorientation and a stronger texture development in comparison to constant strain rate tests. Repeatability of the experiments is currently low, however, the addition of computational simulations may benefit the understanding of this phenomenon due to the expense and time constraints of high energy XRD experiments. Computational simulations would also allow the examination of factors unable to be distinguished experimentally, see Chapter 6.

Is it possible that only the highest strain rate applied matters. If so this may impact continuously loading and unloading specimens to capture in situ EBSD, particularly if the jump has such a profound influence microstructurally. During the jump, the lattice strains increase by a small amount whereas a large increase in macroscopic stress is evident due to the near instantaneous nature of the jump, meaning the macroscopic stress jumps from ∼865 to ∼895 MPa with a negligible difference in lattice strain. The 'jump' therefore has an apparent strain rate of much greater than the prescribed rates during the jump.

Macrozones, as detailed in Section 1.7, are evident in the undeformed and post jump conditions. It is difficult to examine the size of these in three dimensions and therefore difficult to estimate the role they play on the bulk deformation. It is suggested that these play a non-trivial role in the deformation of Ti-6Al-4V [119]. Modelling the incorporation of macrozones and their interactions with a jump in strain rate is also of interest.

Accurate calculation of the dimensionless strain rate sensitivity parameter is significant in the modelling deformation of Ti-6Al-4V, especially at the microscale. For models involving crystal plasticity, it is particularly important to gauge an accurate strain rate sensitivity parameter, particularly where this parameter is used as an exponent in the plastic evolution relations, see Chapter 6. Much work has been done to understand this value [95]. In an effort to accurately determine the SRS parameter, it is evident that a single value for the strain rate sensitivity does not accurately capture behaviour microscopically. There is a need to account for the evolution of strain in different crystallographic directions, and to analyse and understand how this relates to the interplay between different slip systems. Ideally the results of multiple experiments would be combined to reduce the error in these values.

4.3 Conclusions

The action of a 'strain rate jump' in uniaxial tensile tests on billet Ti-6Al-4V has some unexpected consequences, including increased misorientation and texture development, where the effect of the jump is visible at multiple length scales. A strain rate jump is assumed to have no effect on material behaviour thus is used to extract strain rate dependency parameters. The results from the SRJ have application in the machining and manufacture of Ti-6Al-4V as if the jump leads to a change in yield surface, this may be utilised in the

processing of Ti-6Al-4V, where higher, more power intensive processes may be used minimally to break down microstructures, with subsequent heat treatments to remove any undesired effects.

Interpretation of jump and the constant strain rate tests enables the effects of strain rate and strain rate history to be partially distinguished. Therefore, the strain rate evolution must be considered [159]. Titanium alloys are only moderately strain rate sensitive, but the effect of changes in strain rate may be drastic, this could have important considerations in fatigue, and may even contribute to the severity of dwell in titanium alloys. As materials in service do not typically abide by constant strain rates, the addition of this phenomenon may improve performance modelling. It is worth exploring this area as a potential difference between the experimental results and simulated models.

The effect of strain rate jump occurs later in the deformation process, i.e. post yield where the influence of the surrounding plasticity is evident. Of interest is the examination of a SRJ during the elastic deformation.

The lattice strain moduli of different crystallographic directions (Table 4.4) has been captured for billet Ti-6Al-4V. Further investigation to confirm these results should be performed on differently textured specimens of Ti-6Al-4V under the same conditions used in this work.

Chapter 5

High energy XRD of commercial Ti-6Al-4V rolled plates

5.1 Overview

This chapter details in situ high energy XRD experiments on Ti-6Al-4V rolled bar products in the form of unidirectionally rolled (UDR) and cross rolled (CR). These experiments are a continuation of those described in the previous chapter, where the more advanced setup used in this chapter allows analysis of the jump in strain rate at a higher resolution. The Ti-6Al-4V products are expected to contain comparable microstructures with differences in crystallographic texture due to processing. Experiments have been devised primarily to examine the differences in the lattice strain response of UDR and CR materials. The effect of the SRJ on both materials and the timing of the jump is also analysed.

In situ high energy XRD experiments are performed at quasi-static strain rates as described in Table 5.1, where the previous experiments froM Chapter 4 are highlighted in green. The current experiments have been performed using Dexela detectors and therefore an increased data resolution is available compared to those in Chapter 4. Of particular interest is the increased data captured during the jump in strain rate. The initial peak intensities of the undeformed materials, as extracted from the powder diffraction rings, are compared in Figure 5.1 and Table 5.2.

As shown in Figure 5.2, the intensity of the initial diffraction rings is significantly higher for the UDR material due to a higher number of crystals rotated so that they satisfy the Bragg condition in their current orientation. A 'spottier' response observed for the CR material indicating that a wider azimuthal bin size is required to ensure sufficient responses are captured. Figure 5.2 shows the detector output for both UDR and CR material at various stages. The final results show a 'smoother' response due to crystal reorientation during deformation, where crystals reorientate to a preferred orientation.

Table 5.1: In situ uniaxial tension experiments performed at CHESS, where a (✓) denotes the previous experiments (Chapter 4) and black (✓) shows the experiments presented in this chapter.

Experiment	Billet	UDR (rolling)	CR (rolling)	CR (45 deg)
Constant strain rate (10^{-4} s^{-1})	✓	✓	✓	✓
Constant strain rate (10^{-3} s^{-1})	✓	✓	✓	✓
Jump (3% Eng strain) (10^{-4} to 10^{-3} s^{-1})	✓	✓	✓	✓
Jump (2.25% Eng strain) (10^{-4} to 10^{-3} s^{-1})		✓		
Jump (1.5% Eng strain) (10^{-4} to 10^{-3} s^{-1})		✓		

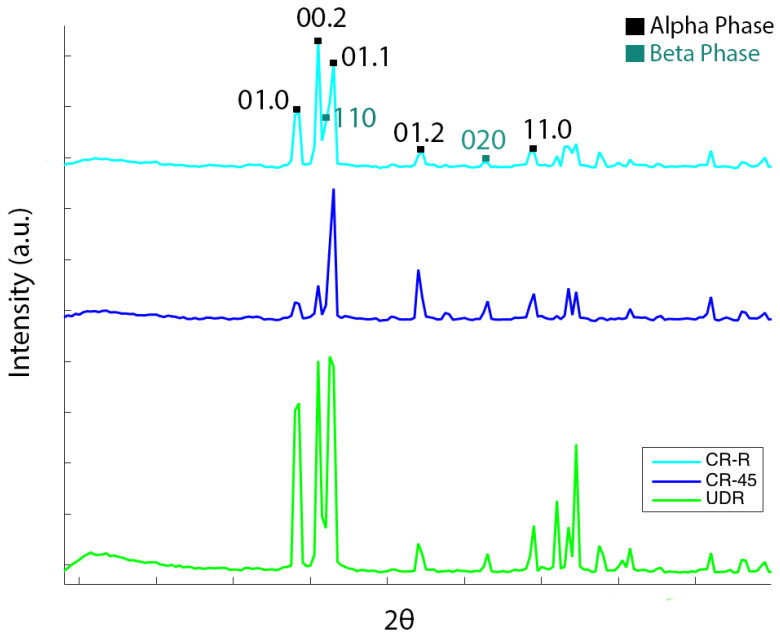


Figure 5.1: Peaks from the individual diffraction rings in the loading direction, shown for all material states; UDR (rolling), CR (rolling) and CR (at 45 deg), where the results have been stacked vertically for comparison and the units of intensity are arbitrary.

	{01.0}	**{00.2}**	**{01.1}**	**{01.2}**	**{11.0}**
UDR (rolling)	163.8	205.6	209.7	26.2	43.8
CR (rolling)	53.4	122.5	101.0	15.5	15.5
CR (at 45 deg)	16.9	33.5	128.6	49.1	25.3

Table 5.2: Relative peak intensities of the undeformed materials (units are arbitrary), comparing CR and UDR material in rolling direction and CR at 45 degrees.

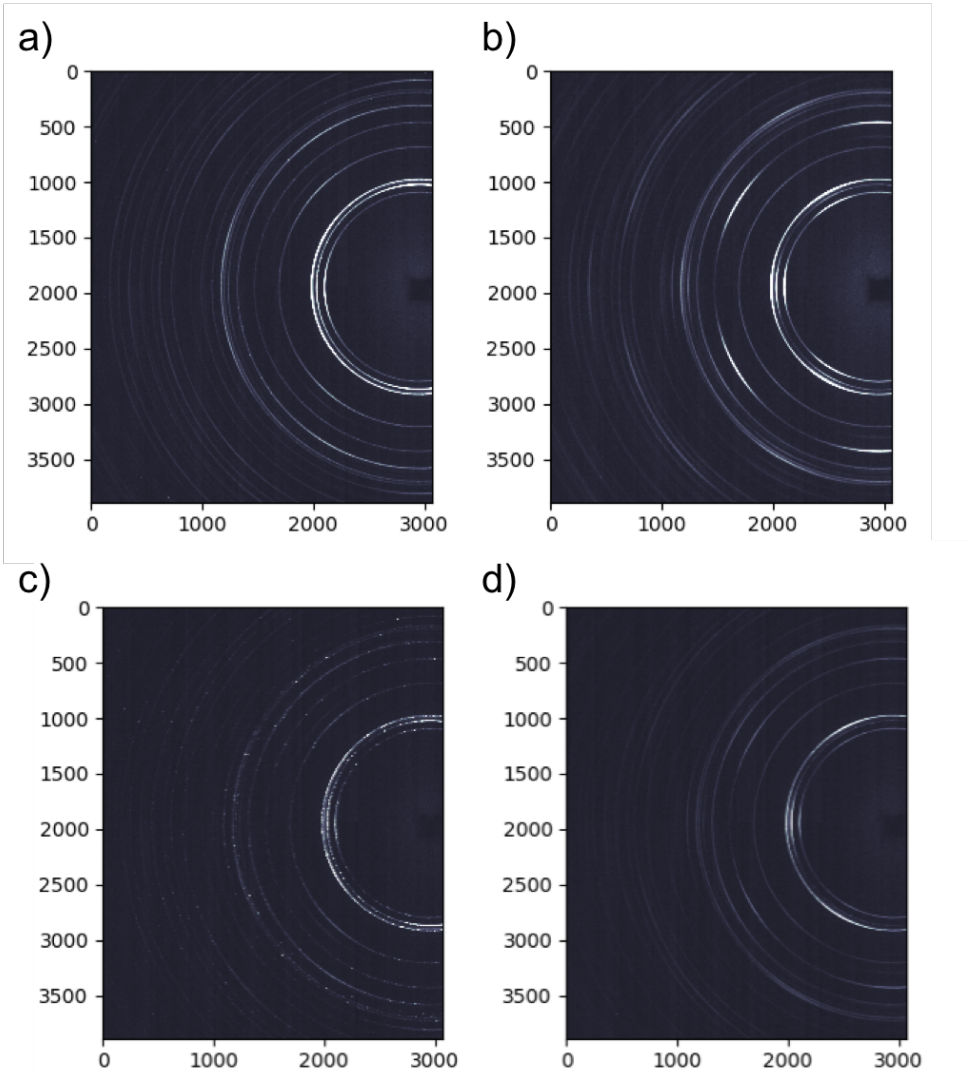


Figure 5.2: Raw detector output from the Dexela FF1 Detector showing a) the as-supplied UDR material, b) the UDR at the end of the jump experiment, c) the as-supplied CR material and d) the CR Ti-6Al-4V after the SRJ experiment.

The format of the chapter is as follows. The effect of the timing of the SRJ is detailed in Section 5.2, showing little effect on the overall response. The differences between the UDR and CR material in the rolling direction are analysed with particular emphasis on the lattice strain evolution in Section 5.3. The CR material, in both the rolling and at 45 degrees to the rolling direction are compared in Section 5.4. A study on the rate sensitivity follows in Section 5.5. Conclusions from this chapter are summarised in the relevant sections and an overall summary may be found in Chapter 9. The effect of the SRJ on the individual Ti-6Al-4V product forms is reviewed in Chapter 6 where it is studied alongside the computational model.

5.2 Effect of the SRJ at different engineering strains

The effect of the timing of the strain rate jump is examined in this section, where tests are performed in situ on the UDR material. The jump in strain rate was performed at 1.5, 2.25 and 3% engineering strain, accounting for the machine compliance, this equivalent to 0.92, 1.64 and 2.67% engineering strain in the sample. The bulk of the comparison is between the results at 0.92 and 2.67% engineering strain as the 0.92% jump occurs at around yield whereas the 2.67% is definitely in the plastic region. In the case of the test at 1.64%, the shutter between the sample and detector did not open as anticipated, preventing the beam from reaching the sample during deformation, therefore no lattice strain evolution was recorded for this experiment. However, the macroscopic response shows good alignment in the post-jump responses of the stress-strain curves for all three of the results, as shown in Figure 5.3.

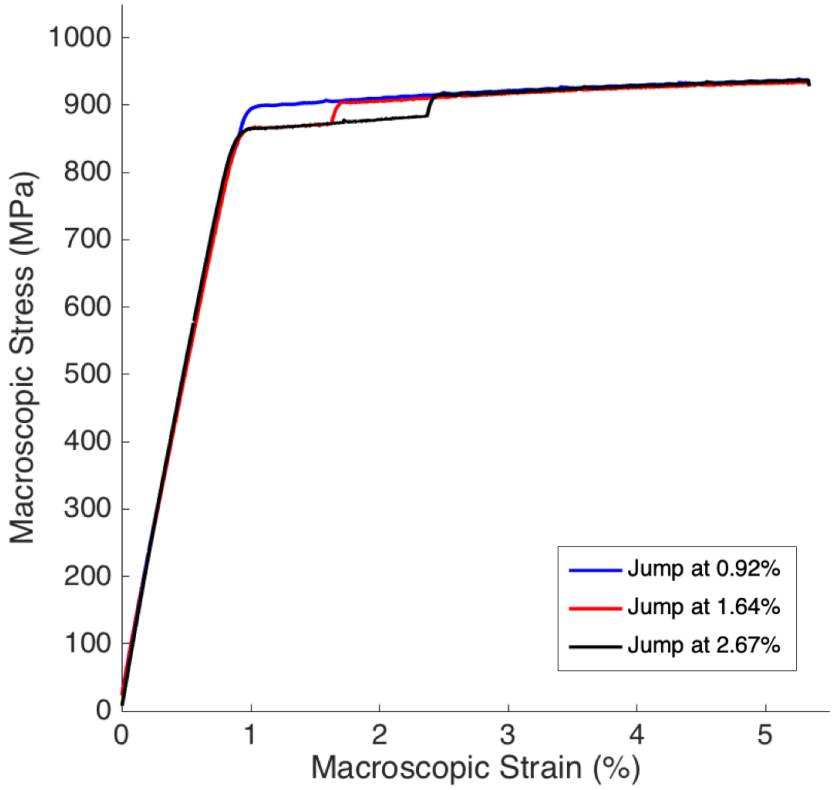


Figure 5.3: Macroscopic response of three experiments on UDR material where jumps are performed at 0.92, 1.64 and 2.67% engineering sample strain.

5.2.1 Lattice Strains

Lattice strain evolution data has been extracted from in situ XRD experiments using the method described in Section 3.3. Significantly more α phase lattice strains are observed due to approximately 90-95% of the alloy consisting of the α phase. Therefore these are more likely to be accurate representations of the average

material behaviour. The lattice strain evolution for α-phase responses are shown for jumps at both 0.92% and 2.67% engineering strain in Figures 5.4 and 5.5 respectively.

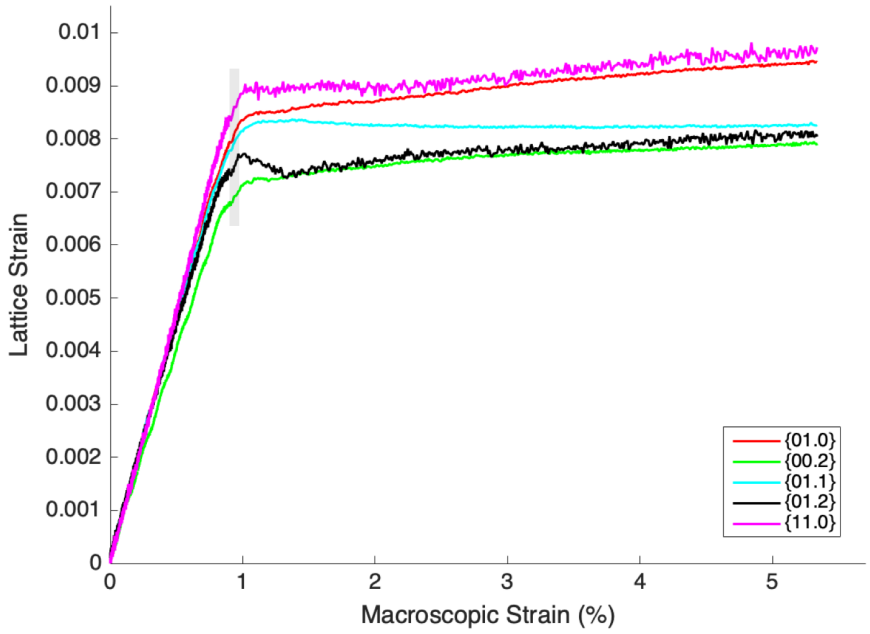


Figure 5.4: Lattice strain responses of UDR Ti-6Al-4V undergoing jump from 10^{-4} to 10^{-3} s^{-1} at 1.5% engineering strain (equivalent to 0.92% engineering strain in the sample) for multiple crystallographic directions.

It is difficult to visually identify the jump in Figure 5.4 due to its occurrence around yield. Post yield, a fairly linear response is observed where the lattice strain steadily increases with increasing macroscopic strain. At around 1.5%, the {01.2} appears to increase where it was previously reducing. The normal to the {01.0} direction steadily reduces post-yield for both cases, this is consistent with other results for this material as outlined in subsequent sections.

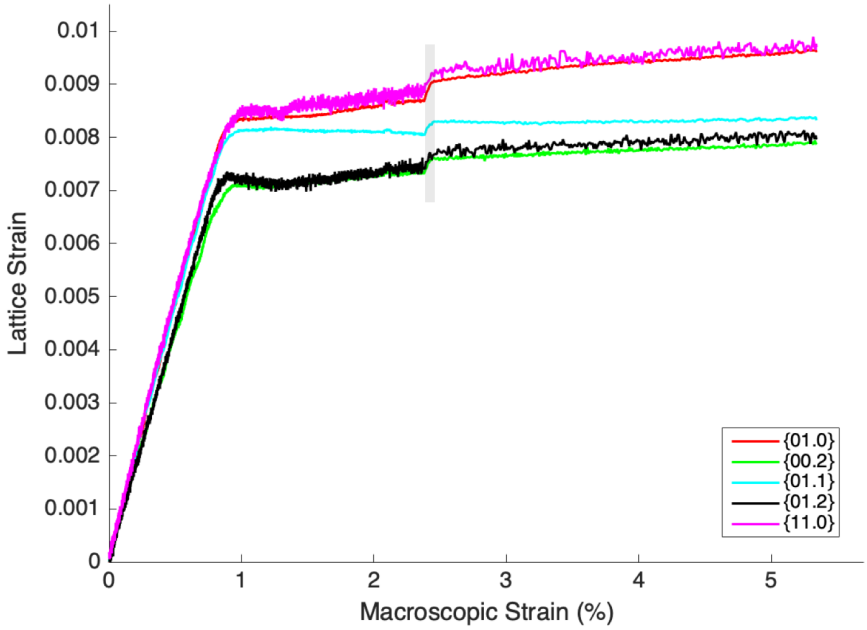


Figure 5.5: Lattice strain responses of UDR Ti-6Al-4V undergoing jump at 2.67% engineering strain in the sample, for multiple crystallographic directions.

An effective modulus for each case has been extracted from macroscopic stress-lattice strain data, see Table 5.3. The effective modulus for all directions are almost identical between the samples and small discrepancies are likely due to the inherent variability in the samples, these are of negligible magnitude. The {10.0} and {11.0} directions have the lowest magnitude with the {01.1} slightly higher and the {01.2} and {00.2} directions higher still.

The macroscopic stress and lattice strain during the jump are plotted for each direction in Figure 5.6, this indicates a non-linear response during the jump, showing how lattice strain accumulates during the jump. This is more realistic than the simple gradient observed previously in Section 4.1.2. The increase in stress is much greater during the jump at 0.92%, however the trends are similar in both. The jump appears to be non-linear with an initial increase in stress with limited corresponding lattice strain increase, progressing to a macroscopic stress increase which correlates with increasing lattice strain.The behaviour, particularly in the latter section is similar and well aligned between strain rates, this is particularly evident when a wider azimuthal sector is examined, see Figure 5.7. These tests have been performed with the same sampling rates.

Table 5.3: Effective moduli calculated at the initial gradient (between 100 - 700 MPa), calculated from the macroscopic stress vs lattice strain data, units are GPa.

[hk.l]	Initial Gradient (0.92%)	Initial Gradient (2.67%)
{01.0}	105.01	103.98
{00.2}	121.64	121.09
{01.1}	107.68	107.30
{01.2}	111.89	112.84
{11.0}	98.98	103.14

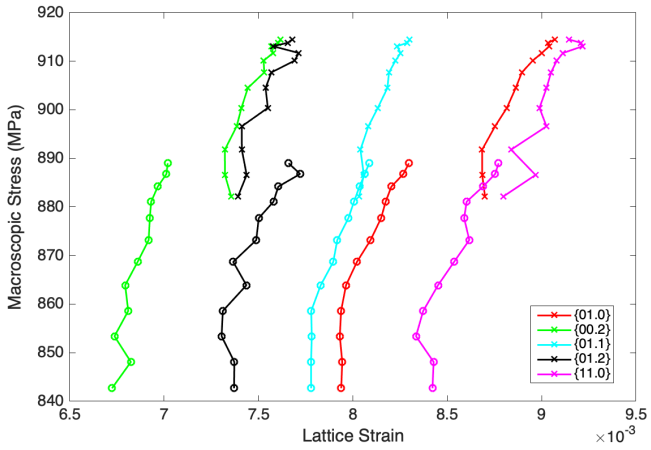


Figure 5.6: Lattice strain data during the jump in strain rate, plotted against macroscopic stress to examine the behaviour during the jump where ● denotes the jump at 0.92% and **X** the jump at 2.67%.

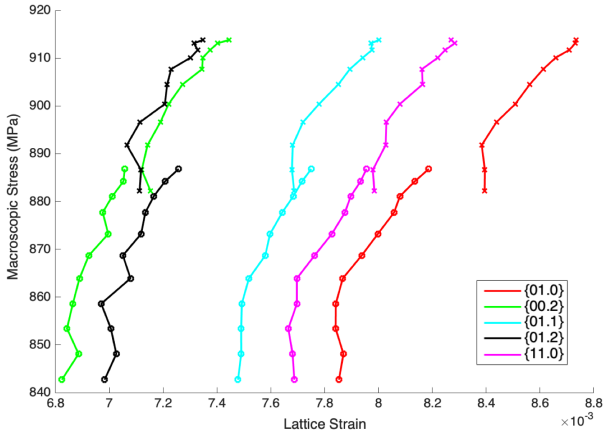


Figure 5.7: Lattice strain data during the jump in strain rate, plotted against macroscopic stress to examine the behaviour during the jump where ● denotes the jump at 0.92% and **X** the jump at 2.67%, where a wider 36 degree azimuthal bin is employed.

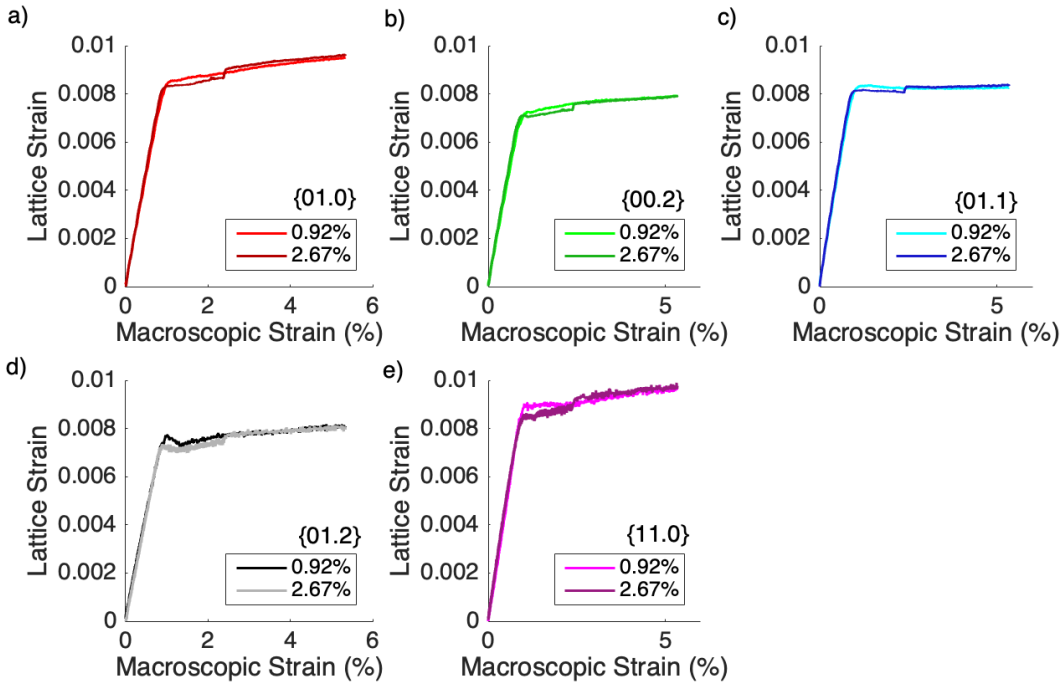


Figure 5.8: Comparison of lattice strain responses for the UDR material at 0.92% and 2.67% engineering strain showing good alignment post jump for all directions considered where a) is normal to the {01.0} b) is normal to {00.2}, c) is normal to {01.1}, d) is normal to {01.2} and e) is the normal to the {11.0} direction.

The lattice strain accumulation for both experiments are compared in Figure 5.8. The crystal scale alignment for all crystallographic directions post jump is high, implying that lattice strains accumulate to the same values irrespective of when the material reaches that particular strain rate. This alignment is remarkable considering these are two individual specimens and variation between specimens is expected. Overall, lattice strain continues to increase post yield for all directions except the {01.1} direction. Alignment is also good in the transverse direction as in Figure 5.9, with the earlier jump causing slightly more compressive strain in some directions. However, all trends remain consistent and the magnitudes are fairly similar. The transverse results are generally deemed to be less accurate than those in the loading direction. In the transverse direction, compressive strains are observed to continue increasing for the {00.2}, {01.0} and {01.2} directions, whereas a steady reduction is observed in the {01.1} and {11.0} directions. Note the increased compressive lattice strain accumulation in the {00.2} direction.

During the jump, a significant elastic component is assumed as the material will not have reached the yield stress for the current strain rate [62]. The strain rate during the jump is significantly higher and this may also impact the response. Thus, a combination of elastic and plastic behaviour is likely to be observed during the jump in strain rate, as seen in Figure 5.6. These results are substantially closer than previous comparisons, perhaps the jump 'shocks' the material and this results in a more consistent response/product.

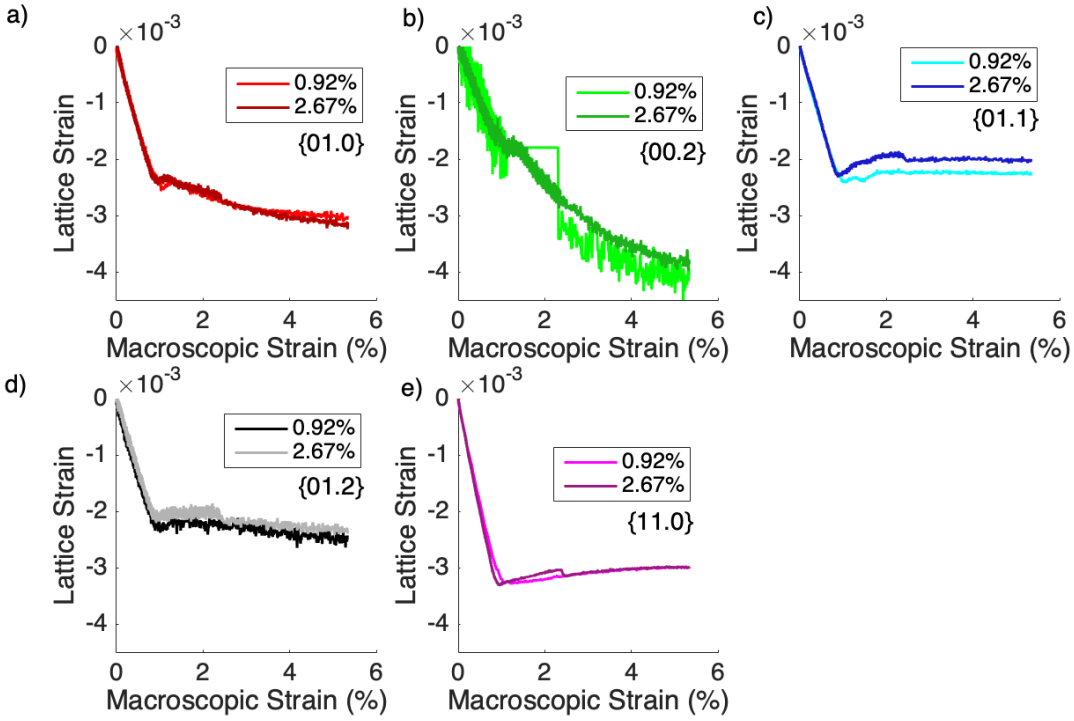


Figure 5.9: Comparison of lattice strain response in the transverse direction for UDR material at 1.5% and 3% engineering strain where a) is normal to the {01.0} b) is normal to {00.2}, c) is normal to {01.1}, d) is normal to {01.2} and e) is the normal to the {11.0} direction.

5.2.2 EBSD

EBSD has been performed at two resolutions, one to generate pole figures over a larger area and another to gain accurate representation of the actual 2D crystallographic structure. Due to the reduced grain size observed in the UDR material, large area scans were performed with a 2.5 micron step size (smaller than previously in Chapter 4) to properly characterise the individual grains. Resultant IPF maps are compared for the initial undeformed material and post-experimental for both jumps at 0.92 and 2.67% engineering strain in Figure 5.10. The Grain Averaged Misorientation (GAM) [125] has been calculated for each case, appearing substantially higher in the results from the jump at 2.67% in areas with generally basal orientated grains. This increase appears relative to the orientation, see RHS of Figure 5.10. Figure 5.11 shows equal area pole figures of the undeformed and both post-jump deformed states. The crystallographic textures for all states are similar, with the maximum magnitudes of both post jump textures being very close (Figures 5.11b & c), again highlighting that the effects of the SRJ are independent of the timing.

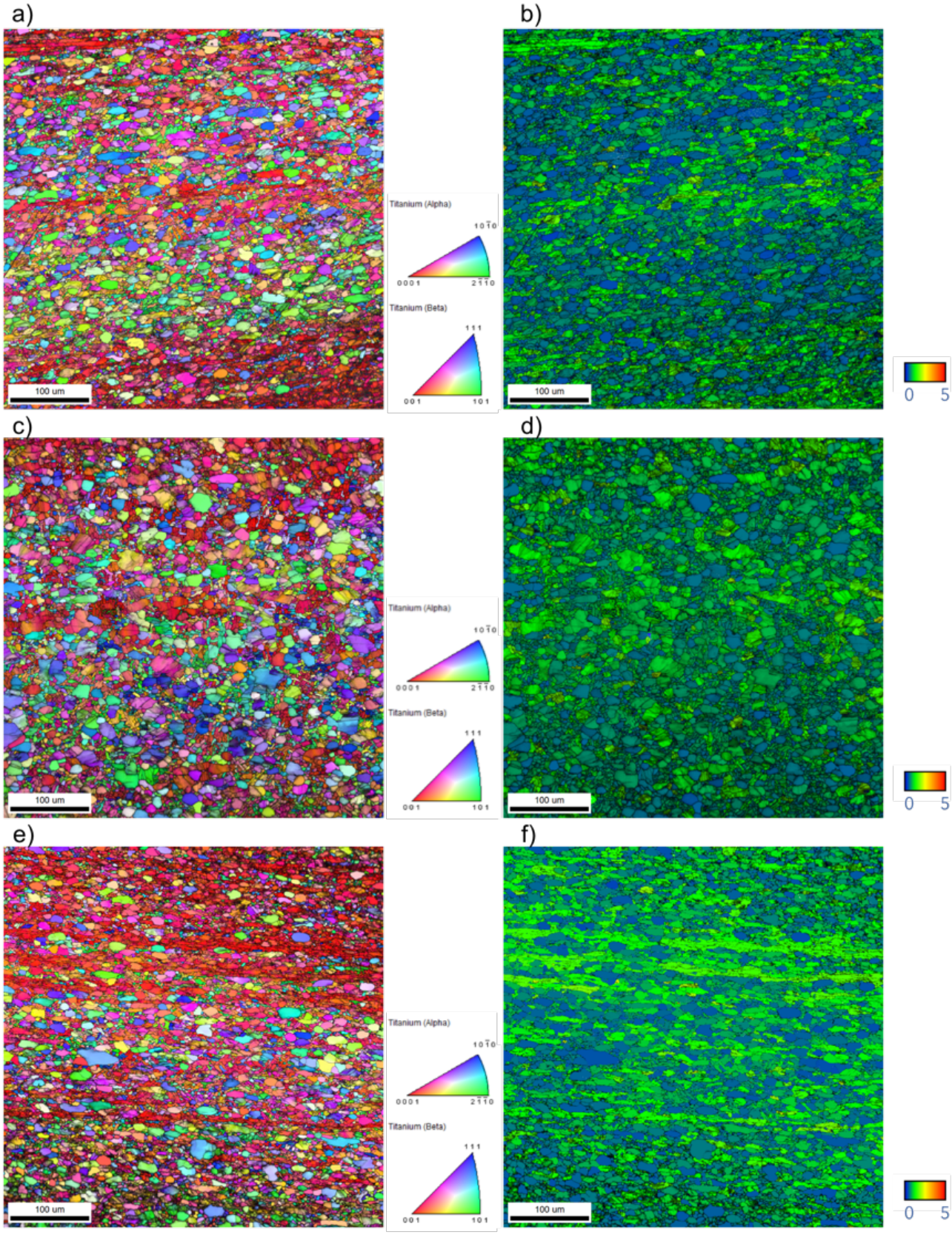


Figure 5.10: IPF maps of a) undeformed UDR c) post jump (at 0.92% strain) and e) post jump (at 2.67% strain) microstructures showing crystallographic orientations. Grain averaged misorientation is plotted over the same areas for b) the undeformed UDR d) post jump (at 0.92% strain) and f) post jump (at 2.67% strain) microstructures. All scale bars = 100μm.

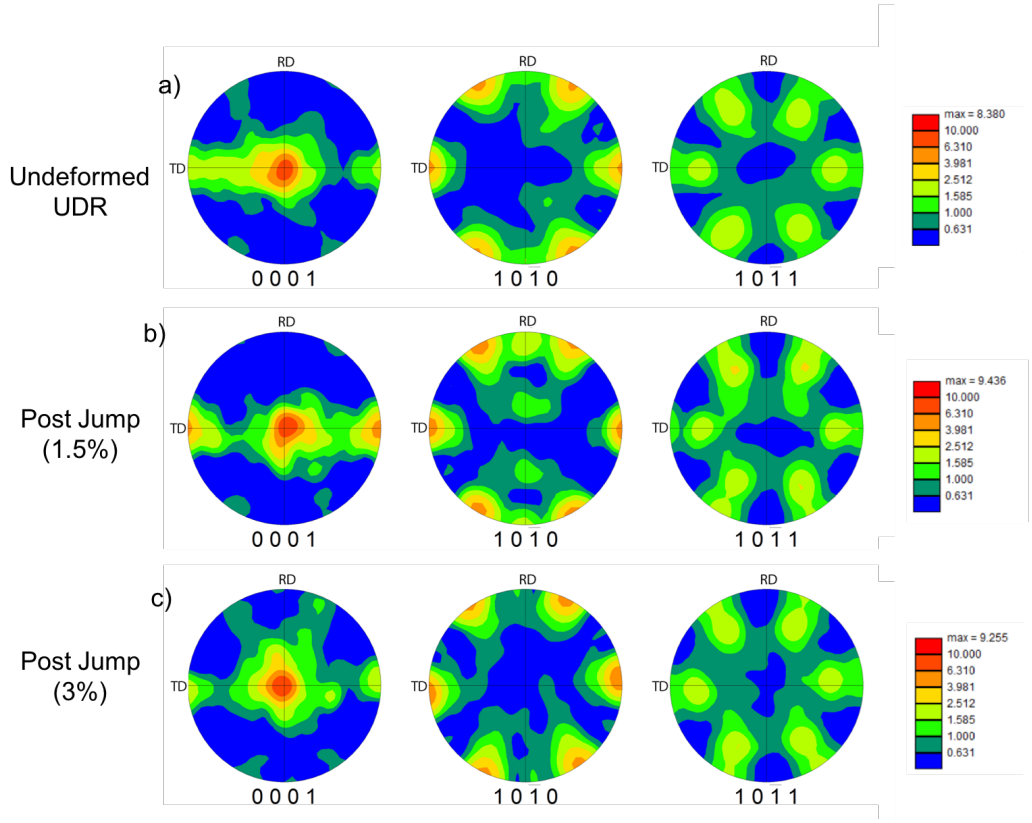


Figure 5.11: Scaled pole figures extracted from large area scans of a) undeformed UDR material b) UDR material post jump at 0.92% and c) UDR material post jump at 2.67%.

A marginal increase in dislocation density is observed in the jump at 2.67% compared to that at 0.92%, see Figure 5.12. Dislocation accumulation may be higher with the jump in the plastic region due to the continuing plastic behaviour, where the jump will have a greater impact as it cannot be accommodated wholly by elastic movement within the material. Alternatively, this may simply be an artefact of the area sampled, with the increased amount of basal-oriented macrozones, and may not be significant [128].

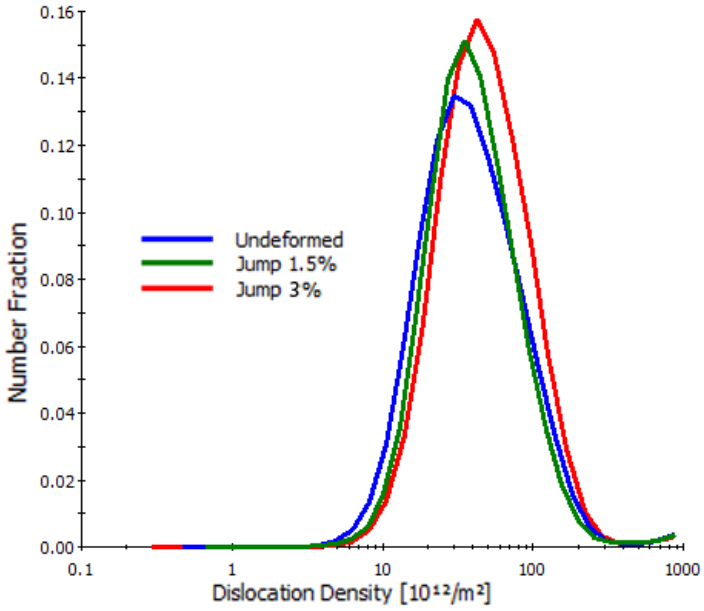


Figure 5.12: Number fraction of geometrically necessary dislocation (GND) density of each microstructure, calculated from high resolution scans (300 x magnification and 0.5 micron step size).

In summary, the effect of the timing of the SRJ on the UDR material is negligible with no significant change in texture and the overall lattice and macroscopic stress-strain values are in agreement post jump. In the future, experiments such as those herein may prove useful in improving the understanding of the effect of the SRJ on a variety of HCP materials.

5.3 Comparison between UDR and CR material

5.3.1 Macroscopic Response

The adoption of cross rolling in Ti-6Al-4V has become standard to minimize the effects of anisotropy in the mechanical properties of titanium alloys [74]. UDR and CR materials are now compared. Both have been cut from same direction from similarly sized plates supplied by Timet. They should contain the same material chemistry and have undergone similar processes, however, the CR has undergone a slightly more complex processing regime (see Section 1.4.3) as the cross rolled material will have undergone more extensive rolling and this is expected to be evident in the microstructure. Two constant strain tests and a SRJ experiment are performed in situ on both materials as described previously. The macroscopic response has been adapted from the cross-head displacement by accounting for load frame compliance using DIC measurements.

Variability in the response is likely due to microstructural differences and the small sample gauge section, this variation is evident in Figure 5.13a. The bulk of the difference appears to be material dependant, with an

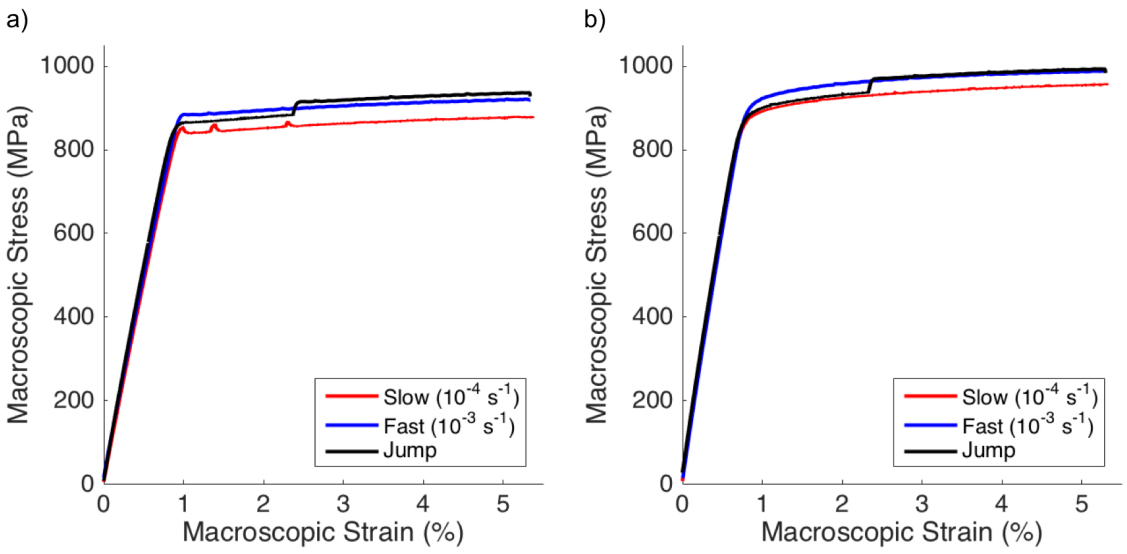


Figure 5.13: Macroscopic stress-strain responses comparing a) the UDR and b) the CR materials in the rolling direction, at both constant strain rates and with a strain rate jump.

apparent Young's moduli of 118.2 GPa and 96.3 GPa for the CR and UDR materials respectively, calculated from the higher strain rate tests, where the CR result is closer to the values observed in the literature [69]. Yielding in the CR material is more gradual than the UDR. The yield stress has been calculated for each experiment in Table 5.4, with the CR material reaching higher levels of stress at yield.

Table 5.4: Yield Stress for CR and UDR experiments, calculated using the 0.2% offset method, (where the UDR at 10^{-4} s^{-1} is likely to be lower than expected).

Test	UDR - Yield Stress (0.2%)	CR - Yield Stress (0.2%)
10^{-4} s^{-1}	839.0 MPa	889.6 MPa
10^{-3} s^{-1}	883.9 MPa	923.6 MPa
Jump	865.1 MPa	896.8 MPa

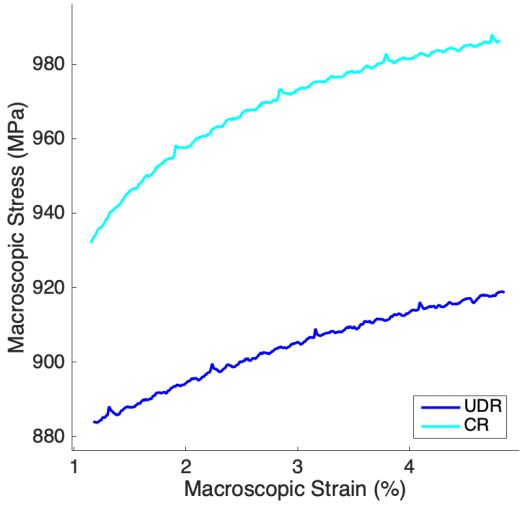


Figure 5.14: Macroscopic stress-strain responses of UDR and CR materials showing difference in hardening behaviour, the 'blips' here are artefacts created due to the surrounding electronics at CHESS.

The overall shape of the stress-strain curve is dependant on the material with the UDR reaching yield and then dipping slightly leading to a flat response whereas the CR is a continuous curve, again tending to a fairly linear response. Fitting functions have been performed on the data, see Figure 5.14 and the area under the curves has been calculated between 1.25% and 5% engineering strain, where the CR material is 7.15% higher than UDR material, showing a greater absorption of energy for equivalent macroscopic strain values. Both materials appear to display similarly strain rate sensitive behaviour where small differences are attributed to the individual initial microstructures and subsequent evolution. It is important to note that the slower strain rate test of the UDR material appears to have been affected, this is likely due to slippage during the experiment, as indicated by the three peaks in the region between yield and ∼3% engineering strain, see Figure 5.13. Therefore, the results of the lower constant strain rate experiment are not studied further in this analysis.

5.3.2 EBSD

The miscrostructures of the undeformed materials are shown in Figure 5.15a and b, where the overall area is the same in both showing the decreased grain size for the UDR material. Additionally, different work hardening evolution is observed between the materials, with the UDR accumulating less stress. This is likely due to the difference in grain size between the materials [124]. The textures are compared in Figure 5.16 where these are significantly stronger in the UDR material. This increased texture strength is due to processing of the material as the cross rolling should reduce the overall texture.

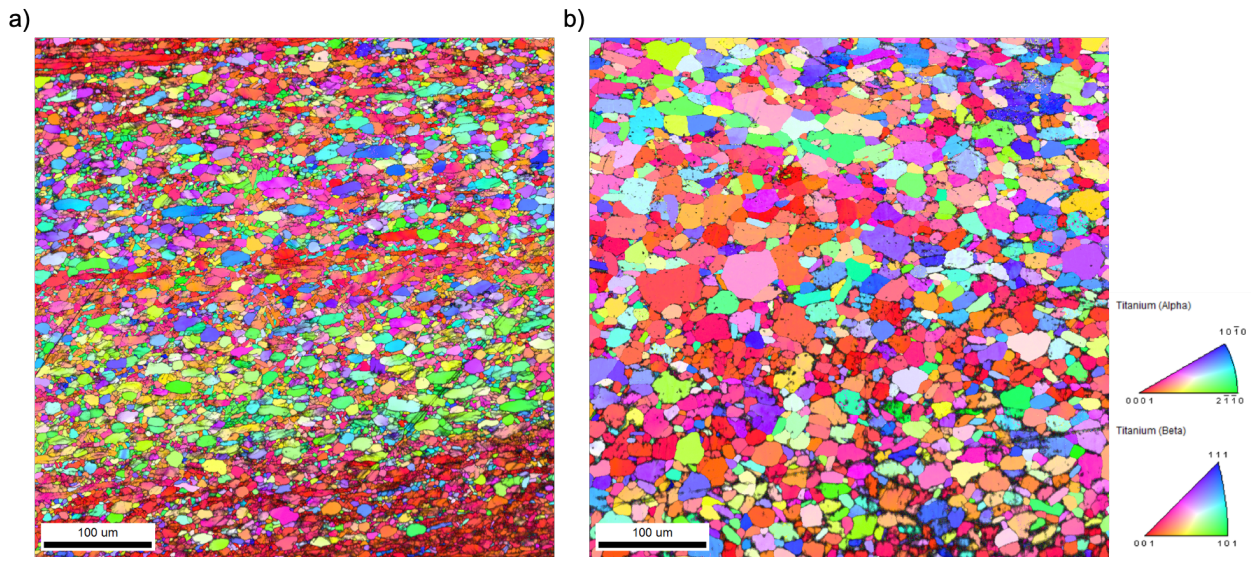


Figure 5.15: IPF maps of the as-received a) UDR material and b) CR material, showing very different grain sizes.

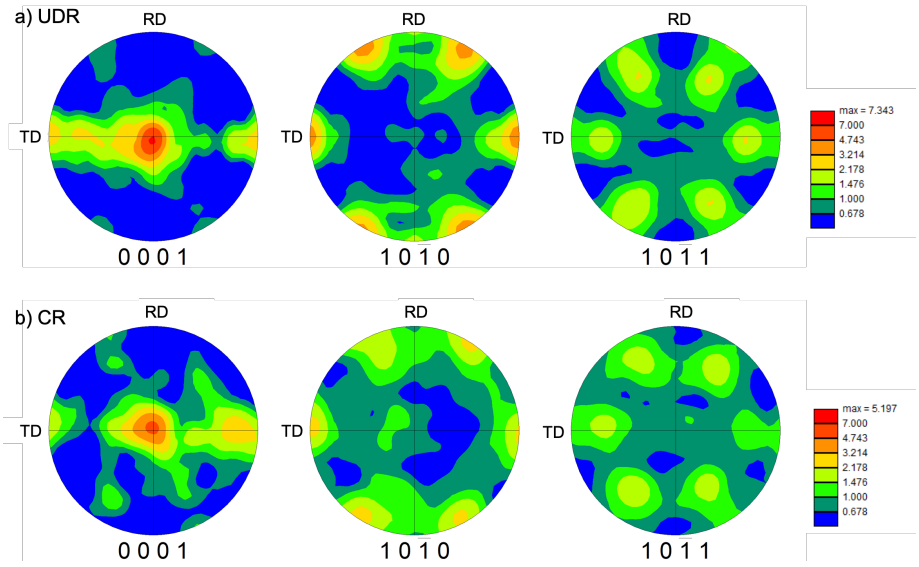


Figure 5.16: Pole figures showing the texture of the as-received a) UDR material and b) CR material.

Post SRJ IPF maps and pole figures are also examined for the materials examined, Figures 5.17and 5.18 respectively. The increased texture strength in the post jump material as previously observed in Section 4.1.1 also exists in the CR and UDR materials, however the increase in magnitude is smaller.

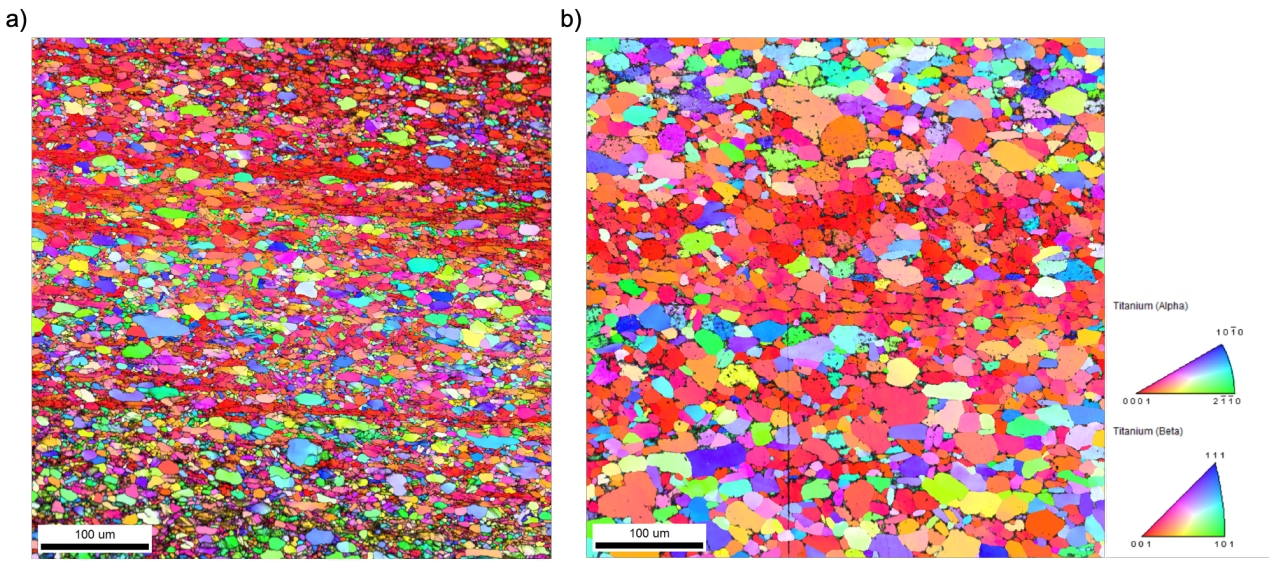


Figure 5.17: IPF maps of the deformed a) UDR material and b) CR material, again showing larger grains in the CR material.

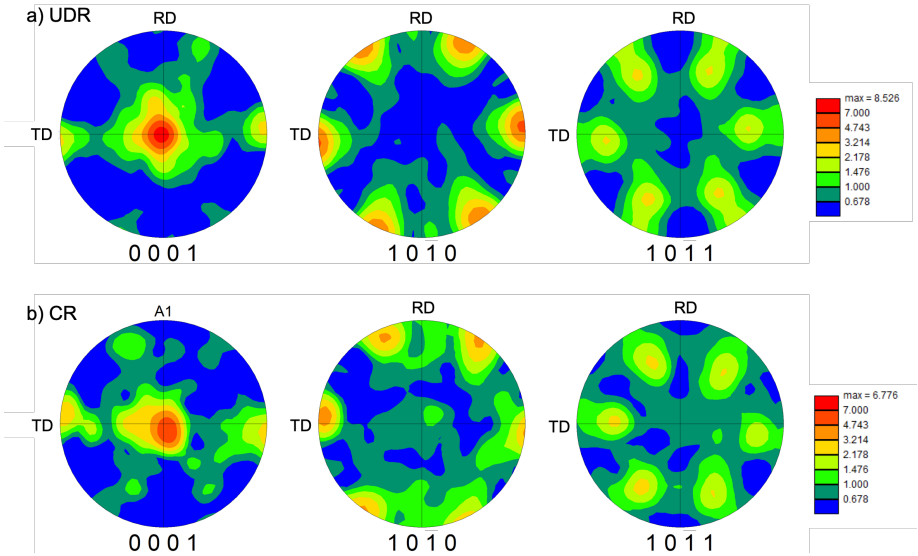


Figure 5.18: Pole figures showing the texture of the deformed a) UDR material and b) CR Ti-6Al-4V.

5.3.3 Lattice Strains - α Phase

The results from the constant strain rate test at 10^{-3} s^{-1} (faster) and jump test are compared respectively for both CR and UDR materials in Figures 5.19 and 5.20. In general, the lattice strain response mirrors the bulk behaviour, continually increasing for the CR material and a more linear UDR response. Lattice strains normal to the {01.0}, {00.2} and {11.0} directions appear to have accumulated higher lattice strains at yield for the UDR material. This is also true when comparing the results of the jump tests, Figure 5.20. The jump is evident in each direction, increasing the lattice strain as outlined in Table 5.6, where the magnitude of the jump is not consistent between material types.

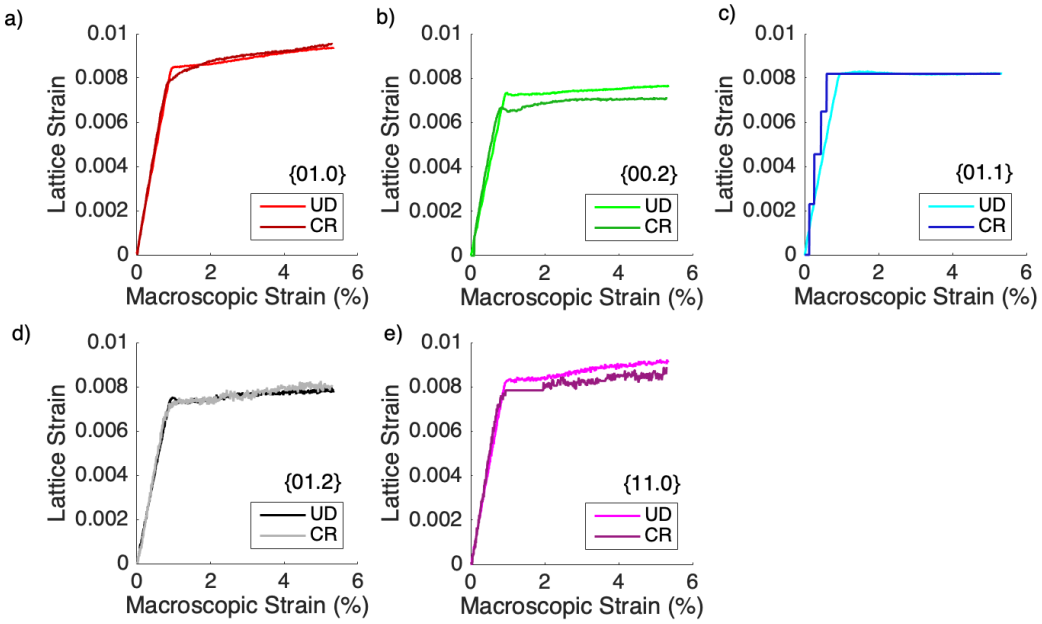


Figure 5.19: Alpha phase lattice strain responses normal to the respective directions, a) {01.0}, b) {00.2}, c) {01.1}, d) {01.2} and e) {11.0} compared for UDR and CR materials. Directions are coloured corresponding to Figure 1.12. Lattice strain evolution has been extracted from the higher constant strain rate experiments (10^{-3} s^{-1}).

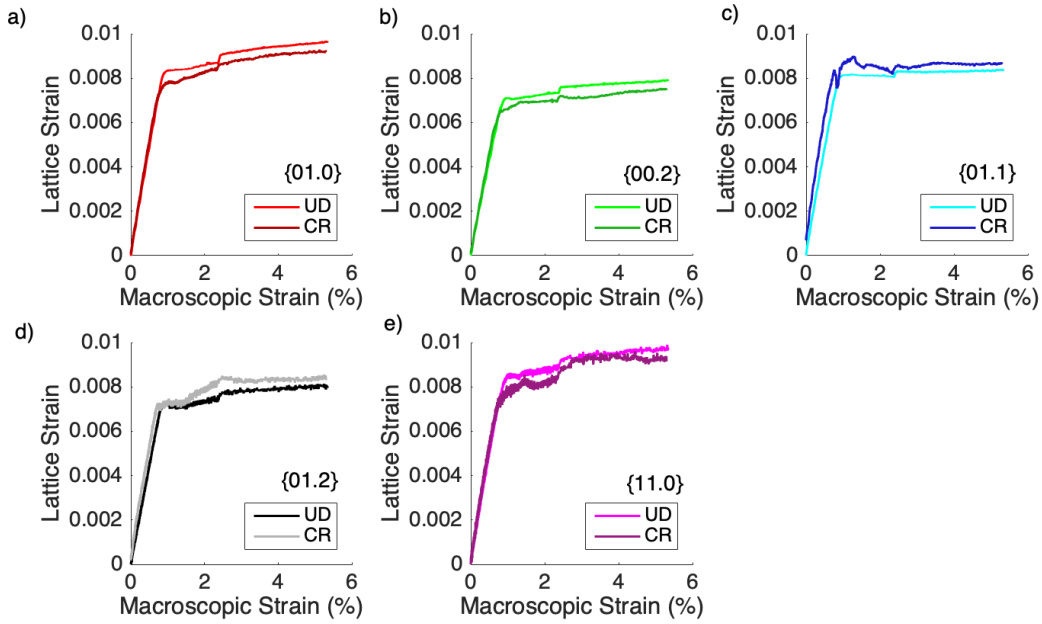


Figure 5.20: Alpha phase lattice strain responses normal to the directions, a) {01.0}, b) {00.2}, c) {01.1}, d) {01.2} and e) {11.0}, extracted from jump tests, where the directions are coloured according to Figure 1.12.

The normalised lattice strain values for each material in Table 5.5 show similar lattice strain distributions. The {01.1} and {11.0} direction indicate the differences between the materials where both are substantially higher

in the CR material. The increase in lattice strain during the jump is recorded in Table 5.6. No correlation between the increase during the jump and the effective moduli is observed.

[hk.l]	UDR		CR	
{01.0}	0.008343	(1.19)	0.007831	(1.20)
{00.2}	0.007025	(1.00)	0.006507	(1.00)
{01.1}	0.008560	(1.22)	0.009472	(1.46)
{01.2}	0.007251	(1.03)	0.007226	(1.11)
{11.0}	0.008521	(1.21)	0.008072	(1.24)

Table 5.5: Lattice strain at yield for the UDR and CR materials showing actual and normalised values for each material for the SRJ experiment.

[hk.l]	UDR Increase	CR Increase
{01.0}	3.710 e^{-4} (4.26 %)	1.932 e^{-4} (2.30 %)
{00.2}	2.626 e^{-4} (3.58 %)	2.879 e^{-4} (4.17 %)
{01.1}	2.650 e^{-4} (3.30 %)	1.849 e^{-4} (2.00 %)
{01.2}	2.880 e^{-4} (3.89 %)	2.499 e^{-4} (3.08 %)
{11.0}	3.466 e^{-4} (3.94 %)	3.590 e^{-4} (4.31 %)

Table 5.6: Increase in lattice strain during the SRJ for both UDR and CR materials.

In the transverse direction, for the higher strain rate test, the compressive lattice strains are generally higher for the UDR than the CR Ti-6Al-4V, except for the normal to the {00.2} direction, see Figure 5.21. This trend is not observed during the SRJ, see Figure 5.22. Note the values of compressive lattice strains in the transverse direction are significantly smaller than those in the loading direction as expected. At approximately 1.5% engineering strain, the CR response begins to reduce where it was previously increasing, the response normal to the {01.1} direction actually ends up with small tensile lattice strains in the transverse direction. This change may also be observed in the loading direction, refer to the {01.1} and {01.2} directions in Figure 5.19 and during the jump. This behaviour is examined further in Section 5.4.

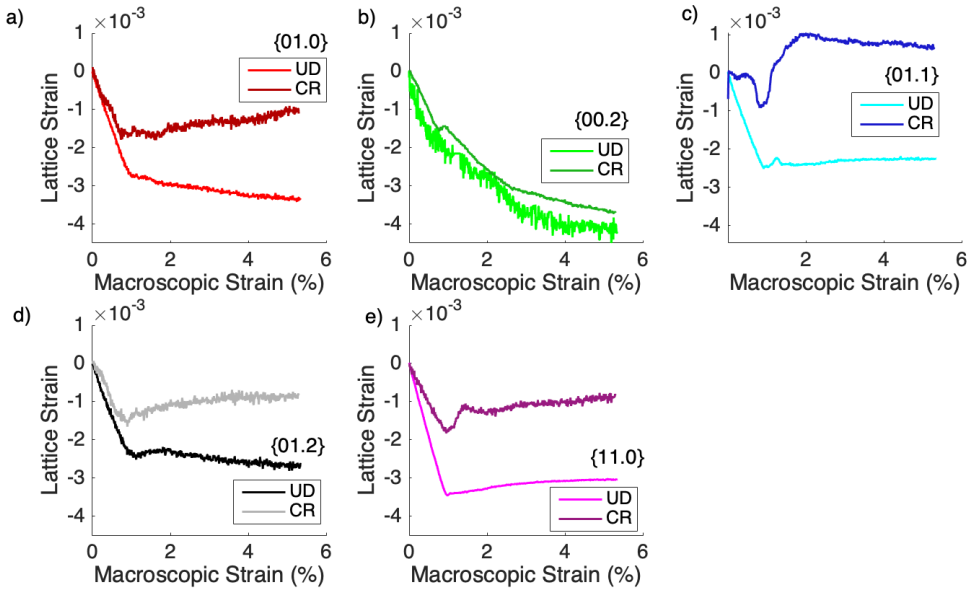


Figure 5.21: Alpha phase compressive lattice strain results from the higher constant strain rate experiments (10^{-3} s^{-1}) from the transverse direction of the powder diffraction ring, for the UDR and CR materials a) normal to the {01.0} direction, b) normal to {00.2}, c) normal to {01.1}, d) normal to {01.2} and e) normal to the {11.0} direction.

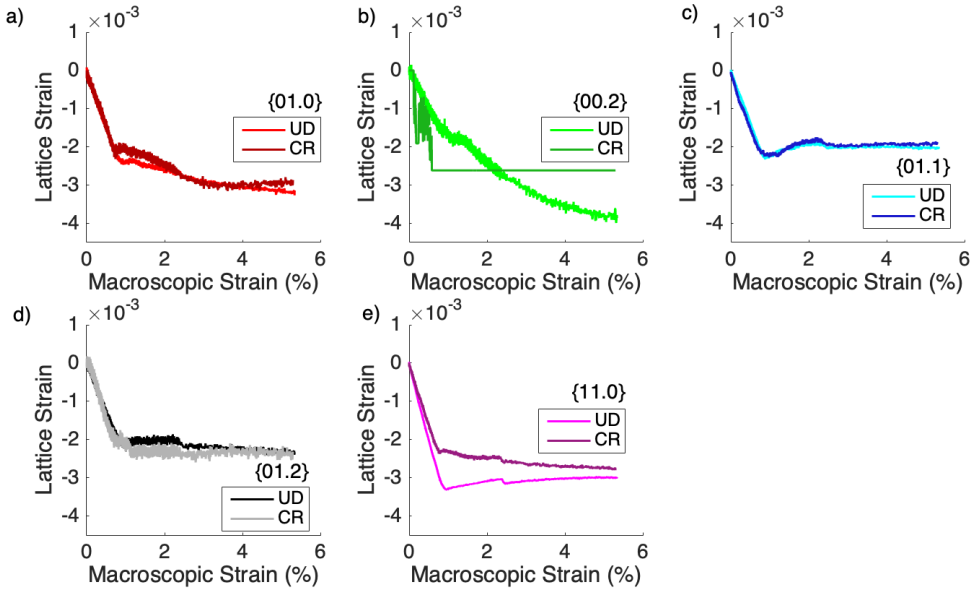


Figure 5.22: Alpha phase compressive lattice strain results from the SRJ experiment from the transverse direction of the powder diffraction ring, for the UDR and CR materials where a) is normal to the {01.0} direction, b) normal to {00.2}, c) normal to {01.1}, d) normal to {01.2} and e) normal to the {11.0} direction.

5.3.3.1 Lattice Strains - β Phase

The β phase lattice strains are compared for both UDR and CR experiments in Figure 5.23. The response contains a substantial amount of noise in the data but overall shows a difference in the β phase lattice strains where the CR material accumulates significantly more lattice strain for the same macroscopic strain. This may be due to the CR material being better oriented for load sharing between phases [186]. The values for the {020} beta phase response at yield are higher than all of those observed in the α phase.

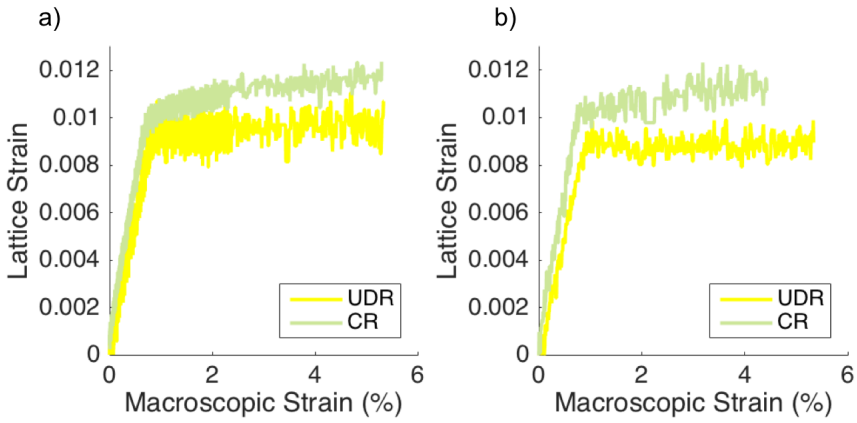


Figure 5.23: β {020} lattice strain response in the loading direction comparing the UDR and CR materials for a) the jump test and b) constant strain rate test (10^{-3} s^{-1}).

5.3.3.2 Lattice Strain & Macroscopic Stress

Lattice strains at yield are generally lower for the CR material despite occurring at higher macroscopic stresses. This may partially explain how the CR material can sustain higher macroscopic stresses. Figure 5.24 shows the lattice strains at yield for the experiments described in this section. It clearly shows the increasing lattice strain at yield with the increased strain rate for each material. This is to be expected particularly if an effective moduli in each direction exists. Therefore higher lattice strain would be expected at a higher yield stress.

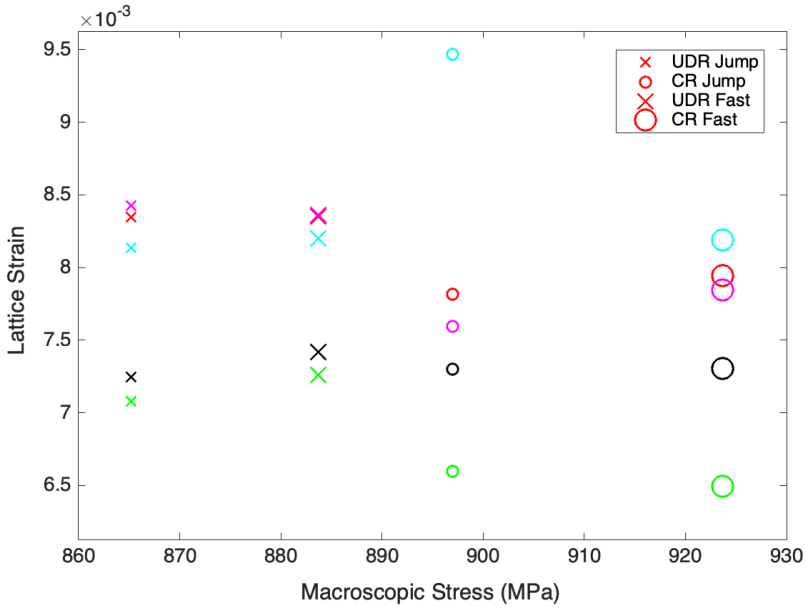


Figure 5.24: Lattice strains plotted at yield against macroscopic stress for a) UDR material and b) CR material comparing the lattice strain at yield, colours are consistent with directions as previous.

Differences between material products are evident. Of particular interest is the CR which reaches and accumulates higher lattice strains for the {002} direction of β phase. The lattice strain in the CR is generally observed as lower than the UDR in the α phase responses. This is suggestive of load sharing where the CR better distributes stresses microscopically thus leading to a stronger bulk response in CR Ti-6Al-4V.

In conclusion, the UDR material has a lower yield point and less hardening is observed than in the CR material. The lattice strain evolution is more consistent across crystallographic directions and results are more linear post yield for the UDR material. At yield, lower lattice strain values are observed in the CR material despite the higher macroscopic stresses. The grain size will also impact the overall response, and in comparing these product forms, the application of heat treatments to ensure comparable grain sizes would have improved the analysis. However, these differences were not observed until after the experiments were performed.

5.4 Comparison between CR material in the rolling direction and at 45 degrees.

The CR material is of particular interest as it is one of the most common product forms of Ti-6Al-4V. This section analyses the effect of the orientation of the Ti-6Al-4V plate on the mechanical properties. CR Ti-6Al-4V plate has been shown to be anisotropic, though less so than the UDR plate material discussed previously [153]. The specimens for the CR material, in both the rolling direction and at 45 degrees, have been cut from the same plate, as detailed in Section 1.4.3, and should therefore contain the same material chemistry and average grain sizes. This section aims to examine the role of anisotropy in situ at the crystal scale.

5.4.1 Macroscopic Response

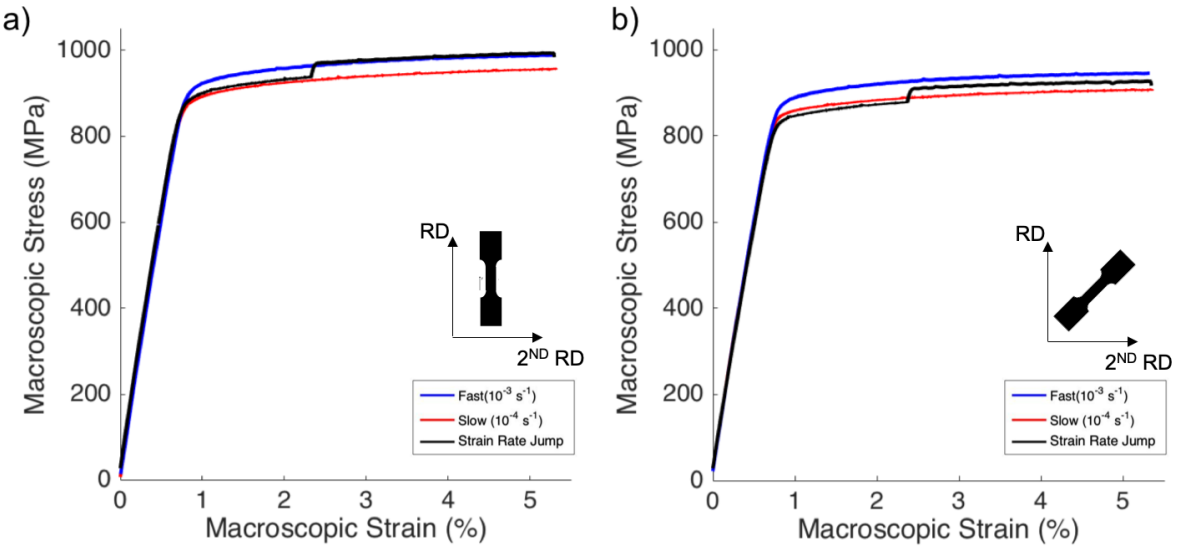


Figure 5.25: Macroscopic stress strain responses for CR material in a) the rolling direction and b) at 45 degrees to the rolling direction..

The results from the CR material at 45 degrees are more variable than in the rolling direction. Both materials have negligible difference in elastic moduli but yield at different stresses, with the CR material in the rolling direction yielding at higher stresses, see Figure 5.25. The difference in macroscopic response is significant and which direction components are cut from the plate will effect the overall strength and failure criteria. A reduction in yield stress of ∼4% results from this orientation change alone, see Table 5.7. The hardening response is comparable between the materials which also appear to be similarly rate sensitive.

Table 5.7: Yield stresses for CR in the rolling direction and at 45 degrees, calculated using the 0.2% offset method.

Test	Yield Stress (rolling)	Yield Stress (at 45 deg)	% Decrease
10^{-4} s^{-1}	889.6 MPa	858.1 MPa	3.54%
10^{-3} s^{-1}	923.6 MPa	891.5 MPa	3.47%
Jump	896.8 MPa	846.7 MPa	5.59%

Initial microstructures are analysed using EBSD in Figure 5.26. Differences in crystallographic textures are expected due to how the specimens have been extracted. Similar texture plots are given as the pole figures are calculated relative to the loading direction, as in Figure 5.27.

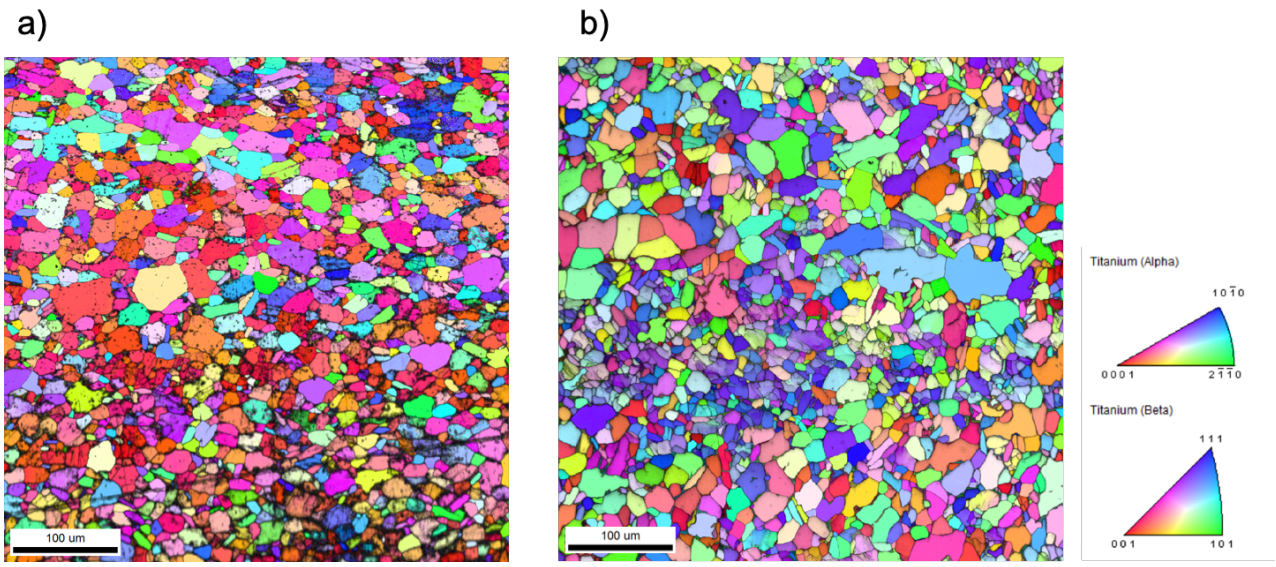


Figure 5.26: IPF maps of a) CR Ti-6Al-4V in the rolling direction in the as-received condition and b) CR material cut 45 degrees to the rolling direction, also in the as-received condition. All maps are parallel to the specimen loading direction.

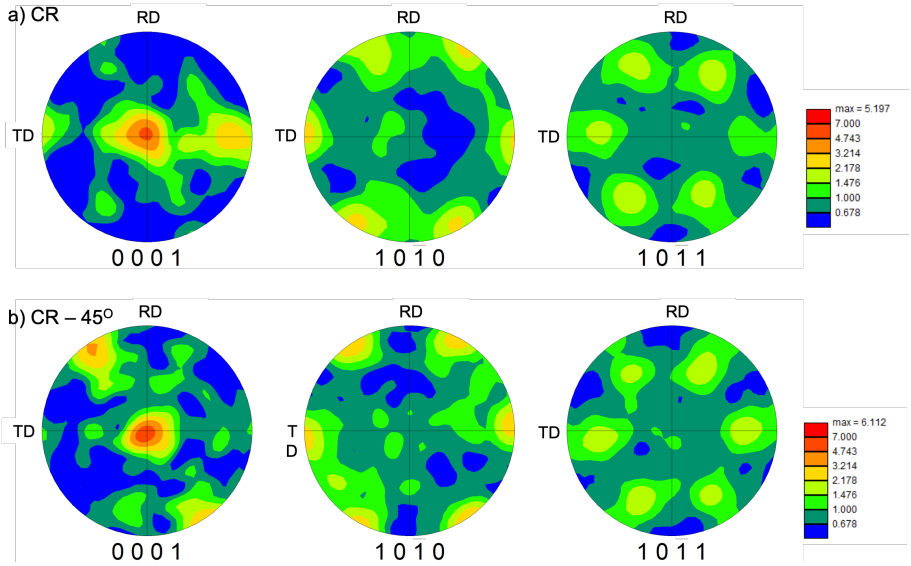


Figure 5.27: Pole figures of a) CR Ti-6Al-4V in the rolling direction and b) CR material cut 45 degrees to the rolling direction post deformation via the SRJ. All maps are parallel to the specimen loading direction.

5.4.2 Lattice Strains

The α phase lattice strain evolution during quasi-static deformation is shown in Figures 5.28, 5.29, and 5.30 where the lower, 10^{-4} s^{-1} , higher, 10^{-3} s^{-1} and SRJ responses respectively are compared for the CR in both directions. A less predictable response is observed where the CR material does not conform to either a continually increasing or decreasing lattice strain post yield as observed previously in UDR Ti-6Al-4V.

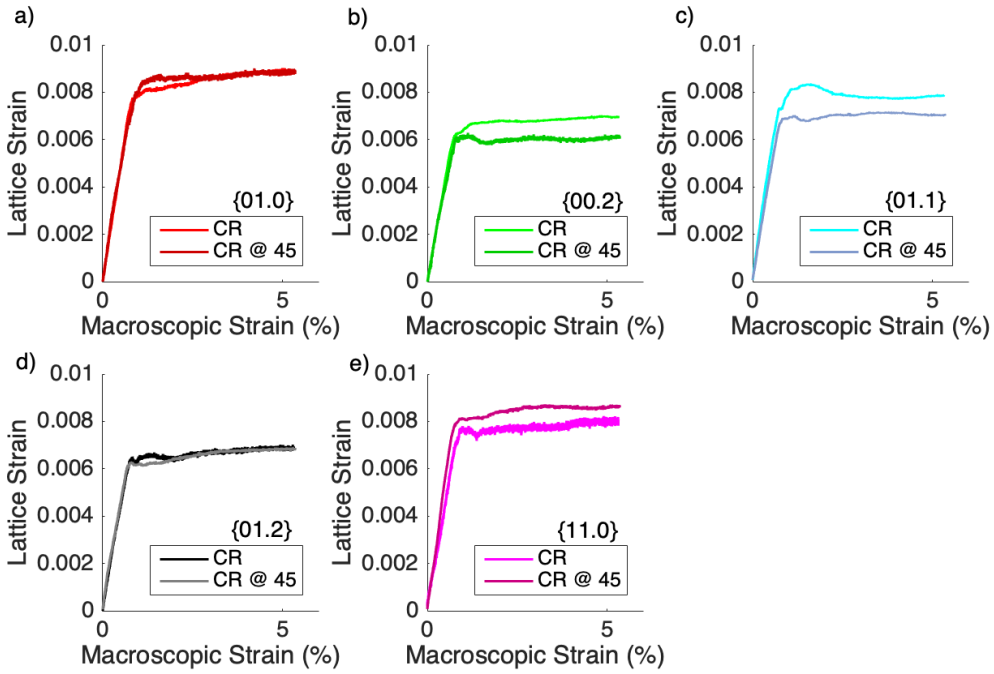


Figure 5.28: Lattice strain responses in the loading direction for strain rate of 10^{-4} s^{-1}, comparing the CR response in the rolling direction and at 45 degrees. Directions examined are normal to a) {01.0}, b) {00.2}, c) {01.1}, d) {01.2} and e) {11.0}.

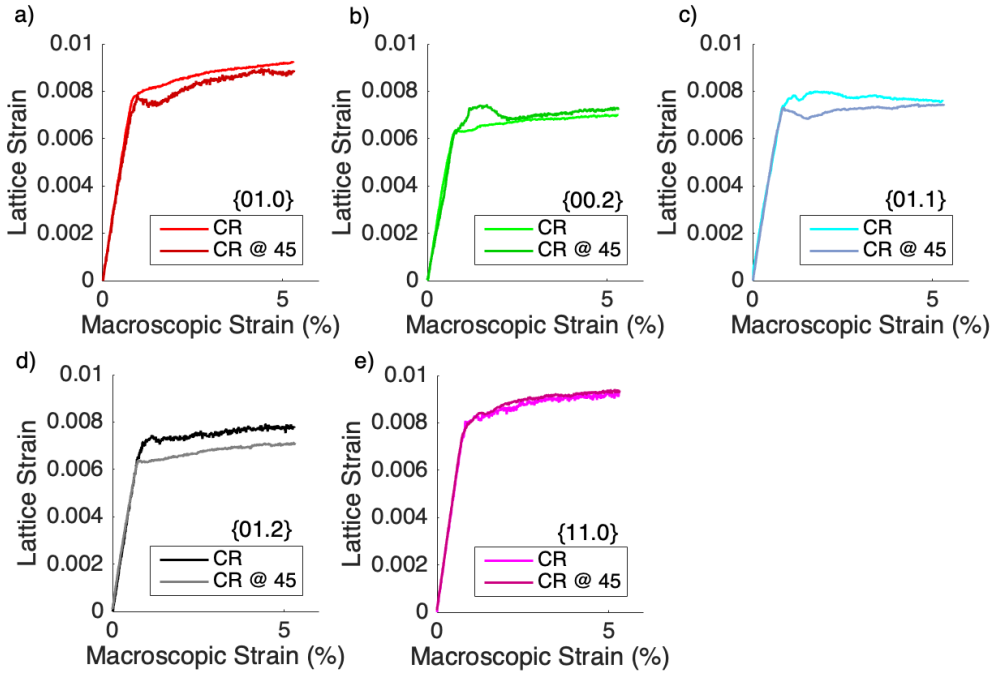


Figure 5.29: Lattice strain responses in the loading direction for the higher strain rate of 10^{-3} s^{-1}, comparing the CR response in the rolling direction and at 45 degrees. Directions examined are normal to a) {01.0}, b) {00.2}, c) {01.1}, d) {01.2} and e) {11.0} directions.

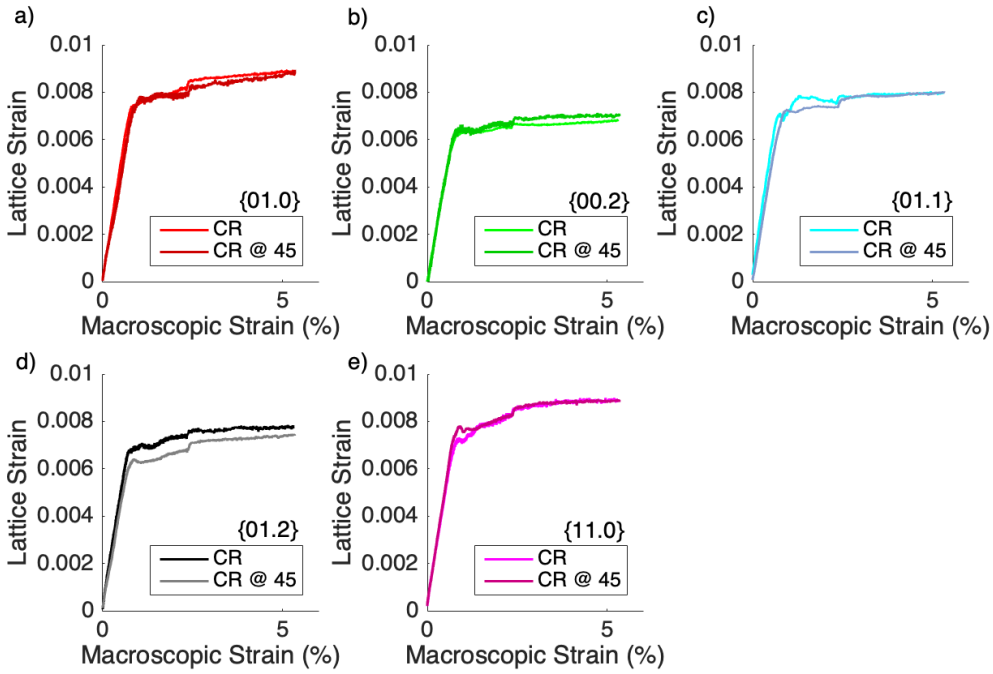


Figure 5.30: Lattice strain responses in the loading direction during the jump test, comparing the CR response in the rolling direction and at 45 degrees. Directions examined are normal to a) {01.0}, b) {00.2}, c) {01.1}, d) {01.2} and e) {11.0}.

Of particular interest is the region immediately post yield where the non uniformity of the response is evident in the CR Ti-6Al-4V at 45 degrees. The magnitude and direction of these responses do not appear to be consistent between experiments or crystallographic directions. The {01.0}, {01.1} and {01.2} directions in Figure 5.28 show differing behaviour in the loading and 45 degrees but both directions tend towards the same values at around 2.5% engineering strain. This may explain the increased variation in strength of the CR material in directions not aligned with the rolling direction.

For the higher strain rate, Figure 5.29, the 'dips' are more pronounced, occurring in multiple crystallographic orientations. the jump conditions show the least variation with both responses having fairly variable results. Post-jump alignment is fairly high between the material under the SRJ, see Figure 5.30. It is not possible to distinguish whether this is due to the less varied initial response or if it is an effect of the SRJ. Examining the transverse directions may allow greater insight into these 'dips'. Figures 5.31 to 5.33 show the crystallographic responses in the transverse direction, as many inconsistencies are observed, no established conclusions can be drawn from this data.

The effective moduli has been compared for all directions in Table 5.8, showing some consistency in the results of particular directions where the {11.0} and {01.1} directions are stronger in the loading and at 45 degrees respectively. The average response from slower and jump tests has been normalised for each material form, the results of which are given in Table 5.9. Ideally, an increased number of experiments would be performed to increase the accuracy of these results to ensure differences are statistically significant.

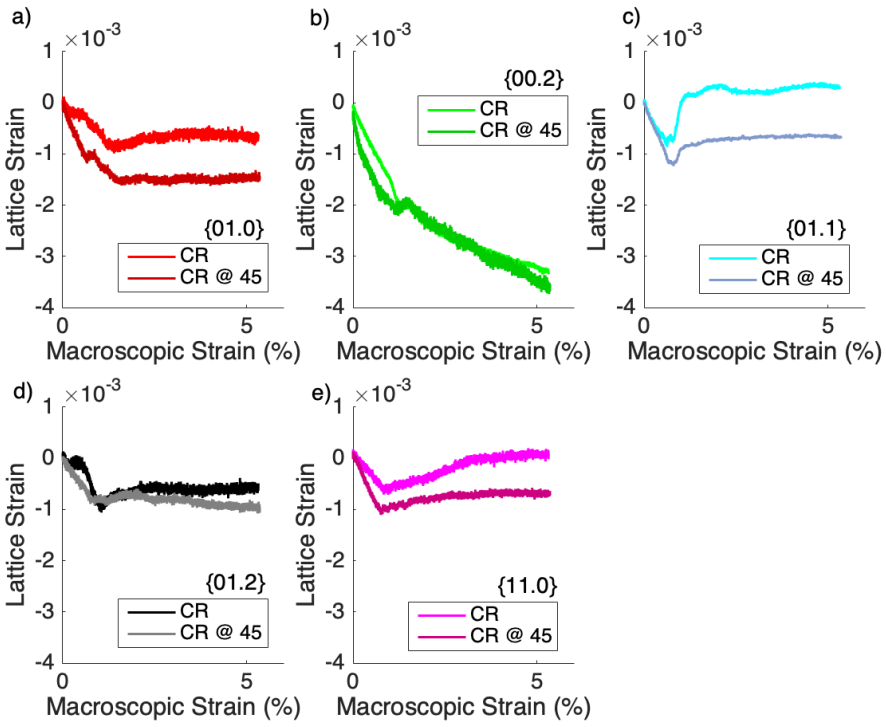


Figure 5.31: Lattice strain responses in the transverse direction for strain rate of 10^{-4} s^{-1}, comparing the CR response in the rolling direction and at 45 degrees. Directions examined are normal to a) {01.0}, b) {00.2}, c) {01.1}, d) {01.2 },and e) {11.0}.

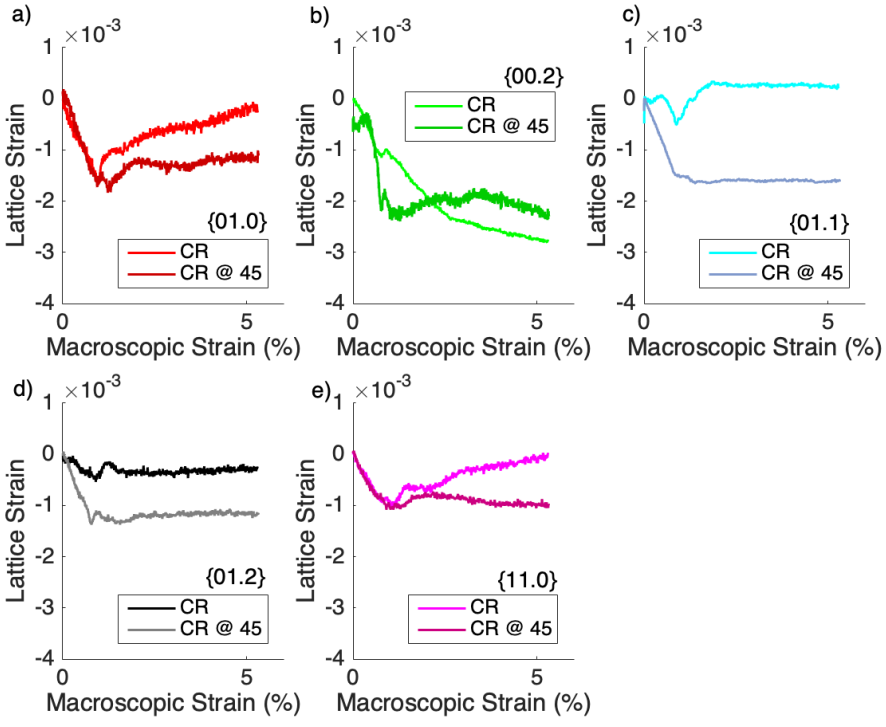


Figure 5.32: Lattice strain responses in the transverse direction for the higher strain rate of 10^{-3} s^{-1}, comparing the CR response in the rolling direction and at 45 degrees. Directions examined are normal to a) {01.0}, b) {00.2}, c) {01.1}, d) {01.2 },and e) {11.0}.

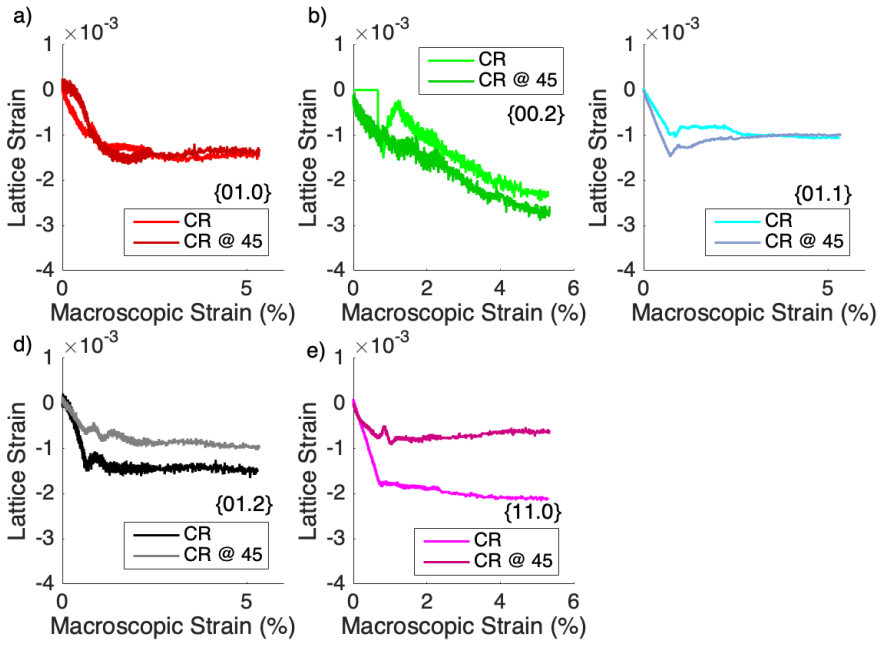


Figure 5.33: Lattice strain responses in the transverse direction during the SRJ, comparing the CR response in the rolling direction and at 45 degrees. Directions examined are normal to a) {01.0}, b) {00.2}, c) {01.1}, d) {01.2 },and e) {11.0}.

Table 5.8: Effective moduli calculated for all experiments where the slow, jump and fast results are compared for CR in the loading direction and at 45 degrees.

Material	Direction	Slow (10^{-4} s^{-1})	Jump	Fast (10^{-3} s^{-1})
CR (RD)	{01.0}	117.33	118.70	118.67
	{00.2}	131.48	132.72	119.14
	{01.1}	100.14	110.65	n/a
	{01.2}	139.84	123.58	122.95
	{11.0}	116.24	114.91	111.64
CR (45 degrees)	{01.0}	112.57	117.43	114.61
	{00.2}	134.79	129.73	148.34
	{01.1}	120.37	108.19	110.40
	{01.2}	134.38	124.26	127.71
	{11.0}	99.24	111.59	108.34

Table 5.9: Normalised effective moduli calculated for CR in the loading direction and at 45 degrees, combined slower and SRJ results.

hkil	CR - RD	CR - 45 degrees
{01.0}	1.12	1.09
{00.2}	1.25	1.25
{01.1}	1.00	1.08
{01.2}	1.25	1.23
{11.0}	1.10	1.00

From the results presented, it is evident that the macroscopic stress is reduced when loading is applied at 45 degrees to the rolling direction. The cross rolled material contains regions of reduced grain sizes. Variation in both the macroscopic and lattice strain response is greater for the 45 degree specimens, making it more difficult to accurately predict lattice strain response. An effective moduli for each direction is calculated, showing the similarities between the material. Differences observed are in the {01.1} and {11.0} directions where the opposite response is observed in each. The {01.1} direction is stronger when 45 degrees is aligned with the loading direction and the {11.0} is stronger where the rolling and loading directions are coincident.

5.5 Strain Rate Sensitivity

Strain rate sensiitivtiy is examined in this section. Experimental loading conditions are generally grouped depending on loading rate, either as low, quasi-static or higher, dynamic loading rates. The stress-strain response of a material under quasi-static loading differs from that at dynamic loading rates, likely due to the different speed of activation of the deformation mechanisms [148, 232]. SRS gradually decreases during plastic deformation for quasi-static loading regimes.

The SRS as defined previously in Section 4.1.3, where $\dot{\epsilon_1}$ and $\dot{\epsilon_2}$ are the prescibed strain rates and σ_1 and σ_2 are the stresses either at the same point in tests at 2 strain rates or immediately before and after a SRJ. A meaningful rate sensitivity exponent is devised from experiments in an attempt to capture the behaviour of Ti-6Al-4V at multiple strain rates [75]. Deformation in titanium alloys is generally more anisotropic (both elastically and plastically) at the grain scale than other non-HCP alloys [82], and it is therefore thought that the strain rate sensitivity is likely to differ with respect to grain orientations and the corresponding slip systems. The intrinsic anisotropy of strain rate sensitivity in single crystal α titanium has been outlined by Zhang et al [231]. This study has important considerations for the current work, particularly in dealing with the validity of determining a single strain rate sensitivity parameter for a material.

For quasi-static loading, as the strain rate increases, strength is seen to increase at the expense of reduced ductility [232]. The quasi-static and dynamic loading responses have been combined with constitutive modelling for titanium alloys [103], and the deformation mechanisms in Ti-6Al-4V have been identified for low

and high strain rates [42]. Povolo [164] recommends a strain rate jump test to extract the m parameter. In situ mechanical strain rate sensitivity techniques for miniature displacement controlled tensile experiments are compared. This study suggests that the techniques compared herein can be reliably and interchangeably used to measure the SRS accurately in a wide variety of materials [211]. Nano-indentation techniques, such as those performed by Jun et al [95], are also used to investigate SRS. However, for materials with high mechanical anisotropy, the nano-indentation techniques tend to underestimate the magnitude of the materials anisotropy [211].

The strain rate jump test is used to extract the strain rate sensitivity of a material [164]. The constant strain rate method (CRSM) has also been employed in this section. Tables 5.10 and 5.11 compare the stresses used to calculate the SRS for each method showing negligible difference in whether single or averaged values are used for the CRSM method. The results of both methods are compared in Table 5.12, where the calculated SRS parameter is very different depending on the method used.

Table 5.10: Comparison between stresses found at 3% engineering strain (top) and averaged between 2.5% and 3.5% engineering strain (bottom), for all materials investigated at constant strain rates of 10^{-4} s^{-1} (lower) and 10^{-3} s^{-1} (higher).

Material	Stress at 3% (Slow)	Stress at 3% (Fast)	Difference	%
UDR (Rolling)	861.7 MPa	905.4 MPa	43.7 MPa	5.07 %
CR (Rolling)	939.4 MPa	973.1 MPa	33.7 MPa	3.59 %
CR (45 deg)	894.5 MPa	933.4 MPa	38.9 MPa	4.35 %
Billet (Radial)	862.5 MPa	891.2 MPa	28.7 MPa	3.33 %
UDR (Rolling)	860.8 MPa	902.5 MPa	41.7 MPa	4.84 %
CR (Rolling)	934.7 MPa	968.8 MPa	31.4 MPa	3.36 %
CR (45 deg)	891.8 MPa	930.3 MPa	38.5 MPa	4.32 %
Billet (Radial)	858.7 MPa	890.2 MPa	31.5 MPa	3.54 %

Table 5.11: Comparison between stresses found at before and after the jump in strain rate, at 2.34% and 2.50% respectively.

Material	Stress prior (2.3%)	Stress after (2.50%)	Difference	%
UDR (Rolling)	883.9 MPa	915.2 MPa	31.3 MPa	3.54 %
CR (Rolling)	935.2 MPa	971.0 MPa	35.8 MPa	3.83 %
CR (45 deg)	878.8 MPa	909.9 MPa	31.1 MPa	3.54 %
Billet (Radial)	862.0 MPa	895.3 MPa	33.3 MPa	3.86 %

Table 5.12: Strain rate sensitivity for each Ti-6Al-4V product form using Equation 7.1 to calculate SRS via the strain rate jump test and constant strain rate method.

Material	SRJ Method	CSR Method
UDR	0.015113	0.02055
CR	0.016315	0.01556
CR (45°)	0.015104	0.01836
Billet	0.016461	0.015925

The slower (10^{-4} s^{-1}) test for the UDR material has been affected by slippage therefore the values for UDR CSRM are likely to be lower than expected, so caution is advised when considering these results.

SRS values for the billet and CR material are similar in both constant strain rate and SRJ methods, however, these methods yield fairly different results, where the strain rate jump results are lower. However the result of the SRJ method is higher for the CR material at 45 degrees. The results of the strain rate jump are cited as being more accurate [164]. There is less variation in terms of microstructural differences using this method, therefore these results have been used to inform material models in future chapters.

5.5.1 Lattice Strain Rate Sensitivity

The strain rate sensitivity may be related to the microstructure. It is hypothesized that strain rate sensitivity at the macroscopic level differs from that microscopically [95]. To analyse this, the difference in lattice strain for each crystallographic direction during the SRJ tests is detailed in Table 5.13 for all product forms. The increase in each direction is compared with an increase in macroscopic stress of 32.3 (3.66%), 33.8 (3.61%) and 32.9 MPa (3.75%) for the UDR, CR and CR at 45 degrees respectively.

Table 5.13: Difference between lattice strain before and after the SRJ. Lattice strain is captured at 2.3 and 2.5% engineering strain (in the sample) for all tests

	HKL	**UDR (Rolling)**	**CR (Rolling)**	**CR (at 45 deg)**	
Increase in lattice strain (x 10^{-4})	{01.0}	3.77 (4.35%)	1.93 (2.30%)	3.77 (4.76%)	x 10^{-4}
	{00.2}	2.72 (3.73%)	2.88 (4.23%)	2.50 (3.63%)	
	{01.1}	2.54 (2.99%)	1.85 (1.99%)	2.98 (4.00%)	
	{01.2}	2.71 (3.62%)	2.50 (3.09%)	32.92 (4.30%)	
	{11.0}	3.91 (4.38%)	3.59 (4.14%)	3.71 (4.50%)	

5.6 UDR Initial Behaviour

For the UDR material, in the elastic regime, a non-linear response for the lattice strain evolution was observed for some directions pre-yield. As these lattice strain responses are captured at the same time from the same material specimen and the effect happens at different times during the deformation, this is unlikely to be an artefact of signal interference. Data has been extracted from the slow strain rate test on UDR material, which has not been considered previously due to slippage, however, as this slip occurred post-yield, this may be safely analysed. The {01.0} and {00.2} directions show this behaviour most prominently, Figure 5.34. A straight line has been fitted to the data and the residuals are plotted emphasising the wave-like response. This unexpected result is only evident in the UDR material in the directions shown.

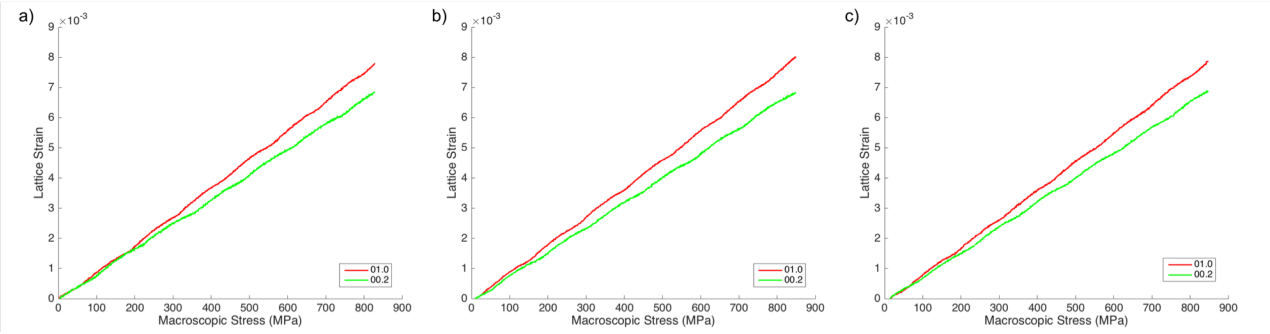


Figure 5.34: Pre-yield lattice strain response normal to the {01.0} and {00.2} directions from three experiments with the same initial loading conditions, where a) is the results of the slower strain rate test, b) is the jump at 3% and c) is the jump at 1.5% engineering strain.

Chapter 6

Crystal Plasticity Finite Element Method

The development of predictive modelling capabilities is improved alongside experimental characterisation abilities [55]. This combined approach informs structure-property relationships. The addition of computational studies alongside more expensive experimental procedures has greatly increased the ability to analyse and predict material behaviour. This section details the computational simulations of the current body of work and details of the initial parameter studies. Computational modelling is of significant benefit here as experiments are limited in terms of access and therefore this repeatability is low. CPFEM has been chosen as it allows examination of individual grains and this will provide the best comparison to the experiments performed, particularly in terms of lattice strain accumulation.

6.1 Building Representative Models

Computational modelling of in situ high energy XRD experiments is complex. To predict the behaviour at multiple length scales, representative material parameters, sufficient grain number and distribution and appropriate boundary conditions are required.

A representative volume element, RVE, is a sample of material that captures the overall bulk material. Here this has been simulated with a variety of grain and element distributions to accurately determine the minimum RVE. To accurately determine the RVE, instantiated polycrystals are tested via displacement control to 5.5% engineering strain to compare with experimental results and ensure the bulk response is accurate.

6.1.1 Pre-processing - Mesh Instantiation & Visualisation

Finite element meshes are instantiated in the software (Neper) at the crystal scale [169]. Neper generates tessellations and meshes these tessellations in an unstructured way. Optimisation of the mesh is then performed to ensure a high quality resultant mesh. Various algorithms and combinations are available with Praxis used in this work. Praxis is a library which minimises a scalar function of a vector argument, without requiring information of the derivative [25]. The method for smoothing the interface meshes, which are reconstructed from raster tessellations, is Laplacian smoothing [185]; an iterative method that modifies the node coordinates using the coordinates of the neighbouring nodes. Neper is particularly well suited to statistical and synchrotron XRD data applications [170]. These experiments allow systematic investigation of the influence of the microstructure on the mechanical properties.

The element type used are 10-noded tetrahedral elements. These are required to allow integration of the FE mesh into FEpX. Image files may also be visualised using Neper, however Paraview [2] has been utilised as the main visualisation tool, as it allows various data sets to be plotted in either 2D or 3D. It's ability to overlay results and optimise parameters allows for effective visual comparison.

6.1.2 Initial Parameter Studies

Initial computational parameter studies have been performed to ensure accurate modelling of the materials involved. Analysis of different grain element densities has been performed to ensure representative volume elements of the bulk polycrystalline material are used. The number of grains included in the sample volume is significant and impacts the overall response. Polycrystalline aggregates of 100, 500 and 3,000 grains are generated using Voroni tessellations, as in Figure 6.1. The grain orientation and plastic strain distribution are shown for a 2D section of the meshes in Figure 6.2 where the deformed polycrystals show the plastic strain within the grains at 6% engineering strain overall.

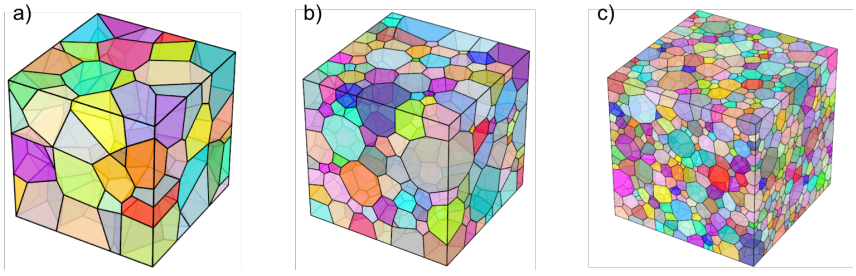


Figure 6.1: Polycrystal instantiations with a) 100, b) 500 and c) 3,000 grains, with all other parameters held constant. Colours are simply used to identify individual grains.

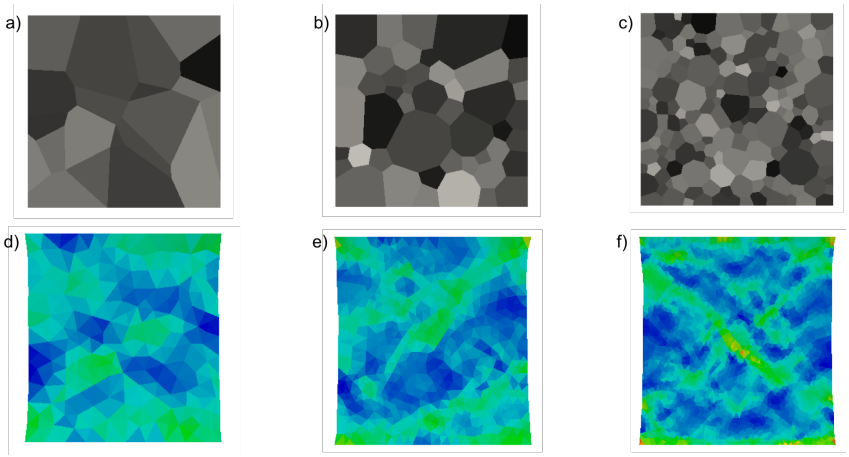


Figure 6.2: Slices through the center of the polycrystal meshes, where a) - c) show the initial grain orientation (greyscale) and d) - f) show the deformed shape with accumulated plastic strain at 6% engineering strain for a constant strain of 10^{-3} s^{-1} (coloured). All images have been uniformly scaled for comparison, showing the distribution of plastic strain for d) the 100, e) the 500 and f) the 3,000 grain instantiations.

Increasing the number of grains leads to an increased number of elements in the analysis, where the average number of elements per grain is consistent. This leads to increased simulation times, this should be balanced to ensure representative microstructures with appropriate simulation durations. The polycrystals contain 13,365 elements (100 grains), 64,000 elements (500 grains) and 390,928 elements (3,000 grains) leading to combined durations for instantiation, meshing and simulation of approximately 20 minutes, 2 hours (118 minutes) and 1.5 days (1,841 minutes) on the current computational setup for 100, 500 and 3,000 grains respectively. The simulations have been performed on a computing cluster which has 2 x XeonGold 6132-2.6 GHz-14-core machines with 28 threads, 9.25MB cache and 12 x 16 GB DDR4 2666 MHz. Testing indicates 16 cores per simulation results in optimal computation times.

Each of the defined instantiations is subject to uniaxial tensile conditions. FEpX has been used to replicate the constant strain rate experiments as performed on in situ specimens previously, see Section 3.1. The macroscopic stress-strain results are shown in Figure 6.3 where the yield stresses are summarised in Table 6.1. Significant differences in the results for the different strain rates are evident with the yield stress increasing with the higher strain rate as expected.

The 100, 500 and 3,000 grain instantiations are all deemed to have random orientations, which ensures there is no defined texture, thus the differences are primarily due to number of grains. The highest yield stresses are observed in the 100 grain simulations, this is lower in the 500 case and the 3,000 grain simulation lies between these results, see Table 6.1. The difference in yield stress between the lower and higher strain rates is consistent despite the different grain counts used.

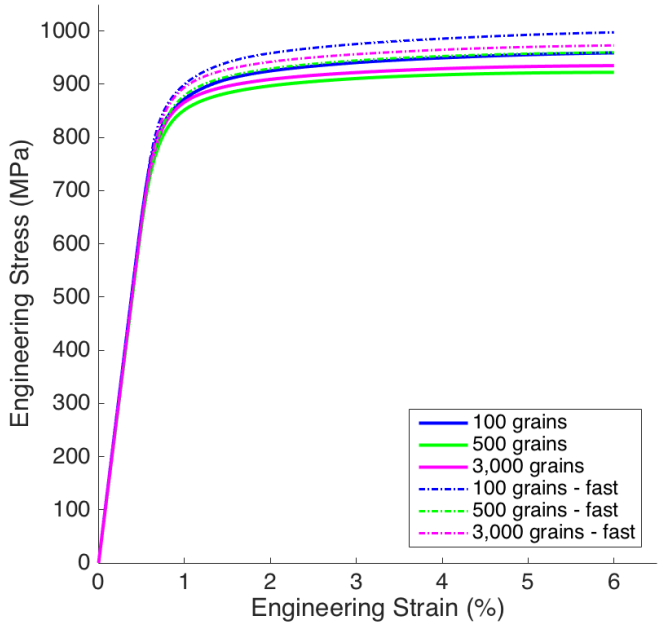


Figure 6.3: Macroscopic stress-strain response extracted from simulated polycrystals with 100, 500 and 3,000 grains at both strain rates, 10^{-4} (solid) and 10^{-3} s^{-1}) (dashed).

Table 6.1: Yield stresses extracted from Figure 6.3 for the lower (10^{-4} s^{-1}) and higher strain rates (10^{-3} s^{-1}).

No. of Grains	**Yield Stress (10^{-4} s^{-1})**	**Yield Stress (10^{-3} s^{-1})**
100	825.1 MPa	846.8 MPa
500	803.2 MPa	823.4 MPa
3,000	818.6 MPa	839.1 MPa

Of particular interest is the lattice strain evolution. This has been extracted from the simulations via the post processing of the FEpX results. A defined incident beam angle is compared to the crystallographic orientation of each element, the elements which meet the Bragg diffraction conditions and are within the angular region of interest are stored, this region is equivalent to the azimuthal bin size experimentally. The elastic strain in these elements is then projected onto the crystal,and the resultant lattice strain measured. The list of hkls to be investigated is cycled through and all of the contributions to the particular crystallographic direction are summed. This is repeated for each time step in the experiment, allowing the evolution of the lattice strain to be plotted.

Differences in the lattice strain response are small between the 100, 500 and 3,000 grain instantiations (Figure 6.4). The increased number of grains should provide a more accurate response to the bulk material. Additionally, lattice strain data is only extracted at increments of 1% engineering strain during this analysis for comparison. In increasing the resolution of these results, as is required in subsequent sections, the computational time increases significantly.

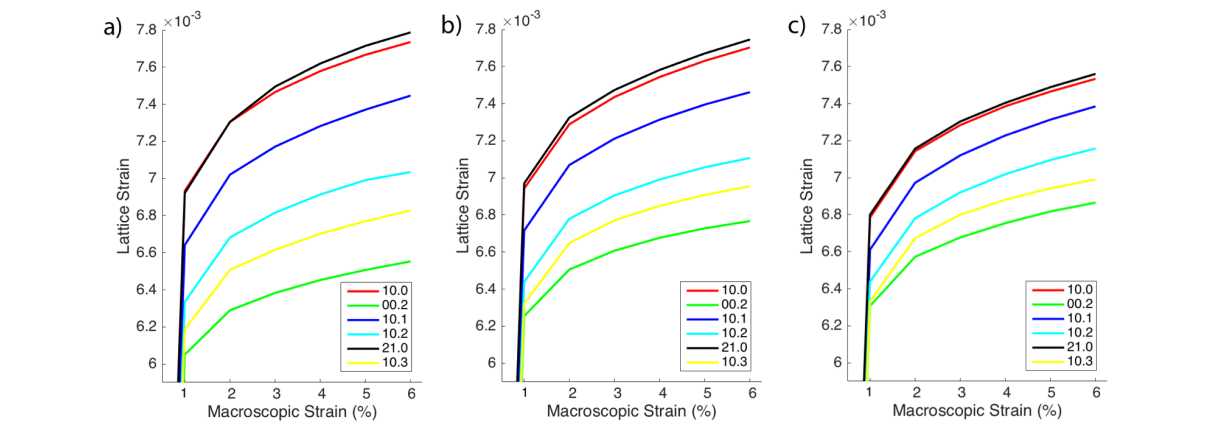


Figure 6.4: Lattice strain response extracted from the constant strain rate experiment (10^{-3} s^{-1}) for a) 100, b) 500 and c) 3,000 grain instantiations.

Lattice strains are compared to experiments, where the average experimental lattice strain has been calculated from the different Ti-6Al-4V product types discussed previously. The deviation from the experimental lattice strain response in the {10.0} direction is determined for each instantiation as

$$e = \left[\int_0^{5.5} \left[(\epsilon_{latt} - \epsilon_{latt_{exp}})\right]^2 d\epsilon\right]^{\frac{1}{2}} \tag{6.1}$$

where ϵ_{latt} is the predicted response from the simulation and $\epsilon_{latt_{exp}}$ is the experimentally determined response. The normalised error is defined by

$$e_{norm} = \frac{\left[\int_0^{5.5} \left[(\epsilon_{latt} - \epsilon_{latt_{exp}})\right]^2 d\epsilon\right]^{\frac{1}{2}}}{\left[\int_0^{5.5} \left[\epsilon_{latt_{exp}}\right]^2 d\epsilon\right]^{\frac{1}{2}}} \tag{6.2}$$

where the error may be expressed as a percentage.

The error e, is calculated as 0.00553 (13.9%) for the 100 grain, 0.00551 (13.8%) for the 500 grain and 0.00484 (12.1%) for 3,000 grain instantiations in the {01.0} direction. The 3,000 grain instantiation is closest to the experimental values showing that this lattice strain response better fits the experimental data as expected.

6.1.3 Boundary Conditions

The effect of the BCs has been studied with a 1,500 grain polycrystal under identical loading conditions as due to the size of the experimental specimens, the loading is not purely uniaxial thus both symmetric and gripped BCs fairly represent the actual physical material state during deformation.

The symmetric boundary conditions (BCs) are employed to replicate the loading conditions and will impose a uniform stress state. The imposition of symmetry conditions constrains the cube where each of the faces with normals in the negative directions have zero velocity in the direction normal to the respective face. This allows fairly consistent stress across the material, replicating the uniform stress state observed experimentally.

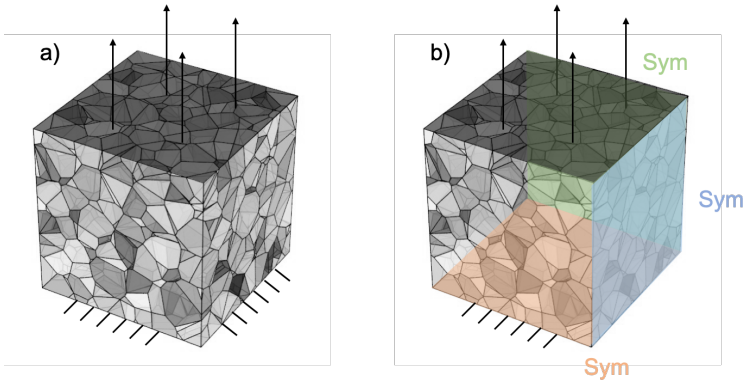


Figure 6.5: Representation of both grip and symmetric boundary conditions used in this section.

Alternative 'gripped' boundary conditions have also been employed. Here, the cube is held fixed in the -Z plane and the load is applied in the Z direction. Both conditions suppress rigid body translation and rotation. A visualisation of both of these boundary conditions is given in Figure 6.5 where the stresses accumulated at the corners are significant for the grip BCs. The resulting macroscopic and lattice strain responses are compared in Figures 6.6 and 6.7.

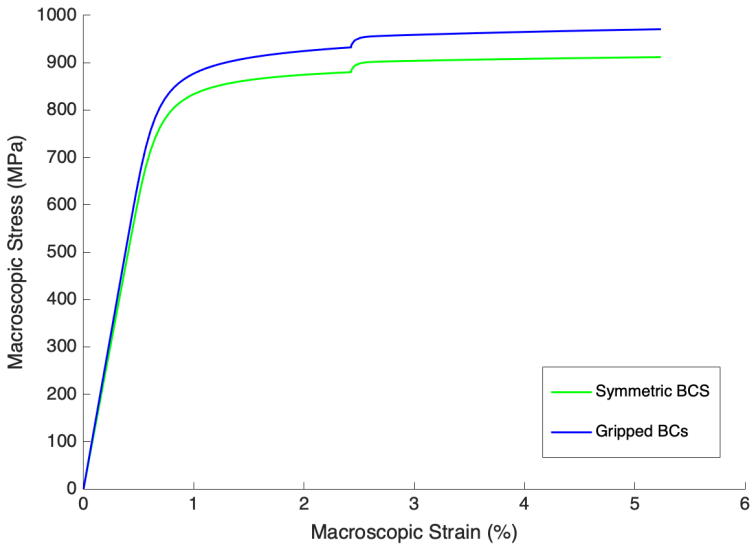


Figure 6.6: Macroscopic stress-strain response of both grip and symmetric boundary conditions used in this section.

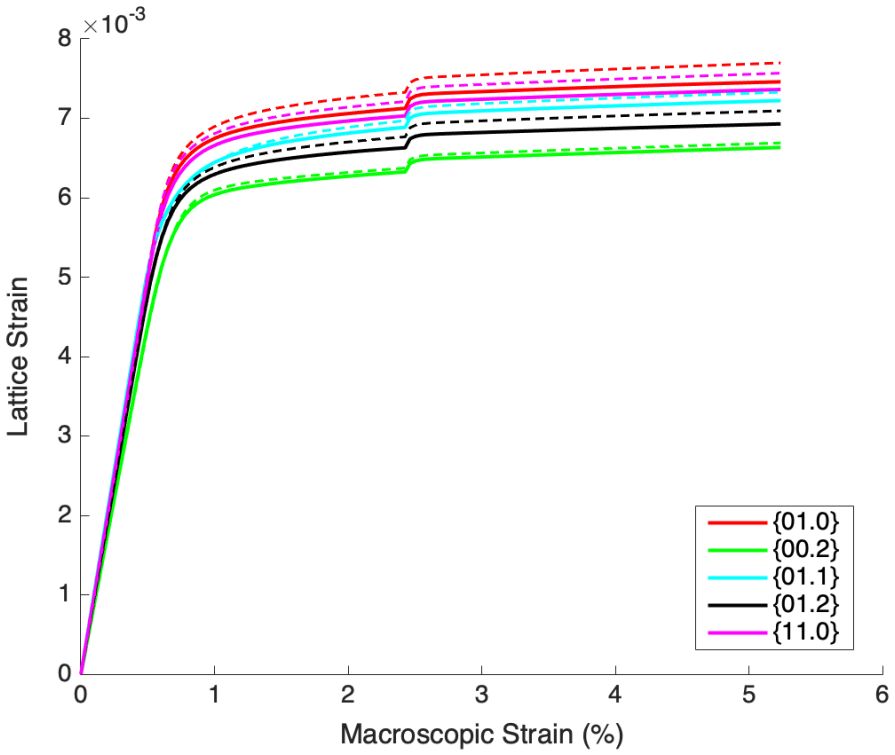


Figure 6.7: Lattice strain response for grip (solid) and symmetric (dashed) BCs.

The strain, σ_{zz}, is seen to be fairly evenly distributed under the symmetric boundary conditions, Figures 6.8 and 6.9, whereas the effects at the corners of the 'gripped' conditions are much greater. This is likely an artefact of the visualisations as small differences next to the constrained surface will appear exaggerated.

Figure 6.9 shows the accumulated stresses in the centre of the material via a 2D slice, where again a more even distribution is observed with the symmetric BCs. The macroscopic yield stresses are found to be 805.9 MPa and 857.5 MPa for the symmetric and grip BCs with the increase in stress during the jump calculated as 19.8 MPa and 18.6 MPa respectively.

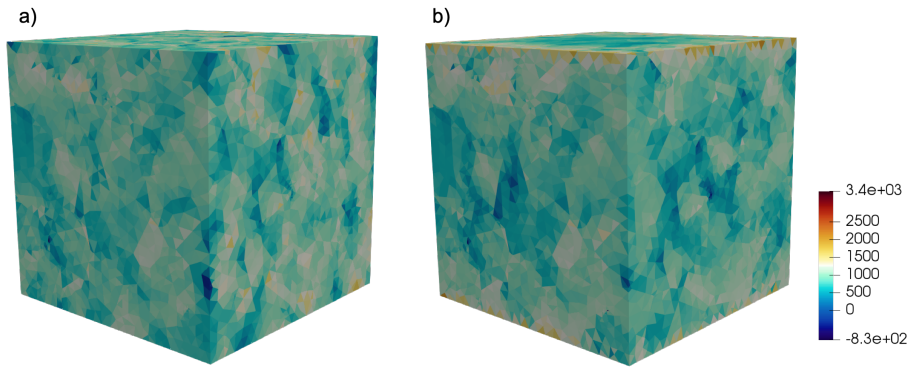


Figure 6.8: Surface representation of σ_{zz} Cauchy stress at 5% engineering strain for a) the symmetric and b) the grip boundary conditions.

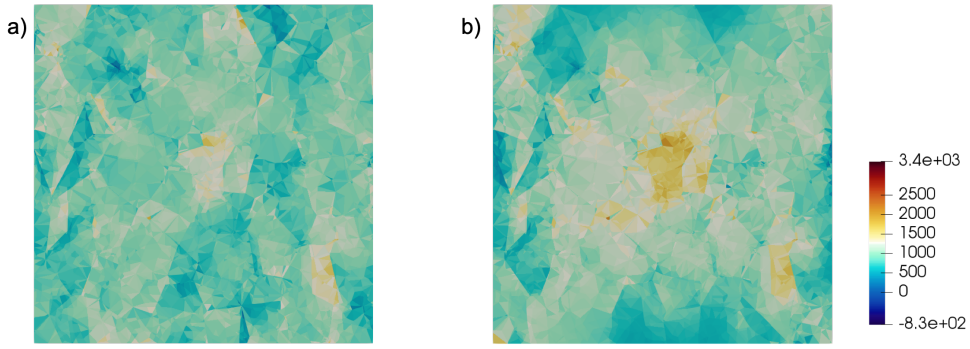


Figure 6.9: Slice through the centre of the microstructure showing the σ_{zz} Cauchy stress at 5% engineering strain for a) the symmetric and b) the grip boundary conditions.

The grip conditions cause regions where stress will not accumulate in the vicinity of the constrained faces, these are prominent in the visualisations. The effect of these areas on the results must be considered. The strains in the central regions of both polycrystals are not only of differing magnitudes but the distribution is also different, therefore leading to dissimilar lattice strain responses.

Table 6.2: Predicted lattice strains at yield for both boundary conditions, where the entire volumes are included in the lattice strain calculations.

Condition	**{01.0}**	**{00.2}**	**{01.1}**	**{01.2}**	**{11.0}**
Grip BCs	0.006863	0.006126	0.006580	0.006400	0.006776
Symmetric BCs	0.007030	0.006181	0.006608	0.006580	0.006930

6.1.4 Mesh Convergence

With FE modelling, a finer mesh typically improves the solution accuracy, however, this increases computational time significantly. To adequately balance time and accuracy, a mesh convergence study is performed where 500 grain RVE is considered. The number of elements per grain is increased to assess convergence. A single crystal extracted from the 500 grain aggregate is shown with differing mesh densities in Figure 6.10. Identical loading conditions have been imposed on polycrystals of various grain counts. The macroscopic and lattice strain responses are compared for various element densities for 100 grain instantiations in Table 6.3.

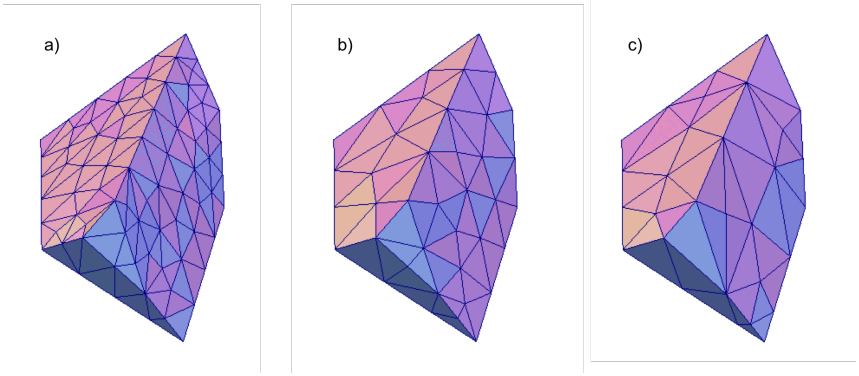


Figure 6.10: Single grain extracted from meshes used in convergence studies showing the surface mesh of, on average a) 438 elements per grain, b) 133 elements per grain and c) 72 elements per grain.

Table 6.3: Mesh convergence study for the number of elements per grain for 100 grain polycrystal.

Average number of elements per grain	Macroscopic stress at 1% engineering strain	Lattice strain normal to the {01.1} direction at 1% engineering strain
438	860.1 MPa	0.006614
284	863.2 MPa	0.006680
200	868.4 MPa	0.006602
134	872.1 MPa	0.006784
100	872.1 MPa	0.006719
73	876.5 MPa	0.006762

Table 6.4: Mesh convergence study for the number of elements per grain for 500 (left) and 1,500 grain polycrystals (right).

Average number of elements per grain	Macroscopic stress at 1% engineering strain	Average number of elements per grain	Macroscopic stress at 1% engineering strain
437	851.8 MPa	402	851.3 MPa
290	855.6 MPa	288	857.5 MPa
206	858.7 MPa	181	854.8 MPa
132	859.3 MPa	109	859.3 MPa
98	861.4 MPa	80	860.7 MPa
78	861.4 MPa	66	862.3 MPa

500 and 1,500 grain instantiations with different element densities are also considered, see Table 6.4, where the same tessellated grains are used in each case. The responses for all three cases are compared in Figure 6.11 where the mesh convergence is evident in simulations with over 1,500 grains.

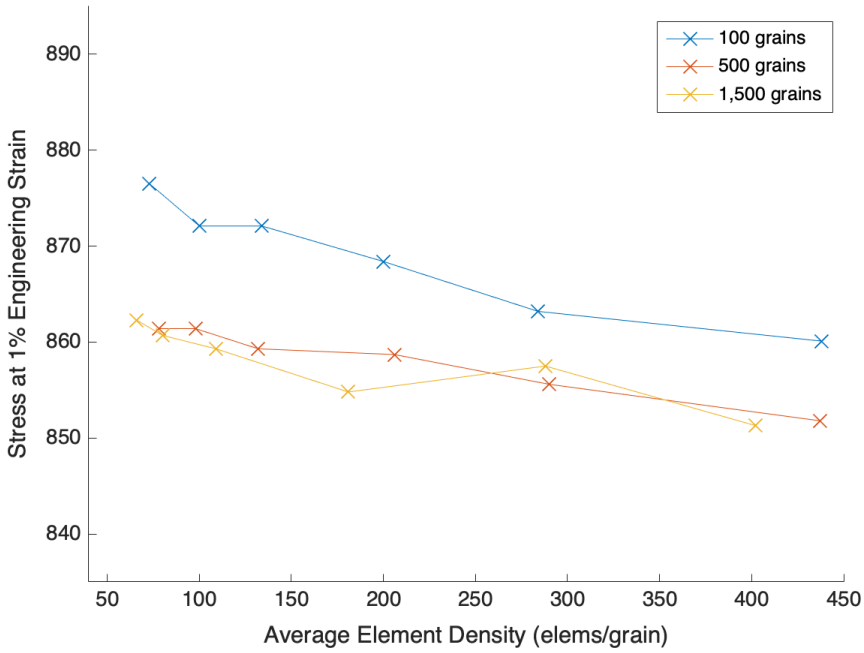


Figure 6.11: Comparison of convergence studies for 100, 500 and 1,500 grains with increasing element densities.

Table 6.5: Mesh convergence study for the total number of grains in the simulation.

Number of Grains	Time (to mesh)	Time (simulation)	Macrostress at 1% Eng Strain
100	3.5 minutes	16.5 minutes	871.8 MPa
500	22.4 minutes	110.4 minutes	863.3 MPa
1,500	96.8 minutes	594.3 minutes	859.8 MPa
3,000	282.8 minutes	1,294.7 minutes	862.8 MPa
5,000	340.7 minutes	2,065.6 minutes	864.5 MPa

It is evident that the computational time increases significantly with increasing grain count, see Table 6.5. Polycrystals with 3,000 grains will be used for the majority of the simulations to ensure sufficient bulk texture and lattice strain response. The actual simulation times are likely to increase from those in Table 6.5 as a higher level of data resolution will be used.

6.1.5 Elastic Constants

Modelling the elastic behaviour requires accurate elastic constants, see Section 2.6. Values for these elastic constants have been identified from the literature [183, 199, 214], and are summarised in Table 6.6. These are of similar magnitude and have negligible effect on both microscopic and macroscopic response, as shown in Figure 6.12. The elastic constants from Wielewski et al [214] are used henceforth.

Table 6.6: Elastic constant values obtained from literature, values in GPa.

Reference	C_{11}	C_{12}	C_{13}	C_{44}
Wielewski et al [214]	169	89	62	43
Shahba et al [183]	164.7	82.5	61.3	48.5
Tromans et al [199]	162.95	76.17	76.17	43.9

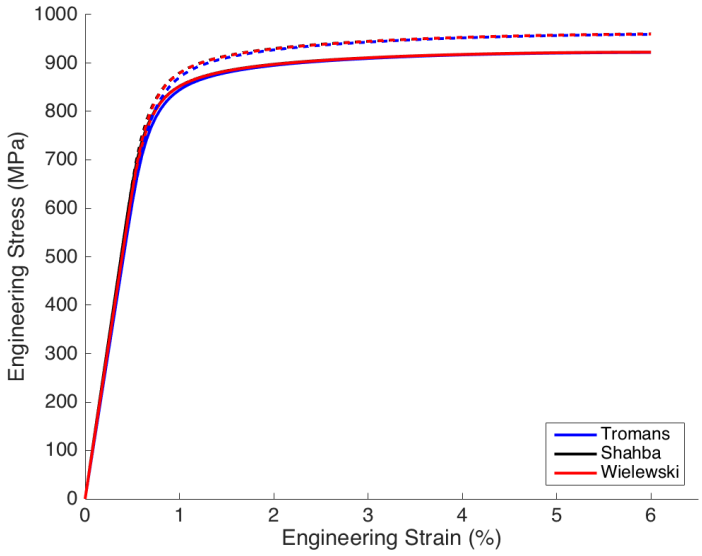


Figure 6.12: Macroscopic stress-strain response for a variety of elastic constants extracted from the literature, Tromans et al [199], Shahba et al [183] and Wielewski et al [214]. The response of 10^{-4} s^{-1} is represented by a solid line and 10^{-3} s^{-1} by a dashed line.

6.1.6 Slip System Strengths

Differences in the strength of different slip systems are evident in Ti-6Al-4V, see Section 2.2.0.1, where slip system strength ratios are used to define these strengths. Slip system strength ratios reported in the literature, namely 3, 1 [135] and 1.7, 1.2 [51] were compared macroscopically, via loading conditions of 10^{-4} s^{-1} in Figure 6.13. The ratios described represent the ratios of the strength of prismatic/basal, and pyramidal/basal slip systems respectively.

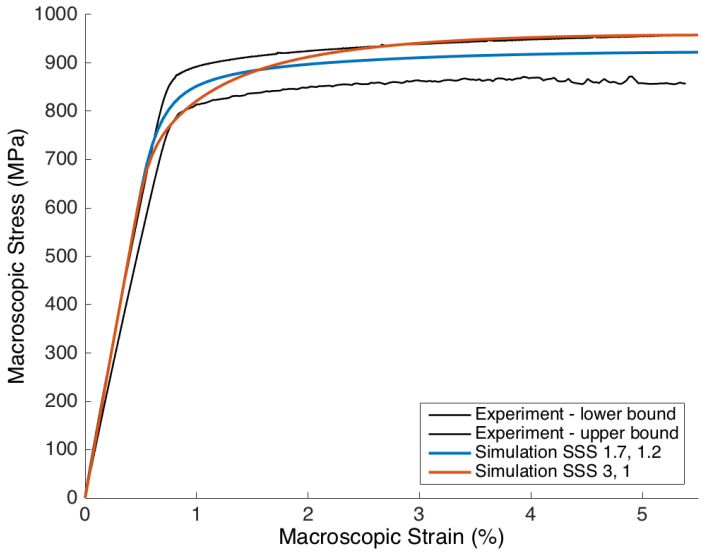


Figure 6.13: Macroscopic response, showing the different behaviour resulting from different slip system strength ratios at a constant strain rate of 10^{-4} s^{-1}, the maximum and minimum experimental results have been included for comparison.

Slip systems strength ratios affect the overall macroscopic response where, for ratios of (3,1), yield occurs at a lower stress but greater evolution is found between the yield point and 6% engineering strain. Macroscopic results of the (1.7,1.2) slip systems strength ratios better represent the observed experimental results.

The lattice strain responses are shown in Figure 6.14. The results of each direction are of similar values at yield for both ratios. However, evolution in the direction normal to the {00.2} direction is greatly increased in comparison. Slip system ratios as calculated by Dawson et al [51] (1.7,1.2) are deemed to be more accurate in mirroring the bulk response. The relative lattice strain values of the crystallographic directions are far more consistent with these ratios, better matching the experimental results observed previously (see Chapters 4 and 5).

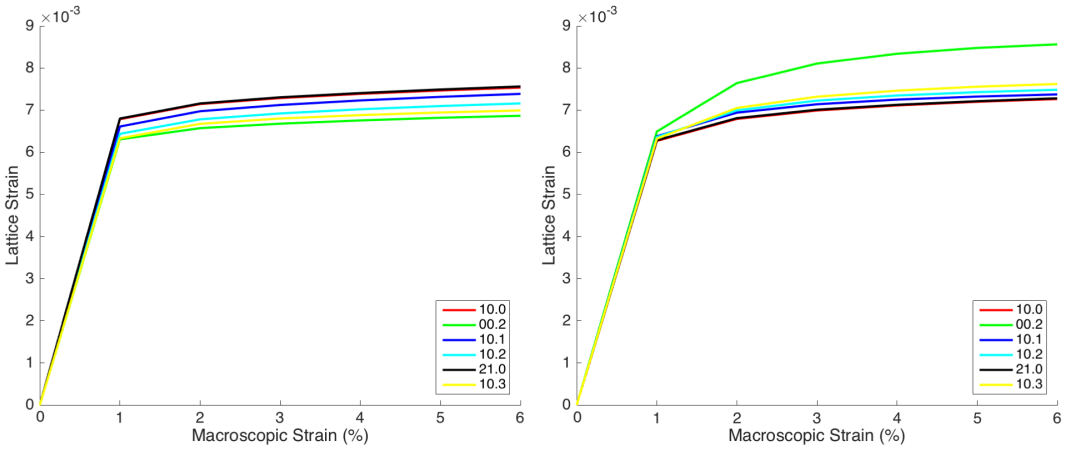


Figure 6.14: Lattice strain response of the simulations in Figure 6.13 for a variety of crystallographic directions, showing the impact of different slip systems strength ratios, a) (1.7,1.2) and b) (3,1) on the predicted lattice strain evolution.

Macroscopic and lattice strain response are sensitive to the SRS parameter m, but as the values obtained from experiments (Section 5.5) are of similar values, the average (0.015965) has been used in these initial parameter studies. However, the relevant SRS value m is employed in the subsequent analysis for each Ti-6Al-4V product form.

6.1.7 Randomised Microstructures

Variation in the results is likely to occur due to the different, randomly generated microstructures. To examine the effect of randomised microstructure with 500 grains on the overall response, three polycrystals have been instantiated, as shown in Figure 6.15 with the resulting yield stresses tabulated in Table 6.7. At 500 grains, there are still differences stemming from the instantiated grains, i.e. there are insufficient grains to average to obtain the same macroscopic bulk behaviour, see Figure 6.16. However, it is expected that an increased number of grains will adequately capture the bulk response and variation will be reduced. It is significantly more computationally expensive to generate multiple randomised instantiations of 3,000 grains therefore

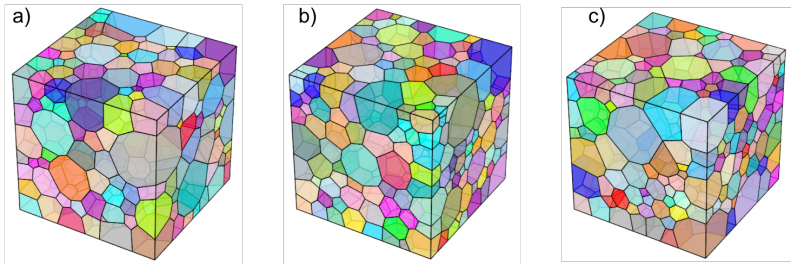


Figure 6.15: Three individual polycrystals with the same number of grains (500), the same distribution of grain sizes and grain sphericity are generated, the comparison of which highlights the effect of randomness due to the different grains and orientations in the instantiations.

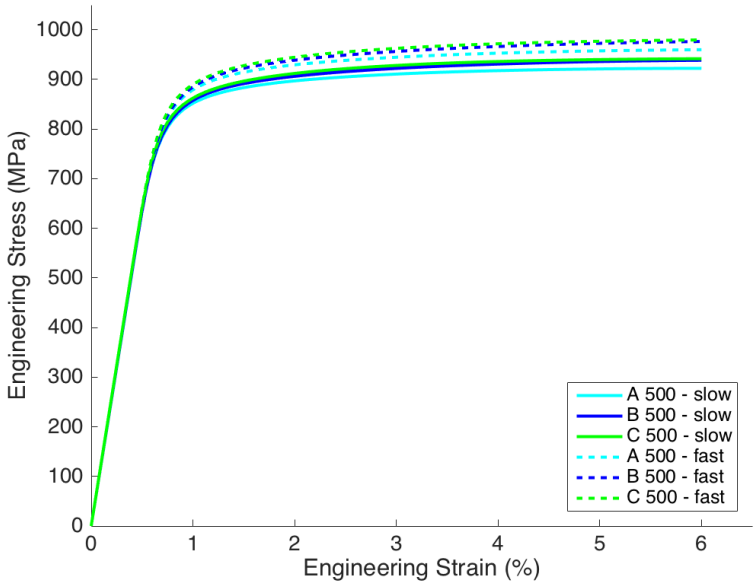


Figure 6.16: Macroscopic stress-strain response of 500 grain simulated polycrystals at strain rates of 10^{-4} s^{-1} and 10^{-3} s^{-1}.

Figure 6.16 shows the variability in the macroscopic response at 500 grains, whereas Figure 6.17 shows the effect on the lattice strain response in the loading direction where lattice strains have been extracted as previously described in Section 6.1.2. The macroscopic stress-strain behaviour appears to vary minimally, remaining within the vicinity of the results observed experimentally. Different crystal instantiations will naturally contain different textures thus the lattice strain response will differ slightly between instantiations.

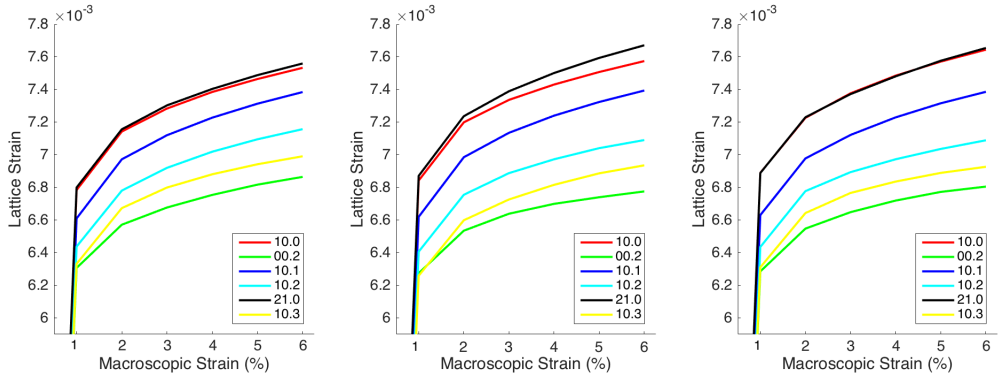


Figure 6.17: Lattice strain responses of the three different 500 grain instantiations, showing similar overall response despite the differing initial microstructures.

Table 6.7: Yield stresses observed from 500 grain simulations.

Simulation	10^{-4} s^{-1} (Lower)	10^{-3} s^{-1} (Higher)
A	845.5 MPa	872.0 MPa
B	851.0 MPa	877.3 MPa
C	855.9 MPa	882.6 MPa

Table 6.8 summarises the parameters usedfor these FE simulations. Values used in the instantiation and meshing of representative polycrystals are outlined, these have been sourced from a variety of works. The strain rate sensitivity vaules m, have been calculated in Section 5.5 from the a strain rate jump tests, where the mean value (0.015965) has been used for control in the initial parameter studies. The anisotropic elastic constants have been extracted from Wielewski et al [214], with strength hardening rate coefficient and the reference value of saturation strength from Kasemer et al [99]. The initial slip system strength has been extracted from [50] and the 1.7, 1.2 slip system strength ratios (hardness ratio) from [51].

Table 6.8: Summary of the parameters used in the FE model.

Material Parameter		Selected Value(s)
Elastic constants	(C_{11}, C_{12}, C_{13}, C_{44})	169.66, 88.66, 61.66,42.5 x 10^3 MPa
Strength hardening rate coefficient	(h_0)	190
Initial slip system strength	(g_0)	330 MPa
Reference value of saturation strength	(g_1)	530 MPa
Saturation strength rate scaling exponent	($\dot{\gamma}_s$)	0.01 s^{-1}
Exponent on the modified Voce hardening term	(n')	1
Saturation strength strain rate scaling coefficient		5 x 10^{10}
Slip system strength ratios (prismatic/basal, pyramidal/basal)		1.7, 1.2

6.2 Modelling Ti-6Al-4V

The overall computational modelling process is given in Figure 6.18. EBSD data is used to inform the tessellations, these are meshed and boundary conditions are imposed. This model is then input into FEpX with the appropriate material properties and loading conditions. The results of which are post-processed to obtain lattice strain evolution and these are compared to the experimental results.

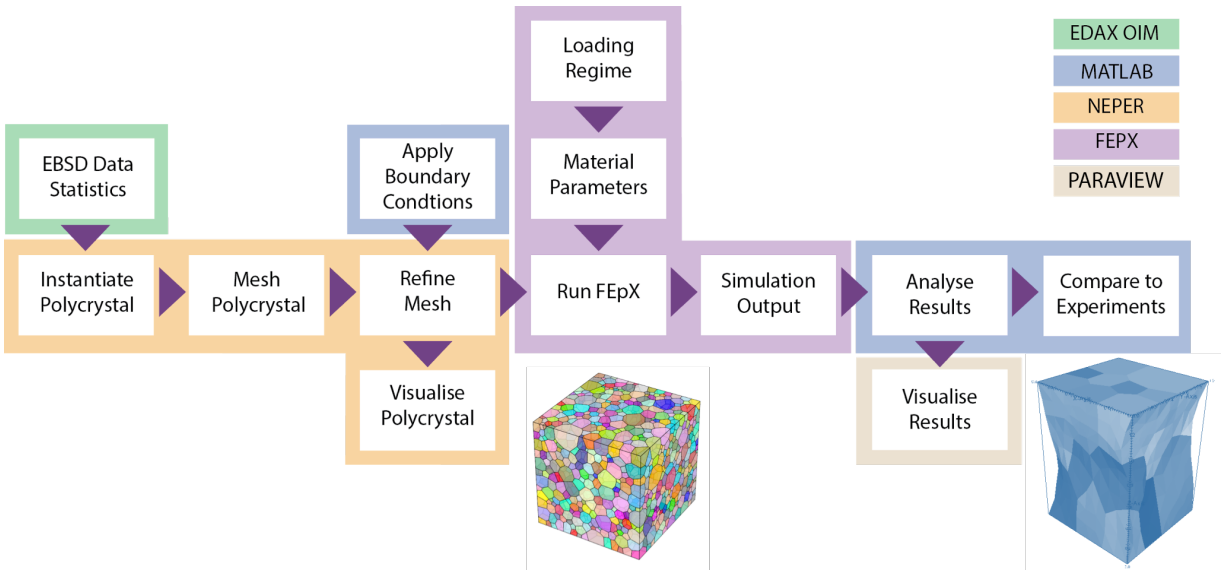


Figure 6.18: Flow chart example outlining the process from model instantiation to experimental comparison, coloured according to the relevant software used.

6.2.1 Product Forms

Texture

EBSD has been performed to quantitatively analyse the initial crystallographic textures, this also allows for polycrystals to be instantiated with representative textures. Each angle observed is included in the generation of the orientation distribution function, ODF. The IPF maps in Figure 6.19 show the crystallographic orientations in the centre of the gauge section, parallel to the loading direction. The differences in average grain size and the distribution of grain sizes are evident and must be considered in the computational simulations.

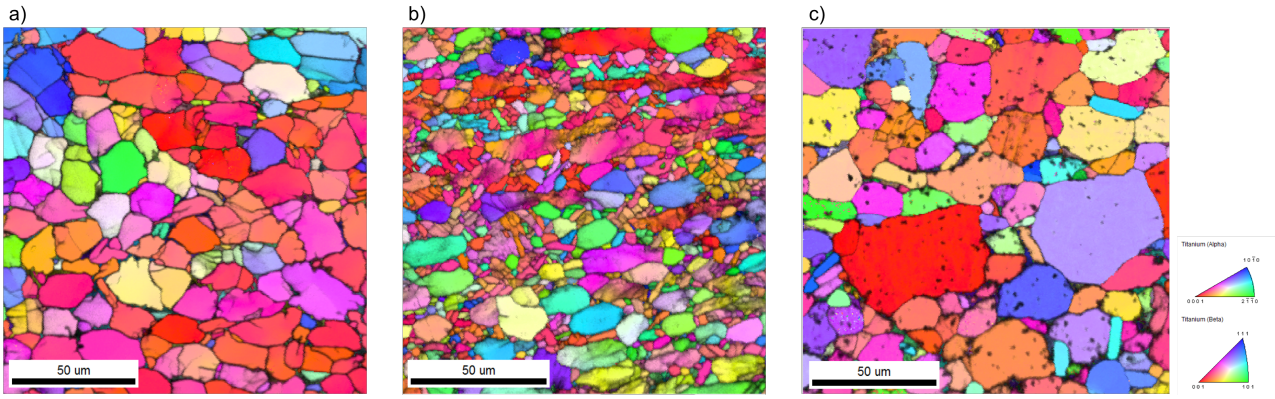


Figure 6.19: EBSD results of a) the billet, b) the UDR material and c) the CR Ti-6Al-4V, all in the undeformed, as-received state, highlighting the differences in the different product forms. All scale bars = 50μm.

Texture effects have been instantiated through the extraction of data from EBSD scan data, allowing the generation of ODFs which can be sampled to create multiple polycrystal instantiations with similar, representative crystallographic textures. The ODF-PF [48] package is used to achieve this. ODF-PF is a collection of Matlab functions which operates on both ODFs and PFs. It handles plotting of the ODF using Rodrigues parameters, plotting and evaluation of pole figures/inverse pole figures from ODF's, and it provides many tools for computing ODF's from pole figures. Using the ODF and microstructure, the anisotropic properties of a polycrystal can be predicted. The ODFs for billet, CR and UDR materials are shown in Figure 6.20 (in Rodrigues Space). Grain size and sphericity have been implemented in the instantiation via the inclusion of the log-normal distribution function of each of these, see Table 6.9.

Table 6.9: Data extracted from EBSD scans, the combination of these and .ang files, also from EBSD are used to accurately model a variety of Ti-6Al-4V product forms.

Material	Sphericity	Std Dev	Avg Grain Size (diameter)	Std Dev
Billet	0.476	0.177	19.07 μm	9.29
UDR	0.500	0.153	10.37 μm	7.06
CR	0.585	0.145	18.28 μm	9.32

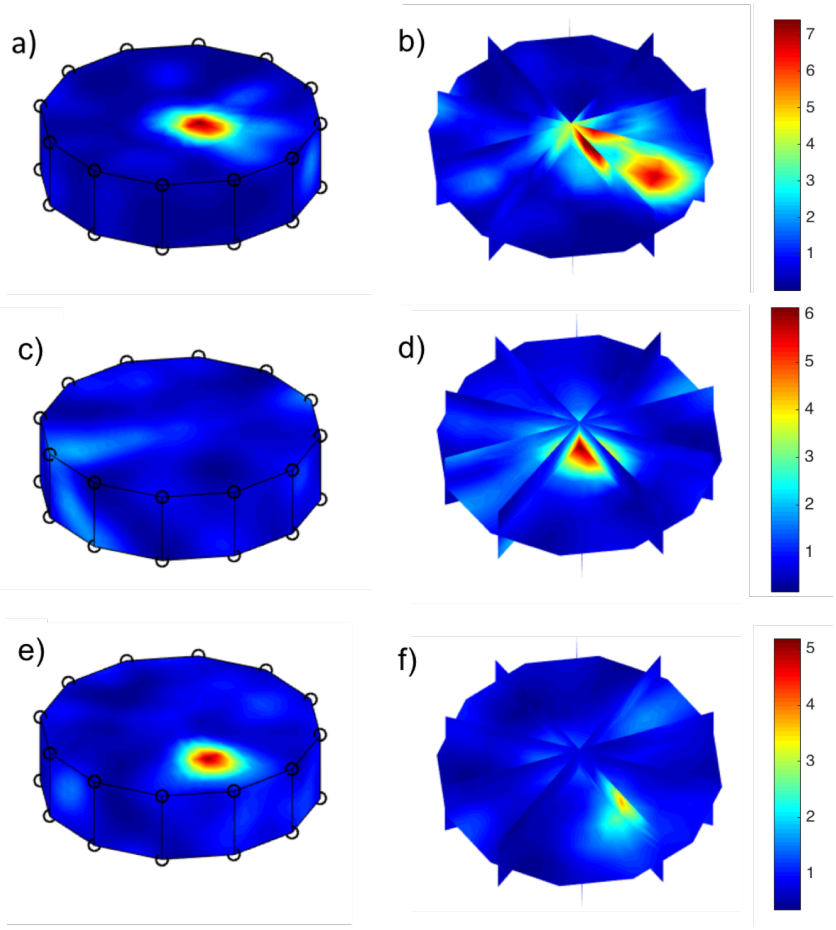


Figure 6.20: ODFs visualised in Rodrigues Space for each product from of Ti-6Al-4V, where a) represents the billet, b) the UDR material and c) the CR material. where the RHS shows sectioned versions, allowing a more comprehensive view of these ODFs.

Crystallographic texture information has been included in the simulations via the introduction of an ODF where the ODF is generated from the results from EBSD (in Euler angles) and hexagonal symmetry. Three ODFs have been generated, one for each product form. The ODF is subsequently sampled and a list of crystallographic orientations that fit the distribution are simulated. An ODF has been sampled for the CR, UDR and billet Ti-6Al-4V product forms respectively with 500 grains.

Pole figures have been generated from the resulting CR instantiation (1,500 grains) and compared to the experimentally derived pole figure in Figure 6.21. Texture is similar between these, showing the ODF generates appropriate material representations.The macroscopic response of the constant strain rate (10^{-3} s^{-1}) on these textured results (500 grains) is shown in Figure 6.22a. Similar trends for billet, UDR and CR behaviour are observed as compared to experimental results.

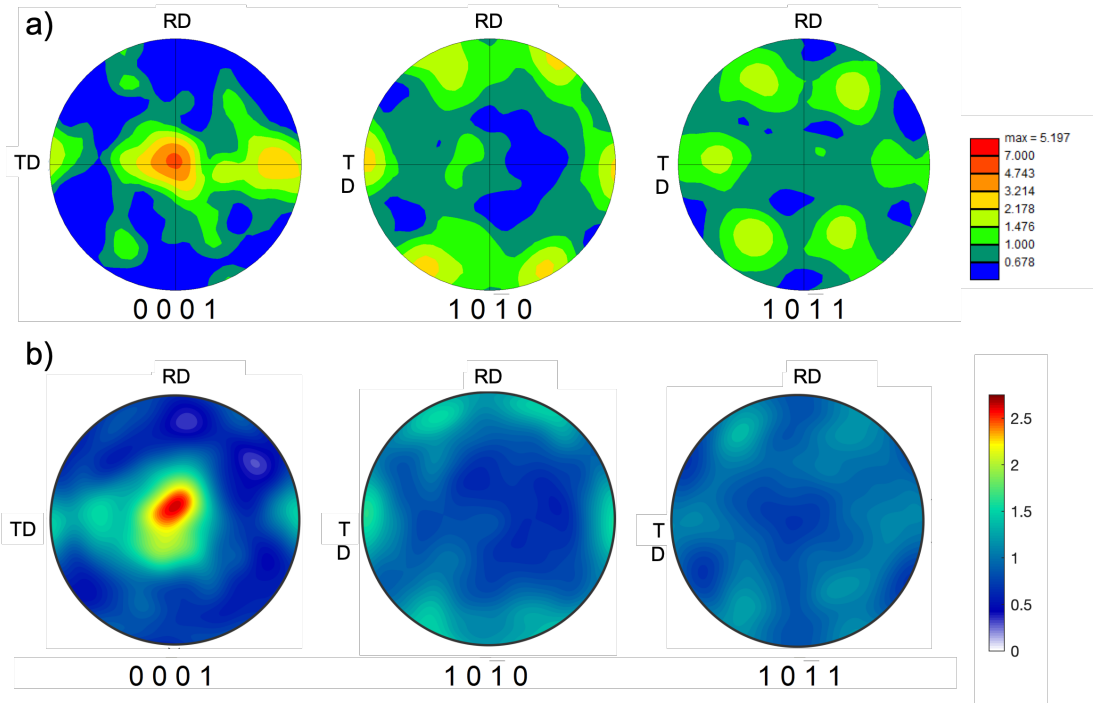


Figure 6.21: Pole figures generated from a) the initial CR microstructure and b) the simulated polycrstal extracted from the ODF of the CR material.

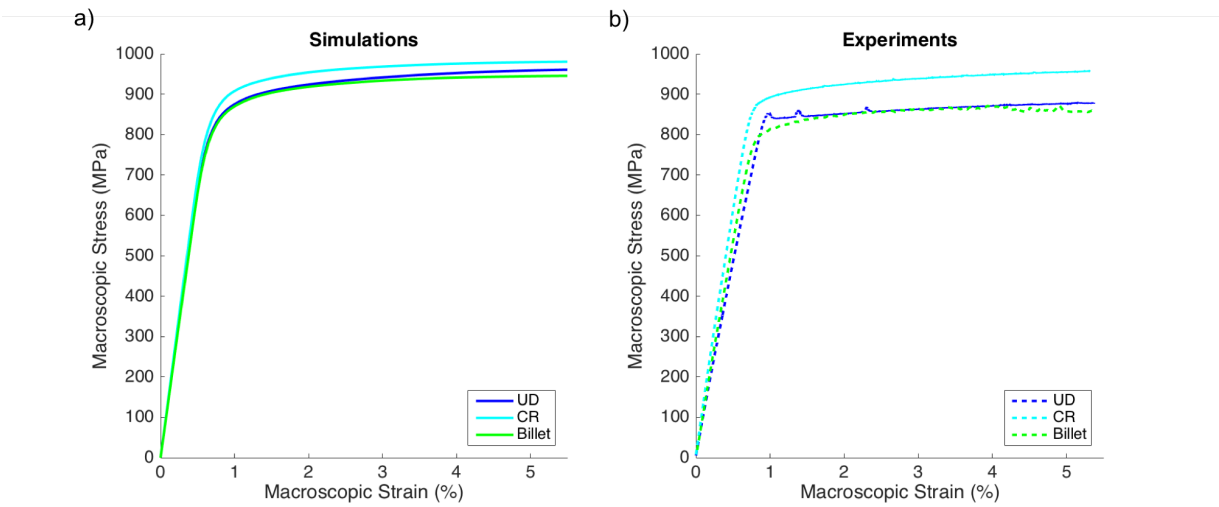


Figure 6.22: a) 500 grain polycrystal instantiations base on actual microstructures are compared to b) experimental results for uniaxial tension tests at 10^{-4} s^{-1}, showing similar trends.

6.2.2 Modelling Macrozones

Macrozones have significant effects on material properties for Ti-6Al-4V (Section 1.7). The inclusion of these has been considered but at no significant depth. Grains within the macrozone have been selected to be randomly within 5 degrees of the initial orientation used. All grains contained in the central 12.5%, 25% or 50% of the polycrystal were included to produce macrozones of different sizes. The macroscopic response of these microstructures, tested at a strain rate of 10^{-4} s^{-1} is shown in Figure 6.24.

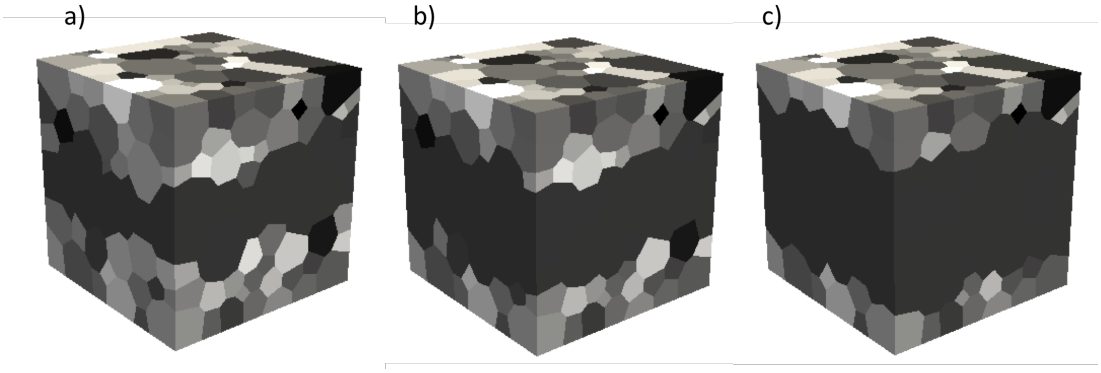


Figure 6.23: Instantiated polycrystals with 500 grains where a section of a) 151 grains (30%) b) 214 grains (43%) c) 342 (68%) grains has been oriented as a macrozone, grains are coloured according to orientation.

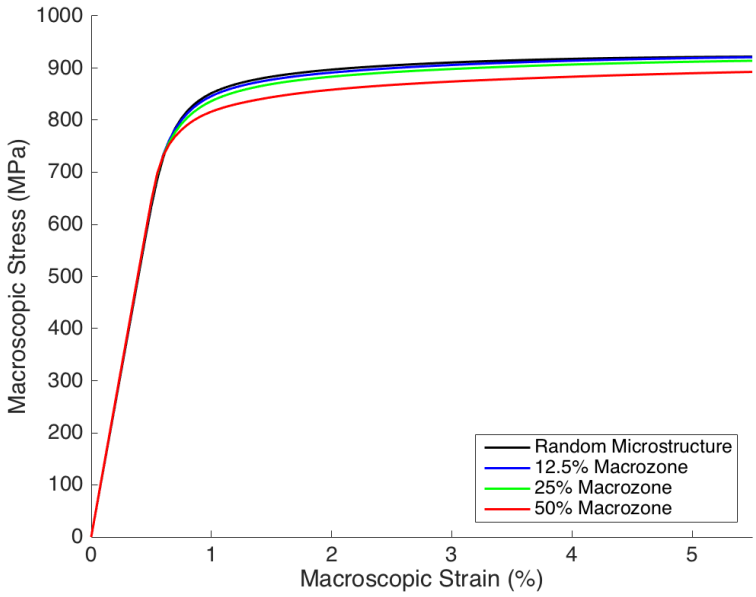


Figure 6.24: Macroscopic stress-strain response of 500 grain polycrystal with macrozones as shown in Figure 6.23.

The yield stress changes with increasing macrozone size as shown in Table 6.10. The orientation of the macrozone relative to the loading direction is also investigated, see Figure 6.25. Three orientations have been considered, where the orientation of the macrozone relative to the loading direction is visualised in Table 6.10. Dependent on the orientation of the macrozone, it either increases or decreases the yield stress. Of particular note is the the difference in behaviour around yield, which is even evident with the smallest macrozones (12.5%), see Figure 6.26.

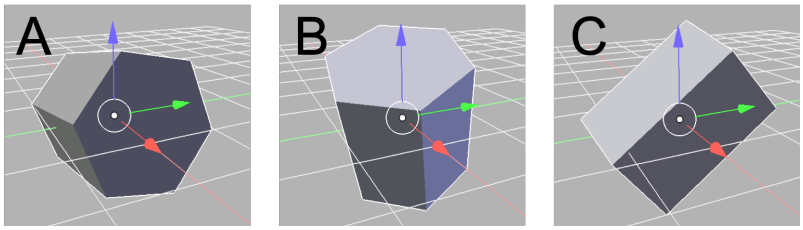


Figure 6.25: Orientation of macrozones simulated in this section, where the blue arrow denotes the loading direction.

Macrozones are often observed as bands so 12.5% is observed to act as a single band through the specimen thickness. A more realistic approach quantifying the clustering of these macrozones is required. Due to difficulties in accurately predicting macrozone volumes from 2D EBSD data, this has not been generally included in further computational simulations. Incorporation of work as performed by Kasemer et al [99], which uses a more detailed model in FEpX, would increase the accuracy of future analyses. It is also suggested that complex interactions occur at the edges of macrozones [89] and the inclusion of such would greatly improve the current predictive capabilities of simulated results.

Table 6.10: Yield stress values depending on macrozone inclusion, decreasing with the inclusion of larger macrozone volume fraction.

Macrozone Volume	 MPa	 MPa	 MPa
50%	783.2	964.9	1,070.0
25%	804.7	917.0	986.5
12.5% s	813.0	893.5	931.0
No Macrozone	817.6	n/a	n/a

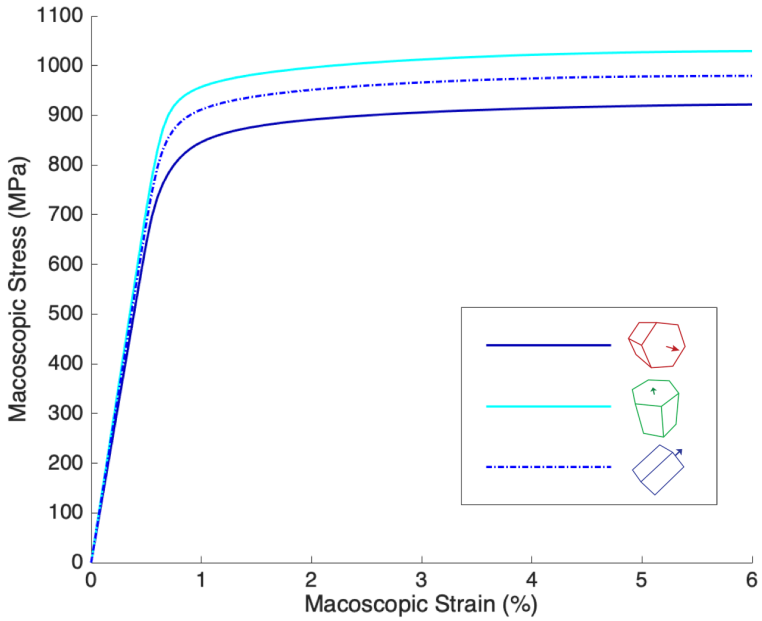


Figure 6.26: Macroscopic stress-strain response of 12.5% macrozones at multiple orientations relative to the loading direction.

6.3 Computational Results

Instantiations of 3,000 and 1,500 grains are generated with the parameters defined in the sections prior. 3,000 grain instantiations with gripped boundary conditions are studied alongside 1,500 grain polycrystals with symmetric BCs. Due to issues in the generation of symmetric BCs, these have only become a viable option recently, thus less computationally intensive simulations are performed.

6.4 3,000 Grain Instantiations

Individual 3,000 grain polycrystal instantiations of each product form have been generated with the appropriate textures, grain sizes and shape distributions, as visualised in Figure 6.27. These are subject to the gripped boundary conditions described previously. Each ODF has been sampled multiple times to create three versions each product form with different crystallographic orientations.

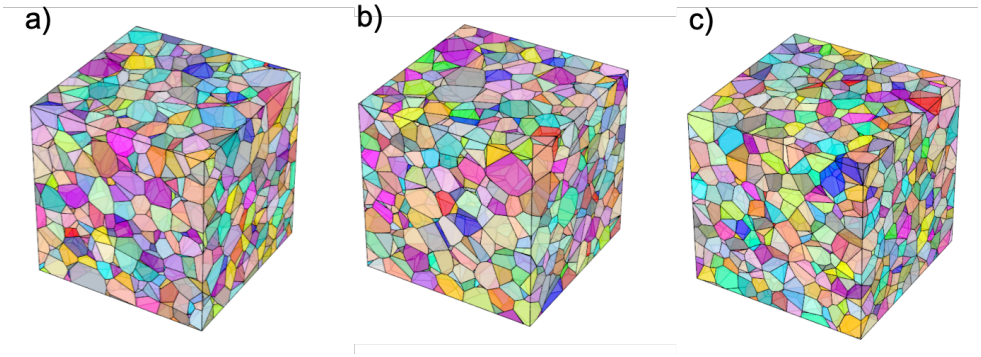


Figure 6.27: Instantiation of 3,000 grain polycrystals for a) a randomly generated polycrystal with default Neper grain properties, b) UDR, c) CR and d) the billet Ti-6Al-4V.

6.4.1 Macroscopic Response

SRJ conditions as prescribed for experiments detailed previously in Section 3.1 are devised for each product form. The macroscopic response of which is shown in Figure 6.28 where the yield stress and the error from experimental results is defined in Table 6.11 as

$$e_\sigma = \left[\int_0^{5.5} \left[(\sigma_{latt} - \sigma_{latt_{exp}})\right]^2 d\epsilon\right]^{\frac{1}{2}} \tag{6.3}$$

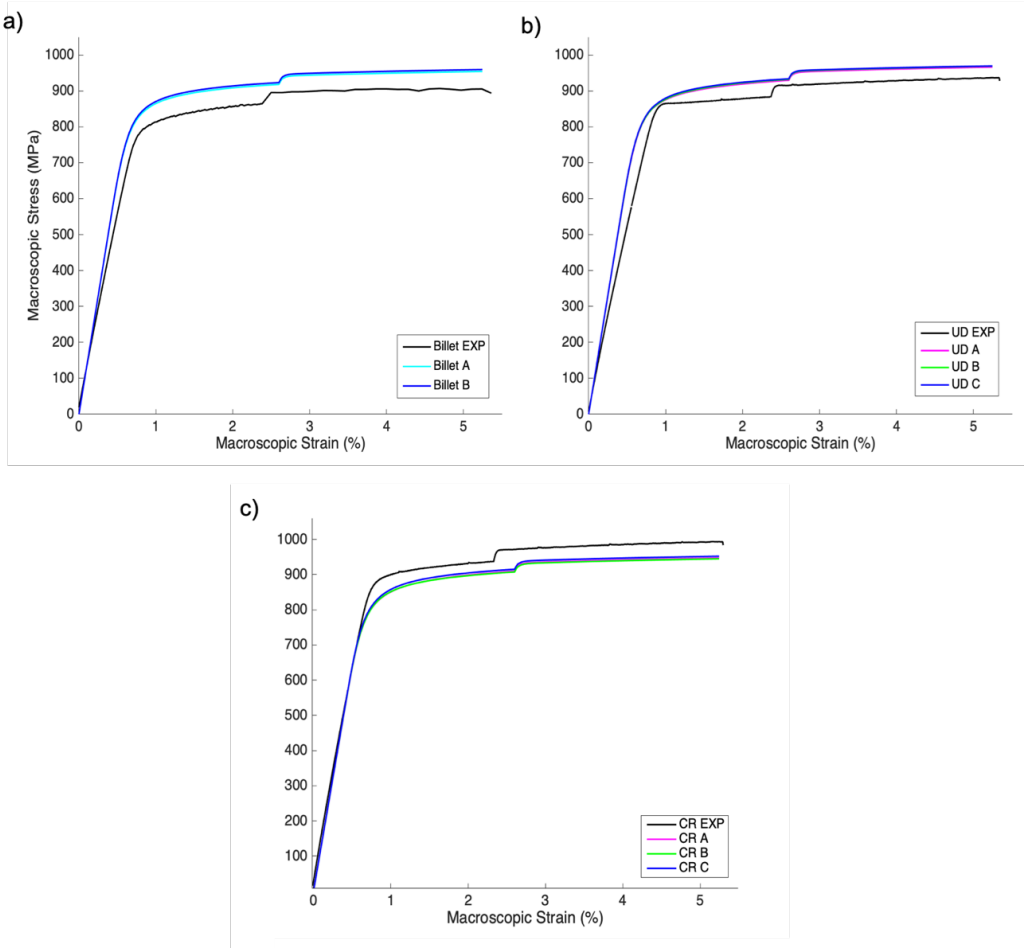


Figure 6.28: Macroscopic stress-strain response of three 3,000 grain billet instantiations, compared to experimental result for a) the billet, b) the UDR and c) the CR material.

Table 6.11: Yield stresses for polycrystal simulations.

Material	Yield Stress	c.f. Experimental results	Overall error (normalised)
Billet	846.9 MPa	+ 36.6 MPa (4.52%)	252.4 (5.78%)
	852.4 MPa	+ 42.1 MPa (5.20%)	277.9 (6.36%)
UDR	832.0 MPa	- 33.1 MPa (3.83%)	111.9 (2.51%)
	832.6 MPa	- 32.5 MPa (3.76%)	84.9 (1.91%)
	838.6 MPa	- 26.5 MPa (3.06%)	131.9(2.96%)
CR	857.4 MPa	- 39.4 MPa (4.39%)	270.3 (5.72%)
	860.9 MPa	- 35.9 MPa (4.00%)	235.3 (4.98%)
	858.2 MPa	- 38.6 MPa (4.30%)	264.0 (5.59%)

The crystallographic orientation distribution in the microstructure leads to appropriate representation of the material at 500 grains as in Figure 6.22. Whereas increasing the grain count to 3,000 grains reduces the variation between product forms significantly.

The computational simulations appear to adequately capture trends in the billet Ti-6Al-4V but further efforts in quantifying the differences in UDR and CR plate is required to further improve the analysis. It is likely that the macrozones induced via rolling play a significant part in the differences observed. Clustering of macrozones and grain sizes are suggested as the CR material appears to display locations of smaller grains which although the spread of grain sizes is captured in the current analysis, see Figure 5.26. The effect of these areas of reduced grain size may need to be accounted for to improve modelling of product forms. ses.

6.4.2 Lattice Strain Response

The lattice strain response has been extracted from the simulations, one for each product form, those which best match the experimental macroscopic results have been selected. The lattice strain evolution for a single response of each product form is shown in Figures 6.29, 6.30 and 6.31 for the billet, UDR and CR respectively. The lattice strain responses are well predicted for the billet and slightly under predicted for both the UDR and CR materials. The effective moduli for crystallographic direction in each material product type is also extracted, Table 6.12, where the ratios between the strengths of different crystallographic directions are generally well predicted.

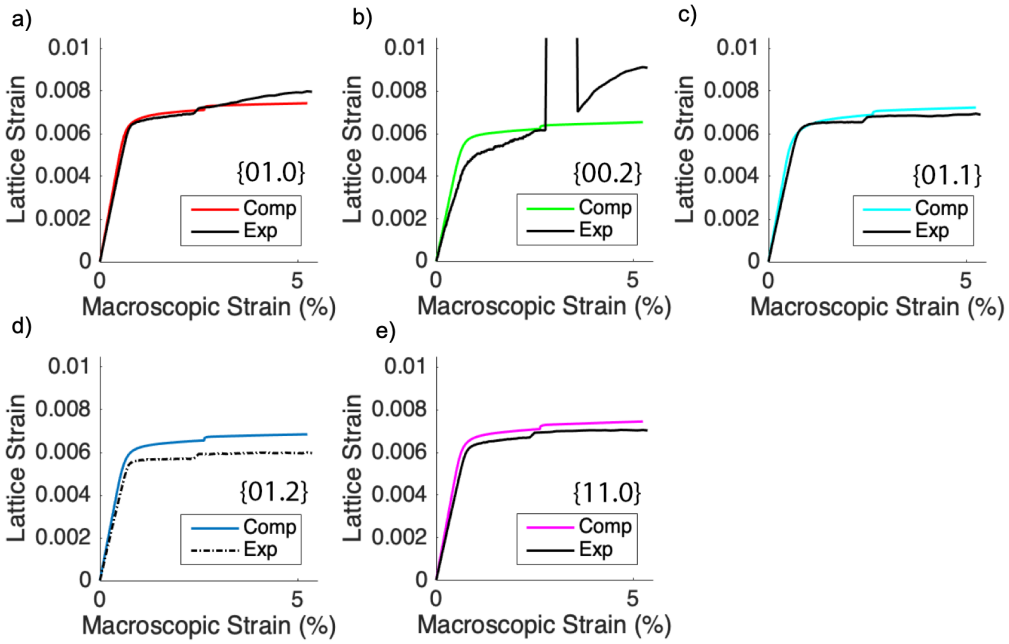


Figure 6.29: Lattice strain response calculated for 3,000 grain billet instantiation under the SRJ conditions, compared to experimental results.

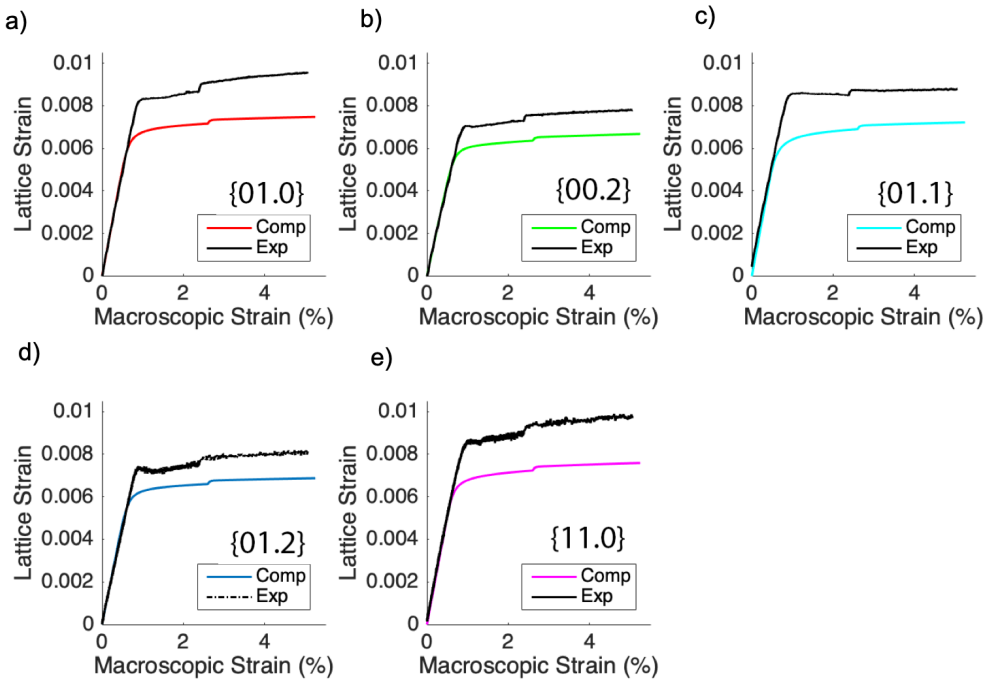


Figure 6.30: Lattice strain response calculated for 3,000 grain UDR instantiation under the SRJ conditions, compared to experimental results.

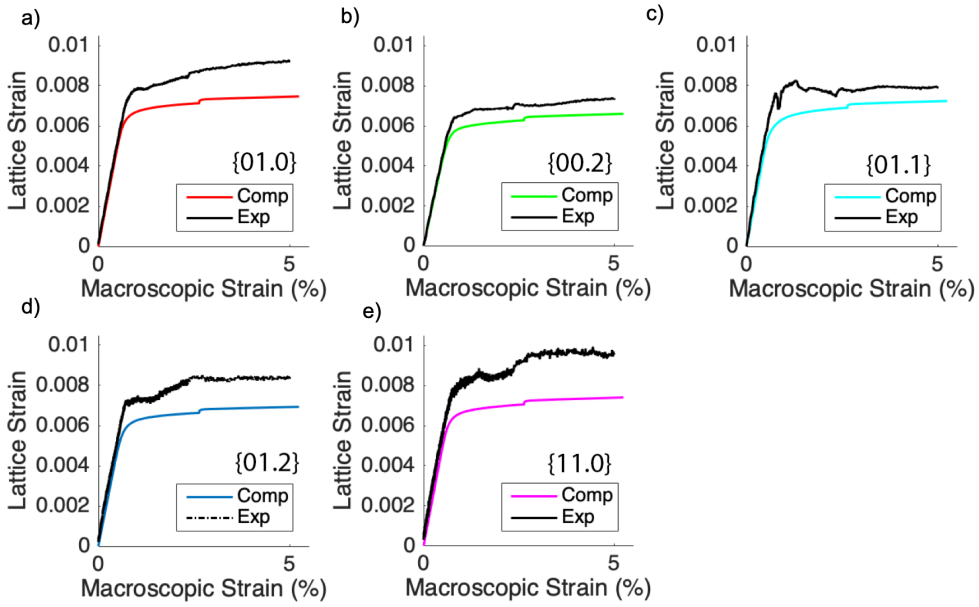


Figure 6.31: Lattice strain response calculated for 3,000 grain CR instantiation under the SRJ conditions, compared to experimental results.

Table 6.12: Effective moduli for each crystallographic direction derived from each experiment, where values have also been normalised for comparison.

Material	hkil	Experimental (1 x 10^{-4})		Simulation (1 x 10^{-4})	
Billet	**{01.0}**	112.368	(1.00)	128.99	(1.00)
	{00.2}	130.500	(1.16)	149.79	(1.16)
	{01.1}	115.788	(1.03)	129.56	(1.00)
	{01.2}	121.612	(1.08)	137.58	(1.07)
	{11.0}	114.796	(1.02)	129.80	(1.01)
UDR	**{01.0}**	103.98	(1.01)	129.93	(1.01)
	{00.2}	121.09	(1.17)	148.56	(1.15)
	{01.1}	107.30	(1.04)	130.28	(1.01)
	{01.2}	112.84	(1.09)	138.23	(1.07)
	{11.0}	103.14	(1.00)	128.75	(1.00)
CR	**{01.0}**	118.70	(1.07)	128.30	(1.00)
	{00.2}	132.72	(1.20)	147.12	(1.15)
	{01.1}	110.65	(1.00)	128.79	(1.00)
	{01.2}	123.58	(1.12)	134.96	(1.05)
	{11.0}	114.91	(1.04)	128.39	(1.00)

The response of the billet material is well predicted, whereas the UDR and CR materials are less well predicted. As stated, it is well known that macrozones are prominent in these materials and the incorporation of these could improve the simulations and better represent these materials. This is beyond the current scope of this work.

6.4.3 Constant Strain Rate comparison

In this section, the computationally derived results from the constant strain rate experiments are compared to the SRJ, where the macroscopic results are shown in Figure 6.32. Again, the 3,000 grain instantiations have been employed here. The lattice strain response is given in Figure 6.33 for 10^{-3} s^{-1} and the SRJ. The plastic strain in the material throughout deformation is tracked throughout; the differences are shown in Figure 6.35 where the strain post jump is reduced compared to the equivalent CSR results. In the constant rate response, the increased strain continues accumulating throughout the experiment leading to significantly more strain at 5% engineering strain than the SRJ. Note, the areas around the bounded edges (top and bottom) show increased levels of strain, however this is an artefact of the visualisation as discussed.

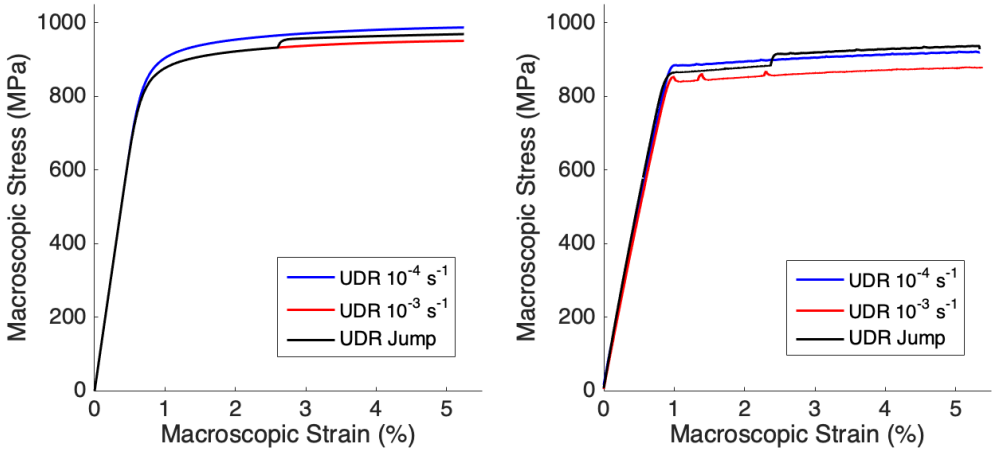


Figure 6.32: a) Macroscopic stress-strain response of three 3,000 grain UDR instantiations, b) experimental response reproduced from Figure 5.13a.

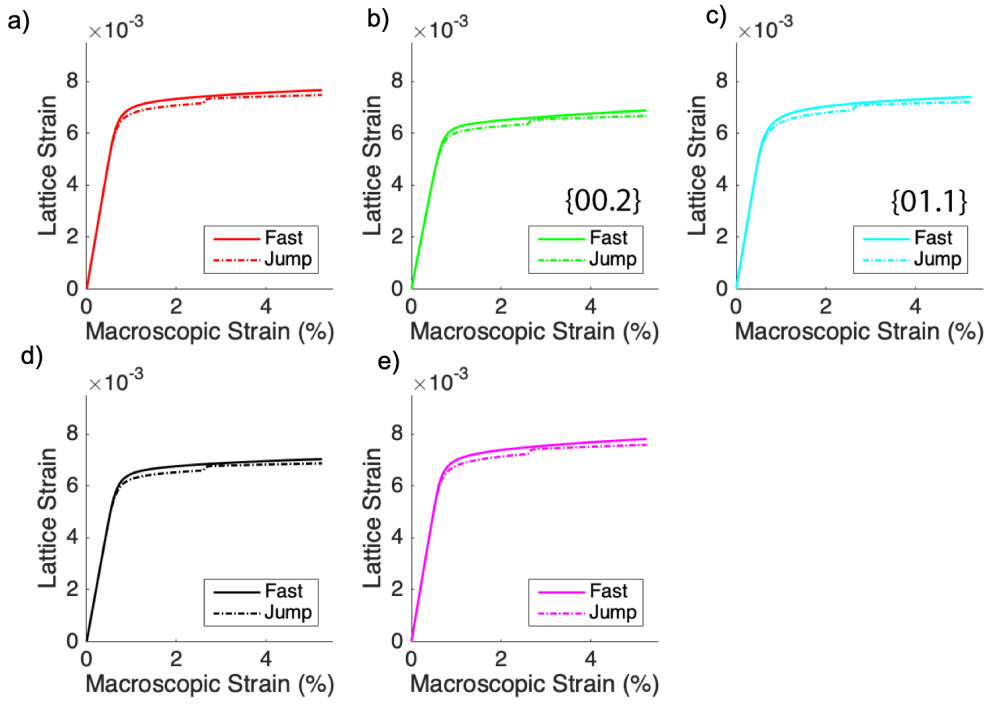


Figure 6.33: Lattice strain response for UDR material under both the 10^{-3} s^{-1} and the SRJ loading conditions.

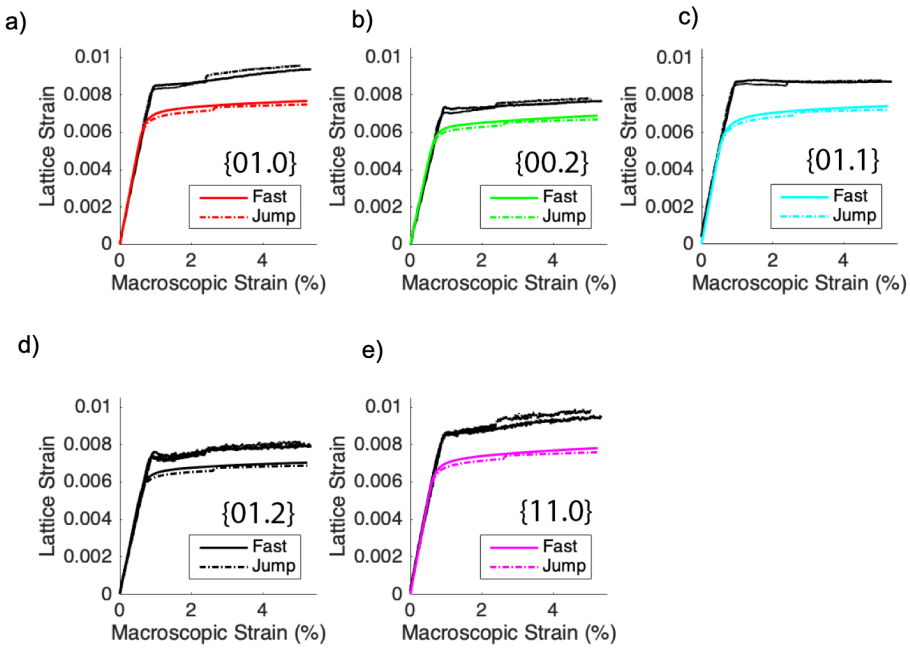


Figure 6.34: Lattice strain response for UDR material under both the 10^{-3} s^{-1} and the SRJ loading conditions, showing reduced values compared to the experimental results (black).

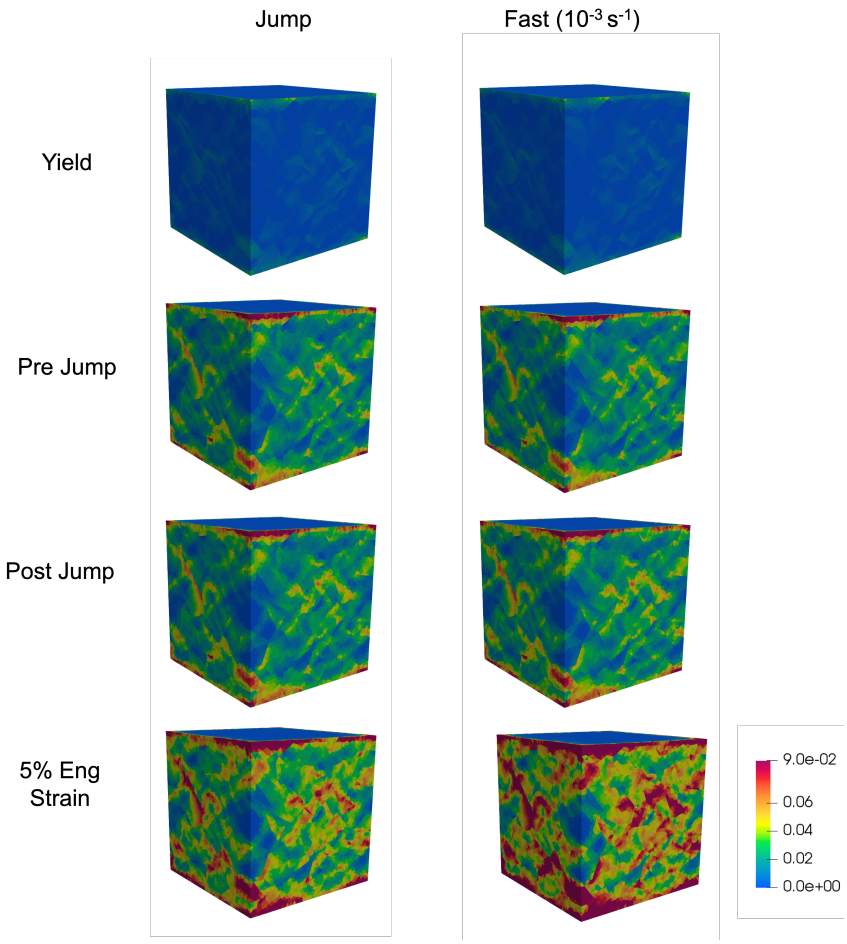


Figure 6.35: Plastic strain for the UDR material under both the higher, 10^{-3} s^{-1}, and the SRJ loading conditions. These have been visualised at yield, immediately before and after the jump, or equivalent and at 5% engineering strain.

Lattice strains are observed as being significantly lower for the simulated response, Figure 6.34. The differences between the constant strain rate and SRJ are fairly consistent between computational and experimental results despite the reductions in predicted lattice strain. While these results do represent the Ti-6Al-4V fairly well, they do not explicitly model each of the product forms with a good degree of accuracy.

The time taken to analyse these results is significant, with the total time taken to create and mesh tessellations, run the simulation and perform basic post processing to obtain lattice strain evolution, running in excess of 40 hours per simulation. This does not include time taken to download/open files or any subsequent analysis. Opening and operating on multiple files simultaneously for comparison is not possible due to the large file sizes.

6.5 1,500 Grains (symmetric)

Nine distinct 1,500 grain polycrystal instantiations, three for each of the product forms have been generated with the appropriate textures, grain sizes and shape distributions, all of which have been visualised in Figure 6.36. All 1,500 grain experiments in this section have been performed with symmetric BCs.

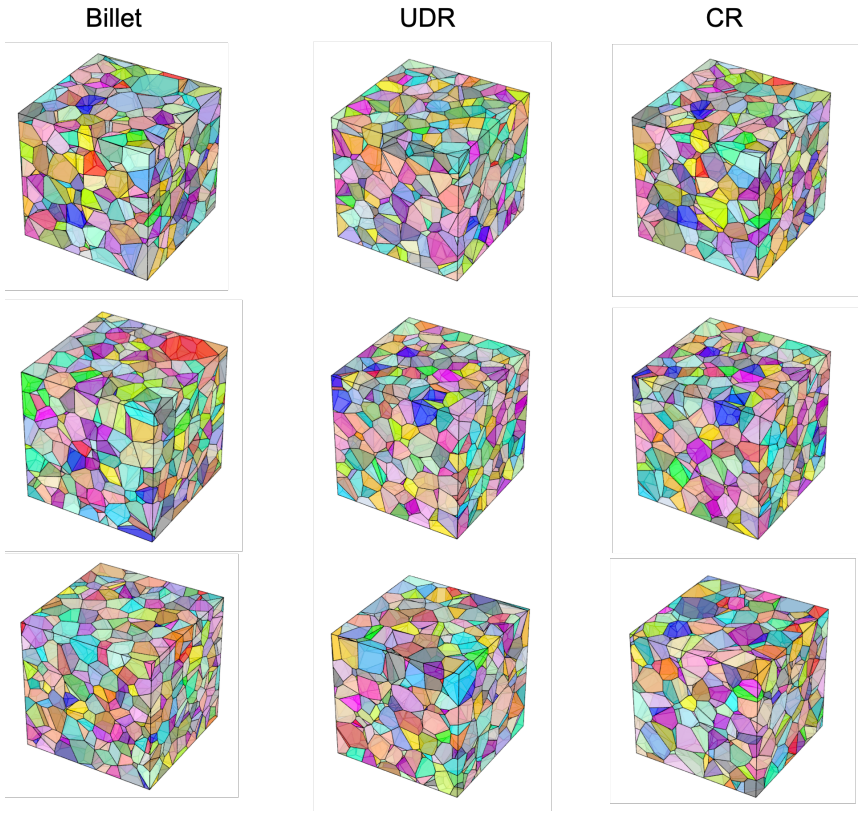


Figure 6.36: Instantiations of 1,500 grain polycrystals where the LHS shows the three billet instantiations, the central column shows the CR polycrystals and the UDR Ti-6Al-4V is shown on the RHS.

The orientations generated for each polycrystal have all been sampled from the appropriate ODF, see Section 6.2.1. A SRJ has been imposed to replicate the loading prescribed experimentally; this allows for direct comparison. The effect of the jump on each of the Ti-6Al-4V products is now examined.

6.5.1 Macroscopic Response

The macroscopic results of the three instantiations of billet, UDR and CR materials are given in Figures 6.37a b and c respectively. There is little deviation in the results despite the different initial instantiations.

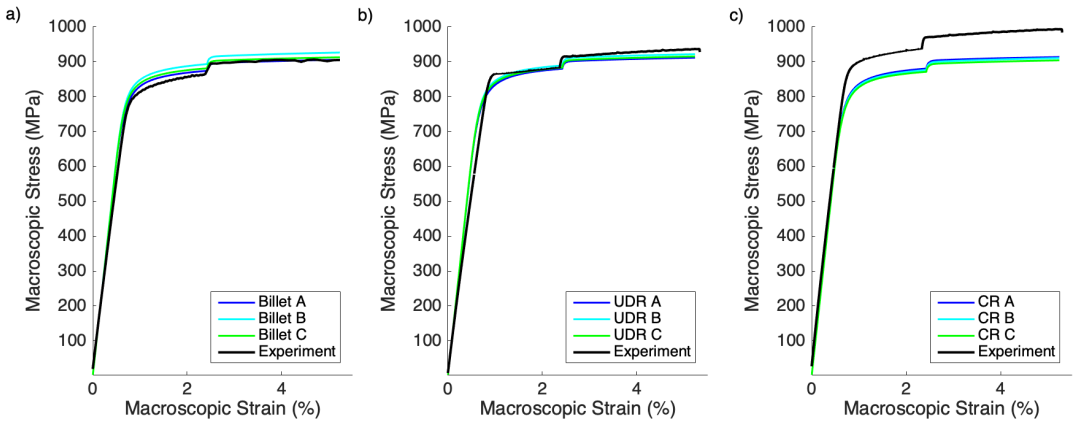


Figure 6.37: Macroscopic stress-strain response of a) billet (radial), b) UDR (rolling) and c) CR (rolling) material instantiations.

The yield stresses of the three materials derived from the prior experiments are 810.3, 865.1 and 896.8 MPa for the billet, UDR and CR materials. The yield stresses and deviation from experimental results are outlined in Table 6.13, where the deviation from the experimental values is calculated as previously (Equations 6.1 and 6.2).

Table 6.13: Yield stresses for polycrystal simulations where deviation is calculated as the difference between simulated and experimental result, see Equation 6.1.

Material	Yield Stress	Difference	Overall Error (e)
Billet	810.9 MPa	+ 0.6 MPa (+0.07%)	35.3 (0.80%)
	830.5 MPa	+ 20.2 MPa (+2.48%)	128.4 (2.94%)
	820.6 MPa	+ 10.3 MPa (+1.27%)	70.6 (1.62%)
UDR	814.6 MPa	- 50.5 MPa (-5.84%)	61.8 (1.39%)
	822.4 MPa	- 42.7 MPa (-4.93%)	13.6 (0.31%)
	827.7 MPa	-37.4 MPa (-4.23%)	41.8 (0.94%)
CR	818.5 MPa	- 78.3 MPa (-8.87%)	330.4 (7.00%)
	814.4	- 82.4 MPa (-9.18%)	349.8 (7.40%)
	809.1 MPa	- 87.7 MPa (-9.79%)	376.2 (7.96%)

The difference in the results between each product form is much smaller than that experimentally observed, indicating that the macroscopic scale, differences between the different material products are not fully captured in this analysis. The billet and UDR material are overall well predicted.

6.5.2 3D Results

The equivalent plastic strain ϵ^p_{eq} is defined by,

$$\epsilon^{\mathbf{p}}_{\mathbf{eq}} = \int_{\mathbf{0}}^{\mathbf{t}} \mathbf{d}^{\mathbf{p}}_{\mathbf{eff}}\, \mathbf{dt} \tag{6.4}$$

where $\mathbf{d}^p_{\mathbf{eff}}$ is the effective plastic deformation rate defined by

$$\mathbf{d}^{\mathbf{p}}_{\mathbf{eff}} = \sqrt{\frac{\mathbf{2}}{\mathbf{3}}\mathbf{d}^{\mathbf{p}} : \mathbf{d}^{\mathbf{p}}} \tag{6.5}$$

and $\mathbf{d}^{\mathbf{p}}$ is the plastic rate of deformation.

Various parameters are tracked through each experiment, including the plastic strain in each element. The evolution of these variables during the jump is of particular interest in this study. A sample of the plastic strain for all material types considered is given in Figure 6.38, where the plastic strain accumulates in different locations but the magnitude is consistent between material types.

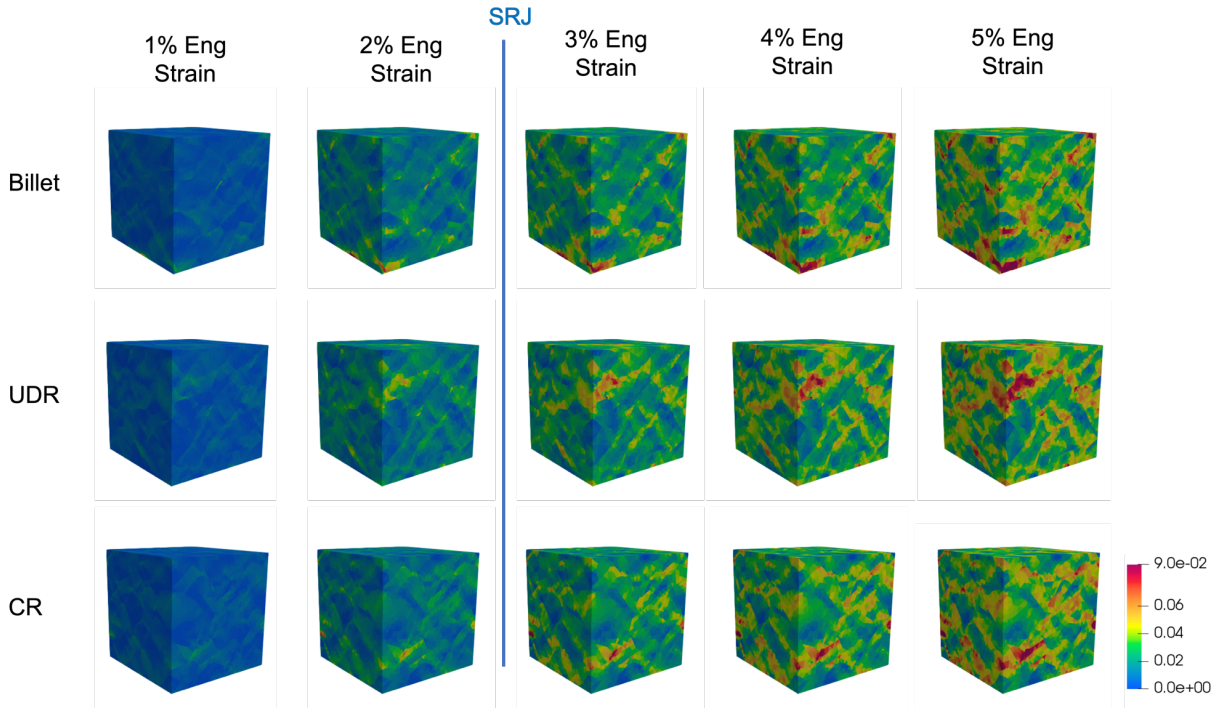


Figure 6.38: Equivalent plastic strain evolution tracked at different engineering stresses during the SRJ experiment for all materials.

The lower, higher and SRJ results of the CR material are shown in Figure 6.39. The jump in strain rate, which occurs at approximately 2.4% engineering strain is clear. Interestingly, the differences in the pre-jump, slower and faster strain rate condition are minimal prior to the jump. After the jump, the level of plastic strain is observed to be reduced in the SRJ condition. The localisation of plastic strain is seen to occur in the same grains, thus it does not appear to be affected by the SRJ. The jump appears to be quite different post SRJ.

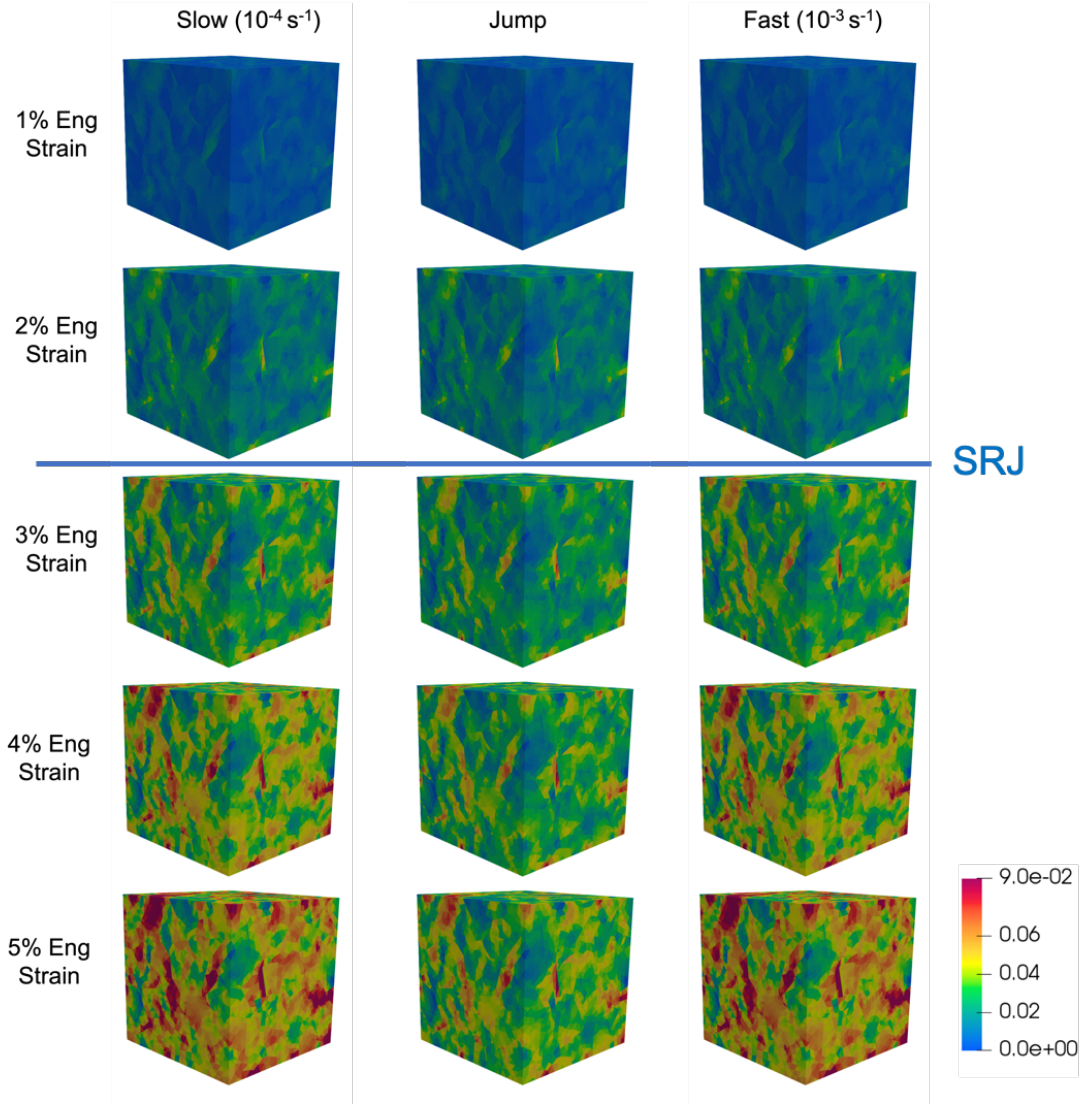


Figure 6.39: Plastic strain in each grain tracked during the jump in strain rate and compared to the equivalent responses for the constant strain rates for the CR material.

6.5.3 Lattice Strain Response

The computed lattice strain accumulation is shown in Figures 6.40 to 6.42 alongside the experimental data. The same azimuthal bin width has been replicated for each Ti-6Al-4V simulation, where in the case of the billet, this is widened to sufficiently capture experimental data.

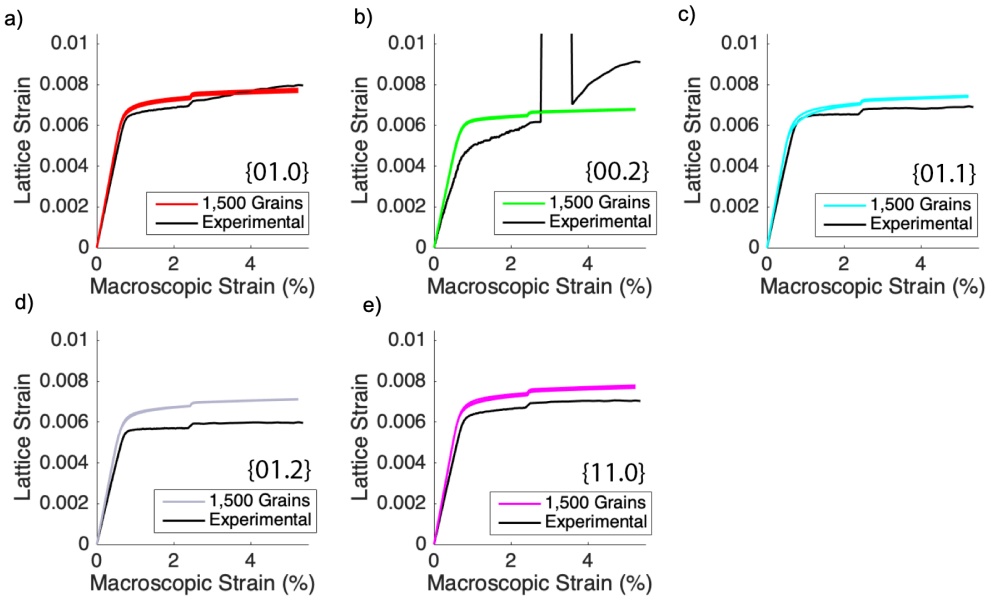


Figure 6.40: Lattice strain accumulation extracted from three 1,500 grain instantiations of billet Ti-6Al-4V and compared to experimental values.

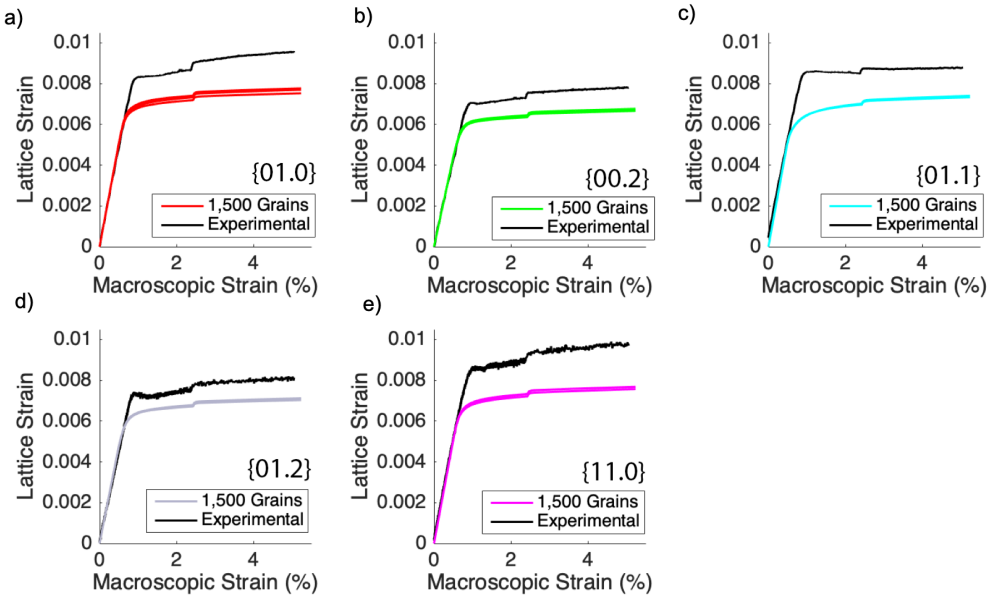


Figure 6.41: Lattice strain accumulation extracted from the 1,500 grain instantiation of UDR Ti-6Al-4V and compared to experimental results.

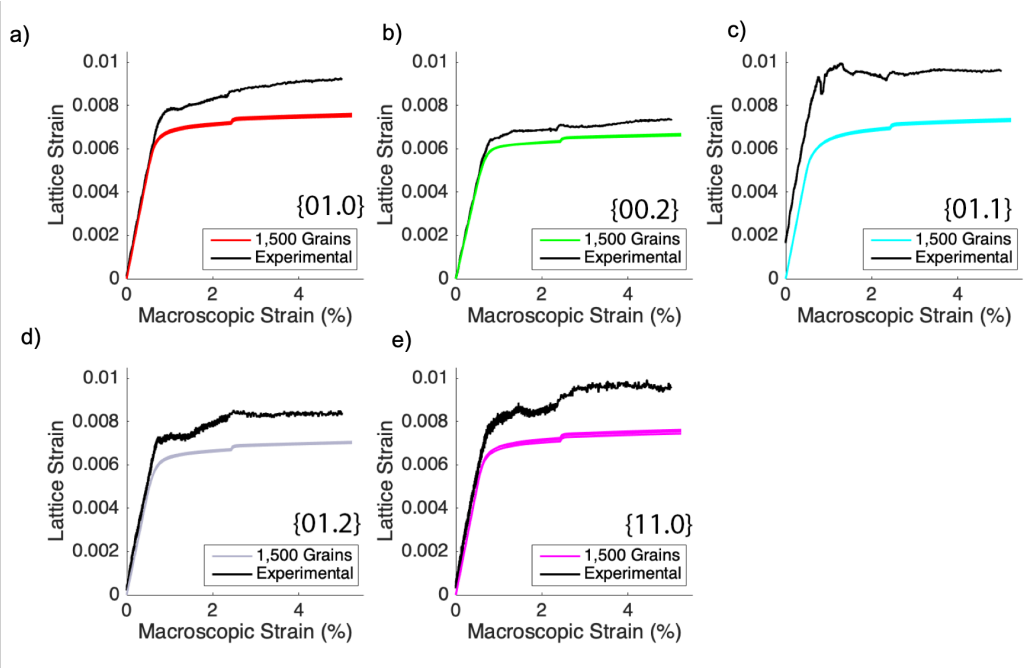


Figure 6.42: Lattice strain accumulation extracted from three 1,500 grain instantiation of CR Ti-6Al-4V and compared to experimental values.

The results of the simulations for each product form are very similar with little difference in the macroscopic response. Again, it is observed that the model predicts the elastic behaviour well. However it under-predicts the yield of the UDR and CR materials whilst slightly over-predicting the billet Ti-6Al-4V behaviour. For the UDR and billet materials, the 1,500 grain symmetric BCs have a reduced error than the previous 3,000 grain gripped results.

The model accurately predicts the spread of lattice strains prior to plastic deformation, with general trends captured. However the magnitudes are generally lower and less spread out in the simulations. Additionally, the effective moduli is captured in each direction, these are summarised in Table 6.15, where the values calculated for the effective moduli are generally representative of those observed experimentally.

Table 6.14: Lattice strain at yield for all polycrystal simulations with a SRJ, where UDR and CR experimental results are replicated from Table 5.5.

Material	hkil	Experimental		Sim A	
Billet	**{01.0}**	0.006499	(1.35)	0.006873	(1.12)
	{00.2}	0.004817	(1.00)	0.006163	(1.00)
	{01.1}	0.006319	(1.31)	0.006491	(1.05)
	{01.2}	0.005598	(1.16)	0.006243	(1.01)
	{11.0}	n/a	(n/a)	0.006814	(1.11)
UDR	**{01.0}**	0.008343	(1.19)	0.006757	(1.13)
	{00.2}	0.007025	(1.00)	0.005979	(1.00)
	{01.1}	0.008560	(1.22)	0.006279	(1.05)
	{01.2}	0.007251	(1.03)	0.006258	(1.05)
	{11.0}	0.008521	(1.21)	0.006681	(1.12)
CR	**{01.0}**	0.007831	(1.20)	0.006694	(1.11)
	{00.2}	0.006507	(1.00)	0.006004	(1.00)
	{01.1}	0.009472	(1.46)	0.006236	(1.04)
	{01.2}	0.007226	(1.11)	0.006218	(1.04)
	{11.0}	0.008072	(1.24)	0.006705	(1.12)

Table 6.15: Effective moduli for each crystallographic direction derived from each experiment, values have been normalised for comparison.

Material	hkil	Experimental (MPa)		Sim A (MPa)	
Billet	**{01.0}**	112.368	(1.00)	120.78	(1.00)
	{00.2}	130.500	(1.16)	135.16	(1.12)
	{01.1}	115.788	(1.03)	121.35	(1.01)
	{01.2}	121.612	(1.08)	126.68	(1.05)
	{11.0}	114.796	(1.02)	120.41	(1.00)
UDR	**{01.0}**	103.98	(1.01)	121.19	(1.00)
	{00.2}	121.09	(1.17)	140.92	(1.17)
	{01.1}	107.30	(1.04)	121.22	(1.00)
	{01.2}	112.84	(1.09)	128.78	(1.06)
	{11.0}	103.14	(1.00)	120.95	(1.00)
CR	**{01.0}**	118.70	(1.07)	122.61	(1.00)
	{00.2}	132.72	(1.20)	140.30	(1.15)
	{01.1}	110.65	(1.00)	122.37	(1.00)
	{01.2}	123.58	(1.12)	129.64	(1.06)
	{11.0}	114.91	(1.04)	122.18	(1.00)

In summary, the SRJ modelled using the 1,500 grain CPFE model shows fair agreement with the experimental results, however, the variation in the computational results is limited suggesting that further discrepancies between the materials exist and must be accounted for, such as macrozones as now discussed.

The CR material consists of approximately 18% by volume macrozones [198], the direction of these has been extracted from EBSD and clusters of comparable size have been generated within the CR microstructure to examine the impact of this on the overall results. Macrozones with deviations of up to 20 degrees have been generated as clusters for 18% of the grains in the 1,500 grain instantiation. The results of this are compared macroscopically in Figure 6.43, where they are almost indistinguishable. The inclusion of macrozones impacts the lattice strain response by increasing the lattice strain at yield in all directions, in particular, the {11.0} direction, see Figure 6.44. Overall, macrozone inclusion better replicates the behaviour of the CR material yet significant improvement to the current model is required.

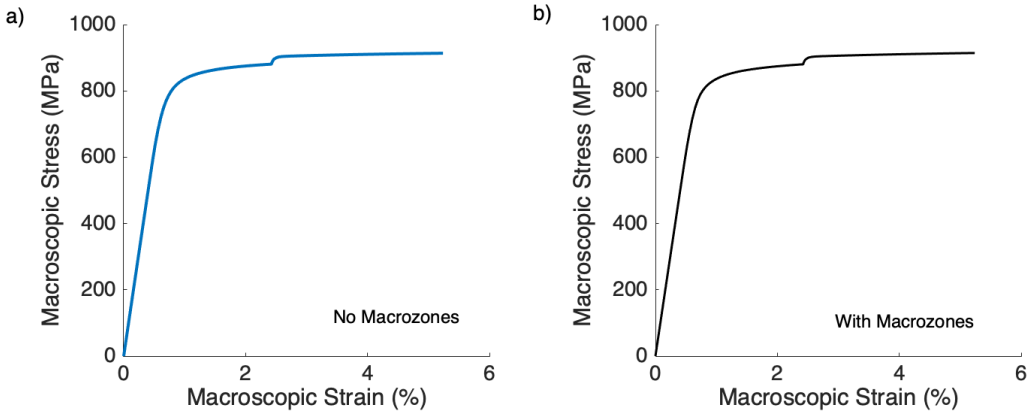


Figure 6.43: Macroscopic stress-strain response of CR Ti-6Al-4V a) without and b) with the inclusion of macrozones.

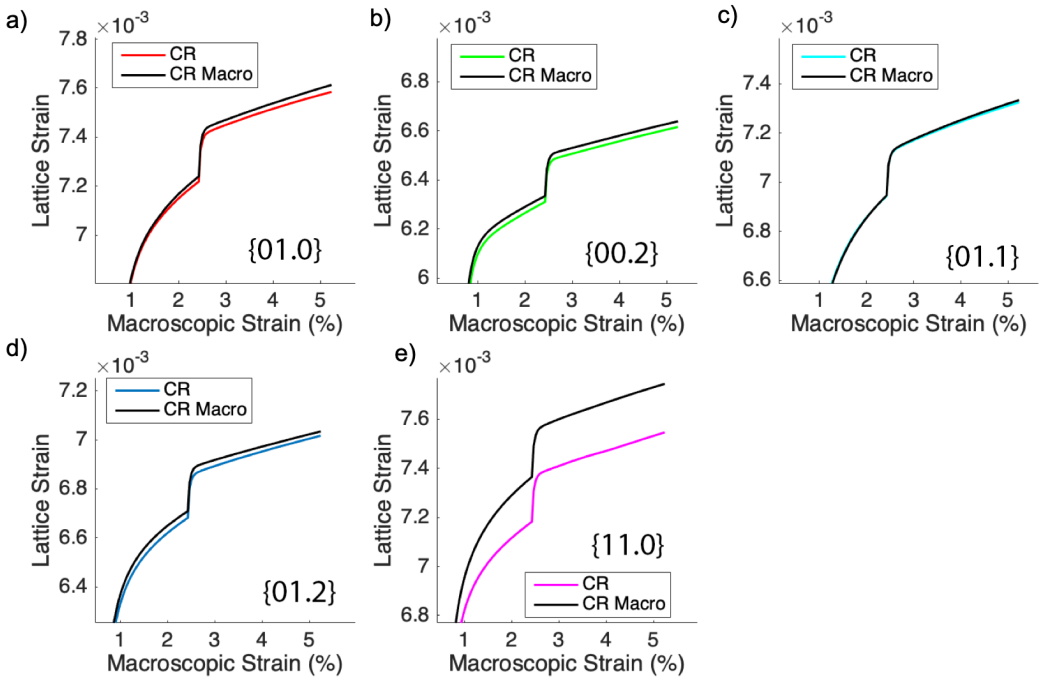


Figure 6.44: Lattice strain accumulation extracted from the 1,500 grain instantiation of CR Ti-6Al-4V with the addition of macrozones, compared to CR with no macrozones.

6.6 Discussion & Conclusions

The choice of boundary conditions impacts both macroscopic and lattice strain responses. Here, the symmetric boundary conditions better replicate the experimental loading macroscopically.

To improve this analysis and enable better prediction of different material products, it is essential to model the macrozones and better quantify each microstructure, this may be achieved with 3D EBSD or a least a more comprehensive dataset of each material product. Sampling 3D microstructure from a single 2D plane is insufficient to provide precise results. The inclusion of these macrozones provides a more accurate prediction of CR Ti-6Al-4V.

The current computational model accurately predicts the macroscopic response and lattice strain accumulation for the billet Ti-6Al-4V. The model predicts the elastic response very well both microscopically and at the lattice strain level. The UDR material is also fairly predicted.

In general, there is huge variability in experimental results, thus it is difficult to establish when results fall outwith realistic expectations. This would suggest a 'modelling first' approach where models are used to predict experimental results prior to observation, providing a better focus for the experimental work. This may even lead to discoveries where results would ordinarily be discarded as spurious.

Part III

Further Experimental Studies of Specific Industrial Interest

Chapter 7

Aluminium Content in Titanium alloys

Understanding the deformation in single phase Ti-Al alloys is a significant step in fully understanding the interplay between the constituent elements, enabling refinement of more complex alloy designs. Aluminium, an α stabiliser, is commonly alloyed with titanium as it has good solid solubility in both phases and raises the β transus temperature. The effect of the aluminium content on the Ti-Al is studied via in situ high energy XRD. This may be used to learn more about intrinsic titanium alloy properties, to compare titanium alloys and to aid in the development of advanced alloy designs.

Low aluminium titanium alloy systems are of interest due to their increased formability compared to Ti-6Al-4V and increased strength compared to cp-Ti. Ti-3Al and Ti-0Al based systems have low ambient fracture resistance, as micro-alloying has been used to increase fracture resistance and balance material properties to improve the desirable properties [35,56]. Titanium aluminides are intermedate Ti-Al systems and may emerge as an important aerospace material in jet engines due to their lower density, higher stiffness and superior strength in high temperature applications compared to traditional titanium alloys, which are susceptible to brittle fracture as they exhibit low fracture toughness [1]. Much work has been performed in utilising the technical benefits of titanium aluminides for rotating and oscillating components for both automotive and aerospace applications [19].

In order to assess the performance of Ti-Al alloys, uniaxial tensile tests have been performed in situ at two strain rates (10^{-4} s^{-1} and 10^{-3} s^{-1}), as described in Section 3.2.3. Each product discussed herein has a 500 ppm oxygen content and the specimens are cut from the rolling direction of the supplied lab-scale bars which have been processed via the routes described in Section 1.4.4. To allow comparison of the different aluminium contents, Ti-0Al, Ti-3Al and Ti-6.5Al have been examined.

7.1 Macroscopic Response

The macroscopic responses for the Ti-0Al, Ti-3Al and Ti-6.5Al show a significant increase in strength with increasing aluminium content, see Figure 7.1. The initial elastic behaviour shows a similar elastic moduli for all aluminium contents studied. The yield stresses (0.2% offset) are given in Table 7.1

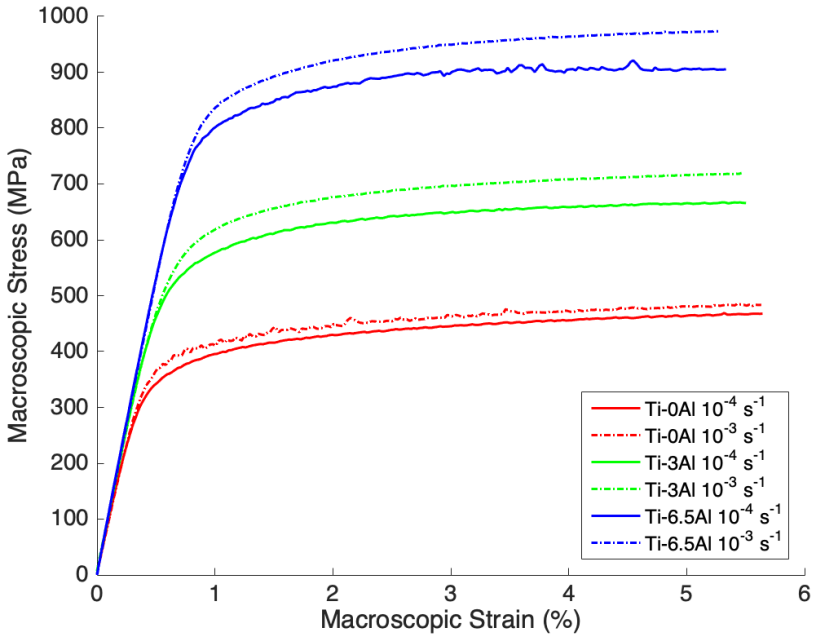


Figure 7.1: Macroscopic stress strain results comparing experiments of increasing aluminium content.

Table 7.1: Yield stress for varying aluminium contents and strain rates.

Material	Strain Rate (s^{-1})	Yield Stress (MPa)
Ti-0Al	10^{-4}	355.8
Ti-0Al	10^{-3}	382.7
Ti-3Al	10^{-4}	545.8
Ti-3Al	10^{-3}	589.3
Ti-6.5Al	10^{-4}	802.1
Ti-6.5Al	10^{-3}	846.6

The rate sensitivity parameter m has been calculated for each material using the constant strain rate method (CSRM) at 3% engineering strain, whereby

$$\left(\frac{\sigma_2}{\sigma_1}\right)^m = \frac{\dot{\epsilon}_2}{\dot{\epsilon}_1}. \tag{7.1}$$

Here, σ_1 and σ_2 are the stress at 3% from the lower and higher strain rate ($\dot{\epsilon}_1$, $\dot{\epsilon}_2$) experiments respectively. All materials examined are moderately strain rate sensitive with increases in yield stress of 8.0%, 8.2% and 6.3% calculated for increasing aluminium content (at strain rates of 10^{-4} s^{-1} and 10^{-3} s^{-1}).

Table 7.2: Strain rate sensitivity of titanium alloys with different aluminium contents, calculated using the CSRM with stresses taken at 3% engineering strain.

Material	Difference in Stress at 3%	% Increase	Strain Rate Sensitivity Parameter (m)
Ti-0Al	17.4 MPa	3.95%	0.016813
Ti-3Al	47.9 MPa	7.48%	0.031308
Ti-6.5Al	44.0 MPa	4.95%	0.020984

The strain rate sensitivity differs with aluminium content where the lowest values are found in Ti-0Al, where these and the Ti-6.5Al results which are comparable to those extracted for Ti-6Al-4V, see Table 7.2. The strain rate sensitivity parameter calculated for Ti-3Al is unexpectedly high, see Table 7.2. The overall difference in stress between experiments is highest for the Ti-3Al alloy system. The strain rate sensitivity is competing with hardening behaviour at 3% engineering strain. By examining the increase in stress during deformation due to strain hardening, (see Table 7.3), it is evident that with increasing aluminium content, the percentage increase post-yield is reduced. Thus, increasing aluminium content leads to a reduction in strain hardening behaviour, the mechanistic reasons for this remain unclear within the materials science community.

Table 7.3: Difference between stress immediately after yield and end of the test for a combination of different strain rates and aluminium contents.

Strain Rate	Material	Increase in stress between yield and end of experiment	% Increase
10^{-4} s^{-1} (slower)	Ti-0Al	109.3 MPa	30.6%
	Ti-3Al	116.2 MPa	21.1%
	Ti-6.5Al	109.7 MPa	13.7%
10^{-3} s^{-1} (faster)	Ti-0Al	97.0 MPa	25.1%
	Ti-3Al	120.6 MPa	20.2%
	Ti-6.5Al	131.2 MPa	15.5%

7.2 Lattice Strain Measurements

Powder diffraction patterns are tracked through the experiments. Lattice strain evolution is tracked for all experiments described previously in this section. The lattice strain response in both the loading and transverse directions are now compared. Lattice strain response is examined normal to the {10.1} crystallographic plane due to its high multiplicity and inherent optimisation in the analysis, see Figure 7.2.

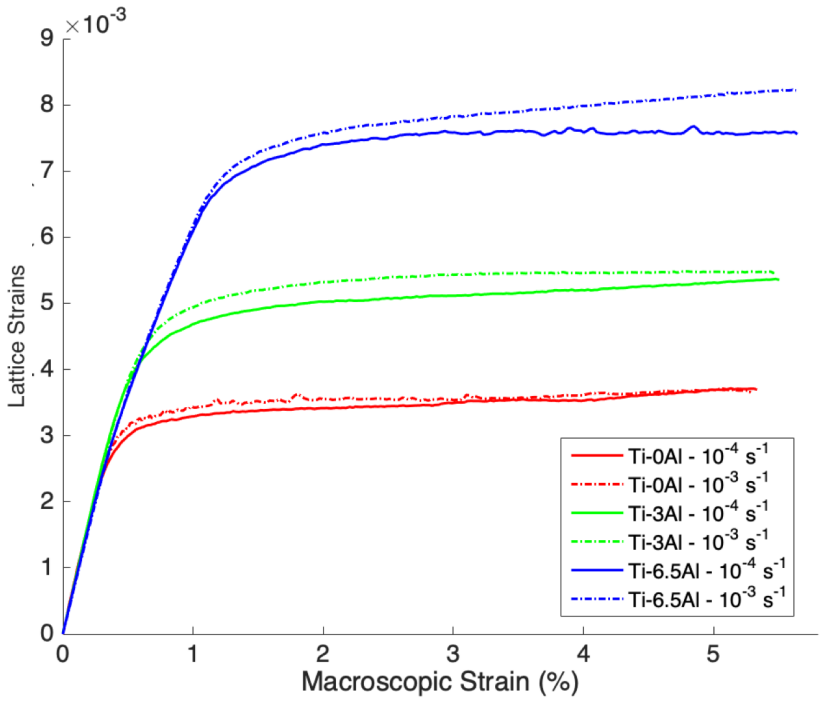


Figure 7.2: Lattice strains normal to the {10.1} crystallographic plane plotted against macroscopic strain for all alloys at both strain rates.

It is immediately apparent that the higher aluminium content increases the strain within the lattice significantly. Higher lattice strain is accumulated at yield before levelling out. Additionally, comparing the results of the 10^{-4} s^{-1} and 10^{-3} s^{-1} strain rates, there appears to be a difference in the rate sensitivity behaviour within the lattice strain response.

Various crystallographic directions will be analysed in the next sections individually for each low aluminium system, where the lattice strains at yield and effective moduli are compared. Representations of the crystallographic directions examined are shown in Figure 7.3.

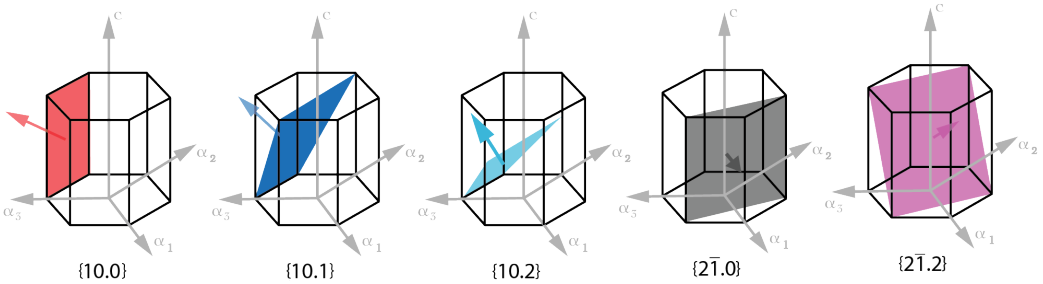


Figure 7.3: Crystallographic directions examined for Ti-0Al, Ti-3Al and Ti-6.5Al.

Ti-0Al

For Ti-0Al, or cp-Ti, in the loading direction, a slight increase is observed in the lattice strain response for the higher strain rate. The {10.0} and {10.2} directions are the only ones that appear to be otherwise affected by the prescribed increased strain rate, Figure 7.4. Note, the lattice strain normal to the {10.0} is higher at the lower strain rate and the trend is reversed normal to the {10.2} direction. Differences may be due to the individual microstructures of each specimen, which may have arisen due to local chemistry as the production of small scale specimens is generally less homogeneous than full scale aircraft grade alloys .

In the transverse direction, the compressive lattice strains are generally greater for the higher strain rate except for normal to the {20.1} direction, however the results may be due to averaging or lack of responses in this direction. Generally, the Ti-0Al shows fairly consistent behaviour in all directions.

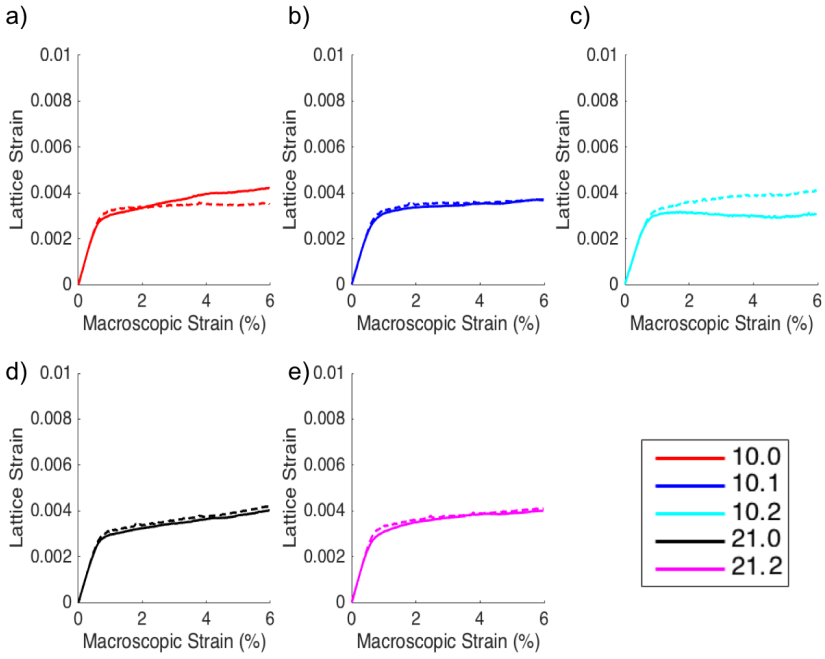


Figure 7.4: Lattice strain evolution in the loading direction for Ti-0Al for the a) {10.0}, b) {10.1}, c) {10.2}, d) {21.0} and e) {21.2} directions, where the dashed line is the corresponding response at the higher strain rate (10^{-4} s^{-1}).

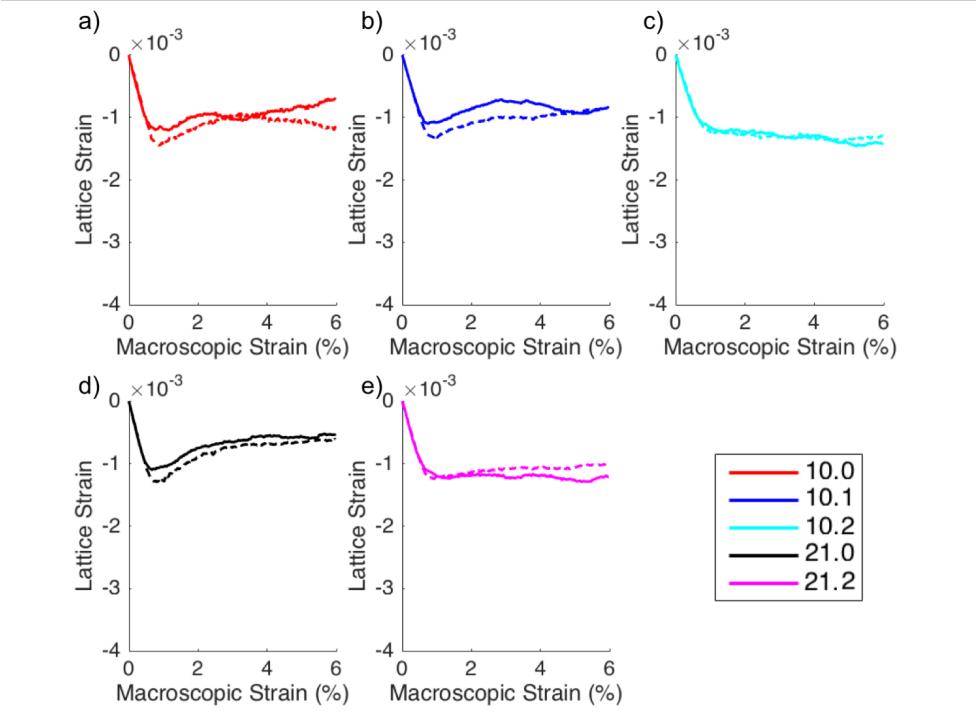


Figure 7.5: Lattice strains in the transverse direction for Ti-0Al for the a) {10.0}, b) {10.1}, c) {10.2}, d){21.0} and e){ 21.2} directions, where the dashed line refers to the higher strain rate (10^{-3} s^{-1}).

Ti-3Al

For the Ti-3Al in the loading direction, the effect of the strain rate is more pronounced and more uniform than the Ti-0Al with the higher strain rate showing an increase in lattice strains for all directions considered. The trends remain fairly consistent for each crystallographic direction. This relationship is not as well defined in the transverse direction.

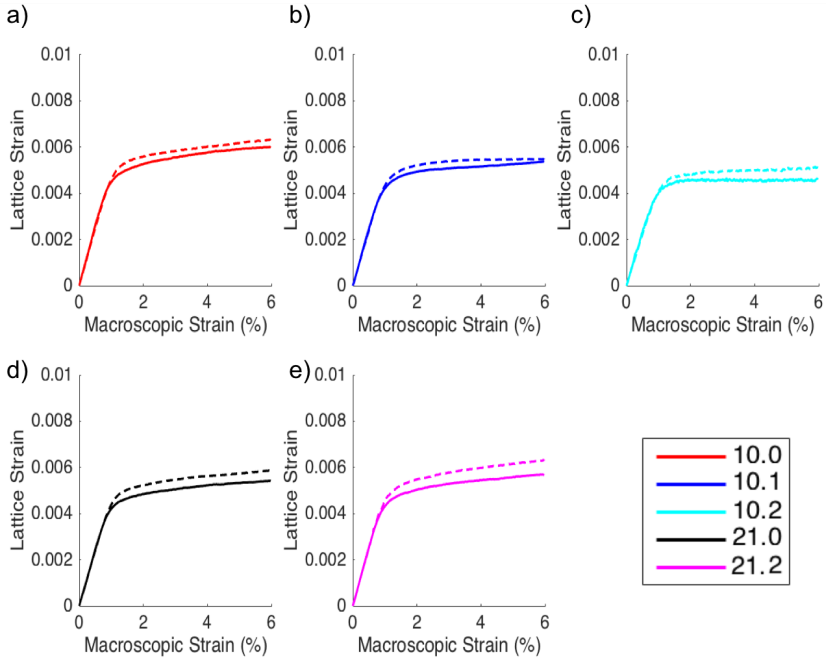


Figure 7.6: Lattice strain evolution in the loading direction for Ti-3Al for the a) {10.0}, b) {10.1}, c) {10.2}, d) {21.0} and e) {21.2} directions, where the dashed line refers to the higher strain rate (10^{-3} s^{-1})).

Table 7.4: Strain rate sensitivity and difference between lattice strain of Ti-3Al (at 3% engineering strain) for various crystallographic directions.

hkil	% Increase	SRS
10.0	5.23%	0.02214
10.1	6.02%	0.02541
10.2	7.86%	0.03288
21.0	8.45%	0.03523
21.2	9.27%	0.04344

Interestingly, the difference between the lower and higher strain rates seems to increase depending on the distance from the centre of the powder diffraction ring. Table 7.4 is ordered by distance from the centre of the powder diffraction rings, and a significant spread of strain rate sensitivity values is observed. In comparison to the macroscopic values, with a 7.48% increase in macroscopic strain (at 3% engineering strain) and a strain rate sensitivity parameter of 0.031308, these values are fairly consistent and are plausibly contribute to the overall average result. Other factors will contribute such as the reflections of directions which are unable to be captured by XRD.

Compressive strains in the transverse direction are plotted in Figure 7.7. At approximately the yield point, the compressive strains begin to reduce significantly, this amount varies depending on the crystallographic direction studied. The normal to the {10.2} and {20.1} planes do not exhibit this reduction in lattice strain but these remain fairly consistent through deformation.

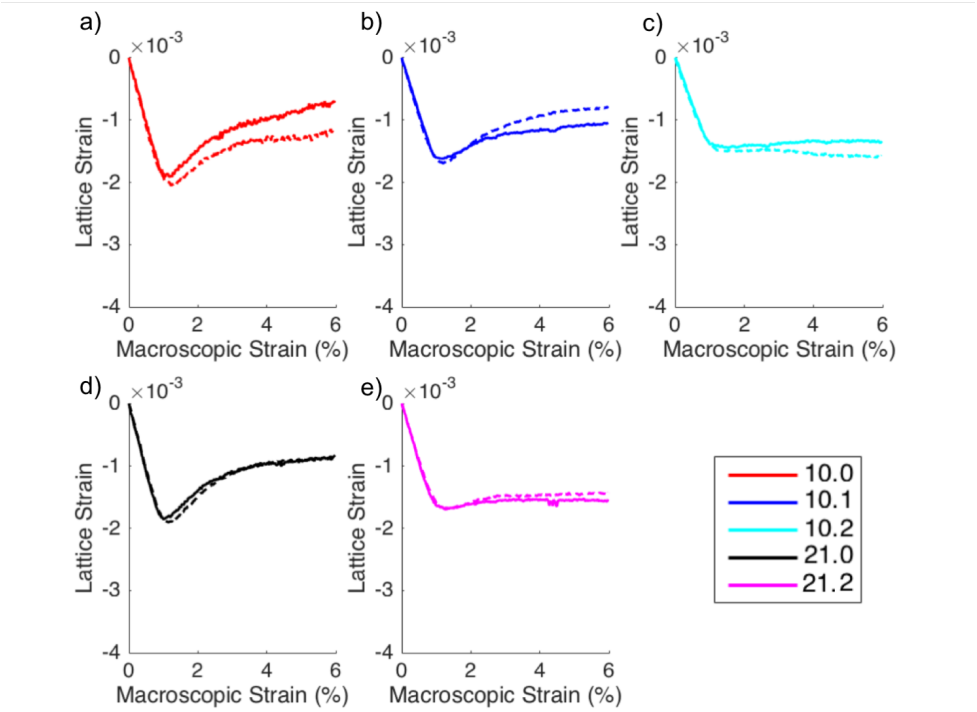


Figure 7.7: Lattice strains in the transverse direction for Ti-3Al for the a) {10.0}, b) {10.1}, c) {10.2}, d) {21.0} and e) {21.2} directions, where the dashed line refers to the higher strain rate (10^{-3} s^{-1}).

Ti-6.5Al

Increased strain rate sensitivity is also observed for Ti-6.5Al in all orientations considered, Figure 7.8. Opposite to the trend observed for Ti-0Al, the lattice strain in the {10.2} direction is fairly consistent for both strain rates, but strain rate sensitivity is evident in all other directions.

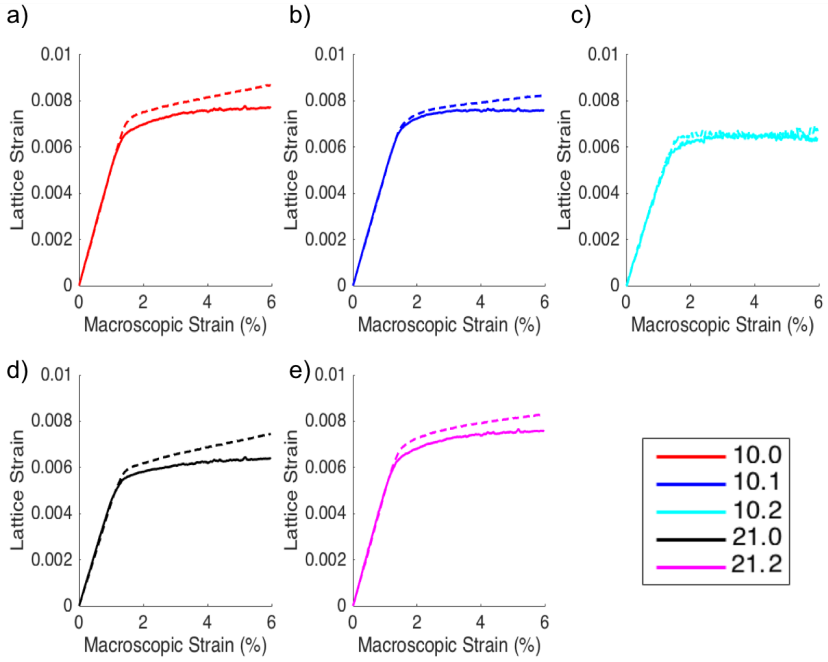


Figure 7.8: Lattice strains in the loading direction for Ti-6.5Al for the a) {10.0}, b) {10.1}, c) {10.2}, d) {21.0} and e) {21.2} directions, where the dashed line refers to the higher strain rate (10^{-3} s^{-1})).

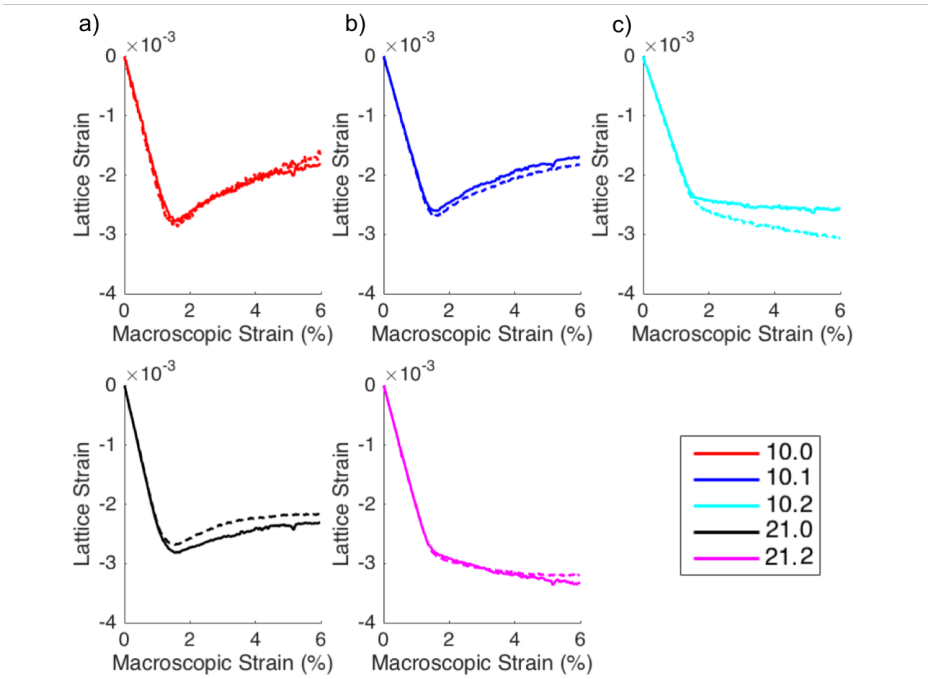


Figure 7.9: Lattice strains in the transverse direction for Ti-6.5Al for the a) {10.0}, b) {10.1}, c) {10.2}, d) {21.0} and e) {21.2} directions, where the dashed line refers to the higher strain rate (10^{-3} s^{-1}).

As in the Ti-3Al case, a significant reduction in compressive lattice strain is observed post yield. Where the {20.1} and {10.2} compressive strains also show differing behaviour and actually continue increasing for Ti-6.5Al (Figure 7.9). These directions are consistently more stable post yield in the transverse direction.

The lattice strains at yield and an effective moduli for each experiment are summarised in Tables 7.5 and 7.7, respectively. The effective moduli generally remain of similar magnitude, however in the {10.2} and {21.0} directions, this increases with increasing aluminium content. The implications of this are that the addition of aluminium increases the strength in these directions. For the Ti-6.5Al, a significant reduction in lattice strain is observed at yield for the {10.2} and {21.0} directions in comparison to other crystallographic directions. This may go some way to explaining the differing compressive lattice behaviour observed. The normalised values for each test for the slower of the strain rates are given in Table 7.6

Table 7.5: Lattice Strains at yield for low aluminium Ti-alloys for both strain rates. Values have been normalised for each experiment in brackets

	hkil	Ti-0Al		Ti-3Al		Ti-6.5Al	
Lower (10^{-3} s^{-1})	{10.0}	0.002922	(1.025)	0.004742	(1.126)	0.006707	(1.191)
	{10.1}	0.002940	(1.032)	0.004441	(1.055)	0.006863	(1.219)
	{10.2}	0.002936	(1.030)	0.004211	(1.000)	0.005907	(1.049)
	{21.0}	0.002850	(1.000)	0.004418	(1.049)	0.005630	(1.000)
Higher (10^{-3} s^{-1})	{10.0}	0.003129	(1.032)	0.005085	(1.336)	0.007303	(1.297)
	{10.1}	0.003114	(1.027)	0.004746	(1.059)	0.007111	(1.263)
	{10.2}	0.003151	(1.039)	0.004813	(1.074)	0.006370	(1.131)
	{21.0}	0.003032	(1.000)	0.004481	(1.000)	0.006019	(1.000)

Table 7.6: Effective moduli calculated for each lattice strain, calculated from the lattice strain and macroscopic stress results of each experiment.

hkil	Ti-0Al		Ti-3Al		Ti-6.5Al	
{10.0}	116.97	117.27	113.14	114.35	117.41	116.66
{10.1}	121.04	119.56	120.04	120.15	121.15	122.75
{10.2}	121.76	124.06	128.36	129.80	136.63	134.44
{21.0}	121.41	120.74	120.42	119.05	133.88	134.44
{21.2}	116.91	113.67	116.43	113.83	116.40	114.82

Table 7.7: Normalised effective moduli for each lattice strain, extracted from Table 7.7 where the strength of the {10.2} direction is greatly altered by increasing aluminium content.

hkil	Ti-0Al	Ti-3Al	Ti-6.5Al
{10.0}	1.00	1.00	1.01
{10.1}	1.04	1.06	1.04
{10.2}	1.04	1.13	1.17
{21.0}	1.04	1.06	1.15
{21.2}	1.00	1.03	1.00

7.3 Discussion

Increased flow stress is observed with increasing aluminium content; the higher flow stress may be indicitave of increased twinning (as plastic deformation occurs at higher stresses). However, slip tends to increasingly localise with increasing aluminium content [71], actually decreasing the material's ability to twin. Powder diffraction rings, which gives insight into the initial, undeformed texture of these materials, are shown in Figure 7.10. It is evident that the Ti-6.5Al has a distinct response which may affect both the crystal scale and macroscopic deformation.

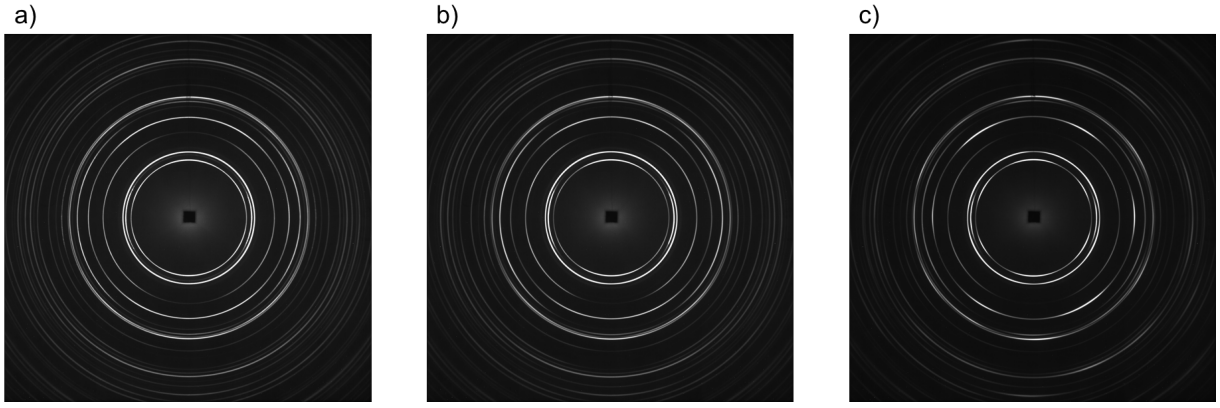


Figure 7.10: Initial powder diffraction rings where a) Ti-0Al and b) Ti-3Al show similar results but c) Ti-6.5Al appears distinct, indicative of a different texture.

All materials have been processed via the same processing regimes and machined using the same method and speeds, therefore the differences in microstructure are exclusively due to the constituent elements. Ideally, future microscopy work would be performed on these deformed samples to analyse the differences in the microstructure. Electro-polishing is required on these materials prior to EBSD.

Of particular interest is the increasing strength of the {10.2} direction with increasing aluminium content. The {10.2} and {20.1} directions in the transverse direction for all aluminium contents operate differently to the others examined where at 0 and 3% aluminium content, lattice strain accumulation plateaus and the 6.5% it continue increasing where all other directions reduce post-yield.

Essential conclusions from this section of work include; an expected increase in strength and yield stress is found with increasing aluminium content. A fairly linear relationship is theorised between the percent of aluminium content and predicted yield stress. Increasing aluminium contents also decreases strain hardening effects.

Lattice strains at yield are found to increase with increasing aluminium content, in both the loading and transverse direction for multiple hkls. The strengths of some crystallographic directions are seen to increase significantly with increasing volume fraction of aluminium. Future extension to this work would include microscopy leading to CPFE modelling and further examination of the effect of texture on Ti-Al systems.

Chapter 8

Single and dual-phase titanium alloys

Ti-6Al-4V is a common engineering alloy in the aerospace sector for the reasons outlined previously in Section 1. In situ tensile experiments performed on Ti-6Al-4V and Ti-6.5Al where the latter is a single phase alloy designed to replicate the α phase observed in Ti-6Al-4V, i.e. with no β phase are now presented. The comparison of these materials allows investigation of the effects of the β phase. Generally, Ti-6Al-4V products contain only 5-10% β phase by volume, therefore this phase tends to be neglected in computational analysis due to increased complexity. The objective of this chapter is to assess the validity of this assumption.

8.1 Macroscopic Response

A single specimen of Ti-6Al-4V and of Ti-6.5Al were deformed via uniaxial tension in situ at CHESS with a SRJ. The macroscopic stress strain responses of Ti-6Al-4V and Ti-6.5Al are compared in Figure 8.1, where the Ti-6Al-4V results have been reproduced from Chapter 4. The initial elastic response appears almost identical until around 600 MPa, after which the results no longer align. The Ti-6Al-4V has a higher yield stress and maintains a flatter response than the Ti-6.5Al even after the strain rate jump. This behaviour indicates a different hardening response due to the inclusion of the β phase. The jump also seems to occur with a steeper gradient for the Ti-6.5Al, although this cannot be confirmed due to the limited number of data points captured. The stress-strain response during the jump implies that the increase in macroscopic stress due to the jump is similar between materials, and the jump is unlikely to be affected by the inclusion of the β phase.

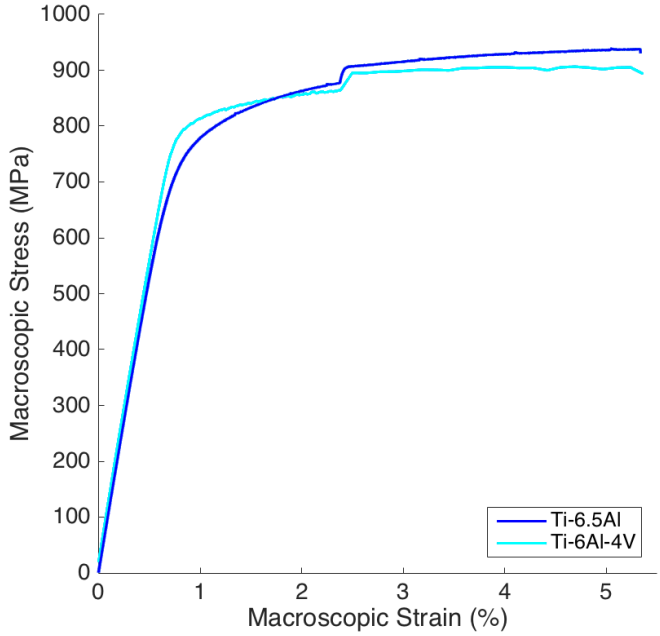


Figure 8.1: Macroscopic stress-strain response of billet Ti-6Al-4V (dark blue) and Ti-6.5Al (light blue) deformed under uniaxial tension with a strain rate jump from 10^{-4} s^{-1} to 10^{-3} s^{-1}.

The strain rate sensitivity, m, for the SRJ is calculated as described previously in Section 5.5,

$$\left(\frac{\sigma_2}{\sigma_1}\right)^m = \frac{\dot{\epsilon}_2}{\dot{\epsilon}_1} \tag{8.1}$$

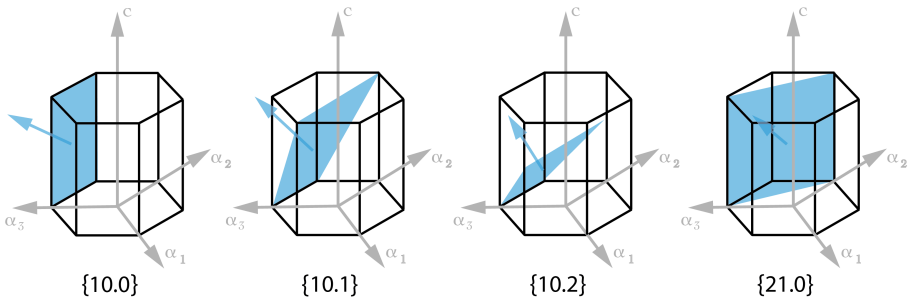
where m is calculated using the stresses immediately before and after the jump, σ_1 and σ_2 respectively.

The m parameter has been calculated as 0.016176 for the Ti-6Al-4V where the increase in strain during the jump is 32.8 MPa (3.80%). The value for Ti-6.5Al is 0.016135 with an increase of 29.4 MPa (3.35%). These SRS values are similar and indicate that m is unlikely to be affected by the presence of the β phase, despite observed differences in yield and work hardening behaviour. For these two materials, there is a large difference in terms of the plastic response, highlighting the importance of the addition of the β phase. It has been suggested that the stress is able to redistribute across phases, increasing the overall material strength [86]. The β phase appears to substantially reduce the level of strain hardening observed.

8.2 Lattice Strain Response

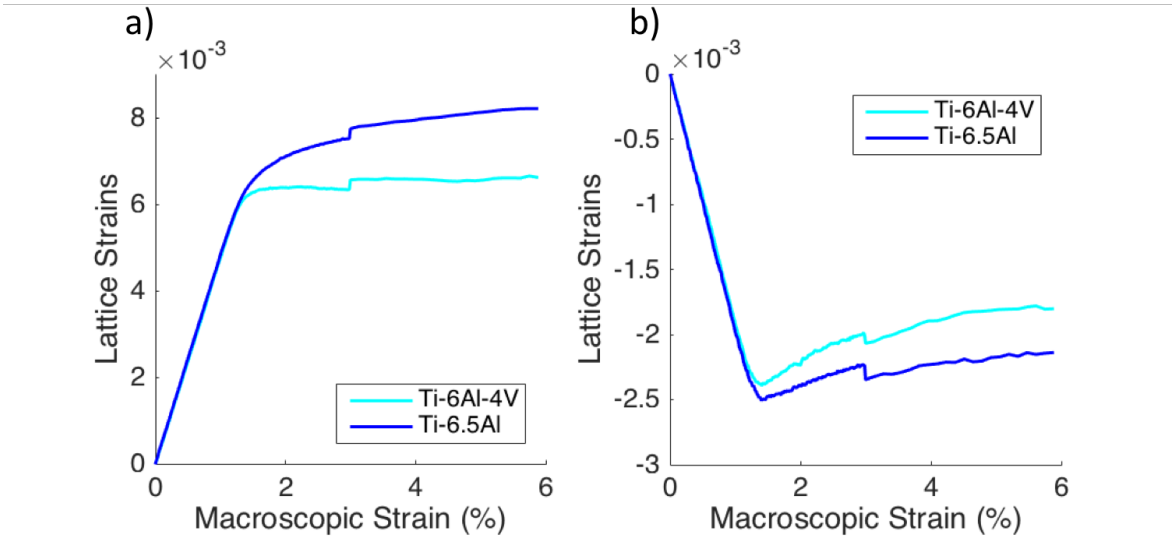
Lattice strain evolution is extracted from the azimuthal sector of powder diffraction rings representing the loading direction, as described in Section 3.3. The crystallographic directions studied here include the normal to the {10.0}, {10.1}, {10.2} and {21.0} planes, as these are of high multiplicity and sufficient points have been collected by the detector for both materials to allow comparative analysis, see Figure 8.2.

Lattice strain accumulation in the {10.1} direction is plotted in Figure 8.3. This shows the difference in lattice strain response is significant, with the flatter response of the Ti-6Al-4V mirroring that of the bulk, macroscopic response. A higher level of lattice strain was accumulated in both the loading direction and compressively in the transverse direction for Ti-6.5Al in the {10.1} direction. Post yield, the lattice strain in Ti-6.5Al continues to increase whereas the Ti-6Al-4V remains at around the same value, suggesting no additional stress is being accumulated but rather it is being redistributed. Overall, the lattice contains significantly reduced stress in the {10.1} direction with the inclusion of the β phase.



[H]

Figure 8.2: Hexagonal unit cells showing the crystallographic directions compared for both materials in this chapter in terms of lattice strain evolution.



[H]

Figure 8.3: Lattice strain response normal to the {10.1} direction compared for both materials, a) in the loading direction and b) in the transverse direction.

The lattice strain evolution normal to the {10.0}, {10.2} and {21.0} directions are shown in Figure 8.4. The {10.0} and {10.2} directions show a similar response to the {10.1} direction, with the Ti-6.5Al reaching marginally higher lattice strains than the Ti-6Al-4V post yield. For the normal to the {10.0} direction, post yield, the

lattice strains for both alloys continue to rise steadily but again the Ti-6.5Al has an increased lattice strain compared with the Ti-6Al-4V.

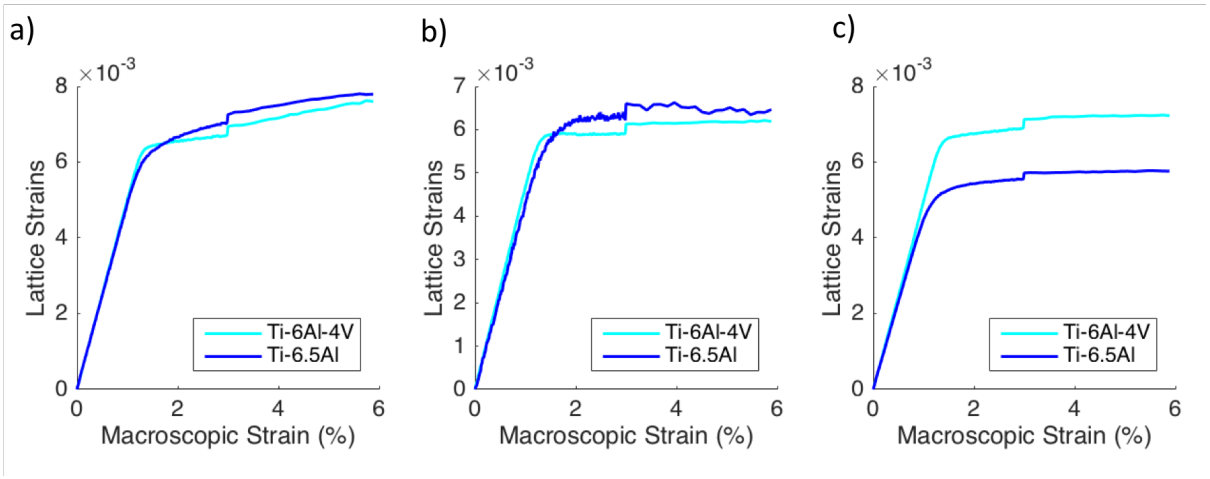


Figure 8.4: Lattice strain response in the loading direction for a) the normal to the {10.0} direction, b) the normal to the {10.2} direction and c) the normal to the {21.0} direction.

The {21.0} direction, Figure 8.4c, shows the reverse trend, with the Ti-6Al-4V results substantially higher than those of Ti-6.5Al. This Ti-6.5Al value appears uncharacteristically low. This flat response for both materials implies no further accumulation of stress along this direction. From the powder diffraction rings, Figure 8.5, it appears that the 26 degree azimuthal bin width chosen does not capture the {21.0} diffraction ring sufficiently due to the distributions of directions. However, investigations by altering the bin size significantly did not noticeably alter the response in the {21.0} direction; it is actually the least sensitive of those considered. In this direction, the behaviours appear identical, with the same flat response, independent of material. The lattice strain at yield is substantially lower for Ti-6.5Al in this direction, whereas in all other directions, comparable levels of lattice strain are observed.

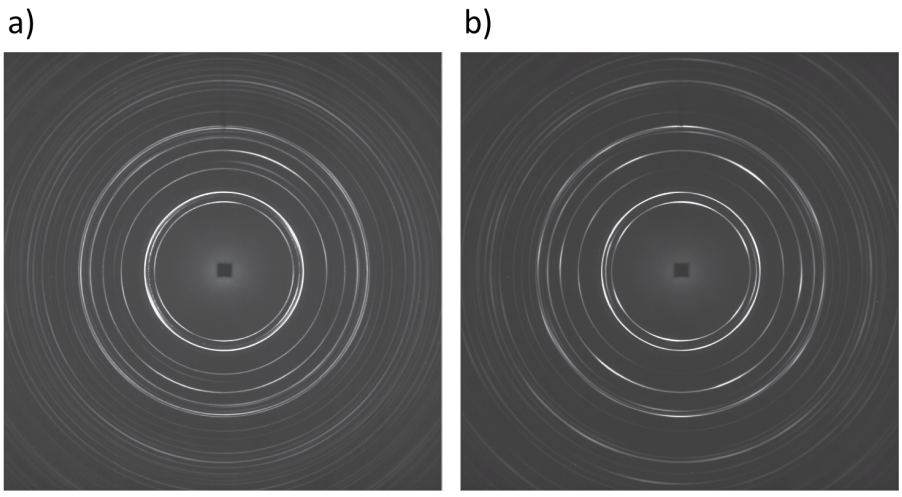


Figure 8.5: Powder diffraction rings, showing the initial state of a) the Ti-6Al-4V and b) the Ti-6.5Al before deformation, captured at CHESS and analysed as in Section 3.3.

8.3 Microstructure

High resolution EBSD scans were performed at 300x magnification with a step size of 0.5 μm, as in Section 3.5, after the polishing regimes described in Section 3.5.2. Figure 8.6 shows IPF maps of Ti-6Al-4V and Ti-6.5Al with low confidence index values (< 0.1) removed from the analysis. Areas coloured black in the IPF maps, more obvious in the Ti-6.5Al case, indicate regions where the crystallographic orientation could not be accurately resolved. These are generally observed at grain interfaces, particularly at the boundaries of macrozones. The IPF maps for both the deformed and undeformed Ti-6Al-4V contain a significant portion of basal oriented macrozones, otherwise showing a fairly randomly oriented, equiaxed microstructure. The average grain size is reduced in the deformed case. This is difficult to accurately quantify due to the reduced scan quality.

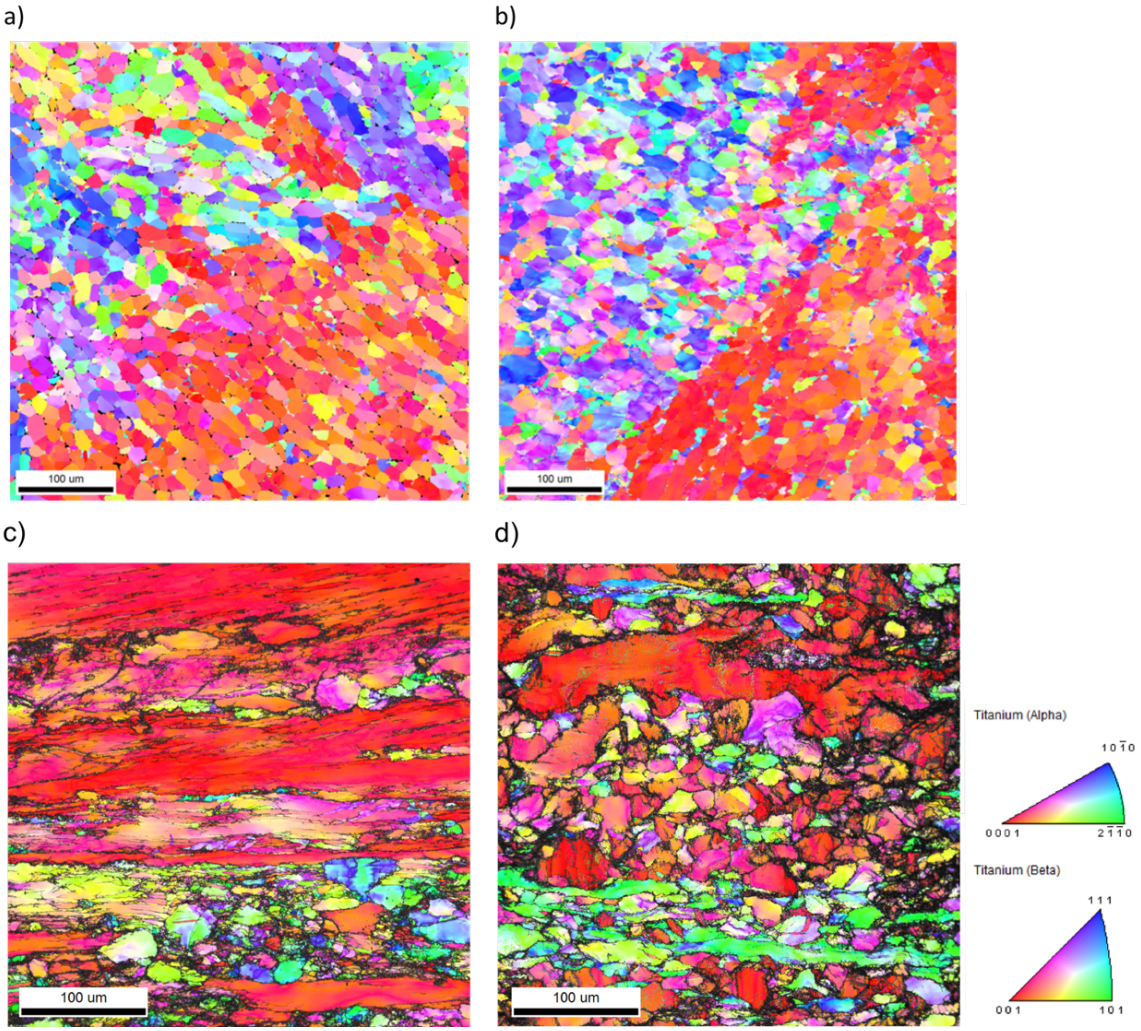


Figure 8.6: EBSD IPF maps of a) Ti-6Al-4V in undeformed condition and b) deformed to ∼5.5% engineering strain after strain rate jump. Where a) and b) have been reproduced from Section 4.1.1 for comparison with c) the undeformed Ti-6.5Al and d) Ti-6.5Al deformed to ∼5.5% engineering strain including a jump in strain rate. Scale bars = 100μm for all IPF maps.

For some areas of the Ti-6.5Al, the grain size is difficult to extract as large sections appear as a single grain. Damage is evident in the undeformed IPF map as shown by the substantial gradients observed across individual crystals, notably yellow-pink in the centre of Figure 8.6a. Again, there is a high percentage of the Ti-6.5Al IPF map consisting of a basal macrozone.

Due to the lab scale quantities of the as-supplied Ti-6.5Al, see Section 1.4.4, the production will have produced a lower quality microstructure. This is evident in the EBSD maps where low quality results have been removed. Lower resolution EBSD scans (105-150x magnification with a step size of 5 microns) were used to generate pole figures, as in Figure 8.7. The strengthening of the texture for the Ti-6Al-4V during a jump in strain rate has been discussed previously in Section 4.2. The texture of the Ti-6.5Al is already well defined from previous thermo-mechanical processing (Section 4.1.1). The basal/transverse texture is consistent between both deformed materials. It is difficult to distinguish whether the observed differences in the macroscopic and crystal scale stress-strain response are due to the lack of β phase or the microstructural differences. Additionally, a non negligible amount of data has been removed from the IPF maps for Ti-6.5Al due to the low confidence index of the data.

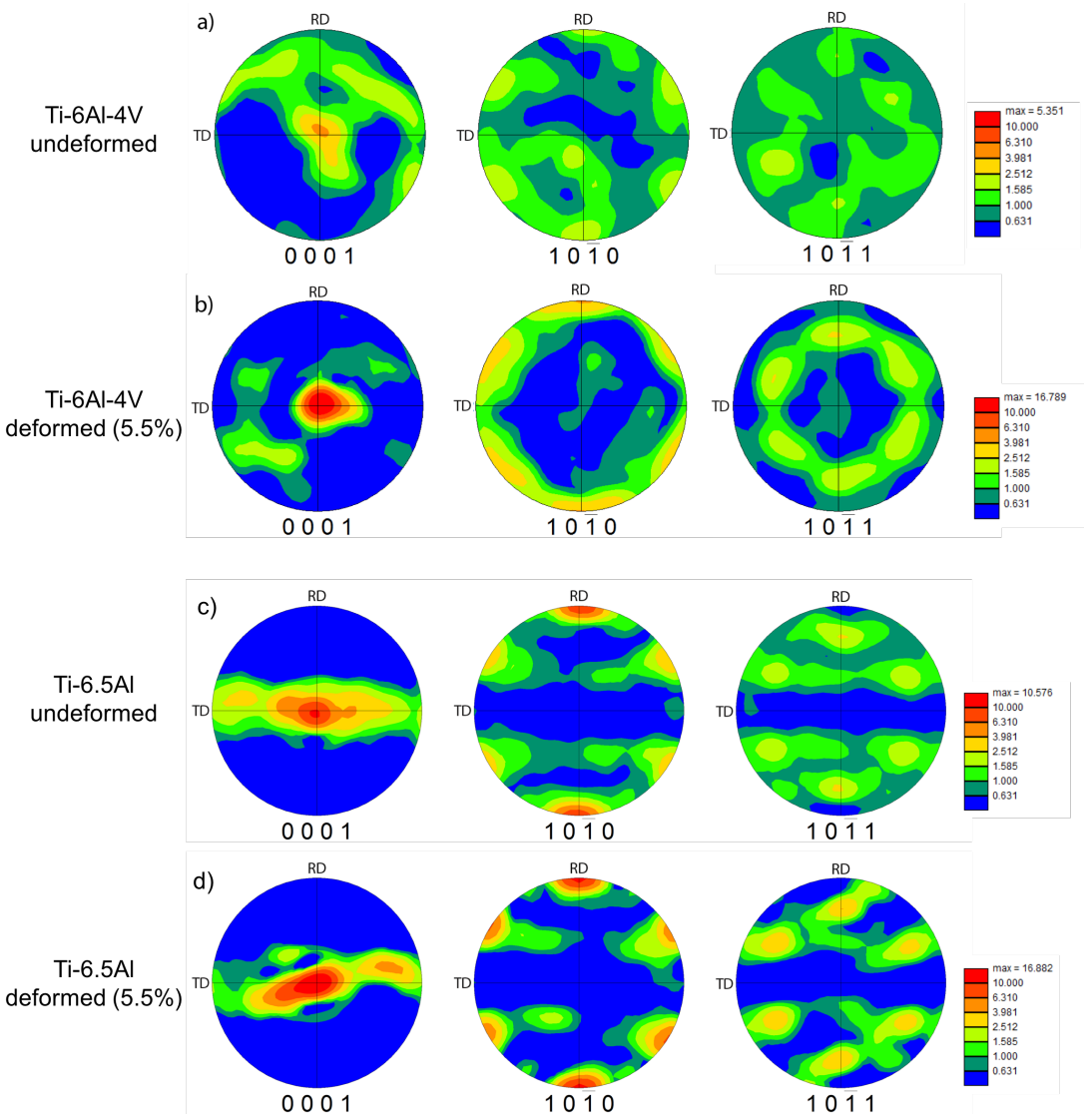


Figure 8.7: Pole figures showing the distribution of orientations for three relevant directions in a) the undeformed Ti-6Al-4V, b) the deformed Ti-6Al-4V, c) the undeformed Ti-6.5Al and d) the deformed Ti-6.5Al condition. Pole figures have been scaled for comparison.

Figure 8.8 shows the local average misorientation (LAM). This is the misorientation between neighbouring crystals. The grain averaged or grain relative misorientations would not produce accurate results as the grains are not well defined in the Ti-6.5Al microstructure. The increased misorientation observed post-jump highlights the effect of the jump in strain rate. However, the initial Ti-6.5Al material contains significant deformation and this is also evident in the local misorientation (Figure 8.8a).

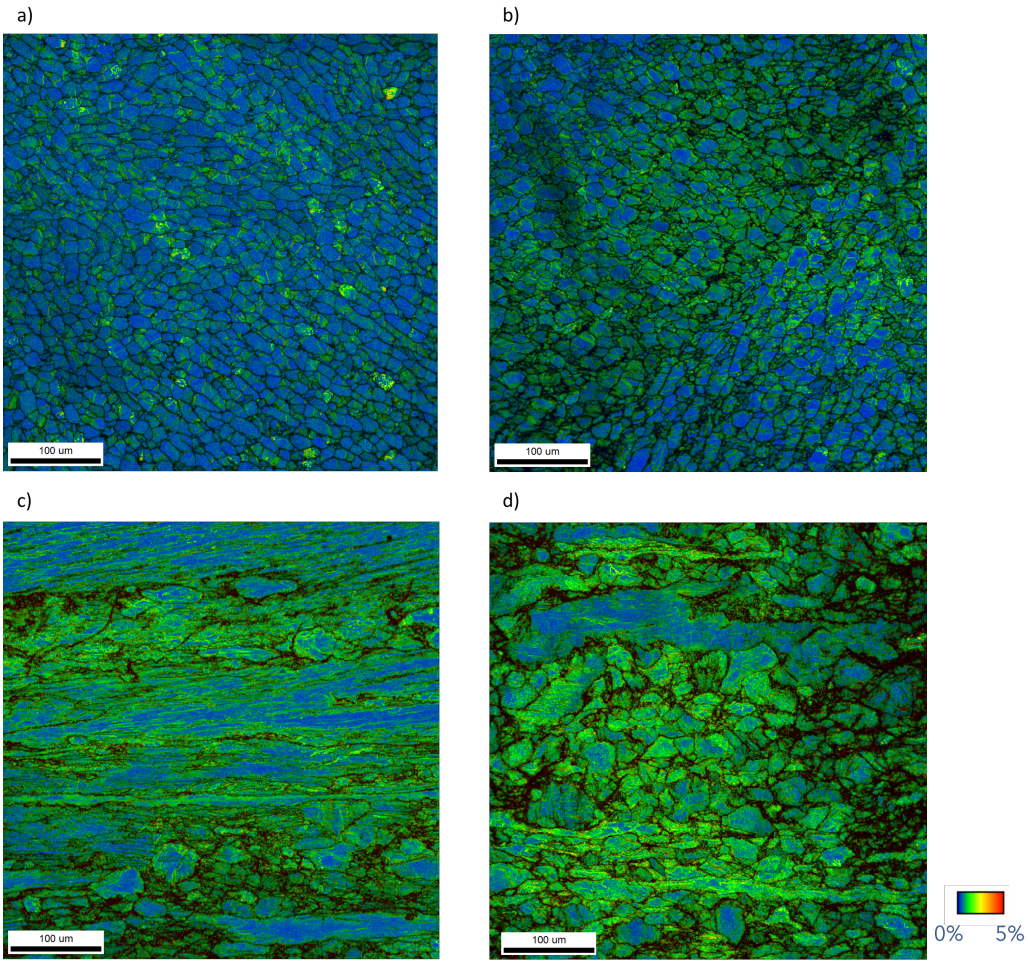


Figure 8.8: Local average misorientation for a) undeformed Ti-6Al-4V, b) Ti-6Al-4V post-jump, c) undeformed Ti-6.5Al and d) Ti-6.5Al post-jump. The crystallographic orientation of these areas is shown previously in an IPF map, Figure 8.6.

8.4 Discussion

Constant strain rate experiments at 10^{-4} and 10^{-3} s^{-1} were also performed on the Ti-6.5Al. Post-experiment EBSD was then performed on the deformed samples. The IPF maps and LAM are compared in Figure 8.9. The LAM observed is significant in all cases for the Ti-6.5Al, however areas of basal-oriented macrozones have lower misorientation values compared to the rest of the material. Areas of highly-deformed, randomly-orientated grains (namely Figure 8.8d and Figure 8.9c) show greater levels of misorientation. It is possible that the post-jump misorientation increases in Ti-6.5Al is due to the observed microstructure. It is of interest to note that the vanadium in Ti-6Al-4V is generally found at the interfaces of the α phase and this may have an effect on the overall results.

Pole figures for the constant strain rates are shown in Figure 8.10. A fairly consistent texture is observed for each case. The maximum intensity values observed in the post jump condition are higher, implying an

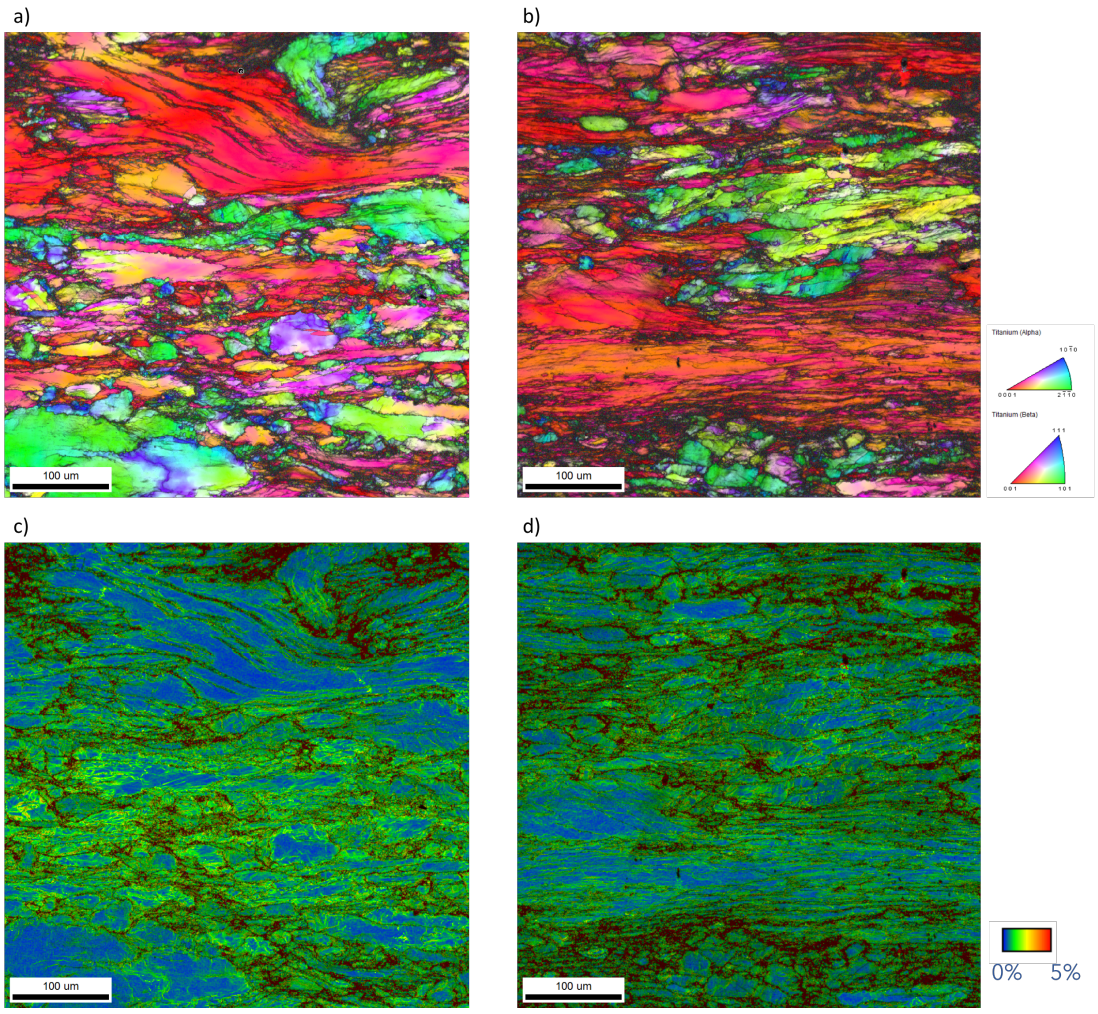


Figure 8.9: IPF maps showing the deformed Ti-6.5Al microstructure for constant strain rate of a) 10^{-4} s^{-1} (lower) and b)10^{-3} s^{-1} (higher). c) and d) show the local average misorientation of the corresponding areas shown in a) and b).

increased texture strength. The observed texture measurements show an increase post-jump, indicating that the jump in strain rate affects Ti-6.5Al and Ti-6Al-4V in the same manner.

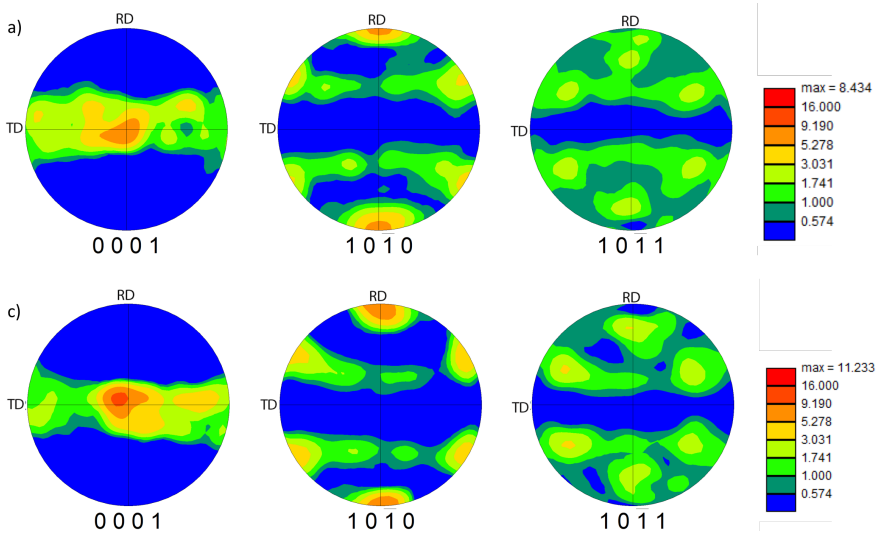


Figure 8.10: Pole figures showing the crystallographic texture of the Ti-6.5Al post deformation (deformed to ∼5.5% engineering strain) via constant strain rates of a) 10^{-4} s^{-1} (lower) and b)10^{-3} s^{-1} (higher).

Grain boundary sliding (GBS) is observed relatively frequently in cp-Ti under uniaxial tension at room temperature at strain rates between 5×10^{-5} s^{-1} and 5×10^{-4} s^{-1} [229]. It is also observed in analysis of room temperature creep. It is however less pronounced where the β phase is evident, suggesting the smaller inter granular β phase can act as a barrier, pinning grain boundary sliding. GBS is often studied in ultra-fine grained materials, however GBS has been detected at small plastic strains and is even suspected to occur within the elastic regime [58, 174]. It has also been suggested that grain boundary sliding exists as a separate deformation mechanism [117]. The jump may be activating grain boundary sliding mechanisms or this could potentially account for the differing hardening responses as the absorption of emitted dislocations by grain boundaries will increase the strain hardening response.

The EBSD performed in this section is not of optimal quality. Future work on this may involve heat treatment prior to testing and electro-polishing of material would greatly improve the quality of scans and allow for an improved overall analysis.

8.5 Conclusions

For the Ti-6Al-4V and Ti-6.5Al compared, macroscopically, there is a substantial difference in terms of the plastic response, highlighting the importance of the β phase. The addition of the β phase appears to significantly dampen the hardening plastic response. The presence and morphology of the β phase has previously been observed altering both the yield stress and work hardening behaviour [95]. Stress redistribution from the α to β phase may account for this lack of increase in stress in Ti-6Al-4V, which would not be possible in single phase Ti-6.5Al.

At the crystallographic scale, the Ti-6Al-4V shows a flat lattice strain response in most directions. The values for both materials are generally similar until yield. The Ti-6.5Al lattice strains all follow the same trend, tending to increase further post yield. The normal to the {10.1} direction however is level post yield for the Ti-6Al-4V yet continues increasing substantially for the Ti-6.5Al.

The crystallographic textures of both materials appear to have the similar basal/transverse texture which is expected from the thermo-mechanical processing [179]. However, the strength is increased after the jump in strain rate for both materials. Macrozones have been observed in both materials and appear to take up a substantial amount of the microstructure. Different microstructures have also been observed with the equiaxed Ti-6Al-4V having fairly regular grain size and shapes and the microstructure of the Ti-6.5Al proving more difficult to quantify with areas of undefinable grain boundaries and evident deformation in the initial samples. Had microstructural analysis been performed before specimens were machined, further heat treatments would have been performed to enable similar initial microstructures, removing some of the deformation and current uncertainties from the analysis.

It is suggested that the β phase plays an important role in Ti-6Al-4V and should be included in subsequent computational analyses. It would also be of interest to repeat these in situ experiments using a detector capable of distinguishing the β phase reflections alongside the α phase discussed herein.

Chapter 9

Summary & Conclusions

A computational and experimental investigation of titanium based alloys with a focus on Ti-6Al-4V, has been presented. Part I served as an introduction to the materials, and details the experiments performed. Experimental methods are described in Chapter 3,where a EBSD and high energy XRD are outlined in detail.

The bulk of the experimental results and computational studies were detailed in Part II. A variety of experiments were performed using high energy synchrotron XRD at CHESS, NY, USA. Lattice strain evolution and crystallographic texture were compared for billet Ti-6Al-4V deformed via quasi-static strain rates. A strain rate jump test was also performed resulting in increased texture and greater misorientation in the microstructure. These tests are repeated for different product forms of Ti-6Al-4V, allowing comparison between UDR and CR plate material. CPFEM was then introduced and Ti-6Al-4V product forms were modelled.

The final part of this work contains supplemental chapters detailing areas of further industrial interest. The strain rate sensitivity of Ti-Al alloys of varying aluminium content was examined. This led to a comparative study of Ti-6.5Al and Ti-6Al-4V in an attempt to study the effect of the addition of the β phase in Ti-6Al-4V .

9.1 Conclusions

A computational and experimental investigation of titanium alloys has been presented. High energy XRD was used to examine the lattice strain response of Ti-6Al-4V with the aim of enhancing the knowledge base by characterising the material. Crystal plasticity based finite element simulations were used to augment these data and determine the feasibility of modelling various product forms to determine accurate predictions of lattice strain evolution.

Initial parameters for the material are required to be extracted from experiments to inform the computational CPFE model. The initial plan involved using FEpX to determine accurately the strain rate sensitivity parameter (m). However, experimental results and continuing research infer a more complex situation than the FEpX software is currently equipped to deal with. The experiments suggest a SRS value for Ti-6Al-4V of 0.016. However variation in product types implies the material exhibits different rate sensitive behaviour in different crystallographic directions. The CPFE framework can account for this complexity but it is beyond the current capabilities of the FEpX software. Current software capability may be expanded to incorporate this. However, this is outwith the scope of the thesis due to time constraints and difficulties in verifying viability.

The strain rate jump experiments show the effect of the jump is visible both macroscopically and at the crystal scale. The results indicate that a jump in strain rate may move the material response from one yield surface to another. There is some evidence to suggest that jump causes increased misorientation and texture development in billet Ti-6Al-4V where the lattice strain moduli of different crystallographic directions has been captured. The SRJ causing the material to 'jump' between yield surfaces has been hypothesised and investigated computationally. Individual crystallographic directions accumulate different amounts of lattice strain during the simulated SRJ, this is seen to be true for all material products examined. The timing of the strain rate jump appears to have negligible impact on the post-jump behaviour with great alignment of macroscopic and lattice strains.

Under uniaxial tension, the CR material showing a greater absorption of energy for equivalent macroscopic strain values than that observed for the UDR material. Both materials appear to display similarly strain rate sensitive behaviour however. The α phase lattice strains at yield are generally lower for the CR than the UDR plate materiel in the same direction. The β phase lattice strains are compared for both, overall showing a large difference in the β phase lattice strain accumulated where the CR material accumulates significantly more lattice strain for the same macroscopic strain. The lattice strains continue increasing post yield for the CR Ti-6Al-4V, implying that the CR is better orientated for load redistribution, increasing the overall material strength.

The CR materiel has been examined parallel to the rollign direction and at 45 degrees. A reduction in the yield stress of $\sim$4% is the difference between the CR material from the rolling direction to 45 degrees from the rolling direction. The hardening response and rate sensitivity however are comparable. Immediately post yield, the lattice strain in numerous directions for the CR Ti-6Al-4V is highly non uniform, where the resulting magnitude and direction do not appear to be consistent crystallographic directions or experiments.

As strain rate sensitivity is important in machining and forming, where varying the strain rate can have a significant impact on the microstructure, cycling between different strain rates may improve processing times/regimes for titanium alloys. Particularly as heat treatments are generally required during processing currently and may be used to control the microstructure after this processing.

Further refinement of computational capabilities is required to accurately predict the Ti-6Al-4V product forms. The results give a decent approximation to the average values of both stress and lattice strain and the models incorporating appropriate microstructures result in simulations with the same trends. However, differences in the real materials are significantly greater. Macrozones should be modelled to improve this analysis where the three dimensional aspect of such must be quantified, this is non-trivial as the size and shape of macrozones is highly variable and this will have a significant impact on the volumes to be modelled.

9.2 Limitations

An inherent limitation on the type of work performed is the repeatability of experiments. This is due to the limited time allocated at the synchrotron. Multiple instances of the same tests would enable quantification of error in the results as the inherent variability due to the microstructural differences could be accounted for. Continual upgrades to facilities mean the results must be occasionally compared to those captured using different detectors which is not ideal as comparisons may not have equivalent data sets. This limitation motivates the use of simulations to augment the data and guide experimental work.

Whilst wire EDM is ideal for the small Ti-6Al-4V CHESS specimens used, one of the issues that arises is surface damage [146]. This should be considered in subsequent studies as surface roughness is known to affect the mechanical properties in Ti-6Al-4V in the HAZ [149], this is particularly important with the small test specimens used here. The heat affected zone (HAZ) has been seen to be approximately 10 microns ($\sim$1% of the specimen length) in the SEM for specimens used.

Issues in acquiring the DIC data during the current setup must be addressed. Changes to the Spec setup allowing reduction of the acquisition rate are required for future analyses. Accurate quantification of macroscopic strain is required for these experiments as the reliance on the corrected load frame data is not ideal.

The computational model has been devised to examine the macroscopic and lattice strain response however it is limited in terms of plastic flow occurs only by slip, neglecting other mechanisms such as twinning. The inclusion of the β phase should be accounted for to improve subsequent analyses. In recent years, the inclusion of the β phase in CPFE modelling has increased significantly [10]. Extension of the current computational work to a dual phase framework would be beneficial.

9.3 Potential Future Work

Examining the microstructure of a sample in three dimensions to better quantify the microstructure and improve accuracy of polycrystal instantiation of polycrystal, should be considered. There is potential to incorporate 3D EBSD or obtain a 3D microstructure from the synchrotron using the Rietveld method to ensure modelling is highly accurate [208]. There is even the possibility to compare the model to post-mortem EBSD

to check if stresses and strains accumulate as expected, this requires non destructive initial characterisation techniques, i.e. not 3D EBSD.

Macrozones are a particular area of interest for future work as their location, orientation and volume are likely to have a significant effect at the crystal scale. Accurate quantification of macrozones in product Ti-6Al-4V could be attempted using 3D EBSD [94, 226]. Recent work to identify macrozones using ultrasonics may provide an alternative method to determine macrozone volume [144]. Computational modelling of these macrozones, as discussed in Section 6.2.2, should be considered in future analysis. Again it is suggested that both phases should be represented in the analysis.

Residual stresses may be extracted from XRD experiments [218]. A setup to allow the inclusion of these results would improve studies by ensuring comparable residual stresses exist within individual specimens, or these are otherwise accounted for. This is desired to improve the overall accuracy of analysis. Particularly in the case of different processing routes. Residual stresses have not been calculated here, this examination would be a useful inclusion in future work.

Appendix A

Specimen Design Drawings

Drawings used to manufacture specimens with tolerances are given in Figures A.1 and A.2.

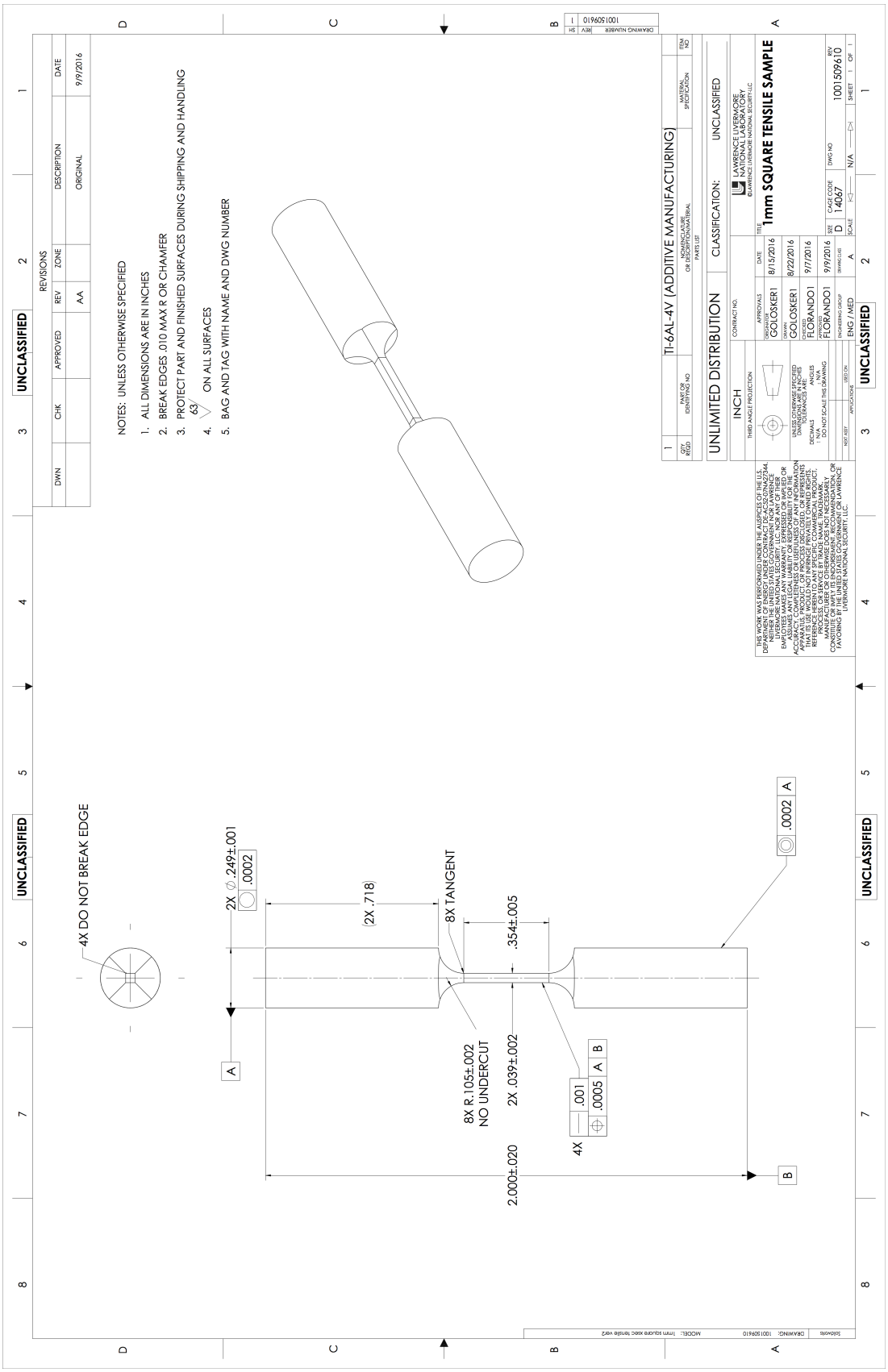


Figure A.1: Specimen Design for use in situ at CHESS.

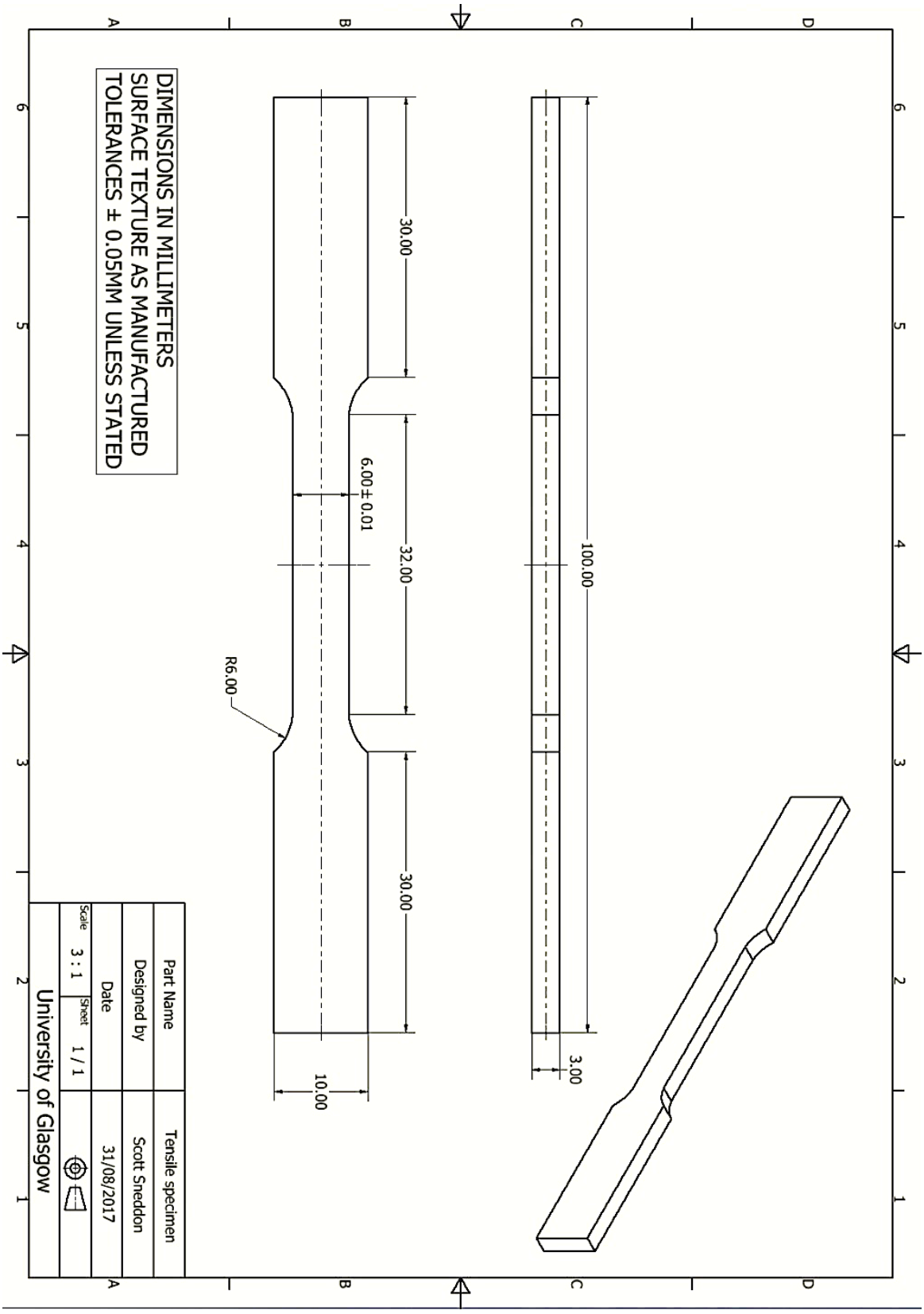


Figure A.2: Standard specimen design used for mechanical tests to failure.

Appendix B

Uniaxial tensile testing - failure behaviour

B.1 Setup

Ti-6Al-4V was deformed under uniaxial tension until failure in test regimes under two constant strain rate tests and two SRJ tests where the jump is defined as previously and the other is the reverse, i.e. from the higher to lower strain rates, see Table B.1. Identical strain rates have been employed in this section to those used previously. Specimen design is provided in Figure A.2 and material information is summarised in Section 1.4.2. These experiments were performed to determine whether an early jump in strain rate impacts the overall failure of the specimen. The experiment performed at 10^{-4} s^{-1} (slower strain rate) should be neglected due to an error causing the instantaneous application of approximately 16kN on the sample, significantly damaging the sample. Macroscopic details have been retained for interest.

A Zwick Roell 250 kN Testing Machine was employed. This universal testing machine has software is capable of instantaneously changing from one strain rate to the next in 'free test' mode. Delays may be introduced due to the machine pneumatics but this remains negligible under these conditions. All experiments were performed in position control mode with a 25mm Epsilon Axial Extensometer (Model 3542) connected. An extensometer is a device used to measure changes in the length of an object, it is used here to accurately capture sample strain during deformation. A contact extensometer was physically attached to the gauge section of the specimen. The machine was controlled from the extensometer reading and position control meant the strain rate was defined as 0.0025mm/s to achieve the equivalent strain rate to retain consistency with synchrotron experiments (10^{-4} and 10^{-3} s^{-1}). Break detection was employed to identify the point of failure.

Broken specimens were viewed through a stereoscopic microscope where a camera was attached to the microscopic optic and photographs were captured. To image the fracture surfaces, a Fujifilm X Pro 1 with a Sigma Mini-Wide II 28mm f2.8 (reverse mounted) with ZY optics Lens Turbo II adapter was employed , this enables a reduced focal length and operates as a macro lens. An additional LED ring light was used to illuminate the specimen from all directions, ensuring even lighting and reducing any visual effects from shadows.

Test	Strain Rate
Fast 10^{-3} s^{-1}	0.025 mm/s
Slow 10^{-4} s^{-1}	0.0025 mm/s
Jump (increase)	0.0025 mm/s to 0.025 mm/s
Jump (decrease)	0.025 mm/s to 0.0025 mm/s

Table B.1: Test parameters set on the Zwick Roell 250kN load frame.

Focus stacking has been used to increase the depth of field available images are combined, this is a digital image processing technique which combines multiple images taken at different focal lengths to give a resulting image with a greater depth of field (DOF) than any of the individual source images. Focus stacking can be incorporated where individual images have a very shallow depth of field; it is often used in macro photography and optical microscopy [81]. Combine ZP software [85] has been used to perform focus stacking.

B.2 Results

The macroscopic stress-strain response for these experiments is shown in Figure B.1 and summarised in Table B.2. These results show a large variation in yield stress despite the fast and decreasing jump tests under identical conditions at this point. The slow (10^{-4} s^{-1}) test has been removed from analysis due to a significant pre-load accidentally applied instantaneously to the specimen. This is unexpected but could be explained by microstructural differences in the individual specimens or surface effects due to EDM manufacture. It has been observed within the research group that the surface finish is indicative of the level of damage where other specimens of this type have seen a reduction in yield stress with visible difference in surface colouration.

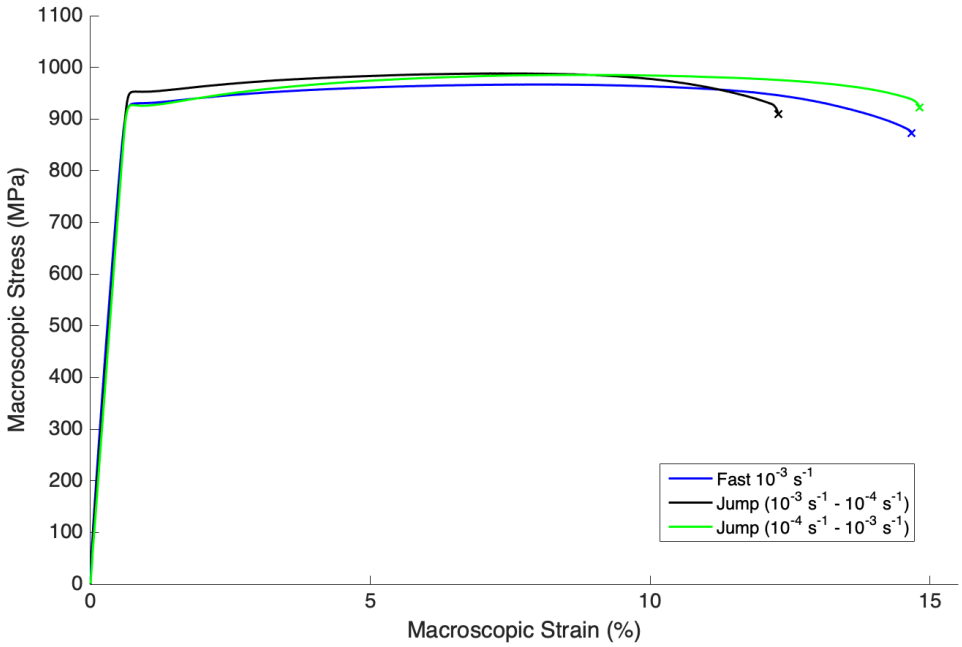


Figure B.1: Macroscopic stress-strain response for successful experiments outlined in Table B.2, the slower strain rate is neglected.

Test	Yield Stress (0.2%)	% Elongation	Material Energy (kJ/m^3)
Fast (10^{-4} s^{-1})	966.8 MPa	14.67 %	13.662
Jump (increase)	988.2 MPa	12.29 %	11.653
Jump (decrease)	985.4 MPa	14.81 %	14.025

Table B.2: Young's Modulus, % elongation at failure and total strain energy for each of the tests on UDR Ti-6Al-4V.

Toughness is defined by area under the stress-strain curve, this is defined as the mechanical energy the material can sustain before failure [31]. The calculated material energy and elongation at break suggests that the increase in strain rate leads to premature failure. The fracture surfaces for each experiment are shown in Figures B.2 to B.4.

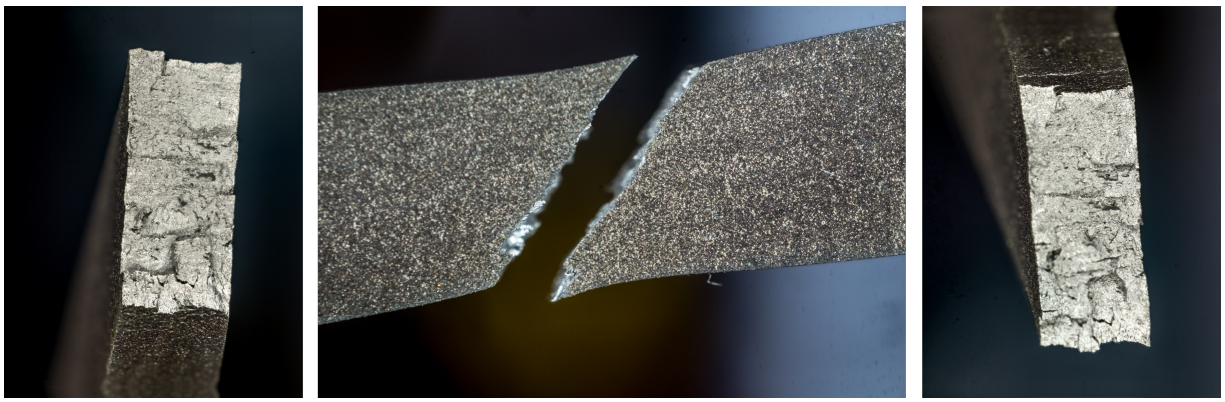


Figure B.2: Image showing result of tensile test to failure at 10^{-3} s^{-1} (higher strain rate).

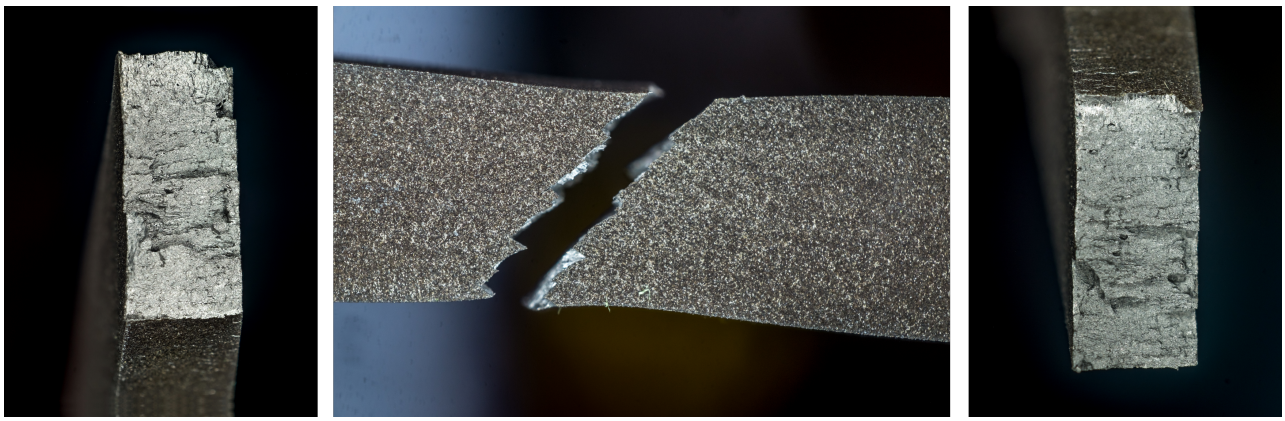


Figure B.3: Image showing fractured specimen resulting from jump in strain rate (10^{-4} s^{-1}).

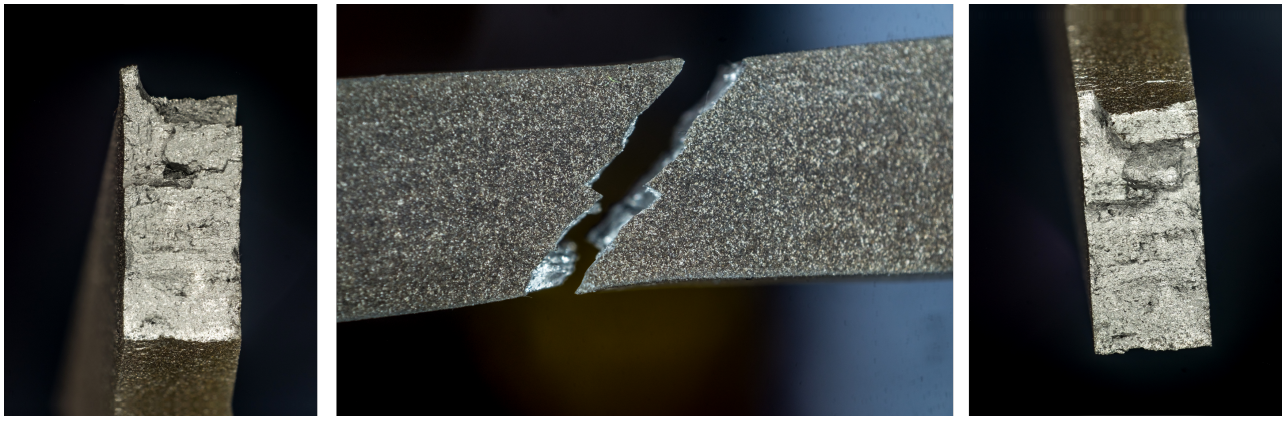


Figure B.4: Image showing result of tensile test to failure at 0.001s^{-1} (higher strain rate).

This preliminary study was used to investigate the effect of the SRJ on failure behaviour. The current results indicate a fairly significant difference in specimen elongation at failure. Repetition of these experiments with multiple samples for each loading regime will establish whether this effect may be substantiated. EBSD and fractographic analysis should be included in the future testing of this jump in strain rate of Ti-6Al-4V. Care must be taken in the analysis of these results as not only is the data set limited but the expectations are that the differences observed would be expected within the normal scatter for this type of experiment.

Bibliography

[1] Titanium alloys for aerospace structures and engines. In A. P. Mouritz, editor, *Introduction to Aerospace Materials*, pages 202 – 223. Woodhead Publishing, 2012.

[2] J. Ahrens, B. Geveci, and C. Law. Paraview: An end-user tool for large data visualization, visualization handbook, 2005.

[3] S. S. Al-Bermani, M. L. Blackmore, W. Zhang, and I. Todd. The origin of microstructural diversity, texture, and mechanical properties in electron beam melted Ti-6Al-4V. *Metallurgical and Materials Transactions A: Physical Metallurgy and Materials Science*, 41(13):3422–3434, 2010.

[4] M. Allahkarami and J. C. Hanan. Three-dimensional x-ray diffraction detection and visualization. *Measurement Science and Technology*, 25(5):1–10, 2014.

[5] C. Andreani, M. Krzystyniak, G. Romanelli, R. Senesi, and F. Fernandez-Alonso. Electron-volt neutron spectroscopy: beyond fundamental systems. *Advances in Physics*, 66(1):1–73, 2017.

[6] R. A. Antunes, C. A. F. Salvador, and M. C. L. de Oliveira. Materials selection of optimized titanium alloys for aircraft applications. *Materials Research, Ibero-american Journal of Materials*, 21(2):1–9, 2018.

[7] A. Arsenlis and D. M. Parks. Crystallographic aspects of geometrically-necessary and statistically-stored dislocation density. *Acta Materialia*, 47(5):1597–1611, 1999.

[8] A. Arsenlis and D. M. Parks. Modeling the evolution of crystallographic dislocation density in crystal plasticity. *Journal of the Mechanics and Physics of Solids*, 50(9):1979–2009, 2002.

[9] M. F. Ashby. The deformation of plastically non-homogeneous materials. *Philosophical Magazine*, 21(170):399–424, 1970.

[10] P. J. Ashton, T. S. Jun, Z. Zhang, T. B. Britton, A. M. Harte, S. B. Leen, and F. P. Dunne. The effect of the beta phase on the micromechanical response of dual-phase titanium alloys. *International Journal of Fatigue*, 100:377–387, 2017.

[11] A. Attanasio, M. Gelfi, A. Pola, E. Ceretti, and C. Giardini. Influence of material microstructures in micromilling of Ti6Al4V alloy. *Materials*, 6(9):4268–4283, 2013.

[12] M. Bache and W. Evans. Impact of texture on mechanical properties in an advanced titanium alloy. *Materials Science and Engineering: A*, 319:409–414, 2001.

[13] A. L. Bail, I. Madsen, L. M. D. Cranswick, J. K. Cockcroft, P. Norby, A. D. Zuev, A. Fitch, J. Rodriguez-Carvajal, C. Giacovazzo, and R. B. e. a. Von Dreele. *Powder Diffraction: Theory and Practice*. Royal Society of Chemistry, 2015.

[14] S. Balasubramanian and L. Anand. Plasticity of initially textured hexagonal polycrystals at high homologous temperatures: Application to titanium. *Acta Materialia*, 50(1):133–148, 2002.

[15] D. Banabic. *Multiscale Modelling in Sheet Metal Forming*. ESAFORM Bookseries on Material Forming. Springer International Publishing, 2016.

[16] D. Banerjee and J. C. Williams. Microstructure and Slip Character in Titanium Alloys. *Defence Science Journal*, 36(2):191–206, 1986.

[17] P. Barnes, S. Jacques, and M. Vickers. *Introduction to Powder Diffraction*. Birkbeck College, University of London., 2006.

[18] A. S. Batsanov. Small Molecule Applications of X-Ray Diffraction. In *Encyclopedia of Spectroscopy and Spectrometry*, pages 2550–2558. 2010.

[19] H. Baur, D. B. Wortberg, and H. Clemens. Titanium aluminides for automotive applications. *Gamma Titanium Aluminides 2003*, pages 23–31, 2003.

[20] J. V. Bernier, N. R. Barton, U. Lienert, and M. P. Miller. Far-field high-energy diffraction microscopy: A tool for intergranular orientation and strain analysis. *Journal of Strain Analysis for Engineering Design*, 46(7):527–547, 2011.

[21] J. V. Bernier, D. Dale, N. R. Barton, and D. E. Boyce. Praxes/hexrd, 2018.

[22] J. Bishop and R. Hill. A theoretical derivation of the plastic properties of a polycrystalline face-centred metal. *The London, Edinburgh, and Dublin Philosophical Magazine and Journal of Science*, 42(334):1298–1307, 1951.

[23] N. Bourne. Viewpoint:unexpected twins. *Physics*, 9:17–19, 2016.

[24] R. Boyer. An overview on the use of titanium in the aerospace industry. *Materials Science and Engineering: A*, 213(1-2):103–114, aug 1996.

[25] R. P. Brent. Algorithms for Minimization Without Derivatives. *IEEE Transactions on Automatic Control*, 19(5):632–633, 1974.

[26] L. N. Brewer, D. P. Field, and C. C. Merriman. Mapping and assessing plastic deformation using EBSD. In *Electron Backscatter Diffraction in Materials Science*, pages 251–262. Springer, 2009.

[27] F. Bridier, P. Villechaise, and J. Mendez. Analysis of the different slip systems activated by tension in a α/β titanium alloy in relation with local crystallographic orientation. *Acta Materialia*, 53(3):555–567, 2005.

[28] F. Bridier, P. Villechaise, and J. Mendez. Slip and fatigue crack formation processes in an α/β titanium alloy in relation to crystallographic texture on different scales. *Acta Materialia*, 56(15):3951–3962, 2008.

[29] T. Britton, J. Jiang, Y. Guo, A. Vilalta-Clemente, D. Wallis, L. Hansen, A. Winkelmann, and A. Wilkinson. Tutorial: Crystal orientations and ebsd — or which way is up? *Materials Characterization*, 117:113 – 126, 2016.

[30] G. Bruno and B. D. Dunn. The precise measurement of Ti6Al4V microscopic elastic constants by means of neutron diffraction. *Measurement Science and Technology*, 8(11):1244–1249, 1997.

[31] W. Callister and D. Rethwisch. *Materials science and engineering: An Introduction, 7th Edition*. 2007.

[32] J. Capus. Titanium powder developments for am - a round-up. *Metal Powder Report*, 72(6):384–388, nov 2017.

[33] B. E. Carroll, T. A. Palmer, and A. M. Beese. Anisotropic tensile behavior of Ti-6Al-4V components fabricated with directed energy deposition additive manufacturing. *Acta Materialia*, 87:309–320, 2015.

[34] P. Castany, F. Pettinari-Sturmel, J. Crestou, J. Douin, and A. Coujou. Experimental study of dislocation mobility in a Ti-6Al-4V alloy. *Acta Materialia*, 55(18):6284–6291, 2007.

[35] K. S. Chan. Toughening mechanisms in titanium aluminides. *Metallurgical Transactions A*, 24(3):569–583, 1993.

[36] P. Chapelle, C. Noël, A. Risacher, J. Jourdan, A. Jardy, and J. Jourdan. Optical investigation of the behavior of the electric arc and the metal transfer during vacuum remelting of a Ti alloy. *Journal of Materials Processing Technology*, 214(11):2268–2275, 2014.

[37] I. Chattoraj. Stress corrosion cracking (SCC) and hydrogen-assisted cracking in titanium alloys. *Stress Corrosion Cracking*, pages 381–408, jan 2011.

[38] A. K. Cheetham and A. P. Wilkinson. Synchrotron x-ray and neutron diffraction studies in solid-state chemistry. *Angewandte Chemie International Edition in English*, 31(12):1557–1570, 1992.

[39] J. Christian and S. Mahajan. Deformation twinning. *Progress in Materials Science*, 39(1):1–157, 1995.

[40] Y. B. Chun, M. Battaini, C. H. Davies, and S. K. Hwang. Distribution characteristics of in-grain misorientation axes in cold-rolled commercially pure titanium and their correlation with active slip modes. *Metallurgical and Materials Transactions A: Physical Metallurgy and Materials Science*, 41(13):3473–3487, 2010.

[41] B. Clausen, T. Lorentzen, M. A. Bourke, and M. R. Daymond. Lattice strain evolution during uniaxial tensile loading of stainless steel. *Materials Science and Engineering: A*, 259(1):17–24, jan 1999.

[42] F. Coghe, W. Tirry, L. Rabet, and P. Van Houtte. Comparison of low and high strain rate deformation mechanisms and texture evolution for a textured Ti6Al4V alloy. *DYMAT 2009 - 9th International Conferences on the Mechanical and Physical Behaviour of Materials under Dynamic Loading*, 2(September 2015):1145–1151, 2009.

[43] G. Correlate. Gom—precise industrial 3d metrology, 2018.

[44] B. D. Cullity and S. R. Stock. *Elements of X-ray diffraction, 3rd edition*. 2001.

[45] J. S. Dai. Euler-Rodrigues formula variations, quaternion conjugation and intrinsic connections. *Mechanism and Machine Theory*, 92:144–152, 2015.

[46] P. S. Davies, B. P. Wynne, M. J. Thomas, and W. M. Rainforth. Quantifying Crystallographic Texture Variation in a Titanium Billet. *IOP Conference Series: Materials Science and Engineering*, 375(1), 2018.

[47] J. R. Davis. *Tensile Testing*. ASM International, 2nd edition edition, 2004.

[48] P. Dawson and D. Boyce. Polycrystal simulation software odf/pf function set., 2011.

[49] P. R. Dawson and D. E. Boyce. Fepx - finite element polycrystals theory, finite element formulation, numerical implementation and illustrative examples. *arXiv [cond-mat.mtrl-sci]*, pages 1–42, 2015.

[50] P. R. Dawson, D. E. Boyce, J.-S. Park, E. Wielewski, and M. P. Miller. Determining the strengths of HCP slip systems using harmonic analyses of lattice strain distributions. *Acta Materialia*, 144:92–106, 2017.

[51] P. R. Dawson, D. E. Boyce, J. S. Park, E. Wielewski, and M. P. Miller. Determining the strengths of HCP slip systems using harmonic analyses of lattice strain distributions. *Acta Materialia*, 144:92–106, 2018.

[52] M. R. Daymond and N. W. Bonner. Lattice strain evolution in IMI 834 under applied stress. *Materials Science and Engineering A*, 340(1-2):272–280, 2003.

[53] G. E. Dieter. *Mechanical Fundamentals*. 1988.

[54] W. Dietrich and H. Stephan. Electron beam melting and casting, 2008.

[55] R. Dingreville, R. A. Karnesky, G. Puel, and J.-H. Schmitt. Review of the synergies between computational modeling and experimental characterization of materials across length scales. *Journal of Materials Science*, 51(3):1178–1203, 2016.

[56] S. Djanarthany, J. C. Viala, and J. Bouix. An overview of monolithic titanium aluminides based on Ti3Al and TiAl, 2001.

[57] J. Donachie and J. M. Titanium - a technical guide. *ASM International 2nd edition*, 55(11):1023–1026, 2000.

[58] V. Doquet and B. Barkia. Combined AFM, SEM and crystal plasticity analysis of grain boundary sliding in titanium at room temperature. *Mechanics of Materials*, 103:18–27, 2016.

[59] R. M. Duncan, P. A. Blenkinsop, and R. E. Goosey. *Titanium Alloys*, pages 63–87. Springer Netherlands, Dordrecht, 1981.

[60] M. P. Echlin, J. C. Stinville, V. M. Miller, W. C. Lenthe, and T. M. Pollock. Incipient slip and long range plastic strain localization in microtextured Ti-6Al-4V titanium. *Acta Materialia*, 114:164–175, 2016.

[61] EDAX. OIM Analysis 5.3 (Manual), 2007.

[62] E. El-Magd. Mechanical properties at high strain rates. *Journal de Physique IV Colloque*, 04, 1994.

[63] T. F. Engineer.

[64] Engineering ToolBox. Metals and alloys - densities. [online], 2004.

[65] O. Engler and V. Randle. *Introduction to Texture Analysis: Macrotexture, Microtexture, and Orientation Mapping, Second Edition*. CRC Press, 2009.

[66] T. Erinosho, D. Collins, A. Wilkinson, R. Todd, and F. Dunne. Assessment of X-ray diffraction and crystal plasticity lattice strain evolutions under biaxial loading. *International Journal of Plasticity*, 83:1–18, 2016.

[67] J. D. Eshelby. The Determination of the Elastic Field of an Ellipsoidal Inclusion, and Related Problems. *Proceedings of the Royal Society A: Mathematical, Physical and Engineering Sciences*, 241(1226):376–396, 1957.

[68] D. Eylon, S. Fujishiro, P. J. Postans, and F. H. Froes. High-temperature titanium alloys - a review. *JOM: Journal of The Minerals, Metals & Materials Society*, 36(11):55–62, 1984.

[69] K. Firm, R. Boyer, and G. Welsch. *Materials Properties Handbook: Titanium Alloys*. 1994.

[70] A. Fitzner. Effects of alloying elements on twinning in alpha titanium alloys. *University of Manchester*, PhD Thesis:313, 2014.

[71] A. Fitzner, D. G. Prakash, J. Q. Da Fonseca, M. Thomas, S. Y. Zhang, J. Kelleher, P. Manuel, and M. Preuss. The effect of aluminium on twinning in binary alpha-titanium. *Acta Materialia*, 103:341–351, 2016.

[72] H. M. Flower. *High Performance Materials in Aerospace*. Springer, Netherlands, 2012.

[73] P. S. Follansbee and G. T. Gray. An analysis of the low temperature, low and high strain-rate deformation of Ti-6Al-4V. *Metallurgical Transactions A*, 20(5):863–874, 1989.

[74] F. H. Froes. *Titanium: Physical Metallurgy, Processing, and Applications*. EngineeringPro collection. A S M International, 2015.

[75] J. Galan-Lopez, S. Naghdy, P. Verleysen, L. A. Kestens, F. Coghe, L. Rabet, and J. Degrieck. Mechanical behavior and texture prediction of Ti-6Al-4V based on elastic viscoplastic self-consistent modelling. *IOP Conference Series: Materials Science and Engineering*, 82(1), 2015.

[76] H. Gao and Y. Huang. Geometrically necessary dislocation and size-dependent plasticity. *Scripta Materialia*, 48(2):113–118, 2003.

[77] S. Ghosh, A. Shahba, X. Tu, E. L. Huskins, and B. E. Schuster. Crystal plasticity FE modeling of Ti alloys for a range of strain-rates. Part II: Image-based model with experimental validation. *International Journal of Plasticity*, 87:69–85, 2016.

[78] M. Glavicic, B. Bartha, S. Jha, and C. Szczepanski. The origins of microtexture in duplex Ti alloys. *Materials Science and Engineering: A*, 513-514:325–328, 2009.

[79] D. Gloaguen, B. Girault, J. Fajoui, V. Klosek, and M. Moya. In situ lattice strains analysis in titanium during a uniaxial tensile test. *Materials Science & Engineering A*, 662:395–403, 2016.

[80] D. Gloaguen, G. Oum, V. Legrand, J. Fajoui, M. J. Moya, T. Pirling, and W. Kockelmann. Intergranular strain evolution in titanium during tensile loading: Neutron diffraction and polycrystalline model. *Metallurgical and Materials Transactions A: Physical Metallurgy and Materials Science*, 46(11):5038–5046, 2015.

[81] N. T. Goldsmith. Deep Focus; a Digital Image Processing Technique To Produce Improved Focal Depth in Light Microscopy. *Image Analysis & Stereology*, 19(3):163–167, 2000.

[82] J. Gong and A. J. Wilkinson. Anisotropy in the plastic flow properties of single-crystal α titanium determined from micro-cantilever beams. *Acta Materialia*, 57(19):5693–5705, 2009.

[83] A. A. M. Group). Titanium aluminides.

[84] L. Guo, X. Fan, G. Yu, and H. Yang. Microstructure control techniques in primary hot working of titanium alloy bars: A review. *Chinese Journal of Aeronautics*, 29(1):30–40, 2016.

[85] A. Hadley. CombineZP Software. http://www.hadleyweb.pwp.blueyonder.co.uk/, 2010. Accessed: 05 2016.

[86] T. S. Han and P. R. Dawson. Lattice strain partitioning in a two-phase alloy and its redistribution upon yielding. *Materials Science and Engineering A*, 405(1-2):18–33, 2005.

[87] E. Hart. Theory of the tensile test. *Acta Metallurgica*, 15(2):351–355, feb 1967.

[88] U. Hejral, P. Müller, M. Shipilin, J. Gustafson, D. Franz, R. Shayduk, U. Rütt, C. Zhang, L. R. Merte, E. Lundgren, V. Vonk, and A. Stierle. High-energy x-ray diffraction from surfaces and nanoparticles. *Phys. Rev. B*, 96:195433, 2017.

[89] S. Hémery, A. Nait-Ali, M. Gueguen, and P. Villechaise. Mechanical study of crystalline orientation distribution in Ti-6Al-4V: An assessment of micro-texture induced load partitioning. *Materials & Design*, 137:22–32, 2018.

[90] D. Hull and D. J. Bacon. 8 - Origin and Multiplication of Dislocations. In D. Hull and D. J. Bacon, editors, *Introduction to Dislocations (Fourth Edition)*, pages 145–156. Butterworth-Heinemann, Oxford, fourth edition edition, 2001.

[91] I. Inagaki, T. Tsutomu, S. Yoshihisa, and A. Nozomu. Application and Features of Titanium for the Aerospace Industry. *Nippon Steel & Sumitomo Metal Technical Report*, 106:22–27, 2014.

[92] Ishii, M, Ando, Y, Nagai, I. Vacuum creep flattening of titaium and titanium alloy plates. *Nippon Steel Technical Report*, No. 62:46–51, 1994.

[93] E. C. Jameson. Electrical Discharge Machining. 2001.

[94] M. Johnson. 3D Characterization of Ti-6Al-4V using the TriBeam System . 2013.

[95] T.-S. Jun, Z. Zhang, G. Sernicola, F. P. Dunne, and T. B. Britton. Local strain rate sensitivity of single α phase within a dual-phase Ti alloy. *Acta Materialia*, 107:298–309, 2016.

[96] W. Kabsch. Evaluation of single-crystal X-ray diffraction data from a position-sensitive detector. *Journal of Applied Crystallography*, 21(6):916–924, 1988.

[97] S. R. Kalidindi. Incorporation of deformation twinning in crystal plasticity models. *Journal of the Mechanics and Physics of Solids*, 46(2):267–290, 1998.

[98] K. Kapoor, Y. S. J. Yoo, T. A. Book, J. P. Kacher, and M. D. Sangid. Incorporating grain-level residual stresses and validating a crystal plasticity model of a two-phase Ti-6Al-4V alloy produced via additive manufacturing. *Journal of the Mechanics and Physics of Solids*, 121:447–462, 2018.

[99] M. Kasemer, M. P. Echlin, J. C. Stinville, T. M. Pollock, and P. Dawson. On slip initiation in equiaxed α/β Ti-6Al-4V. *Acta Materialia*, 136:288–302, 2017.

[100] U. R. Kattner. The calphad method and its role inmaterial and process development. *Tecnologia em Metalurgia Materiais e Mineração*, 13(1):3–15, 2016.

[101] C. Kepler, Johannes. Translated by Hardie. De Nive Sexangula [The Six-sided Snowflake], 1966.

[102] A. S. Khan and S. Huang. *Continuum Theory of Plasticity*. New York Wiley Interscience, 1995.

[103] A. S. Khan, Y. Sung Suh, and R. Kazmi. Quasi-static and dynamic loading responses and constitutive modeling of titanium alloys. *International Journal of Plasticity*, 20(12):2233–2248, 2004.

[104] S. Kikuchi, K. Takemura, Y. Hayami, A. Ueno, and K. Ameyama. Evaluation of the fatigue properties of ti6al4valloy with harmonic structure in 4-points bending. *Journal of the Society of Materials Science, Japan*, 64(11):880–886, 2015.

[105] W. E. King, G. Campbell, T. Gonis, G. Henshall, D. Lesuer, E. Zywicz, and S. Foiles. Theory, simulation, and modeling of interfaces in materials-bridging the length-scale gap: a workshop report. *Materials Science and Engineering A*, 191(1-2):1–16, 1995.

[106] M. Knezevic, R. A. Lebensohn, O. Cazacu, B. Revil-Baudard, G. Proust, S. C. Vogel, and M. E. Nixon. Modeling bending of α-titanium with embedded polycrystal plasticity in implicit finite elements. *Materials Science and Engineering A*, 564:116–126, 2013.

[107] F. Kocks, C. Tomé, and H.-R. Wenk. *Texture and Anisotropy. Preferred Orientations in Polycrystals and Their Effect on Material Properties*. 2000.

[108] U. F. Kocks. The relation between polycrystal deformation and single-crystal deformation. *Metallurgical and Materials Transactions*, 1(5):1121–1143, 1970.

[109] D. E. Kramer, M. F. Savage, and L. E. Levine. AFM observations of slip band development in Al single crystals. *Acta Materialia*, 53(17):4655–4664, 2005.

[110] M. Kraska, M. Doig, D. Tikhomirov, D. Raabe, and F. Roters. Virtual material testing for stamping simulations based on polycrystal plasticity. *Computational Materials Science*, 46(2):383–392, 2009.

[111] W. Kroll. The Production of Ductile Titanium. *Transactions of The Electrochemical Society*, 78(1):35, 1940.

[112] E. Kröner. Zur plastischen verformung des vielkristalls. *Acta Metallurgica*, 9(2):155–161, 1961.

[113] A. Kumar and P. R. Dawson. Modeling crystallographic texture evolution with finite elements over neo-Eulerian orientation spaces. *Computer Methods in Applied Mechanics and Engineering*, 153(3-4):259–302, 1998.

[114] W. M. Lai, D. Rubin, and E. Krempl. *Introduction to Continuum Mechanics*. 2010.

[115] S. J. Laine. *The Role of Twinning in the Plastic Deformation of Alpha Phase Titanium*. 2017.

[116] S. J. Lainé. The role of twinning in the plastic deformation of alpha phase titanium. *University of Cambridge*, PhD Thesis:224, 2017.

[117] T. G. Langdon. Grain boundary sliding as a deformation mechanism during creep. *The Philosophical Magazine: A Journal of Theoretical Experimental and Applied Physics*, 22(178):689–700, 1970.

[118] D. E. Laughlin and K. Hono. *Physical Metallurgy*. Elsevier Science, 2014.

[119] K. Le Biavant, S. Pommier, and C. Prioul. Local texture and fatigue crack initiation in a Ti-6Al-4V titanium alloy. *Fatigue and Fracture of Engineering Materials and Structures*, 25(6):527–545, 2002.

[120] K. Le Biavant, S. Pommier, and C. Prioul. Local texture and fatigue crack initiation in a Ti-6Al-4V titanium alloy. *Fatigue & Fracture of Engineering Materials & Structures*, 25(6):527–545, 2002.

[121] R. A. Lebensohn, P. P. Castañeda, R. Brenner, and O. Castelnau. *Computational Methods for Microstructure-Property Relationships*, chapter Full-Field vs. Homogenization Methods to Predict Microstructure–Property Relations for Polycrystalline Materials, pages 393–441. Springer US, Boston, MA, 2011.

[122] R. A. Lebensohn and C. N. Tomé. A self-consistent viscoplastic model: prediction of rolling textures of anisotropic polycrystals. *Materials Science and Engineering A*, 175(1-2):71–82, 1994.

[123] R. A. Lebensohn, M. Zecevic, M. Knezevic, and R. J. McCabe. Average intragranular misorientation trends in polycrystalline materials predicted by a viscoplastic self-consistent approach. *Acta Materialia*, 104:228–236, 2016.

[124] Lederich, R.J., Sastry, S. M.L., O'Neal, J. E., Rath, B.B. The Effect of Grain Size on Yield Stress and Work Hardening of Polycrystalline Titanium at 295 K and 575 K. *Materials Science and Engineering*, 33:183 – 188, 1978.

[125] E. M. Lehockey, Y.-P. Lin, and O. E. Lepik. *Mapping Residual Plastic Strain in Materials Using Electron Backscatter Diffraction*, pages 247–264. Springer US, Boston, MA, 2000.

[126] U. Lienert, M. C. Brandes, J. V. Bernier, J. Weiss, S. D. Shastri, M. J. Mills, and M. P. Miller. In situ single-grain peak profile measurements on Ti-7Al during tensile deformation. *Materials Science and Engineering A*, 524(1-2):46–54, 2009.

[127] U. Lienert, S. F. Li, C. M. Hefferan, J. Lind, R. M. Suter, J. V. Bernier, N. R. Barton, M. C. Brandes, M. J. Mills, M. P. Miller, B. Jakobsen, and W. Pantleon. High-energy diffraction microscopy at the advanced photon source. *The Journal of The Minerals, Metals Materials Society*, 63(7):70–77, 2011.

[128] P. Littlewood, T. Britton, and A. Wilkinson. Geometrically necessary dislocation density distributions in Ti–6Al–4V deformed in tension. *Acta Materialia*, 59(16):6489–6500, 2011.

[129] D. Lunt. The effect of macrozones in Ti-6Al-4V on the strain localisation behaviour. *[Thesis]. Manchester, UK: The University of Manchester; 2015.*, 2014.

[130] D. Lunt, J. Q. da Fonseca, D. Rugg, and M. Preuss. Microscopic strain localisation in Ti-6Al-4V during uniaxial tensile loading. *Materials Science and Engineering: A*, 680:444–453, jan 2017.

[131] J. Luo, M. Li, W. Yu, and H. Li. The variation of strain rate sensitivity exponent and strain hardening exponent in isothermal compression of Ti-6Al-4V alloy. *Materials and Design*, 31(2):741–748, 2010.

[132] G. Lütjering and J. Williams. *Titanium*. Springer Science & Business Media, 2007.

[133] S. Mahajan and D. F. Williams. Deformation Twinning in Metals and Alloys. *International Metallurgical Reviews*, 18(2):43–61, 1973.

[134] S. S. Mahapatra and A. Patnaik. Optimization of wire electrical discharge machining (WEDM) process parameters using Taguchi method. *International Journal of Advanced Manufacturing Technology*, 34(9-10):911–925, 2007.

[135] A. Mangal and E. A. Holm. Applied Machine Learning to Predict Stress Hotspots II : Hexagonal close packed materials. *International Journal of Plasticity, Pre-print*, 2018.

[136] A. Marmi, A. Habraken, and L. Duchene. Multiaxial fatigue damage modelling at macro scale of Ti–6Al–4V alloy. *International Journal of Fatigue*, 31(11-12):2031–2040, 2009.

[137] J. K. Mason and C. A. Schuh. Representations of texture. In *Electron Backscatter Diffraction in Materials Science*, pages 35–51. 2009.

[138] J. Matthew and J. Donachie. Heat treating titanium and its alloys. *ASM international*, pages 47–57, 2001.

[139] N. McCormick and J. Lord. Digital Image Correlation. *Materials Today*, 13(12):52–54, 2010.

[140] M. K. McQuillan. Phase transformations in titanium and its alloys. *Metallurgical Reviews*, 8(1):41–104, 1963.

[141] M. P. Miller and P. R. Dawson. Understanding local deformation in metallic polycrystals using high energy x-rays and finite elements. *Current Opinion in Solid State and Materials Science*, 18(5):286–299, 2014.

[142] W. H. Miller. *A Treatise on Crystallography*. J. & J. J. Deighton, Trinity Street, Londond, 1839.

[143] A. Molinari, G. R. Canova, and S. Ahzi. A self consistent approach of the large deformation polycrystal viscoplasticity. *Acta Metallurgica*, 35(12):2983–2994, 1987.

[144] A. Moreau, L. Toubal, P. Bocher, M. Humbert, E. Uta, and N. Gey. Evaluation of macrozone dimensions by ultrasound and EBSD techniques. *Materials Characterization*, 75:115–128, 2013.

[145] H. Motra, J. Hildebrand, and A. Dimmig-Osburg. Assessment of strain measurement techniques to characterise mechanical properties of structural steel. *Engineering Science and Technology, an International Journal*, 17(4):260–269, 2014.

[146] T. M. Mower. Degradation of titanium 6Al-4V fatigue strength due to electrical discharge machining. *International Journal of Fatigue*, 64:84–96, 2014.

[147] J. D. Murray and W. vanRyper. *Encyclopedia of Graphics File Formats (2Nd Ed.)*. O'Reilly & Associates, Inc., Sebastopol, CA, USA, 1996.

[148] I. A. L. Nadai. The Flow of Metals under Various Stress Conditions. *Proceedings of the Institution of Mechanical Engineers*, 157(1):121–160, 1947.

[149] R. K. Nalla, I. Altenberger, U. Noster, G. Y. Liu, B. Scholtes, and R. O. Ritchie. On the influence of mechanical surface treatments-deep rolling and laser shock peening-on the fatigue behavior of Ti-6Al-4V at ambient and elevated temperatures. *Materials Science and Engineering A*, 355(1-2):216–230, 2003.

[150] T. Neeraj, M. Savage, J. Tatalovich, L. Kovarik, R. Hayes, and M. Mills. Observation of tension–compression asymmetry in α and $\alpha - \beta$ titanium alloys. *Philosophical Magazine*, 85(2-3):279–295, 2005.

[151] L. Nervo, A. King, A. Fitzner, W. Ludwig, and M. Preuss. A study of deformation twinning in a titanium alloy by X-ray diffraction contrast tomography. *Acta Materialia*, 105:417–428, 2016.

[152] M. Niinomi. Recent research and development in titanium alloys for biomedical applications and healthcare goods. *Science and Technology of Advanced Materials*, 4(5):445–454, 2003.

[153] M. E. Nixon, O. Cazacu, and R. A. Lebensohn. Anisotropic response of high-purity α-titanium: Experimental characterization and constitutive modeling. *International Journal of Plasticity*, 2010.

[154] J. Nye. *Physical Properties of Crystals: Their Representation by Tensors and Matrices*. Oxford University Press, 1957.

[155] G. Obasi, R. Moat, D. Leo Prakash, W. Kockelmann, J. Quinta Da Fonseca, and M. Preuss. In situ observation on the influence of β grain growth on texture evolution during phase transformation in Ti-6A-4V. *Materials Science Forum*, 702-703, 2012.

[156] A. V. Oppenheim, R. W. Schafer, and J. R. Buck. *Discrete-time Signal Processing (2Nd Ed.)*. Prentice-Hall, Inc., Upper Saddle River, NJ, USA, 1999.

[157] A. Orozco-Caballero, F. Li, D. Esqué-de los Ojos, M. D. Atkinson, and J. Quinta da Fonseca. On the ductility of alpha titanium: The effect of temperature and deformation mode. *Acta Materialia*, 149:1–10, 2018.

[158] Oxford Instruments. Basics of automated indexing. http://www.ebsd.com/ebsd-explained/basics-of-automated-indexing, Accessed: Mar 2018.

[159] D. C. Pagan, P. A. Shade, N. R. Barton, J.-S. Park, P. Kenesei, D. B. Menasche, and J. V. Bernier. Modeling slip system strength evolution in Ti-7Al informed by in-situ grain stress measurements. *Acta Materialia*, 128:406–417, 2017.

[160] S. Papanikolaou, Y. Cui, and N. Ghoniem. Avalanches and plastic flow in crystal plasticity: an overview. *Modelling and Simulation in Materials Science and Engineering*, 26(1):13001, 2018.

[161] V. K. Pecharsky and Z. et al. *Fundamentals of Powder Diffraction and Structural Characterization of Materials, Second Edition*, volume 940. 2008.

[162] I. P. Polmear. Light Alloys - From Traditional Alloys to Nanocrystals. *Light Alloys*, 2:273–277, 2006.

[163] E. Poulsen. Safety-related problems in the titanium industry in the last 50 years. *Journal of The Minerals, Metals & Materials Society (JOM)*, pages 13–17, 2000.

[164] F. Povolo. On the measurement of the strain-rate sensitivity parameter with a tensile test. *Journal of Nuclear Materials*, 78(2):309–314, 1978.

[165] A. Powell, J. Van Den Avyle, B. Damkroger, J. Szekely, and U. Pal. Analysis of multicomponent evaporation in electron beam melting and refining of titanium alloys. *Metallurgical & Materials Transactions B*, 28:1227–1239, 1997.

[166] A. C. Powell. Transport Phenomena in Electron Beam Melting and Evaporation. *Materials Science and Engineering*, 1992.

[167] D. G. Prakash, R. Ding, R. J. Moat, I. Jones, P. J. Withers, J. Q. da Fonseca, and M. Preuss. Deformation twinning in Ti-6Al-4V during low strain rate deformation to moderate strains at room temperature. *Materials Science and Engineering A*, 527(21-22):5734–5744, 2010.

[168] A. Pramanik, M. Islam, A. Basak, and G. Littlefair. *Engineering Materials and Application*, volume 651 of *Advanced Materials Research*. Trans Tech Publications, 3 2013.

[169] R. Quey. Neper Reference Manual 2.0.1. 2014.

[170] R. Quey and L. Renversade. Optimal polyhedral description of 3D polycrystals: Method and application to statistical and synchrotron X-ray diffraction data. *Computer Methods in Applied Mechanics and Engineering*, 330:308–333, 2018.

[171] K. P. Rajurkar and B. Zhang. The electrical discharge machining (edm) handbook. *Machining Science and Technology*, 3(1):141–142, 1999.

[172] J. Raphanel and P. Van Houtte. Simulation of the rolling textures of bcc metals by means of the relaxed taylor theory. *Acta Metallurgica*, 33(8):1481–1488, 1985.

[173] W. Rasband. ImageJ. *U. S. National Institutes of Health, Bethesda, Maryland, USA*, page 113903, 1997-2016.

[174] T. Richeton. Incompatibility Stresses and Lattice Rotations Due to Grain Boundary Sliding in Heterogeneous Anisotropic Elasticity. *Crystals*, (7), 2017.

[175] F. Roters, P. Eisenlohr, L. Hantcherli, D. D. Tjahjanto, T. R. Bieler, and D. Raabe. Overview of constitutive laws, kinematics, homogenization and multiscale methods in crystal plasticity finite-element modeling: Theory, experiments, applications. *Acta Materialia*, 58(4):1152–1211, 2010.

[176] A. M. Sabatini. Estimating three-dimensional orientation of human body parts by inertial/magnetic sensing. *Sensors*, 11(2):1489–1525, 2011.

[177] A. K. Sachdev, K. Kulkarni, Z. Z. Fang, R. Yang, and V. Girshov. Titanium for Automotive Applications: Challenges and Opportunities in Materials and Processing. *Journal of The Minerals, Metals Materials Society*, 64(5):553–565, 2012.

[178] G. Sachs. Zur ableitung einer fliessbedingung. *VDIZ 12*, pages 134–136, 1928.

[179] S. E. Schoenfeld and B. Kad. Texture effects on shear response in Ti-6Al-4V plates. *International Journal of Plasticity*, 18(4):461–486, 2002.

[180] J. C. Schuren, P. A. Shade, J. V. Bernier, S. F. Li, B. Blank, J. Lind, P. Kenesei, U. Lienert, R. M. Suter, T. J. Turner, D. M. Dimiduk, and J. Almer. New opportunities for quantitative tracking of polycrystal responses in three dimensions. *Current Opinion in Solid State and Materials Science*, 19(4):235–244, 2015.

[181] J. W. Sears. Current processes for the cold-wall melting of Titanium. *Journal of The Minerals, Metals Materials Society (TMS)*, 42(3):17–21, 1990.

[182] S. L. Semiatin, V. G. Ivanchenko, and O. M. Ivasishin. Diffusion models for evaporation losses during electron-beam melting of alpha/beta-titanium alloys. *Metallurgical and Materials Transactions B*, 35(2):235–245, 2004.

[183] A. Shahba and S. Ghosh. Crystal plasticity FE modeling of Ti alloys for a range of strain-rates. Part I: A unified constitutive model and flow rule. *International Journal of Plasticity*, 87:48–68, 2016.

[184] Y. Shao, L. Zhang, X. Hao, Y. Wu, Y. Dai, Y. Tian, and Q. Huo. Large Area Stress Distribution in Crystalline Materials Calculated from Lattice Deformation Identified by Electron Backscatter Diffraction. *Scientific Reports*, 4:5934, 2014.

[185] O. Sorkine, D. Cohen-Or, Y. Lipman, M. Alexa, C. Rössl, and H.-P. Seidel. Laplacian surface editing. In *Proceedings of the 2004 Eurographics/ACM SIGGRAPH Symposium on Geometry Processing*, SGP '04, pages 175–184. ACM(Association for Computing Machinery), New York, NY, USA, 2004.

[186] A. M. Stapleton, S. L. Raghunathan, I. Bantounas, H. J. Stone, T. C. Lindley, and D. Dye. Evolution of lattice strain in ti-6al-4v during tensile loading at room temperature. *Acta Materialia*, 56(20):6186–6196, 2008.

[187] A. Staroselsky and L. Anand. Inelastic deformation of polycrystalline face centered cubic materials by slip and twinning. *Journal of the Mechanics and Physics of Solids*, 46(4):671–696, 1998.

[188] A. N. Stroh. A theory of the fracture of metals. *Advances in Physics*, 6(24):418–465, 1957.

[189] S. Suwas and N. P. Gurao. *Crystallographic texture in materials*, volume 88. 2008.

[190] S. Suwas and R. K. Ray. *Crystallographic Texture of Materials*. 2014.

[191] E. Svanidze, T. Besara, M. F. Ozaydin, C. S. Tiwary, J. K. Wang, S. Radhakrishnan, S. Mani, Y. Xin, K. Han, H. Liang, T. Siegrist, P. M. Ajayan, and E. Morosan. High hardness in the biocompatible intermetallic compound β-Ti-Au. *Science Advances*, 2(7), 2016.

[192] G. Swislow. X-Ray Diffraction Software User Manual and Tutorials Reference Manual four-circle reference administrator's guide. page 290, 1989.

[193] A. Tabei, F. H. Abed, G. Z. Voyiadjis, and H. Garmestani. Constitutive modeling of Ti-6Al-4V at a wide range of temperatures and strain rates. *European Journal of Mechanics, A/Solids*, 2017.

[194] G. I. Taylor. The Mechanism of Plastic Deformation of Crystals. Part I. Theoretical. *Proceedings of the Royal Society of London A: Mathematical, Physical and Engineering Sciences*, 145(855):362–387, 1934.

[195] G. I. Taylor. Plastic strain in metals. *J. Inst. Metals 62*, pages 307–325, 1938.

[196] Timet Corp. url{http://www.matweb.com/search/DataSheet.aspx?MatGUID=a1fc12bc5d04434a8e617a745f46624b.

[197] Á. G. D. Torre, M. C. Martín-sedeño, L. León-reina, and M. José. Synchrotron X-ray Diffraction in Mineralogy and Materials Chemistry. Possibilities and Applications. 2017.

[198] C. Triantafyllou. The effect of Macrozones on Cold Dwell Fatigue in Ti-6Al-4V. *unpublished*, 2019.

[199] D. Tromans. Elastic Anisotropy of HCP Metal Crystals and Polycrystals. *International Journal of Recent Research and Applied Studies (IJRRAS)*, 6:462–483, 2011.

[200] D. Z. Turner. Digital image correlation engine (dice) reference manual, 2015.

[201] T. J. Turner, P. A. Shade, J. V. Bernier, S. F. Li, J. C. Schuren, J. Lind, U. Lienert, P. Kenesei, R. M. Suter, B. Blank, and J. Almer. Combined near- and far-field high-energy diffraction microscopy dataset for ti-7al tensile specimen elastically loaded in situ. *Integrating Materials and Manufacturing Innovation*, 5(1):5–5, 2016.

[202] T. Ungar, M. G. Glavicic, L. Balogh, K. Nyilas, A. A. Salem, G. Ribarik, and S. L. Semiatin. The use of X-ray diffraction to determine slip and twinning activity in commercial-purity (CP) titanium. *Materials Science and Engineering A*, 493(1-2):79–85, 2008.

[203] A. G. Valdenebro. Visualizing rotations and composition of rotations with the Rodrigues vector. *European Journal of Physics*, 37(6), 2016.

[204] V. Valvoda and U. Voland. Intensities of overlapping peaks in x-ray powder diffraction. *Kristall und Technik*, 16(10):1197–1204, 1981.

[205] P. van Houtte. A Comprehensive mathematical formulation of an extended Taylor-Bishop-Hill model featuring relaxed constraints, the Renouard-Wintenberger theory and a strain rate sensitivity model. *Textures and Microstructures*, 8(9):313–350, 1988.

[206] J. A. Venables. The electron microscopy of deformation twinning. *Journal of Physics and Chemistry of Solids*, 25(7):685–692, 1964.

[207] J. D. Verhoeven. *Fundamentals of physical metallurgy*. Wiley, 1975.

[208] W. J. Vorster, S. Y. Zhang, M. Golshan, D. Laundy, D. Dini, and A. M. Korsunsky. Comparison of X-ray diffraction measurement of residual elastic strains: Monochromatic beam and image plate versus white beam energy-dispersive analysis. *Journal of Strain Analysis for Engineering Design*, 42(1):23–37, 2007.

[209] L. Wang, Z. Zheng, H. Phukan, P. Kenesei, J.-S. Park, J. Lind, R. Suter, and T. Bieler. Direct measurement of critical resolved shear stress of prismatic and basal slip in polycrystalline Ti using high energy X-ray diffraction microscopy. *Acta Materialia*, 132:598–610, 2017.

[210] Y. N. Wang and J. C. Huang. *Materials Chemistry and Physics*. Elsevier Science B.V, 2003.

[211] J. Wehrs, G. Mohanty, G. Guillonneau, A. A. Taylor, X. Maeder, D. Frey, L. Philippe, S. Mischler, J. M. Wheeler, and J. Michler. Comparison of In Situ Micromechanical Strain-Rate Sensitivity Measurement Techniques. *The Journal of The Minerals, Metals & Materials Society (JOM)*, 67(8):1684–1693, 2015.

[212] I. Weiss and S. Semiatin. Thermomechanical processing of beta titanium alloys - an overview. *Materials Science and Engineering: A*, 243(1-2):46–65, 1998.

[213] G. Welsch, R. Boyer, and E. Collings. *Materials Properties Handbook: Titanium Alloys*. Materials properties handbook. ASM International, 1993.

[214] E. Wielewski, D. E. Boyce, J. S. Park, M. P. Miller, and P. R. Dawson. A methodology to determine the elastic moduli of crystals by matching experimental and simulated lattice strain pole figures using discrete harmonics. *Acta Materialia*, 126:469–480, 2017.

[215] E. Wielewski, C. R. Siviour, and N. Petrinic. On the correlation between macrozones and twinning in Ti-6Al-4V at very high strain rates. *Scripta Materialia*, 67(3):229–232, 2012.

[216] A. J. Wilkinson and T. B. Britton. Strains, planes, and EBSD in materials science. *Materials Today*, 15(9):366–376, 2012.

[217] R. L. Williamson. An Overview of SMPC Research Programs to Improve Remelt Ingot Quality. *7th International Symposium on Superalloy 718 and Derivatives*, pages 53–63, 2010.

[218] P. J. Withers. Mapping residual and internal stress in materials by neutron diffraction. 2007.

[219] Z.-H. Wu, H.-C. Kou, B. Tang, J. Shao, F.-B. Han, and J.-S. Li. Crystal plasticity finite-element simulation of ti-6al-4v alloy with 3d polycrystalline models. *2nd AME*, (Ame):321–328, 2016.

[220] J. Wurst and J. A. Nelson. Two-Phase Polycrystalline Ceramics. *Journal of the American Ceramic Society*, 46:1972, 1972.

[221] F. Xu, R. Holt, and M. Daymond. Modeling lattice strain evolution during uniaxial deformation of textured Zircaloy-2. *Acta Materialia*, 56(14):3672–3687, aug 2008.

[222] W. Xu, S. Sun, J. Elambasseril, Q. Liu, M. Brandt, and M. Qian. Ti-6Al-4V Additively Manufactured by Selective Laser Melting with Superior Mechanical Properties. *The Journal of The Minerals, Metals Materials Society*, 67(3):668–673, 2015.

[223] M. Yang, Y. Pan, F. Yuan, Y. Zhu, and X. Wu. Back stress strengthening and strain hardening in gradient structure. *Materials Research Letters*, 4(3):145–151, 2016.

[224] M. H. Yoo and J. K. Lee. Deformation twinning in h.c.p. metals and alloys. *Philosophical Magazine A*, 1991.

[225] S. Zaefferer. A study of active deformation systems in titanium alloys: Dependence on alloy composition and correlation with deformation texture. *Materials Science and Engineering A*, 344(1-2):20–30, 2003.

[226] S. Zaefferer, S. I. Wright, and D. Raabe. Three-dimensional orientation microscopy in a focused ion beam-scanning electron microscope: A new dimension of microstructure characterization. *Metallurgical and Materials Transactions A: Physical Metallurgy and Materials Science*, 39(2):374–389, 2008.

[227] B. Zhang, X. Zhang, C. Li, and K. Zhou. Molecular Dynamics Simulation on Phase Transformation of Ti-Al Alloy with Low Al Content. *Rare Metal Materials and Engineering*, 41(6):1010–1015, jun 2012.

[228] K. Zhang, K. Yang, A. Huang, X. Wu, and C. Davies. Fatigue crack initiation in as forged Ti-6Al-4V bars with macrozones present. *International Journal of Fatigue*, 80:288–297, nov 2015.

[229] M. Zhang, F. Bridier, P. Villechaise, J. Mendez, and D. L. McDowell. Simulation of slip band evolution in duplex ti-6al-4v. *Acta Materialia*, 58(3):1087–1096, 2010.

[230] M. Zhang and D. L. McDowell. Crystal plasticity modelling of ti-6al-4v and its application in cyclic and fretting fatigue analysis. 2008.

[231] Z. Zhang, T.-S. Jun, T. B. Britton, and F. P. E. Dunne. Intrinsic anisotropy of strain rate sensitivity in single crystal alpha titanium. *Acta Materialia*, 118:317–330, 2016.

[232] W. Zhou and K. G. Chew. The rate dependent response of a titanium alloy subjected to quasi-static loading in ambient environment. *Journal of Materials Science*, 37(23):5159–5165, 2002.

[233] O. Zienkiewicz, R. Taylor, and J. Zhu. *The Finite Element Method: Its Basis and Fundamentals, Sixth edition*. Butterworth-Heinemann, 2005.